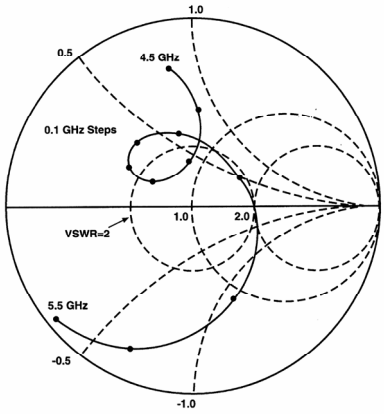


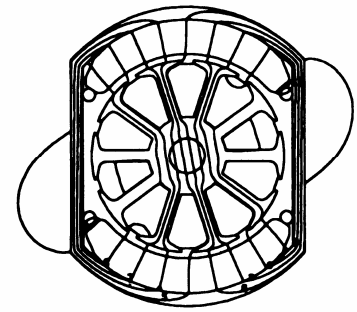

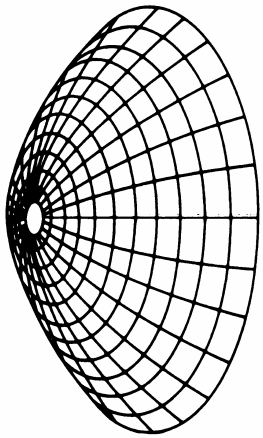

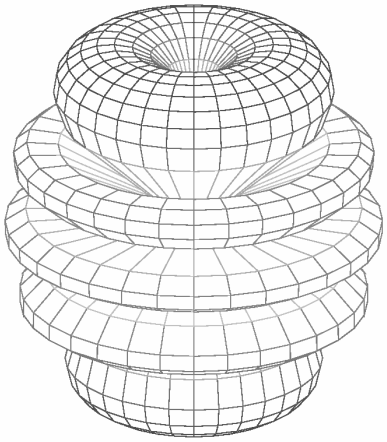

# Applied Computational Electromagnetics Society Journal

Editor-in-Chief
Atef Z. Elsherbeni

Guest Editor
Manos M. Tentzeris

March 2006
Vol. 21 No. 1
ISSN 1054-4887

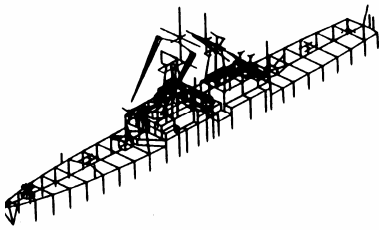

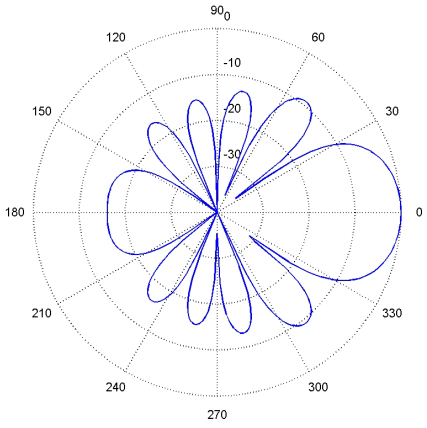

**GENERAL PURPOSE AND SCOPE:** The Applied Computational Electromagnetics Society ***(ACES)*** Journal hereinafter known as the ***ACES Journal*** is devoted to the exchange of information in computational electromagnetics, to the advancement of the state-of-the art, and the promotion of related technical activities. A primary objective of the information exchange is the elimination of the need to "re-invent the wheel" to solve a previously-solved computational problem in electrical engineering, physics, or related fields of study. The technical activities promoted by this publication include code validation, performance analysis, and input/output standardization; code or technique optimization and error minimization; innovations in solution technique or in data input/output; identification of new applications for electromagnetics modeling codes and techniques; integration of computational electromagnetics techniques with new computer architectures; and correlation of computational parameters with physical mechanisms.

**SUBMISSIONS:** The ***ACES Journal*** welcomes original, previously unpublished papers, relating to applied computational electromagnetics. Typical papers will represent the computational electromagnetics aspects of research in electrical engineering, physics, or related disciplines. However, papers which represent research in applied computational electromagnetics itself are equally acceptable.

Manuscripts are to be submitted through the upload system of ***ACES*** web site http://aces.ee.olemiss.edu See "Information for Authors" on inside of back cover and at ***ACES*** web site. For additional information contact the Editor-in-Chief:

**Dr. Atef Elsherbeni**
Department of Electrical Engineering
The University of Mississippi
University, MS 386377 USA
Phone: 662-915-5382 Fax: 662-915-7231
Email: atef@olemiss.edu

**SUBSCRIPTIONS:** All members of the Applied Computational Electromagnetics Society who have paid their subscription fees are entitled to receive the ***ACES Journal*** with a minimum of three issues per calendar year and are entitled to download any published journal article available at http://aces.ee.olemiss.edu.

**Back issues**, when available, are $15 each. Subscriptions to ***ACES*** are through the web site. Orders for back issues of the ***ACES Journal*** and changes of addresses should be sent directly to ***ACES*** Executive Officer:

**Dr. Richard W. Adler**
ECE Department, Code ECAB
Naval Postgraduate School
833 Dyer Road, Room 437
Monterey, CA 93943-5121 USA
Fax: 831-649-0300
Email: *rwa@att.biz*

Allow four week's advance notice for change of address. Claims for missing issues will not be honored because of insufficient notice or address change or loss in mail unless the Executive Officer is notified within 60 days for USA and Canadian subscribers or 90 days for subscribers in other countries, from the last day of the month of publication. For information regarding reprints of individual papers or other materials, see "Information for Authors".

***LIABILITY.*** Neither ***ACES***, nor the ***ACES Journal*** editors, are responsible for any consequence of misinformation or claims, express or implied, in any published material in an ***ACES Journal*** issue. This also applies to advertising, for which only camera-ready copies are accepted. Authors are responsible for information contained in their papers. If any material submitted for publication includes material that has already been published elsewhere, it is the author's responsibility to obtain written permission to reproduce such material.

# APPLIED COMPUTATIONAL ELECTROMAGNETICS SOCIETY JOURNAL

Editor-in-Chief
Atef Z. Elsherbeni

Guest Editor
Manos M. Tentzeris

March 2006
Vol. 21 No. 1

ISSN 1054-4887

**The ACES Journal is abstracted in INSPEC, in Engineering Index, and in DTIC.**

The first, fourth, and sixth illustrations on the front cover have been obtained from the Department of Electrical Engineering at the University of Mississippi.

The third and fifth illustrations on the front cover have been obtained from Lawrence Livermore National Laboratory.

The second illustration on the front cover has been obtained from FLUX2D software, CEDRAT S.S. France, MAGSOFT Corporation, New York.

# THE APPLIED COMPUTATIONAL ELECTROMAGNETICS SOCIETY

## JOURNAL

Vol. 21 No. 1 March 2006

## TABLE OF CONTENTS

# Numerical Modeling of Reconfigurable RF MEMS-based Structures Involving the Combination of Electrical and Mechanical Force

**Kohei Kawano Shafrida Sahrani Takashi Mori Michiko Kuroda**
kuroda@cc.teu.ac.jp
*School of Computer Science, Tokyo University of Technology, Hachioji, Tokyo 192-0982, Japan*

**Manos M. Tentzeris**
*School of ECE, Georgia Institute of Technology, Atlanta, GA 30332-250, USA*

**Abstract**

MEMS are minimized electromechanical devices and systems that are realized using integrated micro fabrication methods. And the technology is growing rapidly in RF field, because of the advantages over p-i-n diode or FET switches. The main application areas of MEMS devices in the future are Information Technology, Bioelectromagnetic, Medical Science. For the accurate design of RF MEMS structures, effective computationally modeling of their transient and steady state behaviors including the accurate analysis of their time-dependent moving boundaries is essential. This is because an accurate knowledge of the electromagnetic field (EM) evolution around a moving or rotating body is very important for the realization of new optical devices or microwave devices, such as the RF-MEMS structures used in phase-shifters, couplers, filters, tuners or antennas. The technique proposed in this paper to model MEMS structures is based on the finite-difference time-domain (FDTD) method with an adaptive implementation of grid generation. Here, this simulation method is applied to the analysis of a two-dimensional MEMS variable capacitor with non-uniform motions, such as accelerated motions. The acceleration of the MEMS capacitor is derived under the equilibrium between the spring force and electrical force. Using this acceleration, the motion characteristic for each time step is derived. The numerical results that express the relationship between the acceleration of the plates and the spring constant and the mass of the plates are shown and the transient effect is accurately modeled.

## 1. Introduction

As compared with PIN diode and Transistor switches, RF MEMS have many excellent advantages such as high isolation and low power consumption, and, as a result, MEMS technology is growing rapidly in RF field [1]-[3]. An addition, RF MEMS have many application areas, such as switches, antennas or tuners. For the modeling and optimization of microwave devices, as in the case of the RF MEMS structures used in phase-shifters, couplers, filters, tuners or antennas, an accurate knowledge of the electromagnetic field distribution around a moving or rotating body is required. But due to the limitations of the conventional numerical techniques for the time changing boundaries, it is tedious to solve these problems numerically for the electromagnetic fields [4]. Computational techniques for moving boundary problems have been pursued mainly in heat and fluid flow area [5]-[8]. In this paper, we propose a new numerical approach for the analysis of this type of problems that alleviates the limitations of the conventional time-domain techniques. This method is expanded to analyze MEMS devices with moving parts with the FDTD method for EM fields [9]-[10]. Employing a transformation in the time factor, it is possible to apply the grid generation technique of [11] to the time-domain analysis of a moving object. With such a grid, the FDTD method [12] can be solved very easily on a "static" (time-invariant) rectangular mesh regardless of the shape and the motion of the physical region, something that makes it an especially good tool to analyze structures of arbitrary shape and motion.

In this paper, this simulation method is applied to the analysis of a two-dimensional MEMS variable capacitor with accelerated motion. The acceleration of the plates are derived from the equilibrium between the spring force and electrical force. Using this acceleration, the relation between the mass, the spring constant and the oscillation of the plates are shown. This acceleration is useful in determining the switching time of the MEMS device. For the validation of this method, the computational results of the transient capacitance are compared with the theoretical results.

## 2. Two-Dimensional Variable Capacitor with Acceleration Effect

The dynamic behavior of the MEMS structure is shown in Fig. 1. The top plate is suspended by a spring.

Under the combined effect of mechanical and electrical force, the top plate moves until the equilibrium between the electrostatic and mechanical forces is reached. $F_m$ means spring force and $F_e$ means electrostatic force, that is defined as the gradient of the stored energies and these forces are expressed in the following equations, respectively,

$$F_m = mx''+bx'+kx\,, \tag{1}$$

$$F_e = \frac{1}{2}\frac{\partial C}{\partial x}V^2\,, \tag{2}$$

where $m$ is the mass of the plate, $b$ is the mechanical resistance, $k$ is the spring constant, and $V$ is the bias voltage. From the equilibrium between the spring force and the electrostatic force, the following equation is derived,

$$mx'' = \frac{1}{2}\frac{\partial C}{\partial x}V^2 - bx' - kx\,. \tag{3}$$

From eq. (3), the acceleration $x''$ is obtained.

The geometry to be considered here is shown in Fig. 2. Under the combined effect of mechanical and electrical force, the two fingers are assumed to move with different velocities for the $x$-direction. For the two-dimensional TM-propagation case, as shown in Fig. 2, there are only *Ex, Ey*, and *Hz* nonzero components with a time variation given by the following equations,

$$\frac{\partial H_z}{\partial t} = \frac{1}{\mu}\left(\frac{\partial E_x}{\partial y} - \frac{\partial E_y}{\partial x}\right), \tag{4}$$

$$\frac{\partial E_x}{\partial t} = \frac{1}{\varepsilon}\left(\frac{\partial H_z}{\partial y} - J_x\right), \tag{5}$$

$$\frac{\partial E_y}{\partial t} = -\frac{1}{\varepsilon}\left(\frac{\partial H_z}{\partial x} + J_y\right), \tag{6}$$

where $\varepsilon$, $\mu$ are the constitutive parameters of the respective medium. The configurations of the physical and of the computational regions are shown in Fig. 2.

Employing the transformation with the time factor, the partial differential equation in the physical region $(x, y, t)$ is related to the computational region $(\xi, \eta, \tau)$ as follows:

$$x = x(\xi,\eta,\tau)\,, \tag{7}$$

$$y = y(\xi,\eta,\tau)\,, \tag{8}$$

$$t = t(\xi,\eta,\tau)\,. \tag{9}$$

The inverse transformation is given by

$$\xi = \xi(x,y,t)\,, \tag{10}$$

$$\eta = \eta(x,y,t)\,, \tag{11}$$

$$\tau = \tau(x,y,t)\,. \tag{12}$$

According to the transformation, the first derivatives are transformed as follows,

$$\begin{bmatrix}\partial/\partial x\\ \partial/\partial y\\ \partial/\partial t\end{bmatrix} = K\begin{bmatrix}\partial/\partial \xi\\ \partial/\partial \eta\\ \partial/\partial \tau\end{bmatrix}\,. \tag{13}$$

The inverse transformation is given by,

$$\begin{bmatrix}\partial/\partial \xi\\ \partial/\partial \eta\\ \partial/\partial \tau\end{bmatrix} = L\begin{bmatrix}\partial/\partial x\\ \partial/\partial y\\ \partial/\partial t\end{bmatrix} \tag{14}$$

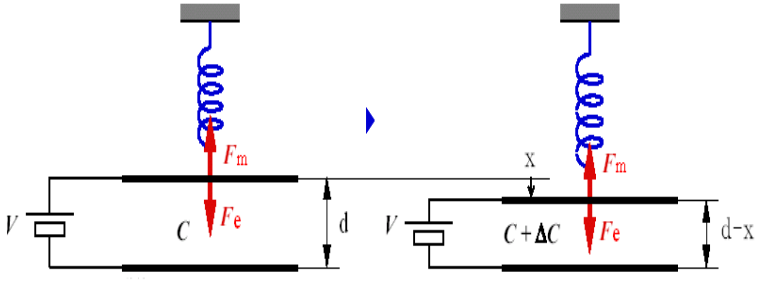


Fig. 1. Functional model of MEMS capacitor

where the matrices *K* and *L* are given by

$$K = \begin{bmatrix} \partial\xi/\partial x & \partial\eta/\partial x & \partial\tau/\partial x \\ \partial\xi/\partial y & \partial\eta/\partial y & \partial\tau/\partial y \\ \partial\xi/\partial t & \partial\eta/\partial t & \partial\tau/\partial t \end{bmatrix} \quad (15)$$

and

$$L = K^{-1} = \begin{bmatrix} \partial x/\partial\xi & \partial y/\partial\xi & \partial t/\partial\xi \\ \partial x/\partial\eta & \partial y/\partial\eta & \partial t/\partial\eta \\ \partial x/\partial\tau & \partial y/\partial\tau & \partial t/\partial\tau \end{bmatrix}. \quad (16)$$

By this transformation, there is a unique correspondence between the computational region and the physical region. The transformed region can be easily solved in the rectangular computational region by FD-TD method.

Under the combined effect of mechanical and electrical force, the plates are assumed to move for *x*-direction with velocities *v* and *u*, and the acceleration $a_v$, $a_u$, respectively. Using a coordinate transformation technique, written from eq. (7) to eq. (16), the time-changing physical region (*x,y,t*)
can evolve to a time-invariant computational domain. For the geometry of Fig. 2, the transform equations between the physical and the computational regions are chosen as:

$$\xi = \frac{x - h_n(t)}{h_{n+1}(t) - h_n(t)}, \quad (17)$$

$$\eta = \frac{y - y_m(t)}{y_{m+1}(t) - y_m(t)}, \quad (18)$$

$$\tau = t, \quad (19)$$

where n=1,2,3, m=1,2,3, and $h_1(t), h_2(t), h_3(t), h_4(t)$ are written in the following form assuming that the plate accelerations and velocities remain time changing values for the whole time of their motion,

$$h_1(t) = x_1 + vt + \frac{1}{2}a_v t^2, \quad (20)$$

$$h_2(t) = x_2 + ut + \frac{1}{2}a_u t^2, \quad (21)$$

$$h_3(t) = x_3 + vt + \frac{1}{2}a_v t^2, \quad (22)$$

$$h_4(t) = x_4 + ut + \frac{1}{2}a_u t^2. \quad (23)$$

The functions $h_1(t)$, $h_2(t)$, $h_3(t)$, $h_4(t)$ describe the movement along the *x* axis, and allow for the realization of a rectangular grid with stationary boundary conditions. The partial time-derivatives in the transformed domain $(\xi, \eta, \tau)$ can be expressed in terms of the partial derivatives of the original domain (*x,y,t*) using eqs. (17)-(23). The FDTD technique can provide the time-domain solution of the rectangular $(\xi, \eta, \tau)$ grid. The stability criterion in this case is chosen as $c\Delta t \le \delta/\sqrt{2}$, where $\delta = \Delta x_0 = \Delta y_0$, assuming the grid is uniformly discretized in both directions. In general, $\delta$ is a space increment for *x* and *y* direction when the grid increment is minimum (minimum cell size).

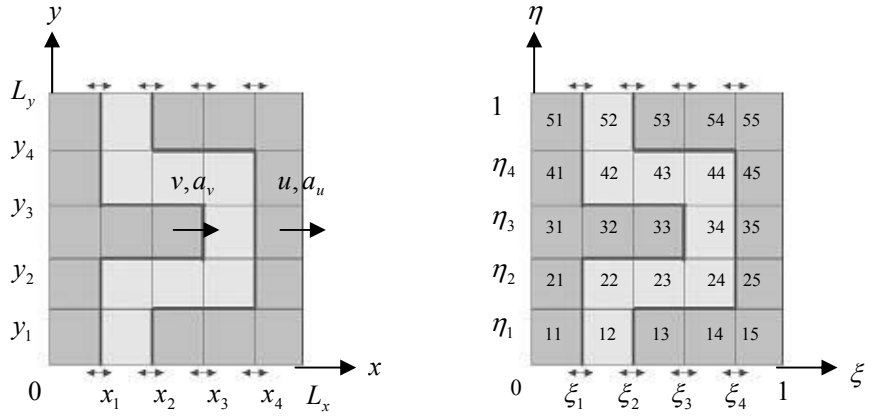


(a) (b)

Fig. 2. (a) Physical region and (b) computational region.

## 3. Numerical Results

To validate this approach, numerical results are calculated for a two-dimensional variable capacitor with the movement of the finger only to the *x*-direction. The grid includes 200 x 200 cells, input frequency is f = 20 GHz and $L_x = L_y = L_z = L = 5\lambda$ , $\Delta x = \Delta y = L/200$ , and $\Delta t = 3.125 \times 10^{-13}$ (sec). The initial plate separation is $L/5$ and the grid is terminated with Mur's absorbing boundary conditions. Here, the left plate is assumed to move due to the coupling of the electrostatic and the

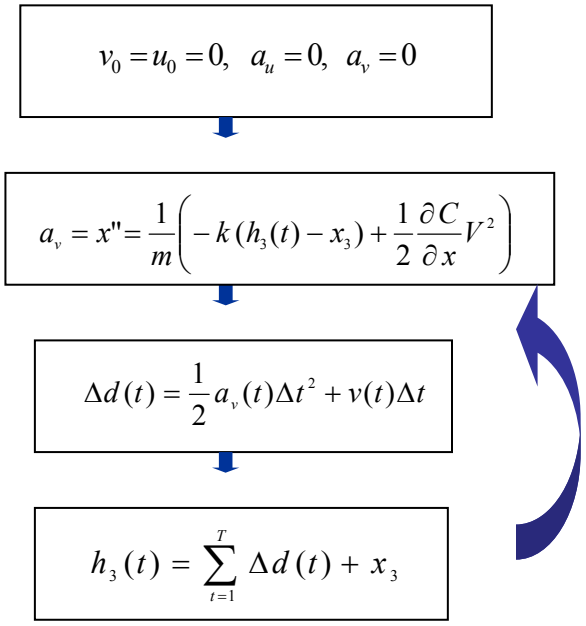


Fig. 3. Computational Algorithm.

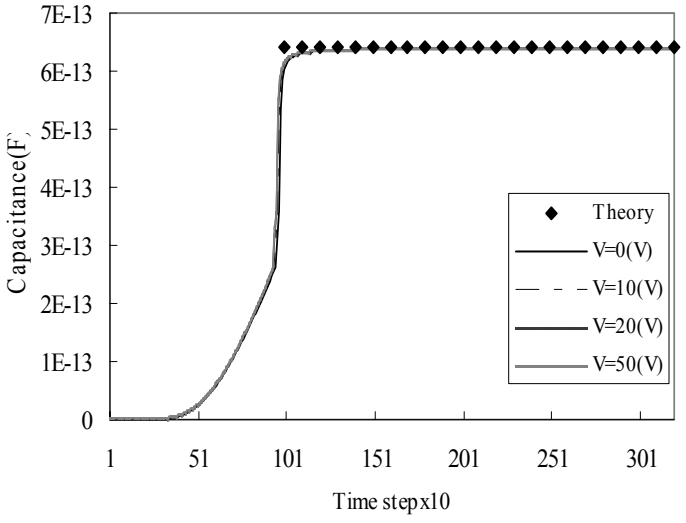


Fig. 4. Time dependence of the capacitance for bias voltage in the range of V=0 (V) to 50 (V) are compared with the theoretical result.

mechanical forces. Fig. 3 displays the computational algorithm used in this calculation. Initial values of the velocity are assumed $u_0=0$, $v_0=0$, and $a_u=0$. From eq.(3), the acceleration value is derived. Inputting this acceleration value into the transform function $h_1(t)$, $h_3(t)$, the new capacitance $C$ and displacement $\Delta d$, transformation function $h_1(t)$, $h_3(t)$, and acceleration $a_v$ are obtained. Then from the capacitance and displacement, the new acceleration is obtained. Iterating this algorithm, it is easy to obtain the capacitance, acceleration and displacement controlled by the coupling of spring and electrostatic force.

Numerical results are given in Fig. 4, Fig. 5, and Fig. 6. Fig. 4 shows the computational results of the time dependence of the capacitance for bias voltage values in the range of $V=0(V)$ to $V=50(V)$, for a motion lasting 3010 time steps. The stationary values, when the velocity is zero, are displayed as a reference, and show that stationary values have good agreement with the theoretical values. Fig. 5 displays the time dependence of the acceleration for each mechanical resonant frequency values in the range of $\omega=\sqrt{k/m}=10^{17/2}$ to $\omega=\sqrt{k/m}=10^{19/2}$, when the plate moves away from the bottom one. The mechanical resonant frequency in Fig. 5(c) is $\sqrt{10}$ times of the resonant frequency in Fig. 5(b) and 10 times of the resonant frequency in Fig. 5(a). According to these values, the ratio of the resonant frequency is shown accurately in each figure. In Fig. 5, when the mechanical resonant frequency is low, the amplitude remains almost constant value. In Fig. 6, time dependence of the acceleration, the velocity and the displacement are shown, where $\omega=10^{17/2}$, $V=10(V)$. It is effectively demonstrated that when the value of the acceleration is zero, the velocity value takes on a stationary value and, conversely, when the value of the velocity is zero, the value of the acceleration takes on a stationary value.

Since the typical MEMS device has low mass around $10^{-10}$ kg and spring constant around 5-30 N/m, the mechanical resonant frequency is 30-100 kHz and bias voltage is 10-30 V [13]. In this paper, the values of the mechanical resonant frequency are in the order of $10^7$, but if a longer computation time is taken, it is possible to obtain results around the order of $10^5$. The results derived in this paper for acceleration and mechanical resonant frequency are very important for determing the switching time.

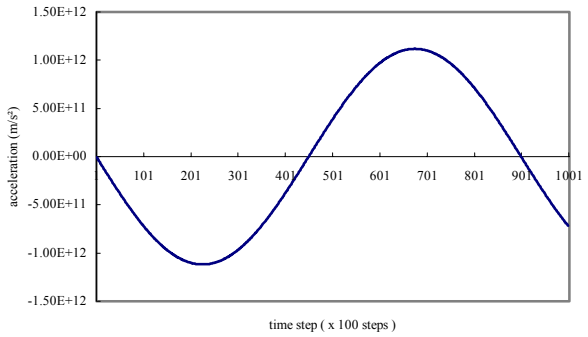


(a)

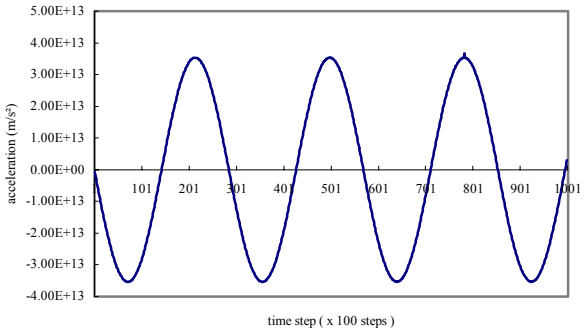


(b)

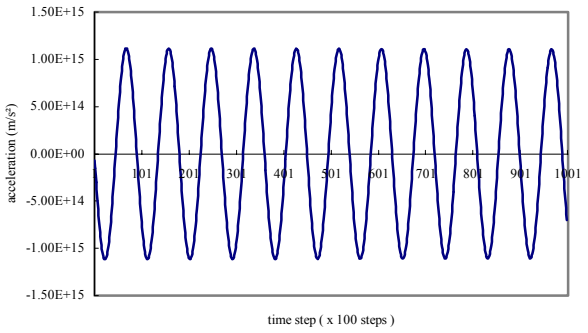


(c)

Fig. 5. Time dependence of the acceleration for each resonant frequency (a) $\omega=10^{17/2}$, (b) $\omega=10^{9}$, and (c) $\omega=10^{19/2}$ for $V=10(V)$.

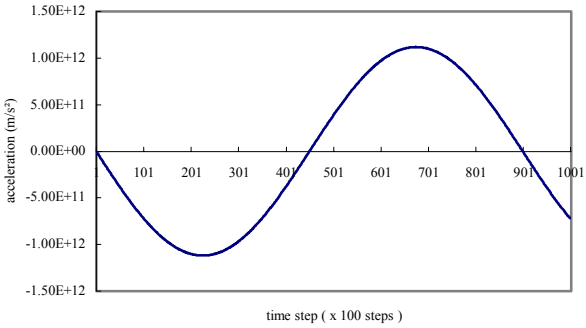


(a) acceleration

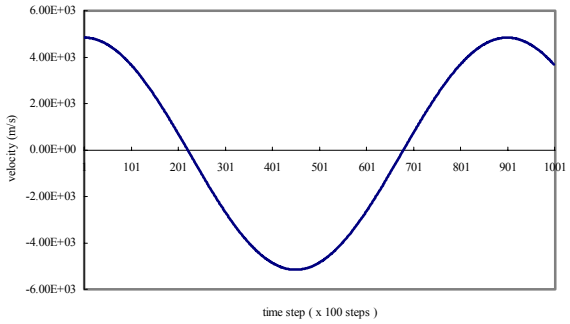


(b) velocity

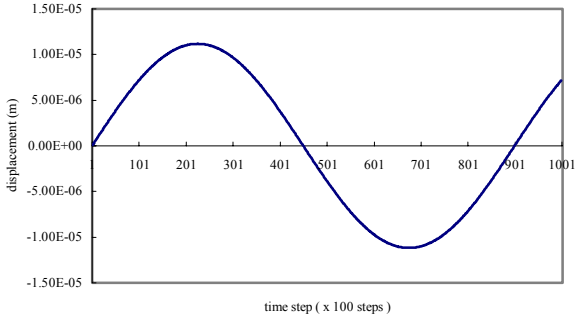


(c) displacement

Fig. 6. Time dependence of the (a) acceleration, (b) velocity, and (c) displacement $\omega = 10^{17/2}$ for $V = 10(V)$.

## Conclusions

A novel time-domain modeling technique that has the capability to accurately simulate the transient effect of variable capacitors with accelerated motion controlled by the coupling of the electrostatic and mechanical forces is proposed. This technique is a combination of the FDTD method and the body fitted grid generation technique. The key point of this approach is the enhancement of a space and a time transformation factor that leads to the development of a time-invariant numerical grid. Using this technique, the numerical results of the relation between the acceleration, the velocity and the displacement of the motion are shown for a MEMS capacitor that demonstrate its unique computational advantages in the modeling of microwave devices with moving boundaries.

## Acknowledgement

The authors wish to acknowledge the support of the Grant-in-Aid for Scientific Research ((c) No.17560320) of The Ministry of Education, Culture, Sports Science and Technology (MEXT), Japan and the NSF Career Award under #9984761, the Yamacraw Design Center of the State of Georgia and the Georgia Tech Packaging Research Center.

## Reference

[1] G. M. Rebeiz, *RF MEMS Theory, Design, and Technology*. John. Wiley & Sons Publication, 2003.

[2] A. Dec, et-at, "Micromachined electro-mechanically tunable capacitors and their applications to RF IC's," *IEEE Trans MTT*, pp. 2587-2596, vol. 46, No.12, Dec.,1998.

[3] A. Dec, et-at, "Microwave MEMS-based voltage-controlled oscillators," *IEEE Trans. MTT*, pp. 1943-1949, vol. 48, No. 11, Nov. 2000.

[4] V. Bladel, Relativity and Engineering. Berlin: Springer-Verg, 1984.

[5] M. Rosenfeldm, and D. Kwak, "Time dependent solution of viscous incompressible flow in moving co-ordinates," *International Journal. for Numerical Method in Fluid*, .vol.13, pp. 1311-1328, 1991.

[6] S. Kuroda, H. Ohba, "Numerical analysis of flow around a rotation square cylinder," *JSME International Journal*, 36-4, B, pp. 592-597, 1993.

[7] J. C. Xu, M. Sen, M. Gad-el-Hak, "Dynamics of a rotatable cylinder with splitter plate in uniform flow" , *Journal of Fluids and Structures*, vol. 7,

Issue 4, pp. 401-416, May 1993.
[8] P. J. Zwart, G. D.Raithby, "Space-time meshing for two dimensional moving boundary problems," *Proc. of the 7th International Meshing Roundtable*, Dearborn, Michigan, Oct. 1998.
[9] M. Kuroda, "A dielectric waveguide with moving boundary," *IEICE Trans*., vol. E74, pp. 3952-3954, Dec. 1991.
[10] M. Kuroda, N. Miura, and M. M. Tentzeris, "A novel numerical approach for the analysis of 2D MEMS-based variable capacitors including the effect of arbitrary motions," *ACES Journal*, vol. 19, no. 1b, pp. 133-138, March, 2004.
[11] J. F. Thompson, *Numerical Grid Generation,* North Holland, Amsterdam, 1985.
[12] A. Taflove, S. Hagness, *Computational Electrodynamics, The Finite Difference Time Domain Method,* Boston: Artech House, 2000.
[13] G. M. Rebeiz, and J. B. Muldavin, "RF MEMS switches and switch circuit," *IEEE Microwave Magazine*, vol. 2, no. 4, pp. 59-71, Dec. 2001.

**Kohei Kawano:** He received the B. E. degree and the M. E. in Information Networks from Tokyo University of Technology, Tokyo, Japan. Now he is a research student at Tokyo University of Technology. His research interests are FDTD method and grid generation method.

**Shafrida Sahrani:** She received the B.E. degree in Information Networks from Tokyo University of Technology, Tokyo Japan. Now she is a graduate student.

**Takashi Mori:** He received the B.E. degree in Information Networks from Tokyo University of Technology, Tokyo Japan. Now he is a graduate student.

**Michiko Kuroda** Professor Michiko Kuroda received the B. E. degree in Electrical Engineering from Shizuoka University, Shizuoka, Japan and the M. E. and D. E. in Electrical Engineering from Waseda University, Tokyo, Japan. She was a visiting researcher at the ElectroScience Laboratory, the Ohio State University, OH from 1986 to 1987. She subsequently became an Associate Professor at Tokyo University of Technology. Since 1998, she has been a professor at the department of Information Networks in 2002. Now she is a professor of the school of Computer Science. Since 2003, she has been a member of the steering committee of Tokyo University of Technology. Since 1994, she has been a Correspondent of URSI (International Union of Radio Science) in Japan. Since 2004, she has been a scientific advisor of Guidance on the Ministry of Public Management, Home Affairs, post and Telecommunications. Since 2004, she has been an advisory committee member of the Saitama Prefecture in Japan and a board of director of ACES. . Her research interests are electromagnetic theory, and numerical methods including FDTD method and grid generation method. She proposed this novel numerical method for the analysis of the moving boundary problems and its application for the analysis of MEMS devices. She is a member of ACES and the IEEE Antennas and Propagation and Microwave Theory and Techniques Societies and OSA, IEICE.

**Manos M. Tentzeris** Professor Manos M. Tentzeris received the Diploma Degree in Electrical and Computer Engineering from the National Technical University of Athens ("Magna Cum Laude") in Greece and the M.S. and Ph.D. degrees in Electrical Engineering and Computer Science from the University of Michigan, Ann Arbor, MI and he is currently an Associate Professor with School of ECE, Georgia Tech, Atlanta, GA. He has published more than 200 papers in refereed Journals and Conference Proceedings and 8 book chapters and he is in the process of writing 3 books. Dr. Tentzeris has helped develop academic programs in Highly Integrated/Multilayer Packaging for RF and Wireless Applications, Microwave MEM's, SOP-integrated antennas and Adaptive Numerical Electromagnetics (FDTD, MultiResolution Algorithms) and heads the ATHENA research group (15 researchers). He is the Georgia Tech NSF-Packaging Research Center Associate Director for RF Research and the RF Alliance Leader. He is also the leader of the RFID Research Group of the Georgia Electronic Design Center (GEDC) of the State of Georgia. He was the recipient of the 2006 IEEE MTT Outstanding Young Engineer Award, the 2004 IEEE Transactions on Advanced Packaging Commendable Paper Award, the 2003 NASA Godfrey "Art" Anzic Collaborative Distinguished Publication Award for his activities in the area of finite-ground low-loss low-crosstalk coplanar waveguides, the 2003 IBC International Educator of the Year Award, the 2003 IEEE CPMT Outstanding Young Engineer Award for his work on 3D multilayer integrated RF modules, the 2002 International Conference on Microwave and Millimeter-Wave Technology Best Paper Award (Beijing, CHINA) for his work on Compact/SOP-integrated RF components for low-cost high-performance wireless front-ends, the 2002

Georgia Tech-ECE Outstanding Junior Faculty Award, the 2001 ACES Conference Best Paper Award and the 2000 NSF CAREER Award for his work on the development of MRTD technique that allows for the system-level simulation of RF integrated modules and the 1997 Best Paper Award of the International Hybrid Microelectronics and Packaging Society for the development of design rules for low-crosstalk finite-ground embedded transmission lines. He was also the 1999 Technical Program Co-Chair of the 54th ARFTG Conference, Atlanta, GA and the Chair of the 2005 IEEE CEM-TD Workshop and he is the Vice-Chair of the RF Technical Committee (TC16) of the IEEE CPMT Society. He has organized various sessions and workshops on RF/Wireless Packaging and Integration in IEEE ECTC, IMS and APS Symposia in all of which he is a member of the Technical Program Committee in the area of "Components and RF". He is the Associate Editor of IEEE Transactions on Advanced Packaging. Dr.Tentzeris was a Visiting Professor with the Technical University of Munich, Germany for the summer of 2002, where he introduced a course in the area of High-Frequency Packaging. He has given more than 40 invited talks in the same area to various universities and companies in Europe, Asia and America. He is a Senior Member of IEEE, a member of URSI-Commission D, an Associate Member of EUMA and a member of the Technical Chamber of Greece.

# Comparative Study of Analytical and Simulated Doubly-Supported RF MEMS Switches for Mechanical and Electrical Performance

Nickolas Kingsley, Guoan Wang, and John Papapolymerou
E-mail: Kingsley@gatech.edu, gtg647e@prism.gatech.edu, papapol@ece.gatech.edu

Georgia Institute of Technology, School of Electrical and Computer Engineering, Atlanta, GA 30308

***Abstract* — Radio Frequency Microeletromechanical System (RF MEMS) switches are useful for providing low-loss switching elements in high frequency devices. Since these devices contain a mechanical and an electrical component to their operation, predicting their performance is not trivial. Computational analysis can be extremely complicated due to the large number of variables that need to be incorporated. Using a multi-physics simulation tool seems like the only solution, but most simulators are optimized for only one engineering realm (i.e. mechanics or electronics). Combining different engineering realms into one simulated model will usually compromise the accuracy of the results. Often simulators cannot model a multi-realm device at all. This paper offers a solution to this problem by proposing a technique for combining computational analysis with simulation to determine the pull-down voltage and RF characteristics of an RF MEMS switch. Measurement results agree closely with the simulated results using this technique.**

## I. INTRODUCTION

RF MEMS switches have become a popular area of research in recent years due to their small size, low loss, good isolation, and low cost. Solid-state switches at high frequencies are lossy and cause more distortion. An example of a doubly-supported (air-bridge type) capacitive MEMS switch is shown in Figure 1.

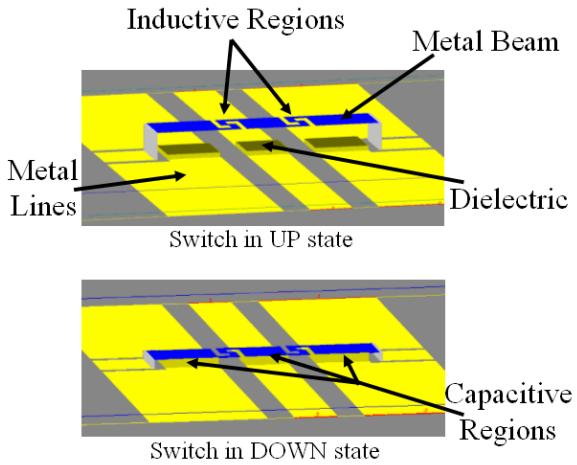


Fig. 1. Rendering of RF MEMS switch in UP and DOWN state.

The switch works by deflecting the beam towards the bottom metal layer and causing an RF short circuit. The inductive regions behave like springs and make it easier to deflect the beam. A spring constant can be determined which evaluates the amount of force necessary to deflect the beam a given distance. Changing the shape or dimensions of the inductive region will increase or decrease the spring constant. The capacitive regions are responsible for creating an electrostatic force between the DC biased beam and the metal layer below it. This force is responsible for decreasing the "gap" between the metal layers. Changing the gap length, height, or the area of the capacitive region will increase or decrease the electrostatic force necessary to deflect the beam.

Across the capacitive region, the charge density in the metal should be uniform. Otherwise, the beam will not deflect parallel to the bottom metal layer. Any skewing of the beam caused by fabrication misalignment or non-symmetric inductive regions will result in a larger capacitance and a poor RF open circuit. As long as the switch is adequately thick (2-3 skin depths), made from a high-quality, highly conductive metal (copper or gold, usually), and properly aligned (to equalize the fringing electric fields on all sides) charge density in the metal will be uniform. MEMS switches that are not deflecting uniformly are usually caused by fabrication misalignment, non-uniform metal thickness, or contaminants in the capacitive region metal. The latter two issues prevent the charge density from being uniform by hampering the flow of electrons in the metal and can be rectified by altering the fabrication recipe.

Electrically, the inductive and capacitive regions behave as their name implies. Changes in these regions will change the RF performance of the switch. The dielectric layer provides high capacitance when the switch is in the down state and is used to prevent stiction between the two metal layers. A very thin layer (~2000Å) of silicon nitride is typically used and generally has a negligible effect on the mechanics of the switch. That is, the bending of the beam is not directly effected by the presence of the silicon nitride. However, electrons can accumulate in this thin layer which can build up a large enough charge to effect the electrostatic actuation of the switch. Dielectric charging is especially pronounced in silicon nitride layers that are deposited using Plasma

Enhanced Chemical Vapor Deposition (PECVD) because of the large number of atomic defects generated from the plasma. Charging effects can be greatly reduced by properly grounding the silicon nitride to prevent electron accumulation. This can be improved further by thermally growing the dielectric layer instead of using PECVD [1].

Modeling MEMS switches for optimal electrical and mechanical performance can be a daunting task and is often substituted with a less accurate method. For instance, MEMS switches are often designed for optimal electrical properties (such as a low RC time constant [2]) or optimal mechanical properties (such as a low actuation voltage [3]). There are four popular inductive region configurations [4]. These designs, labeled 1-4, are shown in Figure 2.

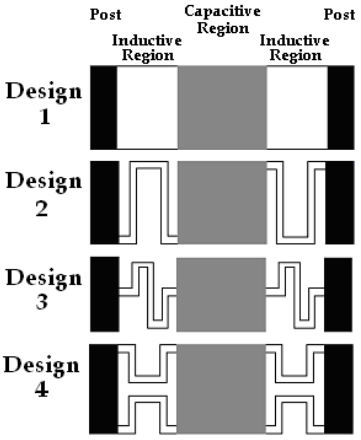


Fig 2. Switch designs 1-4.

Deriving the equations for predicting MEMS switch performance that utilizes these inductive and capacitive regions is difficult. Very general equations can be investigated but the results can only be used as rough estimates [5-6]. Those who have tried predicting MEMS switch behavior using only theory often report a discrepancy upwards of a factor of ten between predicted and measurement results [7]. Certainly design optimization can not be done this way. Using simulation software is the only way to take into account most of the idiosyncrasies of device performance. However, it is not always possible, or effective, to use a simulator to predict mechanical performance due to an electrostatic force.

RF MEMS switch feature sizes are often on the order of λ/1000 or smaller. This is much smaller than the typical element size of a Finite Element Method (FEM) or Finite-Difference Time-Domain (FDTD) simulator, whose typical element sizes are λ/20 to λ/10, although simulations with small feature sizes are still possible with these methods [8]. A Method of Moments (MOM) simulator could be used to model the small feature sizes, but if the switch is being simulated with other devices (i.e. filters or antennas) or on a multilayer substrate then an FEM simulator would be more accurate because of the improved cell size. Clearly there is a trade off. Alternatively, hybrid simulators have been investigated which attempt to utilize the advantages of both types of simulation. No matter which type of simulator is used, when devices with small feature sizes (i.e. RF MEMS switches) are simulated in a complex environment (i.e. when surrounded by an electric field) assumptions must be made within the simulator and results will be compromised [9].

Often, when multiple physical realms are involved in a problem, the optimal solution method is to use a simulator to solve the problem in the more complicated realm and to combine those results manually with theory from the simpler realm. For the RF MEMS switch, we are combining a mechanical beam dynamics problem with an electrostatic problem. The theory that deals with the electrostatics of a capacitive region is well known and straightforward, whereas the dynamics of a beam with complicated springs is much more difficult to solve. Solving the problem in one simulation that couples the two physical realms does not always give the most accurate results because of assumptions and simplifications used in the simulator. Instead, this paper presents a straightforward method for modeling an RF MEMS switch by simulating first in an optimized FEM mechanical simulator then calculating the pull-down voltage by using simple electrostatic equations. The measured results match very closely with the results from this method, which demonstrates its effectiveness.

## II. MECHANICAL ANALYSIS OF RF MEMS SWITCHES

Equations for predicting the bending of cantilever and doubly-supported beams have been around for decades [10]. Unfortunately, applying simplistic equations to complex MEMS devices can be cumbersome. The two most important mechanical features of a MEMS switch are the pull-down voltage and the deflection. Both of these quantities can be calculated by treating the MEMS switch as a mechanical spring. In order to calculate the pull-down voltage, one must equate the force pulling down on the beam by the electrostatic force between the metal layers

$$f_{down} = \frac{\varepsilon A V^2}{2g^2} \tag{1}$$

and the force pushing up from the spring (Hooke's Law) [11],

$$f_{up} = -k(g_o - g)\,. \tag{2}$$

For these equations, ε is the permittivity, A is the area, V is the voltage, k is the spring constant, $g_o$ is the initial gap, and g is the evaluated gap. We can use these simple, spatially independent equations since we know the charge density (and therefore the force) is uniform across the capacitive region. It has been well documented that for parallel plate electrostatic actuation, when the gap reduces to 2/3 of the original gap, the beam becomes unstable and experiences a "pull-in" effect [11]. That is, the MEMS switch does not deflect over the entire gap according to the formula in (1). Instead, when the gap

reaches a certain threshold, namely 2/3 the original gap, the switch will snap down. Magnets experience the same effect. As two magnets of opposite polarity are brought closer together the attractive force is barely noticeable until they reach a certain distance apart. At this point they snap together and the force between them is great.

Equating (1) and (2) where the gap is 2/3 the original gap and solving for the pull down voltage gives

$$V_{PI} = \sqrt{\frac{8kg_o^3}{27\varepsilon A}}. \tag{3}$$

The maximum deflection can also be calculated from the spring constant by the equation [10]

$$\delta = -F/k \tag{4}$$

where δ is the deflection, F is the force pushing down on the spring (in Newtons) and k is the spring constant.

The values for the permittivity, area, and gap can be designed for and implemented in fabrication. The only two unknowns for a given MEMS switch are the spring constant and the downward force. The spring constant can be derived for a meandered line by the equation [4]:

$$k_m = \frac{Ew\left(\frac{t}{L_c}\right)^3}{1+\frac{L_s}{L_c}\left(\left(\frac{L_s}{L_c}\right)^2+12\frac{1+\nu}{1+\left(\frac{w}{t}\right)^2}\right)} \tag{5}$$

where w is the width of the meander, t is the thickness of the metal, v is the Poisson's Ratio of the metal, $L_s$ is the overall width of the spring, and $L_c$ is the distance from the end of the spring to the start of the meander. These dimensions are illustrated below.

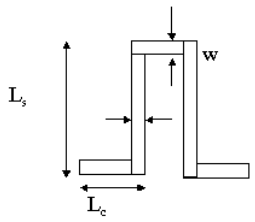


Fig.3. Illustration of dimensions for (5).

For a non-meandered spring, the spring constant is given by [12]

$$k_{non-m} = \frac{32EWH^3}{L^3} \tag{6}$$

where E is the Young's Modulus, W is the width, H is the thickness, and L is the length.

The effective spring constant, $k_{eff}$, for the entire MEMS switch can be determined by combining the simple spring equations in a fashion similar to capacitors. That is, springs in parallel add directly and springs in series add as the inverse of the sum of the reciprocals. Therefore, the effective spring constants for the four switch designs presented in this paper are:

Design 1

$$k_{eff} = \frac{32EWH^3}{L^3} \tag{7}$$

Design 2

$$\frac{1}{k_{eff}} = \frac{1}{k_m} + \frac{1}{k_{n-m}} + \frac{1}{k_m}$$

$$\therefore k_{eff} = \frac{k_m k_{n-m}}{k_m + 2k_{n-m}} \tag{8}$$

Design 3

$$\frac{1}{k_{eff}} = \frac{1}{k_m} + \frac{1}{k_m} + \frac{1}{k_{n-m}} + \frac{1}{k_m} + \frac{1}{k_m}$$

$$\therefore k_{eff} = \frac{k_m k_{n-m}}{k_m + 4k_{n-m}} \tag{9}$$

Design 4

$$\frac{1}{k_{eff}} = \frac{1}{2k_m} + \frac{1}{k_{n-m}} + \frac{1}{2k_m}$$

$$\therefore k_{eff} = \frac{k_m k_{n-m}}{k_m + k_{n-m}} \tag{10}$$

where $k_m$ is the meandered spring constant given by (5) and $k_{n-m}$ is the non-meandered spring constant given by (6). Substituting $k_{eff}$ from (7)-(10) into (3) for k will give the theoretical pull down voltages.

## III. MECHANICAL SIMULATION OF RF MEMS

Before any complex mechanical simulations are performed, it is necessary to validate the model. Careful attention must be given to material properties, boundary conditions, and the applied forces. One way to validate a simulation model is to compare simulated values with theoretical values for a simple case. If the results agree, more complicated configurations can be simulated and the results can be trusted.

### *A. Verification of Simulation Tool*

The FEMLAB 3.0 static structural mechanics module from Comsol was used for the mechanical simulations. FEMLAB is a multiphysics simulation tool, which is commonly used in industry and university settings [13]. The 3D MEMS switch structure with non-meandered springs (Design 1) was simulated with a uniform force pushing down on the center capacitive region.

The theoretical deflection profile can be determined by taking advantage of spring superposition. This procedure

is demonstrated in the figure below for the distribution of force, q.

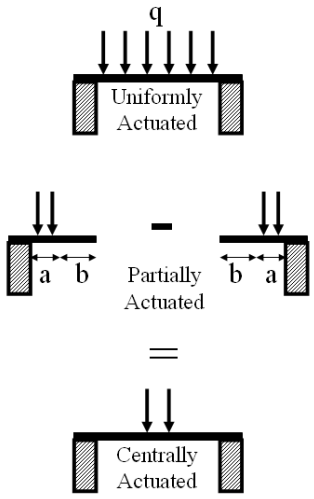


Fig. 4. Spring superposition.

The deflection equation for a uniformly actuated beam is given by [10]

$$\delta(x) = \frac{x^2\left(L^2 - 2Lx + x^2\right)q}{2EWH^3} \tag{11}$$

where x is the position along the beam, L is the length of the beam, and q is the force applied per length. These parameters are exemplified in Figure 5.

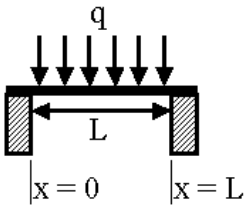


Fig. 5. Illustration of dimensions for (11).

The deflection equation for a partially actuated beam is given by [11]:

$$\delta = \begin{cases} -\dfrac{qbx^2}{12EI}\left(3L + 3a - 2x\right) & \text{for } 0 \le x \le a \\ -\dfrac{q}{24EI}\left(x^4 - 4Lx^3 + 6L^2x^2 - 4a^3x + a^4\right) & \text{for } a \le x \le L \end{cases} \tag{12}$$

where a is the distance from the anchor that the force begins, b is the length of the beam that the force is applied to, and I is the moment of inertia given by [12]:

$$I = \frac{HW^3}{12} \tag{13}$$

where H is the thickness and W is the width of the beam. Figure 6 shows a plot of the deflection given by FEMLAB and the results from the superposition of (11) and (12).

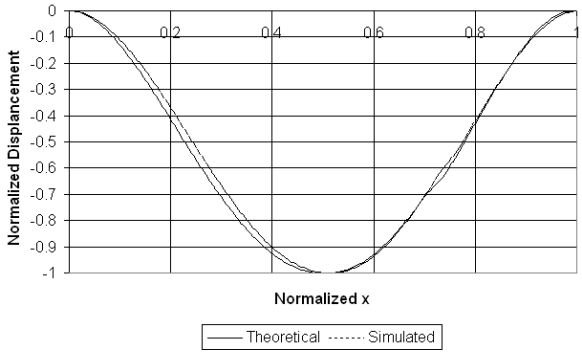


Fig. 6. Comparison of Simulated and Analytical displacement of non-meandered switch.

Since the simulation results agree closely with the analytical results, it is safe to assume that the simulator will be reasonably accurate for the more complicated spring configurations. The simulated deflection profile of the four switch designs is shown in Figure 7.

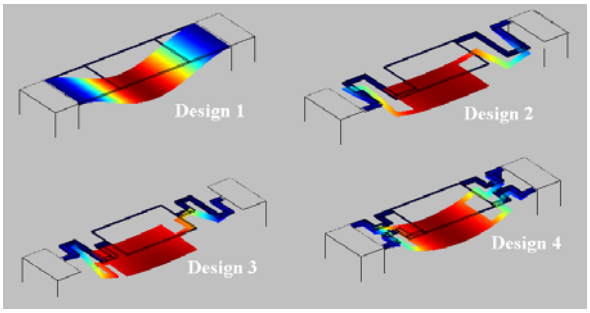


Fig.7. 3D Deflection Profile of RF MEMS Switches.

*B. Deriving Pull-down Voltage from Simulation*

Using FEMLAB, it is easy to determine the force necessary to deflect the MEMS switch a desired distance. Ideally, it is necessary to deflect the MEMS switch the same distance as the gap between the beam and the metal layer below it (usually 1.5-3μm). The equation that relates force to pull-down voltage in terms of the gap is given by [10]

$$V_{PI} = \sqrt{\frac{2g^2F}{\varepsilon}} \tag{14}$$

where F is the force per area. This equation is derived from the pull-down voltage in (3), where F incorporates the spring constant. Doing a unit analysis between (3) and (14) will result in the same outcome, volts.

Changing the force per area acting on the capacitive region until the deflection matches the gap will determine the force. Although a guess-and-check method is necessary to determine the value, this can be performed quickly using interpolation since force and deflection are linearly related. This force can then be used in (14) to calculate the pull-down voltage.

## IV. ELECTRICAL SIMULATION OF RF MEMS

In addition to the mechanical performance of MEMS switches, it is important to evaluate the RF characteristics. The springs exhibit an inductance, the actuation region exhibits a capacitance, and the metal beam exhibits a resistance. All together, the beam behaves like a series RLC circuit. These values can be calculated within an order of magnitude by using fundamental RLC equations. The resistance can be calculated using [14]:

$$R = \frac{\rho L}{HW} \tag{15}$$

where ρ is the metal resistivity and L is the length of the beam. The capacitance can be calculated using [14]:

$$C = \frac{\varepsilon A}{g} \tag{16}$$

Knowing the resonant frequency from measurements, the inductance can be calculated using [14]:

$$L = \frac{1000}{4\pi^2 C f^2} \tag{17}$$

where f is the resonant frequency given in GHz, C is given in pF, and L is calculated in nH. Papers have been published which investigate elaborate circuit models for MEMS switches [15-16]. However, if results within an order of magnitude are suitable, these simple equations are more than adequate.

## V. MEASUREMENTS

All four switch designs were fabricated and measured to determine the actual pull-down voltage and resonance frequency. The process steps are shown in Figure 8. The coplanar waveguide (CPW) signal lines were fabricated by electron beam evaporating a titanium – gold (Ti-Au) layer. Silicon nitride ($Si_3N_4$) was deposited using Plasma Enhanced Chemical Vapor Deposition (PECVD) and patterned using a Reactive Ion Etch (RIE). A sacrificial photoresist layer was spun on and hard baked. The sacrificial layer was removed using a photoresist stripper and a carbon dioxide ($CO_2$) critical point drying process was used to release the switches.

Scanning electron pictures of two of the switches are shown in Figure 9.

Measurements were taken with Thru-Reflect Line (TRL) calibration to deembed the cable and connector losses.

## VI. RESULTS

Results for the mechanical and electrical characteristics of the four spring designs are presented in the following sections. Measurement results were taken for each design. The measured pull-down voltage is within 5V of the minimum pull-down voltage. Voltage ramping must be done quickly to minimize charge accumulation in the underlying dielectric region.

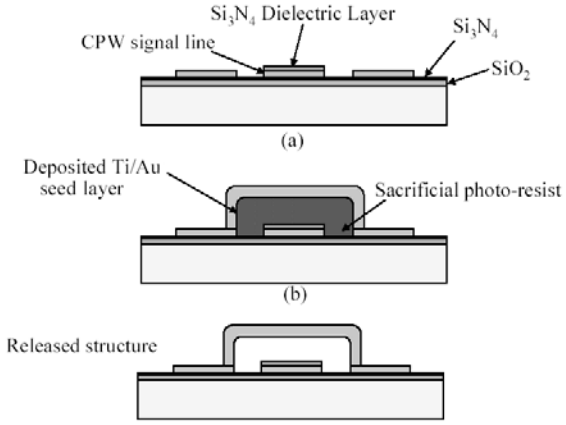


Fig. 8. Fabrication process for MEMS switches.

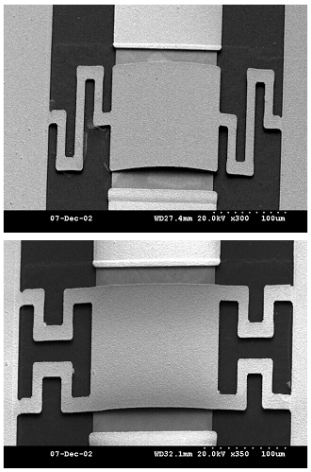

Fig. 9. SEM photos of fabricated switches.

### A. Comparison of Mechanical Analysis

Table 1 displays the comparison between the purely theoretical, the simulated method presented in this paper, and the measured pull-down voltage.

TABLE I
COMPARISON OF THEORETICAL, SIMULATED, AND MEASURED VPI

| Design | Theoretical | Simulated | Measured | Avg Error | Avg % Error |
|---|---|---|---|---|---|
| 1 | 117.135V | 127.5V | 100V | 13.75 | 11.97% |
| 2 | 40.547V | 38.4V | 35V | 3.85V | 10.14% |
| 3 | 31.875V | 27.8V | 30V | 2.98V | 9.97% |
| 4 | 69.050V | 72.8V | 70V | 2.35V | 3.33% |

The measurement results agree closely with the theoretical and simulated results. The average error is within the measurement ramping tolerance (5V).

The theoretical results are generally within 5-8% of the simulated values. The small discrepancy is mainly due to the Poisson ratio of the metal, which the simulator takes into account and theory does not [10,13]. The Poisson ratio relates a change in the width as the length of the beam is increased. There is a small discrepancy between

simulated and theoretical values due to simulator meshing tolerances.

*B. Comparison of Electrical Analysis*

The switches were measured to determine the resonance frequency. This is shown in the figure below.

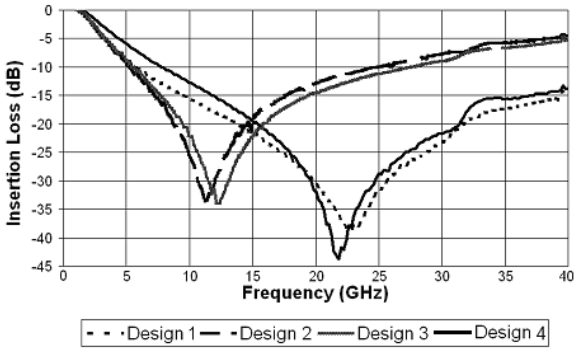


Fig. 10. Resonance frequency of MEMS switches.

Using the measured resonance frequency and the capacitance calculated from (16), the inductance can be determined by (17). The resistance can be calculated from (15). Table 2 shows the resonance frequency values and the calculated capacitance, inductance, and resistance.

TABLE II
CAPACITANCE, INDUCTANCE, AND RESISTANCE OF RF MEMS

| Design | Resonant Frequency | C | L | R |
|---|---|---|---|---|
| 1 | 22.8175GHz | 2.2pF | 22pH | 0.3Ω |
| 2 | 11.3625GHz | 2.9pF | 65pH | 0.6Ω |
| 3 | 12.1525GHz | 2.8pF | 60pH | 0.5Ω |
| 4 | 21.83GHz | 1.9pF | 28pH | 0.2Ω |

The measurement results were compared to a series RLC circuit with the same values as Table 2 to verify the model. One such comparison is shown in Figure 11.

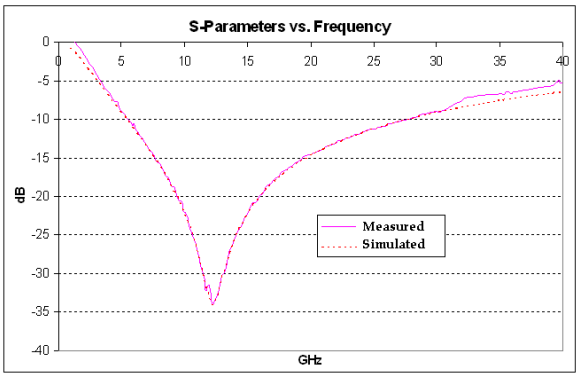


Fig. 11. RLC Circuit vs. Measurement Results.

These results agree very closely with each other. The electrical model is satisfactory.

## VII. CONCLUSION

In this paper, four different RF MEMS switch designs were analyzed using theory and simulations. By combining mechanical simulation results with simple electrostatic equations, a prediction for the pull-down voltage and RF performance was achieved. This prediction was more accurate and much easier to determine than using only theory or only simulations. To verify our mechanical simulation model, it was shown that for a simple switch geometry, the simulated deflection closely matched the theoretical displacement found by using spring superposition. A pull-down voltage for each switch was determined by using the pull-down force given by the mechanical simulator with an equation that relates force to voltage. Measuring the resonant frequency and calculating the resistance, capacitance and inductance determined the electrical circuit model. These RLC values can be used to design other RF MEMS switches. Measurement results agreed very well with predicted values, thus demonstrating that simulation results can be conveniently combined with analytical results to achieve accurate predictions.

## ACKNOWLEDGEMENT

The authors wish to thank Holly Kingsley for her insight on the mechanics of springs and for verifying this paper from a mechanical engineering perspective. The authors would also like to thank Dr.Oliver Brand for inspiring this project.

This work is partially supported by GEDC and partially by NASA under contract #NCC3-1057.

## REFERENCES

[1] Campbell, Stephen, "The Science and Engineering of Microelectronic Fabrication, Second Edition" Oxford University Press, 2001.

[2] S. Simion, "Modeling and design aspects of the MEMS switch," *Semiconductor Conference*, vol. 1, pp. 128, Oct. 2003.

[3] Pacheco, S.P.; Katehi, L.P.B.; Nguyen, C.T.-C., "Design of low actuation voltage RF MEMS switch," *IEEE MTT-S Microwave Symposium Digest*., vol. 1, pp. 165-168, June 2000.

[4] Wang, G., Barstow, S., Jeyakumar, A., Papapolymerou, J., Henderson, C., "Low cost RF MEMS switches using photodefinable mixed oxide dielectrics," *IEEE MTT-S Microwave Symposium Digest*, vol. 3, pp. 1633-1636, June 2003.

[5] Simion, S., "Modeling and design aspects of the MEMS switch," *International Semiconductor Conference2003,* vol. 1, pp. 125-128, 2003.

[6] Mercier, D., Blondy, P., Cros, D., Guillon, P., "An electromechanical model for MEMS switches," *IEEE Microwave Symposium Digest,* vol. 3, pp. 2123-2126, May 2001.

[7] Peroulis, D., Pacheco, S.P., Sarabandi, K., Katehi, L.P.B., "Electromechanical considerations in developing low-voltage RF MEMS switches," *IEEE Transactions on Microwave Theory and Techniques*, vol. 51, issue 1, pp. 259-270, Jan. 2003

[8] Bushyager, N., Lange, K., Tentzeris, M. and Papapolymerou, J., "Modeling and Optimization of RF-MEMS Reconfigurable Tuners with Computationally Efficient Time-Domain Techniques", *Proc. of the 2002 IEEE-IMS Symposium*, pp. 883-886, June 2002.
[9] Wang, Z., Jensen, B., Volakis, J., Saitou, K., Kurabayashi, K., "Analysis of RF-MEMS switches using finite element-boundary integration with moment method," *Antennas and Propagation Society International Symposium*, vol. 2, pp. 173-176, 22-27 June 2003.
[10] E.P. Popov, "Mechanics of Materials, Second Edition," Prentice-Hall, Inc, 1976.
[11] Stephen Senturia, "Microsystem Design," Kluwer Academic Publishers, 2001.
[12] James Gere, "Mechanics of Materials, Fifth Edition," Thompson-Engineering, 2003.
[13] Comsol, Inc. "FEMLAB Multiphysics Modeling," http://www.comsol.com/products/femlab/, November 2004.
[14] David Pozar, "Microwave Engineering, Second Edition," John Wiley & Sons, Inc., 1999.
[15] Muldavin, J. and Rebeiz, G., "High-Isolation CPW MEMS Shunt Switches – Part 1: Modeling," *IEEE Transactions on Microwave Theory and Techniques*, vol. 48, no. 6, pp. 1045-1052, June 2000.
[16] Qian, J., Li, G., deFlavis, F., "A parametric model of MEMS capacitive switch operating at microwave frequencies," *IEEE Microwave Symposium Digest*, vol. 2, pp. 1229-1232, June 2000.

**Nickolas Kingsley** received B.S. (2002) and M.S. (2004) degrees in electrical engineering from the Georgia Institute of Technology, where he is currently pursing a PhD. He is currently researching the integration and packaging of RF MEMS switches into various microwave devices on liquid crystal polymer (LCP) and silicon substrates. He is the recipient of the 2002 President's Undergraduate Research Award from Georgia Tech and the 2001 Armada Award from Compaq Computer Corporation. He is a student member of IEEE, IEEE APS, IEEE MTT-S, and Order of the Engineer.

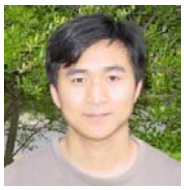

**Guoan Wang** received his Bachelor degree from Central South University, his Master of Science in Materials Science and Engineering from Zhejiang University, and his Master of Science in Electrical Engineering from Arizona State University. He is currently working toward the Ph.D degree in Electrical Engineering at the Georgia Institute of Technology. His research interests include: RF MEMS switches with novel materials and their applications for reconfigurable microwave circuits, integration of RF circuitry onto CMOS grade silicon, and micromachining techniques for microwave applications.

**John Papapolymerou** received the B.S.E.E. degree from the National Technical University of Athens, Athens, Greece, in 1993, the M.S.E.E. and Ph.D. degrees from the University of Michigan, Ann Arbor, in 1994 and 1999, respectively.

From 1999-2001 he was an Assistant Professor at the Department of Electrical and Computer Engineering of the University of Arizona, Tucson and during the summers of 2000 and 2003 he was a visiting professor at The University of Limoges, France. From 2001-2005 he was an Assistant Professor at the School of Electrical and Computer Engineering of the Georgia Institute of Technology, where he is currently an Associate Professor. His research interests include the implementation of micromachining techniques and MEMS devices in microwave, millimeter-wave and THz circuits and the development of both passive and active planar circuits on semiconductor (Si/SiGe, GaAs) and organic substrates (LCP, LTCC) for System-on-a-Chip (SOC)/ System-on-a-Package (SOP) RF front ends.

Dr. Papapolymerou received the 2004 Army Research Office (ARO) Young Investigator Award, the 2002 National Science Foundation (NSF) CAREER award, the best paper award at the 3rd IEEE International Conference on Microwave and Millimeter-Wave Technology (ICMMT2002), Beijing, China and the 1997 Outstanding Graduate Student Instructional Assistant Award presented by the American Society for Engineering Education (ASEE), The University of Michigan Chapter. His student also received the best student paper award at the 2004 IEEE Topical Meeting on Silicon Monolithic Integrated Circuits in RF Systems, Atlanta, GA. He has authored or co-authored over 120 publications in peer reviewed journals and conferences. He currently serves as the Vice-Chair for Commission D of the US National Committee of URSI and as an Associate Editor for IEEE Transactions on Antennas and Propagation. During 2004 he was the Chair of the IEEE MTT/AP Atlanta Chapter.

# Equivalent Network Approach for the Simulation of MEMS Devices

**S. Barmada, A. Musolino, R. Rizzo**

Department of Electric Systems and Automation, University of Pisa
Via Diotisalvi n.2, 56126 Pisa, Italy
{sami.barmada, musolino, rocco.rizzo}@dsea.unipi.it

**Abstract:** In this paper a numerical approach for the analysis of the behaviour of micro electro mechanical systems (MEMS) is presented. The method is applied to the simulation of movable plate MEMS variable capacitors that are of common use in the CMOS voltage controlled oscillators (VCOs). An accurate study of MEMS devices requires a coupled electro-mechanical analysis. The mechanical analysis has to take into account the deformation of the plates of the capacitor and the electromagnetic one has to consider the distribution of charges and currents and the presence of dielectric materials.
We first perform a coupled elastic-electrostatic analysis in order to obtain the tuning characteristic of the system; subsequently, once the positions of the plates have been determined, an electromagnetic analysis of the system is performed via an integral formulation based on an electric equivalent circuit.
The proposed method has been validated by analysing two and three plate tuneable parallel-plate capacitors.

**Keywords:** Integral Formulations, Method of Moments, MEMS, Finite Element Method.

## 1 Introduction

Micro Electro Mechanical System (MEMS) is a technology able to produce miniature mechanical structures, devices and systems by the use of the state of the art of integrate circuit (IC) fabrication [1] - [3]. The advantages inherited by IC technology are mainly the cost reduction (through batch fabrication) and the opportunity of the dimensional downscaling. As a consequence of the latter, the power consumption has been decreased with an important improvement of the overall performance. The mechanical property of silicon has given the opportunity of the fabrication of MEMS by compatible materials with the IC technology. This has led to the realization of monolithic integrated electromechanical systems including accelerometers, pressure sensors and micro switches.
When used as radio frequency (RF) components MEMS devices are showing great potentialities. They demonstrate higher linearity and lower loss than similar components built by other technologies. In this perspective RF MEMS, such as RF switches, tuneable capacitors and high-Q inductors, may serve as fundamental building blocks and are becoming more and more used in several critical applications where increased functionality has to be conjugated with reduced power consumption and severe constraints of electromagnetic compatibility [3] - [5].
As an example it is sufficient to consider modern communication systems, such as the GSM cellular telephone system, where stringent requirements on the intermediate filters and on the VCOs are present. In particular the dynamic range of the filters and the noise level of a RF VCO depend (in opposite fashion) on the overall Q-factor of the resonator.
A proper design procedure for these devices depends on an accurate analysis of the resonator whose tuneable component can be advantageously realized by a MEMS capacitor [6] – [8]. Unbiased base capacitance, tuning ratio, quality factor, associated inductance and consequent electric self resonance frequency are figures of merit of current use in association with tunable capacitors. Their evaluation requires a deep analysis of the device. The long computation times usually required by full wave coupled analysis result in the introduction of approximations with consequent inaccurate predictions producing an unacceptable design process through trial and error.
A MEMS simulator should be able to perform a coupled electro-mechanical analysis [4], [5], [9]. The rigid-body motion hypothesis of the movable plate is no longer valid because of the high width to thickness ratio. The deformations of the moving plate may heavily affect the overall performance of the system as the effective stiffness of the system decreases and as a consequence the mechanic self resonant frequency and the pull-in voltage decrease as well. The accurate determination of the electrical figures of merit of MEMS tunable capacitors requires the evaluation of the charge and current distributions. Fringing effects and the presence of dielectric materials influence the values of the capacity at the various bias levels; the effective distribution of the currents in the device determines the

actual ohmic losses that, in conjunction with the dielectric losses, are used to evaluate the quality factor. A correct evaluation of the quality factor has to take into account the inductive effects of the currents influencing the overall reactance of the system at a given frequency. In addition the evaluation of the inductive effects is essential in the calculation of the electric self resonant frequency.

The mechanic self resonant frequency of a MEMS capacitor usually lies in the range $10 \div 100\,KHz$ while the RF signal is in the range $0.1 \div 10\,GHz$. The RF frequencies are at least three orders of magnitude of mechanical bandwidth; as known this wide separation allows a simplified electromechanical coupling. The position and the deformations of the moving plate are unlikely to be caused by the RF signal and may be determined as a function of the bias voltage only. At the corresponding low frequencies the charge distribution and the electric field play a dominant role in the evaluation of the force distribution. The system in the new geometric configuration so determined is considered at rest under the effects of the RF signal.

This paper discusses various aspects of a method for the electromagnetic analysis based on an integral formulation via an equivalent network.

Conductors and dielectrics (assumed linear) are subdivided in elementary volumes in which uniform distributions of current density and electric polarization are assumed. Ohm's law and continuity equation for the current are written for conductive materials; these are coupled with the constitutive equation for the dielectrics leading to a set of equations that can be viewed as the equilibrium equations of an electric network.

The knowledge of the currents, charges and distribution of the polarization allows evaluating the most important figures of merit of the device.

## 2 Formulation

As stated in the introduction two analyses have to be performed on a MEMS device: first a coupled electromechanical analysis and subsequently an electromagnetic one.

The first one is a fully three-dimensional analysis that iterates between a mechanical Finite Element Method (FEM) solution and an electrostatic Method Of Moment (MOM) solution.

The second one is purely electromagnetic and uses results and parameters obtained by the former.

The electromechanical analysis is explained in detail in the literature and it will be summarized with the objective to define the parameters that will be exported to the electromagnetic analysis.

Let us consider a system constituted by a conductor and by a linear dielectric body. The system is discretized in elementary volumes (slabs, cylindrical sectors of rectangular cross section).

Let $N_d$ be the number of the elementary volumes resulting by the discretization of the dielectric bodies, and $N_c$ the number of the elementary conductive volumes. A uniform distribution of the polarization is assumed in each dielectric elementary volume.

### 2.1 Electro-mechanical Analysis

The discretization of the conductive body produces a discretization of the surface of the body itself in $N_s$ elementary surface elements. Let us assume a uniform distribution of the charges on these surface elements.

The deformable regions (i.e. the moving plate), where a mechanical FEM is used, are further meshed according with the used structural analysis software [10].

Two meshes are defined on the same region: the first one is used to evaluate the force, the second one to calculate the displacements and the deformations.

The force distribution on the moving plate can be evaluated once the charge and polarization distribution are known.

Because of the assumed uniform distribution of the electrical quantities we can write the following expression for the electric scalar potential:

$$\varphi(P) = \frac{1}{4\pi\varepsilon_0}\sum_{j=1}^{N_S}\int_{S_{j,cond}}\frac{\sigma_j(Q)}{r_{P,Q}}dQ + \frac{1}{4\pi\varepsilon_0}\sum_{j=1}^{N_d}\int_{S_{j,pol}}\frac{\boldsymbol{P}_j(Q)\cdot\boldsymbol{n}}{r_{P,Q}}dQ = \sum_{j=1}^{N_S}\alpha_{P,j}\,\sigma_j + \sum_{j=1}^{N_d}\boldsymbol{\beta}_{P,j}\cdot\boldsymbol{P}_j \,. \tag{1}$$

In the above expression $\alpha_{P,j}$ represents the potential in $P$ due to a charge uniformly distributed with unit density on the $j^{th}$ elementary surface of a conductor; the vector $\boldsymbol{\beta}_{P,j}$ relates the electric potential in $P$ to the $j^{th}$ elementary volume where a uniform polarization is assumed. In the second integral in (1) $S_{j,pol}$ represents the entire surface of the $j^{th}$ elementary volume resulting by the discretization of the dielectric regions.

A similar expression can be derived for the electric field at P:

$$\boldsymbol{E}(P) = -\nabla\varphi(P) = \sum_{j=1}^{N_S}\boldsymbol{\delta}_{P,j}\,\sigma_j + \sum_{j=1}^{N_d}\boldsymbol{\Theta}_{P,j}\,\boldsymbol{P}_j \,. \tag{2}$$

The meaning of the symbols in (2) is easily understood: $\boldsymbol{\delta}_{P,j}$ is a vector column and $\boldsymbol{\Theta}_{P,j}$ is a second order tensor represented by a square matrix. The coefficients

$\alpha_{P,j}$, $\boldsymbol{\beta}_{P,j}$, $\boldsymbol{\delta}_{P,j}$, and $\boldsymbol{\Theta}_{P,j}$ can be quickly and accurately evaluated by means of analytical expressions.

The $N_s$ charge densities and the $3N_d$ components of the polarization vector are unknown quantities whose determination is achieved by enforcing the equipotential nature of the conductors and the constitutive equation of dielectrics.

Let $\varepsilon_r$ be the relative permittivity of the linear dielectric materials. We write the relation between $\boldsymbol{P}$, $\boldsymbol{E}$, and $\boldsymbol{D}$ inside the $i^{th}$ dielectric elementary volume:

$$\boldsymbol{D}_i = \varepsilon_0 \boldsymbol{E}_i + \boldsymbol{P}_i . \tag{3}$$

Substituting it in the constitutive equation of the material $\boldsymbol{D} = \varepsilon_r \varepsilon_0 \boldsymbol{E}$ yields:

$$\boldsymbol{P}_i(P) = \varepsilon_0 (\varepsilon_r - 1) \boldsymbol{E}_i(P) . \tag{4}$$

Equation (4) is enforced by using the Galerkin procedure at every dielectric elementary volume [11]:

$$\boldsymbol{P}_i = \varepsilon_0 (\varepsilon_r - 1) \left( \sum_{j=1}^{N_S} \boldsymbol{\delta}_{i,j} \sigma_j + \sum_{j=1}^{N_d} \boldsymbol{\Theta}_{i,j} \boldsymbol{P}_j \right) \quad i = 1,..,N_d \tag{5}$$

and the result is projected along the reference axes.

In the usual operation the bias voltage of every conductor with respect to an arbitrarily chosen reference conductor is known. Galerkin method is used to enforce the equipotential nature of the conductors. If a proper numbering of the elementary surfaces is performed (the indexes of the surfaces of a conductors are contiguous), we can write:

$$V_k = \sum_{j=1}^{N_S} \alpha_{k,j} \sigma_j + \sum_{i=1}^{N_d} \boldsymbol{\beta}_{k,i} \cdot \boldsymbol{P}_i , \qquad k = 1,..,N_s . \tag{6}$$

The terms $V_k$ s have to be constant if the elementary surfaces identified by the index $k$ are on the same (equipotential) conductor.

The coefficients $\boldsymbol{\delta}_{i,j}$, $\boldsymbol{\Theta}_{i,j}$, $\alpha_{k,j}$, and $\boldsymbol{\beta}_{k,j}$ in eqs. (5) and (6) are obtained by the corresponding ones in eqs. (1) and (2) by averaging them on the $i^{th}$ dielectric elementary volume and on the $k^{th}$ elementary surface [12].

Once the linear algebraic system formed by eqs. (5) and (6) is solved (giving the charge and polarization distributions) it is possible to evaluate the force distribution on the moving plate.

The structural analysis software is then able to evaluate the movement and the deformation of the armatures. At this newly evaluated geometric configuration we have to repeat the above described electrostatic analysis. A new force distribution is evaluated and the structural analysis is again performed. Usually a reduced number of iterates are necessary to reach the convergence.

### 2.2 Electromagnetic Analysis

In the most general case the deformed geometry cannot be discretized by using slabs and cylindrical sectors of rectangular cross section. General hexahedral elements are needed. The described analysis can be performed with these volumes but with longer calculation time because of the non availability of fast and accurate analytical expressions for the evaluation of the fields and potentials. Because of the limited extent of the deformations the hexahedra can be "approximated" by slabs with a negligible loss of accuracy and the analytical expressions can still be used.

This same approximation is used in the electromagnetic analysis; the $N_c$ conductive volumes are advantageously considered as slabs or cylindrical sectors of rectangular cross section.

We now consider the centers of the elementary volumes of the discretized conductor and connect the centres of nearby elements (by segments or by circle arches). We also consider the centre of each exterior surface and connect it to the centre of the elementary volume to which it belongs. A 3-D grid is so obtained [13]. The total number of the points of the grid is then: $N_c + N_S$.

We then associate to each segment of the grid a new elementary volume having four edges parallel to the segment and the faces normal to the segment with their centres placed at the nodes of the grid. Inside each elementary volume a uniform distribution of current density $\boldsymbol{J}$ is assumed. This current is directed parallel to the segment above used. Its direction is then perpendicular to the two bases of the new elementary volumes, and is parallel to its lateral surface. These newly built volumes are the branches of the equivalent electric network; let $N_b$ their number. The nodes of this network are the $N_c + N_S$ points introduced above. The procedure is shown in fig. 1.

Let us consider a volume of the original discretization and the associated node; we see that it is located at the centre of an intersection of branches crossing its surfaces. This is shown in the figure 1f. This volume is in the inner part of the conductor and the sum of the currents flowing in the branches leaving the node is zero.

If the node is on the boundary of the conductor, i.e. it is associated to an exterior surface, charges may accumulate on it. The governing equation can be deduced by the continuity equation of the electric current.

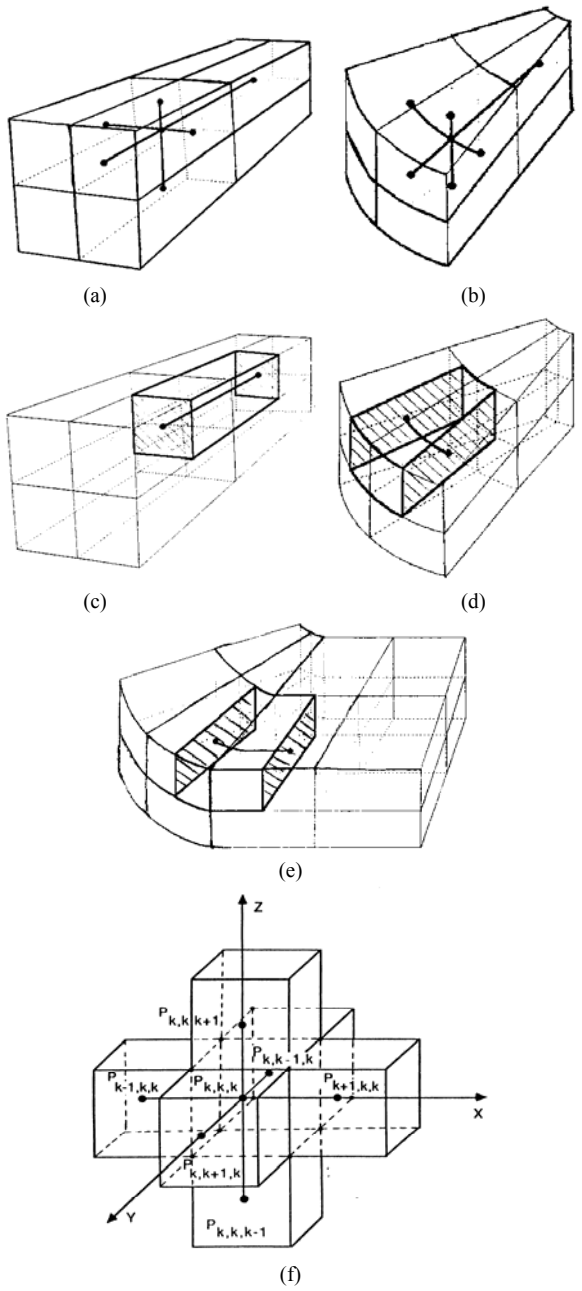


Fig. 1. Construction of the branches of the equivalent network.

Because of the assumed (uniform) distribution of currents and charges we can write:

$$J_{k,h}^{in} = -\frac{\partial \sigma_k^{ext}}{\partial t} . \qquad (7)$$

In eq. (7) $h$ refers to the node associated with a volume in the inner part of a conductor and $k$ refers to the node associated to an exterior surface. $J_{k,h}^{in}$ and $\sigma_k^{ext}$ respectively are the current leaving the surface and the charge densities on it.

Because of the assumed distribution of the currents on the branches, the vector potential at a point $P$ can be written as:

$$\boldsymbol{A}(P,t) = \frac{\mu_0}{4\pi} \sum_{j=1}^{N_b} \int_{V_{j,branch}} \frac{\boldsymbol{J}_j(t)}{r_{P,Q}} dQ = \sum_{j=1}^{N_b} \gamma_{P,j} \boldsymbol{J}_j(t) \quad . \qquad (8)$$

Let us consider the $i^{th}$ branch and write the Ohm's law at a point $P$ inside it:

$$\rho \boldsymbol{J}(P,t) = \boldsymbol{E}(P,t) = -\nabla \varphi(P,t) - \frac{\partial}{\partial t} \boldsymbol{A}(P,t) \quad .$$

Evaluating the line integral along the direction of the current, and averaging the result on the transverse cross section we obtain:

$$R_i I_i(t) = -\Delta U_i(t) - \sum_{j=1}^{N_b} M_{i,j} \frac{d}{dt} I_j(t) \quad , \qquad (9)$$

where $R_i$ is the resistance of the $i^{th}$ branch along the direction of the current, $M_{i,j}$ is the coefficient of magnetic coupling with the current of the $j^{th}$ branch and $\Delta U_i(t)$ is the voltages between the terminals of the branch produced by the distribution of charges on the surface of the conductors and by the polarization charges on the dielectrics.

The electromagnetic analysis of the system can be carried on the electric network formed by the interconnection of the $N_b$ branches described by eq. (9). Kirchhoff laws can be used to solve for the currents in this circuit. When the Kirchhoff Current Laws (KCLs) are written at the boundary volumes they assume the form of eq. (7) and the charge densities are added to the set of the unknown branch currents.

Let us now consider a path inside the conductors and write the total voltage along this path; this results in imposing the Kirchhoff Voltage Law (KVL) and the resultant of the $\Delta U_i(t)$s is zero on the closed loops.

The introduction of new unknowns calls for new equations. A relationship has been already obtained involving the charge densities on the surfaces and the voltages between points on the armatures; it is given by the last electrostatic problem solved in iterative procedure used to solve for the coupled electro-mechanical problem. Equations (5) and (6) have to be added to the eqs. (7) and (9).

Before using (5) and (6) we have to consider that at RF the armatures cannot be considered as equipotential regions. As a consequence elementary surfaces lying on the same armature can have different voltages $V_k$.

We solve eq. (5) in terms of the unknown polarizations of the dielectric elementary volumes expressing them as a linear function of the charge densities:

$$\boldsymbol{P}_i = \sum_{j=1}^{N_S} \boldsymbol{\lambda}_{i,j}\,\sigma_j\,, \qquad i = 1,..\,,N_d\,. \tag{10}$$

Substituting in eq. (6) we obtain:

$$V_k = \sum_{j=1}^{N_S} \alpha_{k,j}\,\sigma_j + \sum_{i=1}^{N_d} \boldsymbol{\beta}_{k,i} \cdot \sum_{j=1}^{N_S} \boldsymbol{\lambda}_{i,j}\,\sigma_j = \sum_{j=1}^{N_S} \xi_{k,j}\,\sigma_j\,, \quad k = 1,..\,,N_s\,. \tag{11}$$

Performing the inversion we have:

$$\sigma_k = \sum_{j=1}^{N_S} \eta_{k,j} V_j\,, \qquad k = 1,..\,,N_s\,. \tag{12}$$

Substituting eq. (12) in (7) we write:

$$J^{in}_{h,k} = -J^{in}_{k,h} = \frac{\partial}{\partial t} \sum_{j=1}^{N_S} \eta_{k,j} V_j\,, \qquad k = 1,..\,,N_s\,. \tag{13}$$

Equation (13), written at the $N_S$ nodes corresponding to the exterior surfaces, may be viewed as the nodal equilibrium equations of a network. Each node is fed with current generators ($J^{in}_{h,k}$) entering it, and is connected to $N_S$ purely capacitive branches. The reference for the voltages involved in (13) is the external to the circuit and coincides with the reference potential used in the determination of the coefficients $\alpha_{P,j}$ and $\boldsymbol{\beta}_{P,j}$ in eq. (1).

This capacitive network has to be coupled to the network formed by the branches described by eq. (9) connected in correspondence of the $N_c$ nodes associated to the inner elementary volumes. The coupling is performed by observing that the feeding currents of the capacitive subnetwork flow through the impedances built by the procedure described in fig. 1 that connect the centres of the external faces with the centre of the elementary volume they belong to. It is worth to note that these latter impedances are described by eq. (9) too.

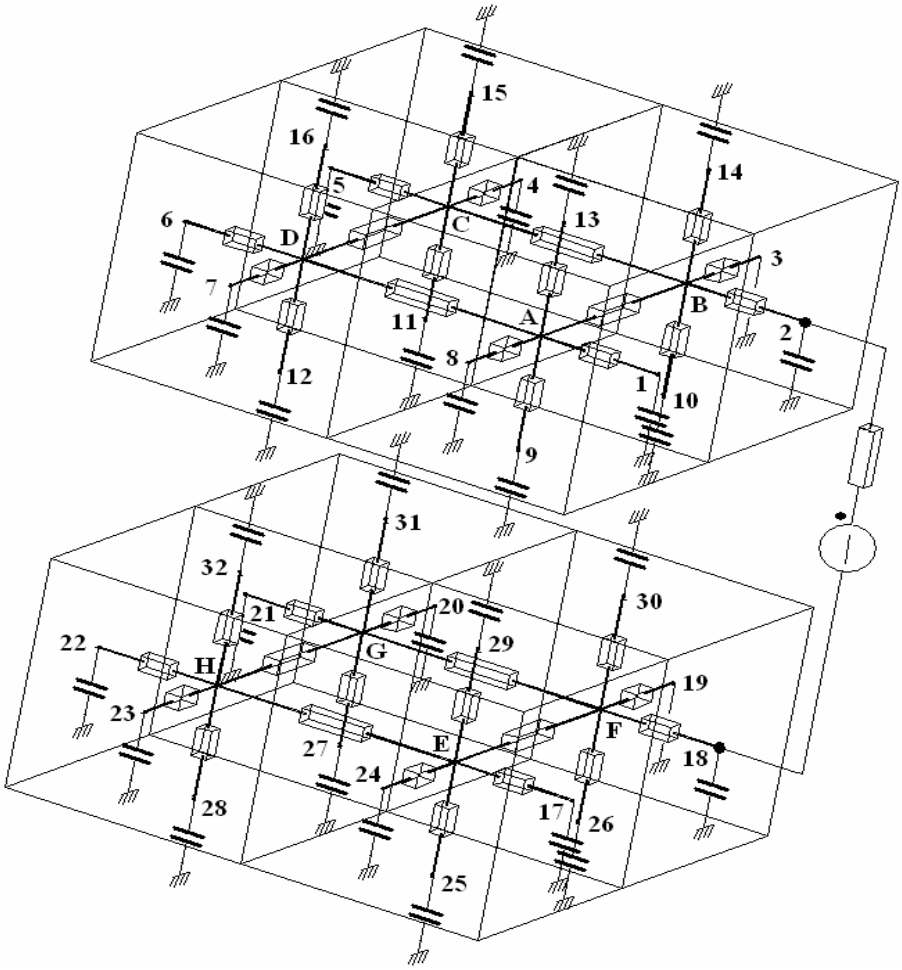


Fig. 2. An example of the equivalent network.

Figure 2 shows an example of the complete equivalent network used for the electromagnetic analysis of a MEMS capacitor in the RF range. A very coarse discretization consisting in four elementary volumes for each armature has been adopted and the system is fed by a voltage generator. For the sake of clarity the capacitors connecting each couple of exterior nodes (those labelled with integer numbers) are not shown; only the capacitors with respect to the reference node of the voltages are indicated. For the same reason the inductive coupling between the impedances is not shown. The nodes labelled with capital letters (A - H) are in the inner of the armature; the nodes labelled with integer numbers (1 - 32) are on the external surfaces. Node A is connected to the inner nodes B and D and to the external nodes 1, 8, 9, and 13.

Modified Nodal Analysis (MNA) can be used to evaluate currents and voltages of the equivalent network. The structure of the network and the "localization" of the inductive coupling mostly in the inner branches and of the capacitive coupling in the exterior ones of the network suggest an "ad hoc" procedure.

Figure 3 shows a simplified version of equivalent network and it is used to illustrate the procedure under the hypothesis of sinusoidal steady state.

Let us consider the subnetworks derived by the armatures; for each subnetwork we can build a surface that cuts the branches connecting the inner with the outer nodes. The capacitors, not shown in fig. 3, are all outside the dashed closed lines that represent the surface in this simplified scheme. Let us label with $I_j^b$ the current on the cut branch directed toward the $j^{th}$ outer node exiting the surface. The total number of these currents is $N_{S_1} + N_{S_2}$, having indicated with $N_{S_1}$ and $N_{S_2}$ the number of external surfaces of the armature. The portion of network enclosed by these surfaces does not contain capacitors and it is constituted by branches that are magnetically coupled each other.

A mesh analysis of the subnetworks enclosed by the surfaces may be advantageously performed. Let us label the $N_m$ loop currents with $I_j^m$. The mesh equations written to the central loops of the two subcircuits are:

$$0 = \sum_{j=1}^{N_m} Z_{k,j}^{m,m} I_j^m + \sum_{j=1}^{N_{S_1}+N_{S_2}} Z_{k,j}^{m,b} I_j^b \,, \quad k = 1, ..., N_m \,. \qquad (14)$$

Superscript *m* stands for *mesh* and *b* stands for *branch*. The first superscript in the coefficients $Z_{k,j}^{m,m}$ and $Z_{k,j}^{m,b}$ indicates that we are performing a mesh analysis, the second superscript selects between "*mesh*" or "*branch*" current.

The nodal equations at the nodes outside the surfaces are:

$$I_k^b = \sum_{j=1}^{N_{S_1}+N_{S_2}} Y_{k,j}^{n,n} V_j^n \quad k = 1, ..., N_{S_1} + N_{S_2};\ k \neq 6;\ k \neq 22. \qquad (15a)$$

The equations at node 6 and 22 respectively are:

$$I_6^b = \sum_{j=1}^{N_{S_1}+N_{S_2}} Y_{6,j}^{n,n} V_j^n + I_E^b \,, \qquad (15b)$$

$$I_{22}^b = \sum_{j=1}^{N_{S_1}+N_{S_2}} Y_{22,j}^{n,n} V_j^n - I_E^b \,, \qquad (15c)$$

where $I_E^b$ is the current on the voltage generator directed from node 6 to node 22 and *n* stands for *nodal.*

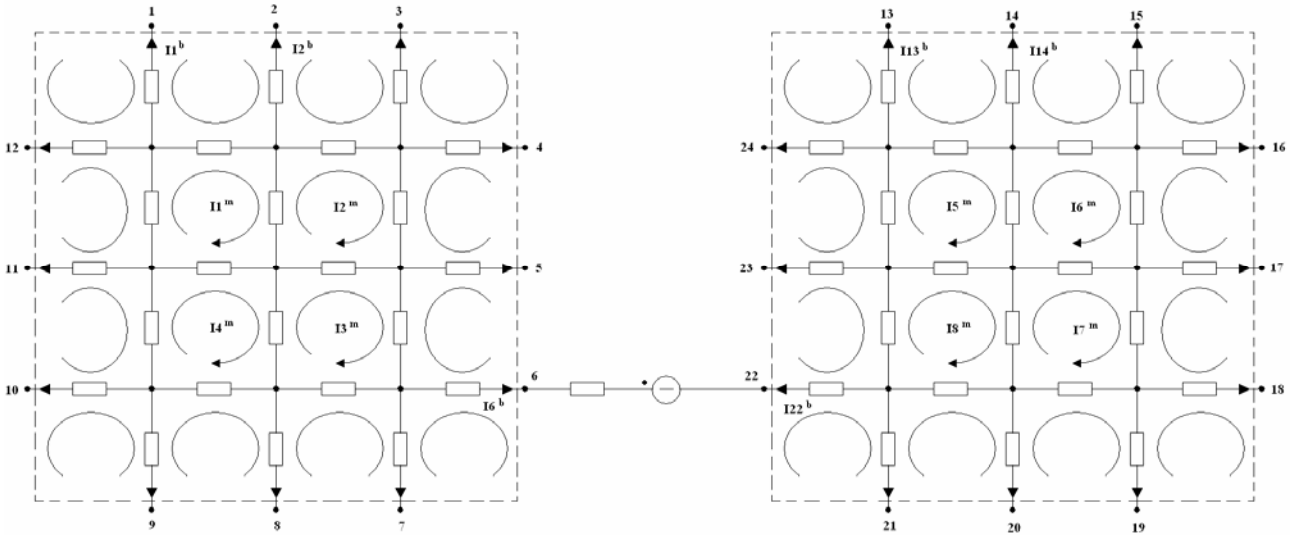


Fig. 3. Simplified equivalent network.

The KCL has to be explicitly imposed on the two closed surfaces:

$$0 = \sum_{j=1}^{N_{S_1}} I_j^b \,, \tag{16a}$$

$$0 = \sum_{j=1+N_{S_1}}^{N_{S_2}} I_j^b \,. \tag{16b}$$

The coupling of the mesh and nodal equations is performed by expressing the voltage between couples of external nodes in terms of the voltage drops along paths that connect the two nodes and that are constituted by branches lying in the inner parts of the subnetworks.
As an example we can write:

$$V_1 - V_2 = \sum_{j=1}^{N_m} Z_{(1,2),j}^{v,m} I_j^m + \sum_{j=1}^{N_{S_1}+N_{S_2}} Z_{(1,2),j}^{v,b} I_j^b \,. \tag{17}$$

The superscript *v* is for *voltage*; the meaning of the symbols is similar to that of eq. (14). The number of independent paths is $N_{S_1} - 1$ for the first subnetworks and $N_{S_2} - 1$ second one.

A further equation governing the branch with the voltage generator connected to the armatures has to be added,

$$V_6 = Z_E I_E^b + E + V_{22} \,. \tag{18}$$

The total number of the eqs. (14) – (18) is $N_m + 2 \cdot \left( N_{S_1} + N_{S_2} \right) + 1$ and it is the same as the number of the unknown quantities.
By inverting eq. (14) we write:

$$\boldsymbol{I}^m = -\left( \boldsymbol{Z}^{m,m} \right)^{-1} \boldsymbol{Z}^{m,b} \boldsymbol{I}^b \tag{19}$$

where bold characters are used to denote vectors and matrices.
Coupling eqs. (15) and (18) we can write for the voltages at the external nodes the expression:

$$\boldsymbol{V} = \boldsymbol{K} \boldsymbol{I}^b + \boldsymbol{H} E \,. \tag{20}$$

Equation (17) may be written in matrix form by the introduction of the matrix $\boldsymbol{D}$ that performs the difference between two elements of the vector $\boldsymbol{V}$,

$$\boldsymbol{D}\boldsymbol{V} = \boldsymbol{Z}^{v,m} \boldsymbol{I}^m + \boldsymbol{Z}^{v,b} \boldsymbol{I}^b \,. \tag{21}$$

Substituting eqs. (19) and (20) in (21) we obtain:

$$\boldsymbol{D}\left( \boldsymbol{K} \boldsymbol{I}^b + \boldsymbol{H} E \right) = -\boldsymbol{Z}^{v,m} \left( \boldsymbol{Z}^{m,m} \right)^{-1} \boldsymbol{Z}^{m,b} \boldsymbol{I}^b + \boldsymbol{Z}^{v,b} \boldsymbol{I}^b \tag{22}$$

that coupled with eq.(16) allows the evaluation of the currents $\boldsymbol{I}^b$. Back substitution in (19) and (20) completes the solution of the equations.

## 3 Example of application

Before showing two examples of application let us discuss some properties of the proposed formulation that can be of great usefulness in the analysis of MEMS capacitors.
The typical geometries of the conductive and dielectric domains are characterized by poor aspect ratios. The thickness of the armatures of the capacitor is of the order of micron or less, while the other dimensions are more than two magnitude orders greater. Realistic discretizations of these domains (in terms of number of elementary volumes) result in elementary volumes with very poor aspect ratio. As a consequence the use of analysis tools based on the Finite Element Method (FEM) may result in low accuracy. The proposed formulation belongs to the class of the integral formulations and inherits their properties. In particular the aspect ratio of the elementary volumes produced by the discretization does not affect the accuracy of the computations as in the FEM formulations.
Without appreciable loss of accuracy it is possible to use elementary volumes with poor aspect ratio especially in the central portions of the domains where the polarization vector, the current and the charge densities are likely to be uniformly distributed over relatively large regions. The presence of elementary volumes having one dimension (the thickness) a magnitude order lower than the other two is a common practice in those regions.
The regions near the edges where fringing effects are present may be discretized using elementary volumes "stick" shaped parallel to the edges. The corners and the points where the currents are injected require a finer discretization. This is automatically obtained because of the structured nature of the discretization.
The use of elementary volumes with poor aspect ratio may cause long computation times in the evaluation of the coefficients in eqs. (5) and (6) and of the auto and mutual inductance terms in eq. (9). The availability of analytical expressions for these coefficients mitigates this drawback.
The presence of the holes in the moving armature can be easily modelled and does not result in a dramatic increase of the unknowns because the limited fringing effects in correspondence of the edges of the holes do not require a refinement of the discretization.
Dielectric materials that at RF may present dispersive behaviour with consequent power losses may be easily modelled by the proposed method. A complex frequency dependent electric permittivity in eqs. (4) and (5), when they are written in the frequency domain, implies the presence in eq. (13) of complex $\eta_{k,j}$ coefficients. As a consequence the equivalent network portion built starting from eq. (13) has to be completed by inserting proper resistances parallel connected to the

capacitors already inserted. If a transient analysis has to be performed convolution integrals appear in the equilibrium equations and long computational time may be required unless the dispersive medium is a Lorentz or Debye one [14].

The reduction of the electromagnetic analysis to a network analysis makes very easy the coupling of the MEMS capacitors with the external circuit and allows an accurate, though extremely CPU consuming, analysis of the overall system.

The proposed formulation has been used to analyse two tunable parallel plate capacitors. The complete description of the geometries of the devices is reported in [6]. The principle of operation assumes that the moving plates in both the capacitors behave as rigid bodies, i.e move without deformation. This hypothesis is not valid because of the shape of the plates whose thickness is far less than the other two dimensions. The effective stiffness of the systems is lower than that estimated by considering the stiffness of the T-type suspension only. As a result the pull in voltage and the natural frequency also decrease.

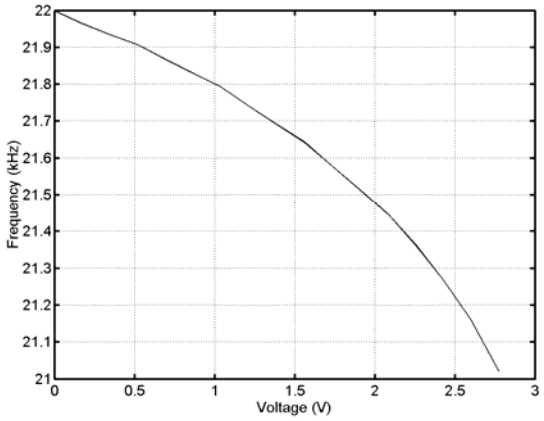


Fig. 4. Two plate MEMS capacitor natural frequency.

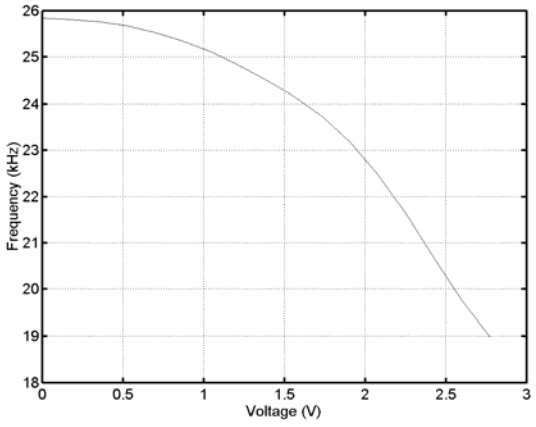


Fig. 5. Three plate capacitor natural frequency vs. $V_2$ with $V_1$=0.

Figures 4 - 6 show the natural frequency versus the bias voltage for the two and three plates MEMS capacitors respectively.

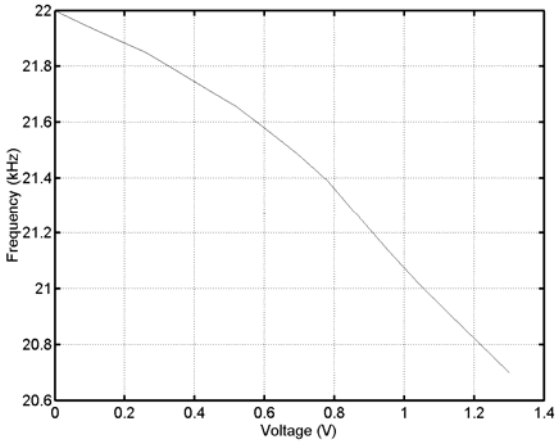


Fig. 6. Three plate capacitor natural frequency vs. $V_1$ with $V_2$=0.

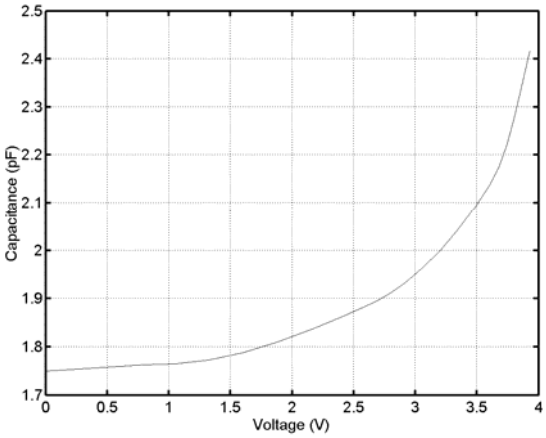


Fig. 7. Tuning characteristics of the two plate capacitor.

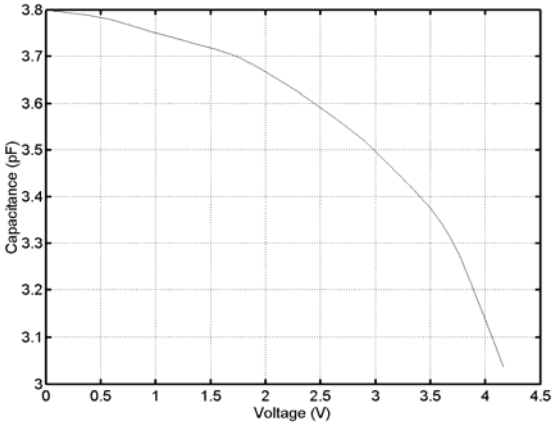


Fig. 8. Tuning characteristics of the three plate capacitor vs. $V_2$ with $V_1$=0.

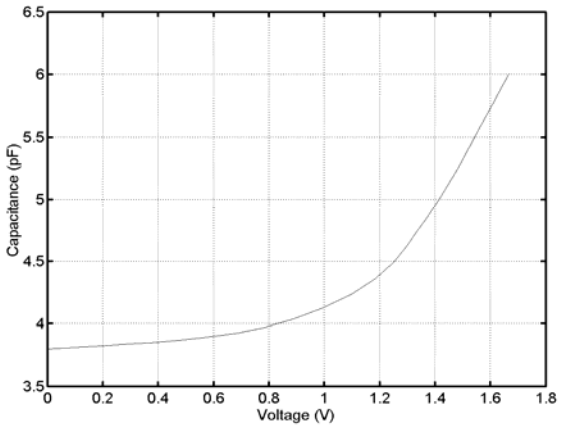


Fig. 9. Tuning characteristics of the three plate capacitor vs. $V_1$ with $V_2$=0.

As expected the natural frequencies are smaller than those evaluated in [6] where the rigid motion of the armature is assumed; furthermore a dependence of the natural frequencies with the applied bias voltage is evidenced.

Figure (7) shows the tuning characteristic of the two plate tunable capacitor. The tuning ratio is approximately 1.45 and the pull-in occurs at about 4 V. Figures 8 and 9 show the tuning characteristics of the three plates capacitors with respect to two bias voltages. Figure 8 refers to the voltage between the bottom and the suspended plate, and fig. 9 to the voltage between the top and the moving plate. Pull –in occurs when 4.2 V are applied to the bottom plate and when 1.65 V are applied to the top plate.

All the three simulated tuning characteristics significantly differ from the experimental ones reported in [6]. The cause of these differences is likely due to the effects of the deformations produced by the compressive stress in polysilicon layer that in our analysis has been neglected.

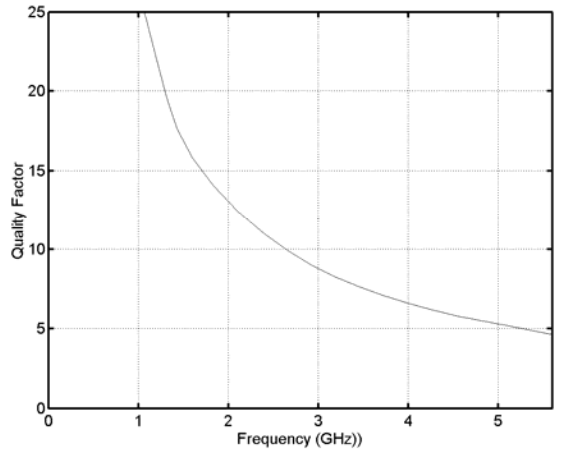


Fig. 10. Simulated "Q" quality factor.

Figure 10 shows the simulated quality factor for the two plate capacitor. A satisfactory agreement with the data reported in [6] is obtained so confirming the ability of the proposed method.

## 4 Conclusion

In this paper we propose a numerical technique for the simulation of MEMS devices. The method is based on the coupling between electrical and mechanical analysis, taking into account both the deformations and the electromagnetic interactions. A standard FEM structural formulation is coupled with the MoM for the bias analysis; an equivalent network approach based on an integral formulation is used for the electromagnetic analysis and allows to be interfaced with a full wave model of the entire devices.

The method has been tested on a MEMS capacitor, giving consistent results.

## References

[1] S. D. Senturia, N. Aluru, J. White, "Simulating the behaviour of MEMS Devices: Computational Methods and Needs," *IEEE Computational Science & Engineering*, pp. 30-43, January – March 1997.

[2] S. D: Senturia, "CAD Challenge for Microsensors, Microactuators, and Microsystems," *Proceedings of the IEEE,* Vol. 86, No. 8, pp. 1611 – 1626, August 1998.

[3] J J. Yao, "RF MEMS from a device perspective," *J. Micromech. Microeng.* 10, pp. 9-38, 2000.

[4] N. Bushyager, B. McGarvey, E. M. Tentzeris, " Introduction of an Adaptive Modeling Technique for the Simulation of RF Structures Requiring the Coupling of Maxwell's, Mechanical, and Solid – State Equations," *ACES Journal*, Vol 17, No. 1 pp. 104-111, March 2002.

[5] M. Kuroda, N. Miura, M. M. Tentzeris, "A Novel Numerical Approach for the Analysis of Ed MEMS – Based Variable Capacitors with Motion to Arbitrary Directions," *The 19Th Annual Rev. of Progress in Applied Computational Electromagnetic*, pp. 48- 53, Monterey March 2003.

[6] A. Dec, K. Suyama, "Micromachined Electro-Mechanically Tunable Capacitors and Their Applications to RF IC's," *IEEE Transactions on Microwave Theory and Techniques,* Vol. 46, No. 12, pp. 2587-2596, December 1998.

[7] A. Dec, K. Suyama, "A 1.9-GHz CMOS VCO with Micromachined Electromechanically Tunable Capacitors," *IEEE Journal of Solid-State Circuits,* Vol. 35, No. 8, pp. 1231-1237, August 2000.

[8] A. Dec, K. Suyama, "Microwave MEMS-Based Voltage-Control Oscillators," *IEEE Transactions on Microwave Theory and Techniques*, Vol. 48. No. 11, pp. 1943- 1949, November 2000

[9] E. S. Hung, S. D. Senturia, "Generating Efficient Dynamical Models for Microelectromechanical Systems from a Few Finite-Element Simulation Runs," *IEEE*

*Journal of Microelectromechanical Systems,* Vol. 89, No. 3, pp.280-289, September 1999.
[10] *Ansys User Manual*, Ansoft Corp.
[11] R. F. Harrington, *Field Computation by Moment Method*, Mcmillan New York, 1968.
[12] A. E. Ruehli, P.A. Brennan, "Efficient Capacitance Calculations for Three-Dimensional Multiconductor Systems," *IEEE Trans. Microwave Theory and Techniques,* Vol. 21, pp. 76–82, Feb. 1973.
[13] N. Esposito, A. Musolino, M. Raugi "Modelling of three dimensional nonlinear eddy current problems with conductors in motion by an integral formulation", *IEEE Trans. On Magn.* Vol 32, No. 3, pp. 764-767, May 1996.
[14] D. F. Kelley, R. L. Luebbers, "Piecewise Linear Recursive Convolution for Dispersive Media Using FTDT" *IEEE Trans. On Ant. And Prop.,* Vol. 46, No. 6, pp. 792-797, June 1996.

**Sami Barmada** was born in Livorno, Italy, on November 18, 1970. He received the Master and Ph.D. degrees in electrical engineering from the University of Pisa, Italy, in 1995 and 2001, respectively. From 1995 to 1997, he was with ABB Teknologi, Oslo, Norway, where he was involved with distribution network analysis and optimisation. He is currently an Assistant Professor with the Department of Electrical Systems and Automation, University of Pisa, where he is involved with numerical computation of electromagnetic fields, particularly on the modeling of multiconductor transmission lines and to the application of wavelet expansion to computational electromagnetics. He was the technical chairman of the Progress In Electromagnetic Research Symposium (PIERS), Pisa, Italy, 2004 and has served as chairman and session organizer of international conferences.
Dr. Barmada was the recipient of the 2003 J F Alcock Memorial Prize, presented by The Institution of Mechanical Engineering, Railway Division, for the best paper in technical innovation.

**Antonino Musolino** was born in Reggio Calabria on January the 7th 1964. He received the Master degree in Electronic Engineering and the Ph. D degree in Electrical Engineering from the University of Pisa in 1990 and 1995 respectively. He is currently an Associate Professor of electrical engineering with the Department of Electrical Systems and Automation, University of Pisa.
His main research activities are the numerical methods for the analysis of electromagnetic fields in linear and nonlinear media, the design of special electrical machines and the application of the WE to computational electromagnetics.

**Rocco Rizzo** was born in Tricase (Lecce), Italy on August 11, 1971. He received the PhD in Electrical Engineering from university of Pisa in 2002. He is currently an Assistant Professor with the Department of Electrical Systems And Automation, University of Pisa. His primarily area of research is focused on the development of analytical and numerical methods for the analysis of electromagnetic fields in linear and non-linear media, applied to the design of electromagnetic devices for special purposes.
In April 2004 he has been elected as a member of Academy of Nonlinear Sciences (ANS) in Russia.

# TWO-DIMENSIONAL COUPLED ELECTROSTATIC-MECHANICAL MODEL FOR RF MEMS SWITCHES

Ehab K. I. Hamad [1], Atef Z. Elsherbeni [2], Amr M. E. Safwat [3], and Abbas S. Omar [1]

[1] Chair of Microwave and Communications Engineering, University of Magdeburg, P.O. Box 4120, Magdeburg D-39106, Germany, http://iesk.et.uni-magdeburg.de/hf
[2] Center for Applied Electromagnetic Systems Research (CAESR), Electrical Engineering Department, The University of Mississippi, University, MS 38677, USA
[3] Electronics and Communications Engineering Department, Ain Shams University, Cairo 11517, Egypt

Ehamad@iesk.et.uni-magdeburg.de, atef@olemiss.edu, asafwat@ieee.org, and a.omar@ieee.org

***Abstract*:** Two-dimensional (2-D) coupled electrostatic-mechanical model of RF MEMS switches has been developed, in which the effect of residual stress due to the fabrication process and axial force resulting from the beam stretching have been taken into account. The electrostatic model is based on the application of the finite difference (FD) technique to quasi-static solution of a 2-D plane cut of the MEMS switch structure. The electrostatic model calculates the induced electrostatic force on the membrane due to the applied dc bias voltage. From the resulting electrostatic potential, the force distribution, the switch capacitance, and the beam deformation have been calculated. The computed pull down voltage for different structures agrees well with published data. The developed simulation program combines the electrostatic and mechanical analyses together and gives accurate results in short running time.

**Keywords:** 2-D MEMS modeling, Residual stress, Axial force, Coupled electro-mechanics, Shunt Capacitive MEMS switch, RF MEMS switches.

## 1. Introduction

RF MEMS switches are constructed using thin metal membrane, which can be electrostatically actuated using dc-bias voltage. Since they are designed on scales where the electrostatic force is capable to move or deform the membrane, 3-D or at least 2-D coupled electrostatic-mechanical model is needed for accurate prediction of the switch behavior. A simple one-dimensional lumped model, assumes that the shape of the deformed beam remains flat independent of its position has been presented earlier in [1]. This model is the simplest and most intuitive analytically, but its accuracy is very poor. Its purpose is for quick analysis to gain physical insight and understand overall behavior of the MEMS switches for RF and microwave application.

Two-dimensional electromechanical simulations assuming that the beam is made up of many horizontal-plate-to-ground-plane capacitors connected in parallel along the length of the beam have also been analyzed [2]. A three-dimensional quasi-static electro-mechanical model, as an application of CoSolve-EM software by combining the electromagnetic and mechanical simulators to determine the beam deformation, has been addressed in [3]. Although the latter gives very accurate results, the 3-D EM and mechanical simulators are sophisticated, expensive and require huge simulation time. An accurate solution, without sophistication, can easily be obtained using a two-dimensional mechanical model that is coupled to the electrostatic force distribution, and this is the core of this article.

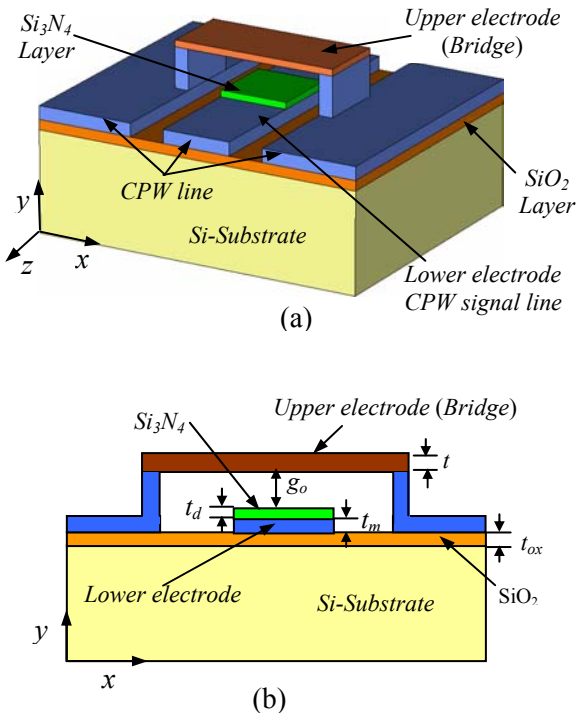


Fig. 1. Schematic diagram of fixed-fixed beam RF MEMS switch, (a) 3-D structure, (b) 2-D structure, *x*- *y* plane section.

The studied switch in this paper is electrostatically actuated and is doubly supported beam. A doubly supported or fixed-fixed beam RF MEMS switch usually consists of two parallel plates. One plate is fixed on the substrate, lower electrode, and the other is a movable membrane and is formed by a thin film metal that has good mechanical properties like Au or Cu prepared by electroplating process. A schematic diagram of a fixed-fixed beam shunt-capacitive RF MEMS switch is shown in Fig. 1. When a dc voltage is applied between the fixed and movable plates of the switch, the movable plate can move down onto the fixed electrode as a result of the electrostatic force induced due to the applied voltage. When the threshold (pull down) voltage is reached, the switch goes into the down state or OFF-state, and when no voltage is applied it goes into the up state or ON-state.

The purpose of this paper is to improve the algorithm, which has been presented elsewhere [4] to determine the deformation of the bridge in the shunt-capacitive RF MEMS switch as a function of the applied voltage. In [4] the effects of the residual and the axial stresses were not considered and also the electrostatic model was based on solving Laplace's equation. Most of the publications, either neglect the effect of the residual stress or the axial force or both of them [5]. To the authors' knowledge, the electrostatic force calculated in the literature is not in very accurate; some time the fringing field is neglected or used an approximate expression or the electrostatic force assumes uniformly distributed along the membrane [6-7]. Through this study the effect of the residual stress and the axial stress have been considered as well as the electrostatic force which has been calculated very accurately and as a non-uniform force distributed along the beam. The electrostatic model is based on Gauss's law applied to an inhomogeneous region with non-uniform discretization for accurate numerical simulation. The pull down voltage required to actuate the MEMS switch has been evaluated using the developed simulator. The main advantages of the proposed solution is that both electrostatic and mechanical models are combined in one simple Matlab-based program to determine the deformation of the switch's bridge, which is based on quasi-static solution in two-dimensions using the finite difference method (FDM). The choice of the fixed-fixed beam is based on the fact that this mechanical structure is the most common and the most basic to the surface-micro-machined MEMS structures. However, the developed simulation tool is easy to adapt to other configurations of MEMS structures.

## 2. Mathematical Algorithm

The starting point is to solve for the quasi-static potential in two-dimensions. Hence, the field distributions and the force induced on the membrane can be determined. Having the force distribution on the membrane makes it possible to activate the mechanical model in order to calculate the deformation in the membrane, which in turns alters the electrostatic field distribution. This cycle of electromechanical model is considered as one iteration. The program goes back and forth between the electrostatic and mechanical models until the difference between the maximum-deformation in the membrane in two successive iterations is less than $10^{-4}$ μm, which can be the program convergence criterion as defined by the user.

### *A. Electrostatic Model*

The electrostatic model starts by generating the meshes with non-uniform grid sizes in both directions to get the minimum execution time with the highest possible accuracy. Next, Gauss's law is applied in the meshed region along with the finite difference technique to approximate the derivatives. The boundary conditions are $V = V_o$ on the lower electrode (CPW signal line) and $V = 0$ on the upper electrode (MEMS bridge) and the outer boundary. On the dielectric interface and at any node in the computational domain other than those on the electrodes, Gauss's law is applied.

The solution of the potential at the nodes of the grid inside the computational domain based on Gauss's law starts with

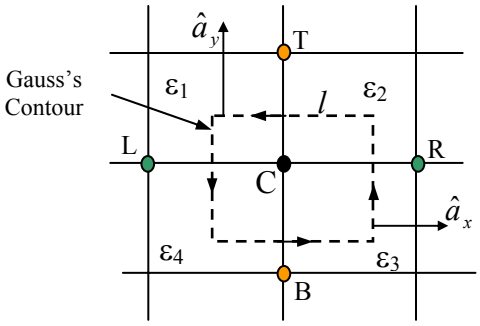


Fig. 2. A general voltage node C in the computational domain is surrounded by four voltage nodes, L, R, B, and T with four different media and the Gauss's contour.

$$-\oint_l \varepsilon \left( \frac{\partial V}{\partial x}\hat{a}_x + \frac{\partial V}{\partial y}\hat{a}_y \right) \bullet \hat{a}_n \, dl = 0 \qquad (1)$$

where the finite difference approximations translate this integral equation on the closed contour described in Fig. 2 to the following [8],

$$\frac{V_R-V_C}{x_R-x_C}\left[(y_T-y_C)\varepsilon_2+(y_C-y_B)\varepsilon_3\right]-\frac{V_C-V_L}{x_C-x_L}\left[(y_T-y_C)\varepsilon_1+(y_C-y_B)\varepsilon_4\right]$$
$$+\frac{V_T-V_C}{y_T-y_C}\left[(x_C-x_L)\varepsilon_1+(x_R-x_C)\varepsilon_2\right]-\frac{V_C-V_B}{y_C-y_B}\left[(x_R-x_C)\varepsilon_3+(x_C-x_L)\varepsilon_4\right]=0 \quad (2)$$

where the subscripts L, R, T, and B denote left, right, top, and bottom, respectively. This equation can be rearranged in the following general form:

$$V_C = C_R V_R + C_L V_L + C_T V_T + C_B V_B \quad (3)$$

where $C_R = C_o \dfrac{(y_T - y_C)\varepsilon_2 + (y_C - y_B)\varepsilon_3}{x_R - x_C}$,

$$C_L = C_o \frac{(y_T - y_C)\varepsilon_1 + (y_C - y_B)\varepsilon_4}{x_C - x_L},$$

$$C_T = C_o \frac{(x_R - x_C)\varepsilon_2 + (x_C - x_L)\varepsilon_1}{y_T - y_C},$$

$$C_B = C_o \frac{(x_R - x_C)\varepsilon_3 + (x_C - x_L)\varepsilon_4}{y_C - y_B},$$

and

$$C_o = \frac{1}{\left[\left(\frac{y_C-y_B}{x_R-x_C}+\frac{x_R-x_C}{y_C-y_B}\right)\varepsilon_3+\left(\frac{y_T-y_C}{x_R-x_C}+\frac{x_R-x_C}{y_T-y_C}\right)\varepsilon_2 + \left(\frac{y_C-y_B}{x_C-x_L}+\frac{x_C-x_L}{y_C-y_B}\right)\varepsilon_4+\left(\frac{y_T-y_C}{x_C-x_L}+\frac{x_C-x_L}{y_T-y_C}\right)\varepsilon_1\right]}.$$

Equation (3) has been solved using an iterative technique to find out the potential distribution everywhere in the computational domain. After solving for the potential distribution, the electric field vector can be calculated from the relation $\overline{E} = -\nabla V$ at every node, such that

$$E_x = -\frac{\partial V}{\partial x} \quad \text{and} \quad E_y = -\frac{\partial V}{\partial y}.$$

Since we are using non-uniform grid, the potential can best be described at any arbitrary node using Lagrange's polynomials approximation, where

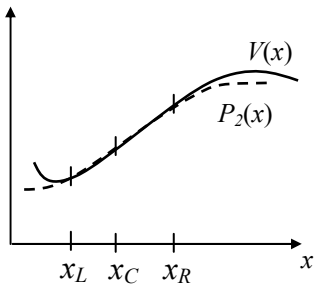


Fig. 3. Lagrange interpolation.

Lagrange's interpolating polynomial is described as:

$$V(x) \approx P_2(x) = \frac{(x-x_C)(x-x_R)}{(x_L-x_C)(x_L-x_R)}V(x_L) + \frac{(x-x_L)(x-x_R)}{(x_C-x_L)(x_C-x_R)}V(x_C) + \frac{(x-x_L)(x-x_C)}{(x_R-x_L)(x_R-x_C)}V(x_R)$$

where $P_2(x)$ is a second order degree polynomial which coincides with the exact function $V(x)$ at three nodes *L, R,* and *C* as shown in the Fig. 3.

Lagrange's interpolating polynomial is differentiated to obtain an approximation for the first order derivative and thus, the electric field vector components can be computed at any node *x* by

$$E_x(x) = -\frac{dV(x)}{dx} = -\frac{2x-x_C-x_R}{(x_L-x_C)(x_L-x_R)}V_L - \frac{2x-x_L-x_R}{(x_C-x_L)(x_C-x_R)}V_C - \frac{2x-x_L-x_C}{(x_R-x_L)(x_R-x_C)}V_R. \quad (4)$$

In the same way, the *y*-component at any node *y* can be computed.

The electrostatic model calculates the electrostatic force induced on the movable beam when a dc-bias voltage is applied between the upper and lower electrodes. When a dc-bias voltage is applied between the two plates, charges are induced on the membrane and opposite charges accumulate on the lower electrode. The induced charges per unit length $\rho$ induced on the membrane are calculated using Gauss's law in two-dimensions as follows:

$$\rho = -\oint_l \varepsilon \frac{\partial V}{\partial n}\hat{n} \bullet \hat{a}_n dl \quad (5)$$

where *l* is a closed contour surrounding each subsection of the membrane as shown in Fig 4. Here $\hat{a}_n$ is the normal unit vector to the contour segments. By dividing the contour to four segments we obtain,

$$\rho = -\int_{right} \varepsilon(y)\frac{\partial V}{dx}dy - \int_{top} \varepsilon(x)\frac{\partial V}{dy}dx + \int_{left} \varepsilon(y)\frac{\partial V}{dx}dy + \int_{bottom} \varepsilon(x)\frac{\partial V}{dy}dx.$$

Assuming the field outside the metallic boundary and the voltage applied to the bridge to be zero, and the adjacent medium to the bridge surface is air with $\varepsilon_r = 1$. Thus, the accumulated charge per unit length distributed in the *z*-direction for any segment on the membrane centered at $(x_c, y_c)$ can be calculated as:

$$\rho\ (x_C) = \varepsilon_o \frac{V_B}{y_C - y_B}\left[\frac{x_R - x_L}{2}\right].$$

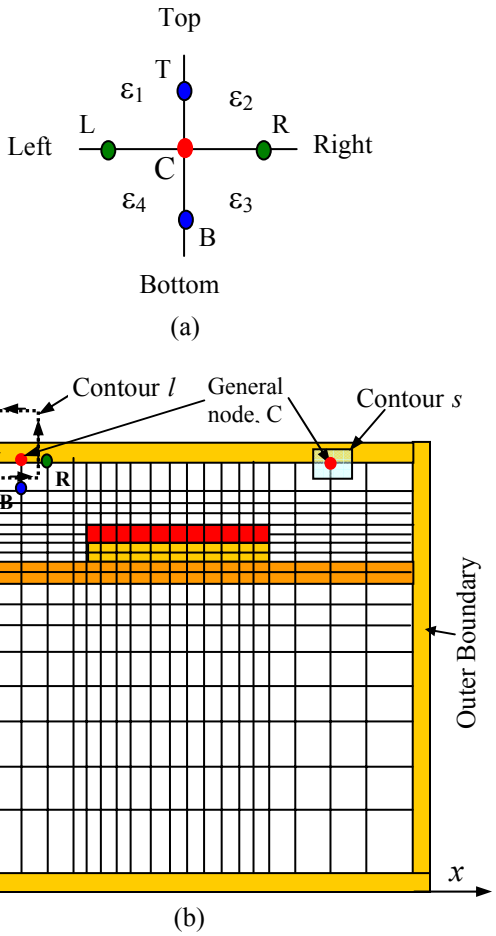


Fig. 4. (a) Notation of the potential and media properties in terms of the node coordinates for 2-D problem (b) Computational domain with the mesh distribution.

Dividing this equation by the segment length $(x_R - x_L)/2$ to find the charge density and multiplying it by $b$, the beam width, one can obtain the distributed charge per unit length on the bridge along the $x$-axis for any segment centered at $x_c$ as:

$$\rho(x_C) = \varepsilon_o \frac{V_B}{y_C - y_B} b \ . \tag{6}$$

Having the electric field components, the electrostatic force induced on the bridge can be determined. The normal electrostatic force per unit length can be determined in terms of the storage energy $U$ per unit length as: $f(x) = -dU(x,y)/dy$, where $U$ is defined as $U = (1/2)\int_s \varepsilon\, E^2 dxdy$, and $s$ is the surface contour shown in Fig. 4. Thus, $f(x) = (1/2)\int_l \varepsilon\, E^2 dx$ in Newton per unit length along the $z$-direction. Therefore, the amount of the electrostatic force induced on a certain segment of length $\Delta x$ on the membrane is calculated by:

$$\Delta f(x) = (1/2)\,\varepsilon_o\, E^2(x, y \text{ at the bridge})\Delta x \ .$$

Dividing this equation by $\Delta x$ to find the force density and multiplying it by the beam width $b$ gives the distributed force per unit length in the $x$-direction induced on the bridge, thus at any arbitrary node $x$ the distributed force per unit length is given as:

$$f(x) = \frac{b}{2}\varepsilon_o \left(E_x^2 + E_y^2\right). \tag{7}$$

In order to calculate the switch capacitance one needs to compute the total charge on the lower electrode then divide it by the applied voltage. Applying Gauss's law around the lower electrode as shown in Fig. 5. This leads to the following expression for the total enclosed charge.

$$\begin{aligned}\rho^{enc} = &-\sum_{right}\frac{V_R - V_C}{x_R - x_C}\left[\frac{\varepsilon_2(y_T - y_C) + \varepsilon_3(y_C - y_B)}{2}\right] \\ &-\sum_{top}\frac{V_T - V_C}{y_T - y_C}\left[\frac{\varepsilon_1(x_C - x_L) + \varepsilon_2(x_R - x_C)}{2}\right] \\ &+\sum_{left}\frac{V_C - V_L}{x_C - x_L}\left[\frac{\varepsilon_1(y_T - y_C) + \varepsilon_4(y_C - y_B)}{2}\right] \\ &+\sum_{bottom}\frac{V_C - V_B}{y_C - y_B}\left[\frac{\varepsilon_4(x_C - x_L) + \varepsilon_3(x_R - x_C)}{2}\right].\end{aligned} \tag{8}$$

The capacitance $C$ per unit length is given next by $C = \rho^{enc}/V_o$, where $V_o$ is the applied voltage between the lower and upper electrodes.

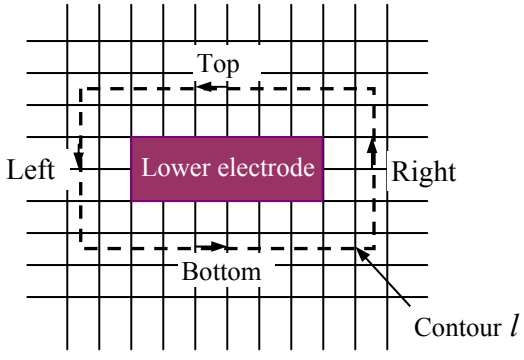


Fig. 5. Computation of the total charge accumulated on the lower electrode.

The accuracy of the results is completely dependant on the number of iterations, for this reason the program has been run for different numbers of iterations to get the optimal number. The maximum induced electrostatic force, the maximum deformation, and the switch capacitance in terms of the number of iterations are illustrated in Fig. 6-a, 6-b, and 6-c, respectively. The CPU time on a PC with Pentium IV, 1.4 GHz processor, and 2.0 GB RAM in terms of the number of iterations is plotted in Fig. 6-d as well. The maximum electrostatic force and the maximum deflection have been saturated after about 1000 iterations but the capacitance saturated after 2000 iterations. All subsequent data presented in this paper are generated on basis of 2000 iterations.

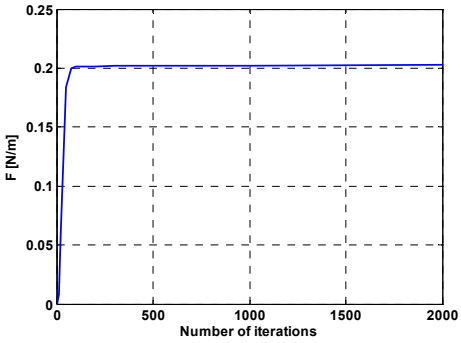


(a)

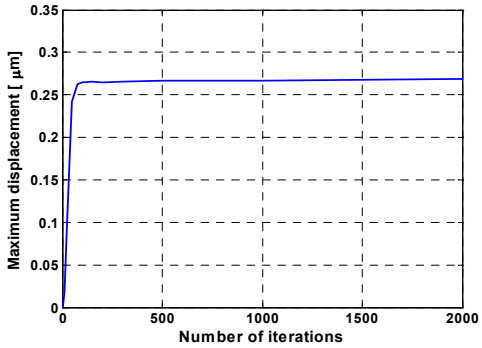


(b)

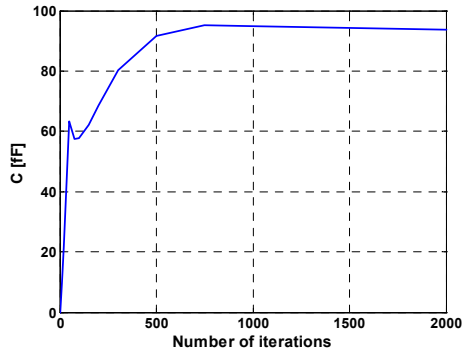


(c)

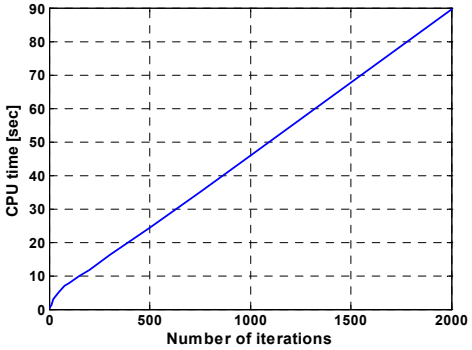


(d)

Fig. 6. (a) Maximum force vs. number of iterations (b) Maximum displacement vs. number of iterations (c) Capacitance vs. number of iterations (d) CPU time vs. number of iterations. The number of meshes are $n_x$ = 72, $n_y$ = 88 in the $x$ and $y$ directions, respectively. The mesh size is non-uniform in both $x$ and $y$ directions for more accurate solution, and it's minimized where fine geometrical details are present. $dx_{min}$ = 2.8 (over the lower electrode region, where most of the field is confined), $dx_{max}$ = 9 (at the end of the bridge, where approximately no field), $dy_{min}$ = 0.0375 (in dielectric layer, the smallest thickness in the $y$-direction), and $dy_{max}$ = 2.23 (at the bottom of substrate, where the field is decayed), all dimensions are in µm.

For the shunt-capacitive RF MEMS switch given in [1], where $L$ (bridge length) = 300 µm, $b$ (membrane width) = 80 µm, $t$ (membrane thickness) = 2 µm, $g_o$ (initial gap height) = 1.5 µm, $W$ (lower electrode width) = 100 µm, $t_m$ (lower electrode thickness) = 0.8 µm, $t_{ox}$ (oxide layer thickness) = 0.4 µm, $t_d$ (dielectric layer thickness) = 0.15 µm, the potential distribution after solving the static problem in the computation region is shown on Fig. 7. The charge distribution per unit length on the bridge based on Eq. (6) has been calculated with dc bias voltage of 30 Volts and plotted in Fig. 8-a. The corresponding distributed electrostatic force per unit length calculated using Eq. (7) is depicted in Fig. 8-b.

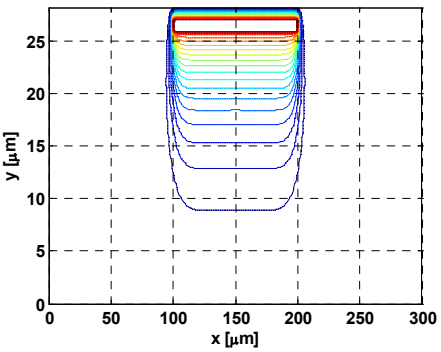


Fig. 7. Potential distribution in the computational domain with dc bias voltage of 30 Volts.

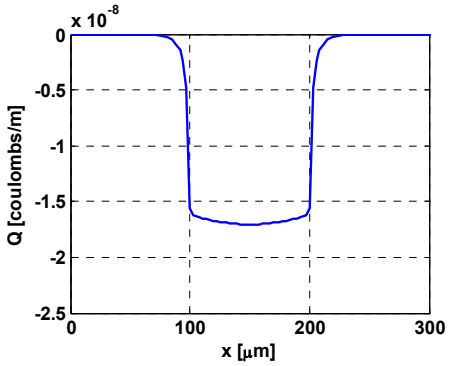


(a)

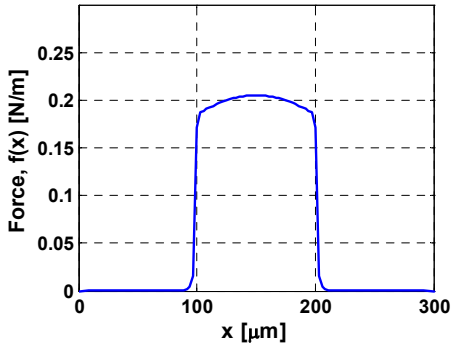


(b)

Fig. 8. (a) Charge distribution per unit length over the membrane with bias voltage of 30 Volts, (b) Force distribution per unit length induced on the membrane at bias voltage of 30 Volts.

### *B. Mechanical Model*

Figures 1 and 9 show the fixed-fixed beam diagram and the load configuration, respectively. The step-up support in this beam has been approximated as a "fixed" boundary condition [9]. The transverse deflection of the movable beam $w(x)$ is governed by Euler-Bernoulli beam equation given in [10] as:

$$\hat{E}\tilde{I}\,\frac{\partial^4 w}{\partial x^4} - (T_r + T_a)\frac{\partial^2 w}{\partial x^2} = f(x) \qquad (9)$$

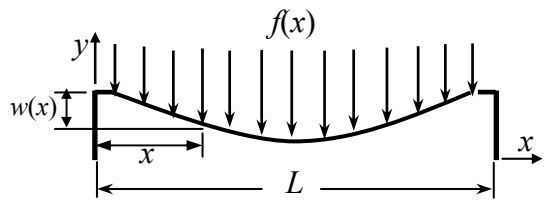


Fig. 9. Schematic diagram of the deformed electrostatic loaded double-supported beam.

where $f(x)$ is the distributed force per unit length (the beam here is electrostatically loaded and $f(x)$, which is the electrostatic force calculated from the electrostatic model couples the mechanical model and the electrostatic model). $w(x)$ is the beam displacement, $\hat{E} = E/(1\text{-}\nu^2)$ is the beam modulus where $E$ is Young's modulus, $\nu$ is Poisson's ratio, $\tilde{I} = bt^3/12$ is the beam moment of inertia, $t$ and $b$ are the beam thickness and width, respectively. $T_r$ is the residual force and is formulated by $T_r = \hat{\sigma}bt$, where $\hat{\sigma}$ is the residual stress which equals $\sigma_o(1-\nu)$ for the doubly supported beam, where $\sigma_o$ is the biaxial residual stress. $T_a$ is the axial force and is formulated by $T_a = \frac{\hat{E}bt}{2L}\int_0^L \left(\frac{dw}{dx}\right)^2 dx$.

To find the general solution of equation (9), it is more convenient to rewrite it in the form:

$$\frac{d^4 w}{dx^4} - k^2\frac{d^2 w}{dx^2} = F(x) \qquad (10)$$

where $k^2 = \frac{\hat{\sigma}bt}{\hat{E}\tilde{I}} + \frac{6b}{Lt^2}\int_0^L \left(\frac{dw}{dx}\right)^2 dx$, and $F(x) = \frac{f(x)}{\hat{E}\tilde{I}}$.

Equation (10) is a fourth order nonlinear, non-homogenous differential equation. If the axial force term $\frac{6b}{Lt^2}\int_0^L \left(\frac{dw}{dx}\right)^2 dx$ is neglected $k$ will be constant equals to $\sqrt{\frac{\hat{\sigma}bt}{\hat{E}\tilde{I}}}$. Thus the 4th order differential equation will be linear but still non-homogenous. The general solution of a higher order non-homogenous linear differential equation can be found easily using the method of variation of parameters [11]. The general solution of this equation while, initially, assuming $k$ is constant can be found by assuming the general solution of the homogenous equation of (10) to be in the form

$$w_c(x) = a_o + a_1 x + a_2 e^{kx} + a_3 e^{-kx}. \qquad (11)$$

Furthermore, by setting $w_o(x) = 1$, $w_1(x) = x$, $w_2(x) = e^{kx}$, and $w_3(x) = e^{-kx}$ in the last equation, one can use the method of variation of parameters for determining the particular solution $w_p(x)$ of Eq. (10) by determining four functions $u_o$, $u_1$, $u_2$, and $u_3$ such that

$$w_p(x) = u_o(x)\,w_o(x) + u_1(x)\,w_1(x) + u_2(x)\,w_2(x) + u_3(x)\,w_3(x). \qquad (12)$$

For these functions to be determined, four conditions must be specified. The Wronskian $W$ of functions $w_o$, $w_1$, $w_2$, and $w_3$ is the determinant:

$$W(w_o, w_1, w_2, w_3) = \begin{bmatrix} w_o(x) & w_1(x) & w_2(x) & w_3(x) \\ w_o'(x) & w_1'(x) & w_2'(x) & w_3'(x) \\ w_o''(x) & w_1''(x) & w_2''(x) & w_3''(x) \\ w_o'''(x) & w_1'''(x) & w_2'''(x) & w_3'''(x) \end{bmatrix}$$

while $u_k' = \frac{W_k}{W}$, where $W_k$ is the determinant obtained by replacing the $k^{th}$ column of the Wronskian by the column consisting of the elements $(0,0,0, F(x))$. Simple integration can be used to obtain $u_o(x)$, $u_1(x)$, $u_2(x)$, and $u_3(x)$, while substitution in Eq. (12) yields the particular solution

$$u_o(x) = \frac{1}{a_o k^2}\int xF(x)dx\,,\; u_1(x) = -\frac{1}{a_1 k^2}\int F(x)dx\,,$$

$$u_2(x) = \frac{1}{2a_2 k^3}\int e^{-kx}F(x)dx,\; u_3(x) = -\frac{1}{2a_3 k^3}\int e^{kx}F(x)dx$$

with

$$w_p(x) = \frac{1}{k^2}\int xF(x)dx - \frac{x}{k^2}\int F(x)dx + \frac{e^{kx}}{2k^3}\int e^{-kx}F(x)dx - \frac{e^{-kx}}{2k^3}\int e^{kx}F(x)dx.$$

Thus, the general solution of $w(x)$ equals $w_c(x) + w_p(x)$, which can be found as:

$$w(x) = a_o + a_1 x + a_2 e^{kx} + a_3 e^{-kx} + \frac{1}{k^2}\int_0^x \lambda F(\lambda)\,d\lambda - \frac{x}{k^2}\int_0^x F(\lambda)\,d\lambda + \frac{e^{kx}}{2k^3}\int_0^x e^{-k\lambda}F(\lambda)\,d\lambda - \frac{e^{-kx}}{2k^3}\int_0^x e^{k\lambda}F(\lambda)\,d\lambda \tag{13}$$

where $a_0$, $a_1$, $a_2$, and $a_3$ are constants to be determined by applying the boundary conditions $w(0) = 0 = w'(0)$ and $w(L) = 0 = w'(L)$, with assumed clamped-clamped beam. The coefficients $a_0$, $a_1$, $a_2$, and $a_3$ can be determined from the following matrix equation:

$$\begin{bmatrix} a_0 \\ a_1 \\ a_2 \\ a_3 \end{bmatrix} = \begin{bmatrix} 1 & 0 & 1 & 1 \\ 0 & 1 & \mathrm{k} & -\mathrm{k} \\ 0 & \mathrm{L} & \mathrm{e}^{\mathrm{kL}} & \mathrm{e}^{-\mathrm{kL}} \\ 0 & 1 & \mathrm{ke}^{\mathrm{kL}} & -\mathrm{ke}^{-\mathrm{kL}} \end{bmatrix}^{-1} \begin{bmatrix} 0 \\ 0 \\ b_1 \\ b_2 \end{bmatrix} \tag{14}$$

where

$$b_1 = -\frac{1}{k^2}\int_0^L \lambda F(\lambda)\,d\lambda + \frac{L}{k^2}\int_0^L F(\lambda)\,d\lambda - \frac{e^{kL}}{2k^3}\int_0^L e^{-k\lambda}F(\lambda)\,d\lambda + \frac{e^{-kL}}{2k^3}\int_0^L e^{k\lambda}F(\lambda)\,d\lambda$$

and

$$b_2 = \frac{1}{k^2}\int_0^L F(\lambda)\,d\lambda - \frac{e^{kL}}{2k^2}\int_0^L e^{-k\lambda}F(\lambda)\,d\lambda - \frac{e^{-kL}}{2k^2}\int_0^L e^{k\lambda}F(\lambda)\,d\lambda\,.$$

The integrals for the $b$ coefficients are all finite and are computed numerically.

Now to include the axial force in this analysis, we use the resulting $w(x)$ to determine the axial force term $\frac{6b}{Lt^2}\int_0^L \left(\frac{dw}{dx}\right)^2 dx$ and then calculate the new value of $k$ and substitute back in Eq. (13) using the new values of the $a$ coefficients calculated from Eq. (14) to determine the new $w(x)$. Repeating this process until the difference between two successive iterations for $k$ is within pre-determined value. In our procedure the error was set to be lower than $10^{-10}$ m$^{-1}$.

### *C. Coupled Electrostatic-Mechanical Model*

When a dc voltage is applied to the un-actuated MEMS switch shown in Fig. 1, it induces charges on the surface of the membrane that in turn induce a normal electrostatic force over the membrane, as given by Eq. (7). The electrostatic force causes the beam to deform. Such deformation will lead to a reorganization of the surface charges. The force distribution on the beam is schematically shown in Fig. 6-b. If this reorganization of charges is large enough to cause further deformation, the process is necessary to resolve the electrostatic problem to recalculate the new induced electrostatic force and this is considered as a coupled electro-mechanical behavior. The new electrostatic force is used by the mechanical model to determine the new transverse deflection. Going back and forth between these two models is carried out until the difference between two successive iterations for the transverse deflection is in a pre-determined specified error. In our procedure the error has been set to be less than $10^{-10}$ m.

For MEMS analysis, it is usually assumed that the pull down occurs when the microstructure deflects down to $(2/3)g_o$, where $g_o$ is the initial gap height. This is considered the unstable mechanical position of the bridge. Hence the back and forth switching between the electric and mechanical models converges as long as the switch works in the mechanical stability region other-wise it may diverge. Therefore, the iterations is stopped when the maximum deflection is greater than or equal $(2/3)g_o$, which corresponds to the pull down voltage for the MEMS switch.

### 3. Results and Discussion

To validate the obtained numerical results, we compare the results of the maximum deflection calculated using our approach to those reported in [1] with the parameters shown in Fig. 1 for doubly supported beam of the dimensions given in section 2-A. The silicon-nitride $Si_3N_4$ and silicon-oxide $SiO_2$ dielectric layers have relative dielectric constants of 7.6 and 3.9, respectively. The Young's modulus $E$ amounts to 80 GPa, the Poison's ratio $\nu$ is equal to 0.42, and the biaxial residual stress $\sigma_o$ is equal to 20 MPa.

The computed maximum displacement and the gap capacitance as functions of the number of iterations are shown in Fig. 10. The steady state condition has been reached after 9 iterations between the electrostatic and mechanical solutions. The iterations stopped when the error in the maximum deflection curve falls below a tolerance value (here given as $10^{-4}$ μm) or the maximum deflection increases than $(2/3)g_o$, which means the applied voltage is greater than or equals the pull down voltage. Figure 11-a illustrates the gap height versus applied voltage, while Fig. 11-b illustrates the gap capacitance versus applied voltage. The shape of the bridge as a function of applied voltage is investigated in Fig. 12. The computed pull down voltage amounts to 35 Volts while the experimental value for similar configuration is usually reported to be in the range of 30 Volts. The computed up-position capacitance of the MEMS switch is 85 fF while the experimental value is 70 fF. The theoretical results are very close to the experimental values reported in the literatures.

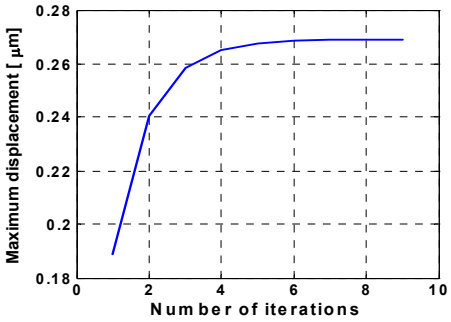


Fig. 10. (a) Maximum displacement and (b) Switch capacitance as a function of the number of iterations of going and back between the electrostatic and mechanical models at dc bias voltage of 30 Volts.

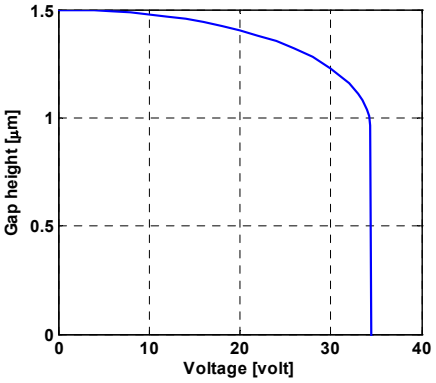


Fig. 11-a. Gap height versus applied voltage.

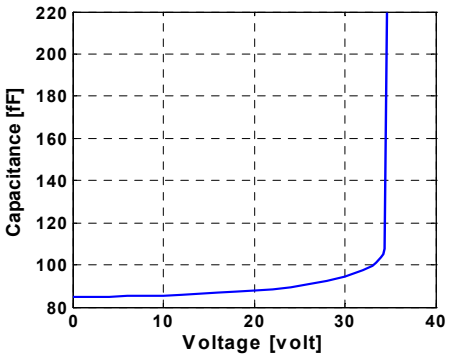


Fig. 11-b. Capacitance versus applied voltage.

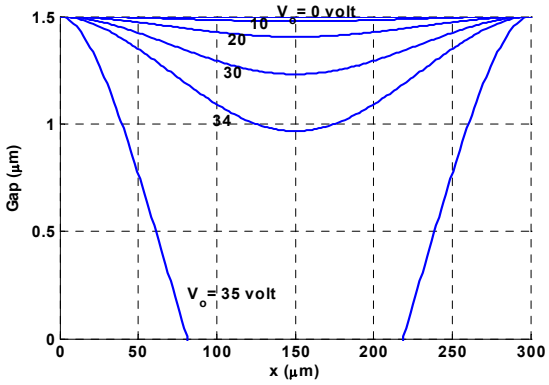


Fig. 12. Shape of the membrane as a function of applied voltage.

### 4. Conclusion

In this paper, a novel two-dimensional coupled electro-mechanical model has been developed, where the axial and residual stresses are taken into consideration. A Simulation program is developed to

determine the deformation of the bridge in RF MEMS switches as a function of the applied voltage. The electrostatic model is based on solving Gauss's law in a two-dimensional Cartesian coordinates system using the central difference approximation for the derivatives. An iterative procedure is implemented for the solution of the potential distribution. The algorithm is very efficient to determine the pull down voltage of the shunt-capacitive MEMS switch. However, it can be used for other types of MEMS switches like series or shunt configuration, capacitive or resistive contact as well.

The developed algorithm and the program presented are capable to determine the bridge deformation, pull-in voltage and to investigate the effect of source fluctuations on the switch performance efficiently. Due to its numerical efficiency and small CPU time requirement, the proposed technique can be integrated easily in computer-aided design tools for MEMS switches.

## References


[1] J. B. Muldavin, G. M. Rebeiz, "High-Isolation CPW MEMS Shunt Switches-Part 1: Modeling", *IEEE Transaction on Microwave Theory and Techniques*, Vol. 48, No. 6, pp. 1045-1052, June 2000.

[2] E. K. Chan, K. Garikipati, and R. W. Dutton, "Characterization of Contact Electromechanics Through Capacitance-Voltage Measurements and Simulations", *IEEE Journal of MEMS*, Vol. 8. No. 2, pp. 208-217, June 1999.

[3] J. R. Gilbert, R. Legtenberg, and S. D. Senturia, "3D coupled electro-mechanics for MEMS: application of CoSolve-EM," Proceeding of *Int. IEEE MEMS Conference*, pp. 122-127, 1995.

[4] E. K. I. Hamad, A. M. E. Safwat, and A. S. Omar, "2-D Coupled Electrostatic-Mechanical Model for Shunt-Capacitive MEMS Switch Based on Matlab Program," Proceeding of *the IEEE/ACES International Conference*, Honolulu, Hawaii, USA, April 2005.

[5] Q. Meng, M. Mehregany, and R. L. Mullen, "Theoretical Modeling of Microfabricated Beams with Elastically Restrained Supports", *IEEE Journal of MEMS*, Vol. 2, pp. 128-137, Sept. 1993.

[6] B. Choi and E. G. Lovell, "Improved Analysis of Microbeams under Mechanical and Electrostatic Loads", *Journal of Micromech Microeng*, Vol. 7, pp. 24–29, 1997.

[7] L. X. Zhang, Y.-P. Zhao, "Electromechanical Model of RF MEMS Switches", *Microsystem Technologies* 9, pp. 420–426, 2003.

[8] A. Z. Elsherbeni, "The Finite Difference Technique for Electromagnetic Applications", Electrical Engineering Department, The University of Mississippi, University, MS 38677, USA, May 2005.

[9] P. Osterberg, H. Yie, X. Cai, J. White, and S. Senduria "Self-Consistent Simulation and Modeling of Electrostatically Deformed Diaphragms", Proceeding of *Int. IEEE MEMS Conference*, Oiso, Japan, pp. 28-32, January 1994.

[10] S. P. Timoshenko and J. M. Gere "Theory of Elastic Stability", *McGraw-Hill Inc.,* New York, 2nd ED., 1961.

[11] W. E. Boyce and R. C. Diprima, "Elementary Differential Equations and Boundary Value Problems", *John Wiley & Sons, Inc*. New York, 6th ED. 1997.


**Ehab K. I. Hamad** was born in Assiut, Egypt in 1970. He received his B.Sc. in Electrical Engineering and M.Sc. in Electronics and Communications Engineering from Assiut University, Assiut, Egypt, in 1994 and 1999, respectively. From 1999 to 2001 he was a Teaching/ Research Assistant in Electrical Engineering Department, Aswan Faculty of Engineering, South Valley University, Aswan, Egypt. He is currently working toward the Ph.D. degree in Microwave and Communications Engineering at Otto-von-Guericke-University Magdeburg, Magdeburg, Germany.

Mr. Hamad has jointed the Chair of Microwave and Communication Engineering, University of Magdeburg since 2001. His research interests include MEMS analysis, design, modeling, and fabrication with special interest in RF MEMS switches and filters for RF and microwave applications. He is interested also in planar microwave circuits for wireless applications.

**Atef Z. Elsherbeni** received an honor B.Sc. degree in Electronics and Communications, an honor B.Sc. degree in Applied Physics, and a M.Eng. degree in Electrical Engineering, all from Cairo University, Cairo, Egypt, in 1976, 1979, and 1982, respectively, and a Ph.D. degree in Electrical Engineering from Manitoba University, Winnipeg,

Manitoba, Canada, in 1987. He was a Research Assistant with the Faculty of Engineering at Cairo University from 1976 to 1982, and from 1983 to 1986 at the Electrical Engineering Department, Manitoba University. He was a part time Software and System Design Engineer from March 1980 to December 1982 at the Automated Data System Center, Cairo, Egypt. From January to August 1987, he was a Post Doctoral Fellow at Manitoba University. Dr. Elsherbeni joined the faculty at the University of Mississippi in August 1987 as an Assistant Professor of Electrical Engineering. He advanced to the rank of Associate Professor on July 1991, and to the rank of Professor on July 1997. He became the director of The School of Engineering CAD Lab at the University of Mississippi on August 2002, and the associate director of The Center for Applied Electromagnetic Systems Research (CAESR) at The University of Mississippi on August 2002. He was appointed as Adjunct Professor, at The Department of Electrical Engineering and Computer Science of the L.C. Smith College of Engineering and Computer Science at Syracuse University on January 2004. He spent a sabbatical term in 1996 at the Electrical Engineering Department, University of California at Los Angeles (UCLA) and was a visiting Professor at Magdeburg University during the summer of 2004.

Dr. Elsherbeni received The Mississippi Academy of Science 2003 Outstanding Contribution to Science Award, The 2002 IEEE Region 3 Outstanding Engineering Educator Award, The 2002 School of Engineering Outstanding Engineering Faculty Member of the Year Award, the 2001 Applied Computational Electromagnetic Society (ACES) Exemplary Service Award for leadership and contributions as Electronic Publishing Managing Editor 1999-2001, the 2001 Researcher/Scholar of the year award in the Department of Electrical Engineering, The University of Mississippi, and the 1996 Outstanding Engineering Educator of the IEEE Memphis Section.

Dr. Elsherbeni has conducted research in several areas such as: scattering and diffraction by dielectric and metal objects, inverse scattering, finite difference time domain analysis of passive and active microwave devices, field visualization and software development for EM education, dielectric resonators, interactions of electromagnetic waves with human body, and development of sensors for soil moisture and for monitoring of airports noise levels, air quality including haze and humidity, reflector antennas and antenna arrays, and analysis and design of printed antennas for radars and communication systems. His recent research has been on the application of numerical techniques to microstrip and planar transmission lines, antenna measurements, and antenna design for radar and personal communication systems. He has published 82 technical journal articles and 17 book chapters on applied electromagnetics, antenna design, and microwave subjects, and contributed to 230 professional presentations and offered 16 short courses and 17 invited seminars. He is the coauthor of the book entitled "MATLAB Simulations for Radar Systems Design", CRC Press, 2003 and the main author of the chapters "*Handheld Antennas"* and "*The Finite Difference Time Domain Technique for Microstrip Antennas"* in Handbook of Antennas in Wireless Communications, CRC Press, 2001.

Dr. Elsherbeni is a senior member of the Institute of Electrical and Electronics Engineers (IEEE). He is the Editor-in-Chief for the Applied Computational Electromagnetic Society (ACES) Journal, an Associate Editor to the Radio Science Journal, and the electronic publishing managing editor of ACES. He serves on the editorial board of the Book Series on Progress in Electromagnetic Research, the Electromagnetic Waves and Applications Journal, and the Computer Applications in Engineering Education Journal. He was the Chair of the Engineering and Physics Division of the Mississippi Academy of Science and the Chair of the Educational Activity Committee for the IEEE Region 3 Section. Dr. Elsherbeni's home page can be found at http://www.ee.olemiss.edu/atef and his email address is Elsherbeni@ieee.org.

**Amr M. E. Safwat** was born in Cairo, Egypt in May 1970. He received the B. S. and the M.S. from Ain Shams University, Cairo, Egypt in 1993 and 1996 respectively and the Ph.D. from University of Maryland, College park in 2001. All are in Electrical Engineering.

He was a Research and Teaching Assistant at Ain Shams University from 1993-1997. From 1997- 2001 he was a Research Assistant in Laboratory for Physical Sciences, University of Maryland. From Aug. 2001 to Aug. 2002 he was with Cascade Microtech, Inc, where he co-developed the infinity probes and the on wafer differential calibration standards. In Aug. 2002, he joined the Electronics and Communications Engineering Department, Ain Shams University as Assistant Professor. He was a Researcher/ Visiting Professor in the Institute Polytechnique de Grenoble (INPG) France in 1994 and in the Otto-von-Guericke-University Magdeburg Germany in 2004. His research interests include microwave opt-electronic oscillator,

high-speed photo-detectors, on-wafer probing and microwave integrated circuits.

**Abbas S. Omar** received the B.Sc., M.Sc. and Doktor-Ing. degrees in Electrical Engineering in 1978, 1982 and 1986, respectively. He has been Professor of Electrical Engineering since 1990 and head of the Chair of Microwave and Communication Engineering at the University of Magdeburg, Germany since 1998. He authored and co-authored more then 200 technical papers extending over a wide spectrum of research areas. Recently, he directed his search activities to the solution of inverse problems related to remote sensing and microwave tomography. His current research fields cover the areas of remote sensing and microwave imaging, in- and outdoor wireless communication, wideband satellite and mobile communication, electromagnetic bullets and their applications to secure, low power, wideband communications and subsurface tomography, stochastical electromagnetics and their meteorological, environmental and biomedical applications, field theoretical modeling of microwave systems and components, microwave measurements and sub-millimeter wave signal generation and processing.

Dr. Omar is member of the Technical Program Committee of IEEE MTT-S Symposium and member of the editorial board of IEEE Trans. MTT, IEEE Trans. AP, IEEE Trans. MI, IEEE Microwave and Wireless Components Letters, Proceeding IEE, Electronics Letters, Journal of Electromagnetics, Canadian Journal of Physics and Radio Science.

# FDTD Analysis of a Probe-Fed Dielectric Resonator Antenna in Rectangular Waveguide

Yizhe Zhang, *Student Member, IEEE,* Ahmed A. Kishk, *Fellow, IEEE,* Alexander B. Yakovlev, *Senior Member, IEEE,* and Allen W. Glisson, *Fellow, IEEE*

***Abstract*— Dielectric resonator antennas (DRA) are characterized for operation in a guided-wave environment with the ultimate goal of their use in modeling of waveguide-based DRA amplifier arrays for spatial power combining. Performance of a single probe-fed DRA element in rectangular waveguide is analyzed by varying design parameters of the DRA and the feeding probe to optimize the structure for the scattering characteristics (port matching and coupling). The effect of hard walls on the DRA behavior is also studied. The numerical analysis of waveguide-based DRA elements is based on the Finite-Difference Time-Domain (FDTD) method and a coaxial probe is modeled by a thin wire approximation implemented in the FDTD algorithm. The numerical results are compared with those generated by using commercial software and exhibit a very good agreement.**

***Index Terms*— Dielectric resonator antenna, rectangular waveguide, hard wall, Finite-Difference Time-Domain method.**

## I. Introduction

DIELECTRIC resonator antennas (DRA) became potentially useful as antenna elements a few decades ago [1]. The DRA's have several attractive features, such as small size, light weight, inherently wideband nature, high radiation efficiency, and high power handling capability as compared with microstrip antennas, which suffer from higher conduction loss and surface waves in antenna array applications. The use of additional structural parameters (shape, volume, etc.) and a wide range of permittivities makes the design of DRA's more flexible. In addition, different feeding mechanisms can be used for the excitation of DRA elements, which allows for control of DRA input impedance, bandwidth, and radiation pattern. This includes the excitation by slots, probes, microstrip lines, coplanar lines, and dielectric image guides [2]-[4]. Also, the use of dielectric materials with high permittivity in DRA's enables enhancement of the radiation resistance of electrically short probes and loops [5]. Subsequently, systematic theoretical and experimental investigations of DRA's have been reported in [6]-[12] and extensive results of DRA's of cylindrical [1], [3], [8]-[10], rectangular [6], and spherical [7] shapes have been published.

In this paper, coaxial probe-fed DRA elements are studied for operation in a rectangular waveguide with the ultimate goal of their use in waveguide-based DRA amplifier arrays for spatial power combining. Traditionally, the spatial power combiner is formed by an array of amplifying unit cells, with each cell receiving, amplifying, and then radiating a signal into free space [13]-[15]. The key challenges of spatial power combining design are the modeling of receive/transmit antenna elements and the uniform excitation of the antenna arrays. Thus, modeling of one element in rectangular waveguide is important to fully understand the behavior of the DRA in the waveguide environment. Regarding the uniform excitation of amplifier arrays, hard electromagnetic walls have been recently realized by dielectric loading along narrow sides of the waveguide to obtain a uniform field distribution in the waveguide cross-section [16], [17]. The interaction between the DRAs and the hard walls needs to be studied since it significantly affects the resonance frequency and matching characteristics of the DRA.

Here, a single probe-fed DRA element is first investigated for operation in a rectangular waveguide. The scattering parameters are studied by varying geometrical and material parameters of the DRA and the coaxial probe feed. Then, the effect of a dielectric-loaded waveguide on the DRA performance is analyzed. The FDTD method [18], [19] is chosen for the numerical analysis since it provides a full-wave solution of the electrically large and complicated structures, which include different dielectric materials. In the proposed FDTD algorithm, DRA elements and the rectangular waveguide are discretized by using a traditional Yee-cell gridding and the coaxial probe is modeled by a thin wire approximation. The scattering parameters are computed using the FDTD method and compared with the results obtained using the commercial software QuickWave3D [20] and HFSS [21].

The paper is organized as follows. In Section II, a brief description of the FDTD method used in the numerical analysis of waveguide-based probe-fed DRA's is presented. In Section III, an initial design of a single free-space DRA element is presented, followed by the analysis of DRA behavior in an open-ended rectangular waveguide using WIPL-D [22]. Next, the developed FDTD algorithm is used for the parametric analysis of a probe-fed DRA element in a rectangular waveguide to optimize the structure for the scattering characteristics (port matching and coupling). Section IV presents the analysis of a dielectric-loaded waveguide and the effect of hard walls on the DRA performance. Conclusions are summarized in Section V.

## II. Theory

The structure to be analyzed here consists of a coaxial probe-fed DRA element inside a rectangular waveguide as shown in Fig. 1. The geometry is analyzed by using the FDTD

The authors are with the Department of Electrical Engineering, University of Mississippi, University, MS 38677, USA (e-mail:zyz@olemiss.edu; ahmed@olemiss.edu; yakovlev@olemiss.edu; aglisson@olemiss.edu).

method, wherein the DRA element and rectangular waveguide are discretized by traditional Yee cells. A sinusoidally modulated Gaussian pulse is used for the excitation, and the PML absorbing boundary [23] is implemented to terminate both the waveguide port [24] and the coaxial line port. The scattering parameters are calculated in terms of port voltages normalized by characteristic impedances of the waveguide and coaxial probe, respectively. The S-parameters of the waveguide section with coaxial probe-fed DRA are given by

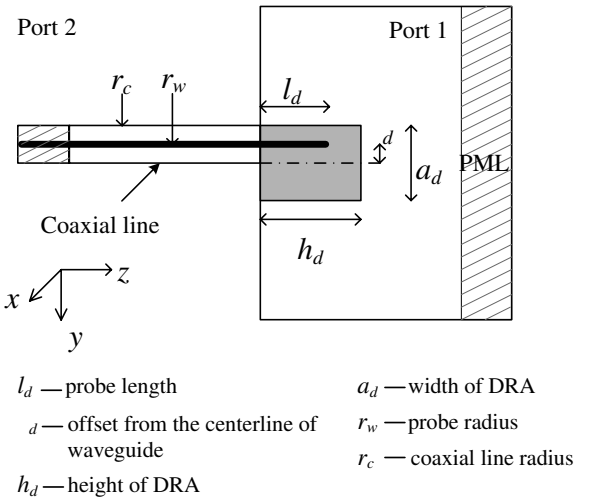


Fig. 1. Geometry of a waveguide-based coaxial probe-fed DRA.

$$S_{11} = \frac{V_w^-}{V_w^+} = \frac{V_w^{total} - V_w^+}{V_w^+}$$
$$S_{21} = \frac{V_c^+}{V_w^+}\sqrt{\frac{Z_w}{Z_c}} \tag{1}$$

where $V_w^-$ is the voltage calculated from the re ection eld at the waveguide port, $V_{w(c)}^+$ is the voltage calculated from the incident eld at the waveguide (coaxial) port, $V_w^{total}$ is the voltage obtained from the total (incident plus re ected) eld at the waveguide port, and $Z_{w(c)}$ is the characteristic impedance of the waveguide (coaxial line), given by

$$Z_w = \frac{\omega\mu}{\beta} = \frac{\omega\mu c}{\sqrt{\omega^2 - \omega_c^2}}$$
$$Z_c = \frac{V_k e^{-j\omega\Delta t/2}}{\sqrt{I_{k-1} I_k}}. \tag{2}$$

Here, $c$ is the velocity of light, $\beta$ and $\omega_c$ are the phase constant and cutoff frequency of the dominant mode of rectangular waveguide, and $V_k$ and $I_k$ are the voltage and current of the $k$th cell in the coaxial line. Since both the electric and magnetic elds are separated by half a cell in space and time, the geometric average of two currents ($I_{k-1}$ and $I_k$) is taken to compensate for the space difference, and a time delay (exponential term in (2)) is introduced to compensate the difference in time [25].

The time-domain modal voltage in the rectangular waveguide can be calculated from the total electric eld as the following integral over the waveguide cross-section $a \times b$

$$V(z_0, t) = \int_0^b \int_0^a \vec{E}(x, y, z_0, t) \cdot \vec{e}(x, y)\ dxdy \tag{3}$$

where $V(z_0, t)$ is the time-domain modal voltage of the dominant mode at $z = z_0$, $\vec{E}(x, y, z_0, t)$ is the total time-domain electric eld in the waveguide cross-section, and $\vec{e}(x, y)$ is the electric- eld vector wave function of the dominant mode [26].

The integral over the waveguide cross-section in (3) can be discretized as follows (Fig. 2),

$$V(z_0, t) = \sum_{i=1}^{N_x} \int_0^b \int_{x_{i-1}}^{x_i} E_x(x_i, y, z_0, t) e_x(x, y)\ dxdy + \sum_{j=1}^{N_y} \int_{y_{j-1}}^{y_j} \int_0^a E_y(x, y_j, z_0, t) e_y(x, y)\ dxdy \tag{4}$$

where $N_x$ and $N_y$ are the numbers of cells in the $x-$ and $y-$direction, respectively. The components of electric- eld vector wave function can be written in the following form by separating the $x-$ and $y-$variables

$$e_x(x, y) = C_x \phi_x(x) \phi_x(y)$$
$$e_y(x, y) = C_y \phi_y(x) \phi_y(y) \tag{5}$$

where $C_x$ and $C_y$ are constants.

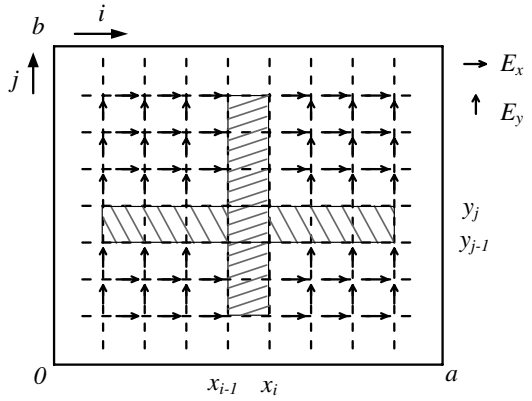


Fig. 2. Discretization of waveguide cross-section in the calculation of voltage.

Substituting equations (5) into equation (4), we obtain

$$V(z_0, t) = C_x \sum_{i=1}^{N_x} \int_0^b E_x(x_i, y, z_0, t) \phi_x(y) dy \int_{x_{i-1}}^{x_i} \phi_x(x) dx + C_y \sum_{j=1}^{N_y} \int_0^a E_y(x, y_j, z_0, t) \phi_y(x) dx \int_{y_{j-1}}^{y_j} \phi_y(y) dy \tag{6}$$

where the integrals in (6) can be discretized as follows,

$$\int_0^b E_x(x_i, y, z_0, t) \phi_x(y) dy = \sum_{j=1}^{N_y} \int_{y_{j-1}}^{y_j} E_x(x_i, y, z_0, t) \phi_x(y) dy$$

$$= \sum_{j=1}^{N_y} \frac{\Delta y_j}{2}[E_x(x_i, y_j, z_0, t)\phi_x(y_j) + E_x(x_i, y_{j-1}, z_0, t)\phi_x(y_{j-1})],$$

$$\int_0^a E_y(x, y_j, z_0, t)\phi_y(x)dx = \sum_{i=1}^{N_x} \int_{x_{i-1}}^{x_i} E_y(x, y_j, z_0, t)\phi_y(x)dx$$

$$= \sum_{i=1}^{N_x} \frac{\Delta x_i}{2}[E_y(x_i, y_j, z_0, t)\phi_y(x_i) + E_y(x_{i-1}, y_j, z_0, t)\phi_y(x_{i-1})]. \quad (7)$$

Integrals $\int_{x_{i-1}}^{x_i} \phi_x(x)dx$ and $\int_{y_{j-1}}^{y_j} \phi_y(y)dy$ in (6) are calculated in closed form.

The coaxial line is modeled by rectangular prisms instead of two concentric cylinders, since the amount of power travelling into the coaxial line is mainly dependent on the characteristic impedance of the coaxial line [27] and weakly dependent on its speci c shape. The inner conductor of the coaxial line can be represented either by a thin wire or by a number of cells. In our work the inner conductor is approximated as a thin wire with radius smaller than half of the FDTD mesh size [28]. With $E_z(i, j, k) = 0$ along the wire axis, the spatial dependence of magnetic elds in the vicinity of the wire can be calculated by

$$H_y^{n+\frac{1}{2}}(i, j, k) = H_y^{n-\frac{1}{2}}(i, j, k) + \frac{\Delta t}{\mu \Delta z}[E_x^n(i, j, k) - E_x^n(i, j, k+1)] + \frac{2\Delta t}{\mu \Delta x \ln(\frac{\Delta x}{r_0})} E_z^n(i+1, j, k), \quad (8)$$

$$H_x^{n+\frac{1}{2}}(i, j, k) = H_x^{n-\frac{1}{2}}(i, j, k) + \frac{\Delta t}{\mu \Delta z}[E_y^n(i, j, k+1) - E_x^n(i, j, k)] - \frac{2\Delta t}{\mu \Delta y \ln(\frac{\Delta y}{r_0})} E_z^n(i, j+1, k), \quad (9)$$

where the wire radius $r_0$ is assumed to be less than half of the cell size.

## III. Single DRA element in rectangular waveguide

Our investigation begins with information available in the literature and then we learn step by step about the DRA in different environments. Therefore, we start with a DRA in free space and end up with a DRA in a waveguide loaded with hard walls. Since the FDTD method is one of the methods used in the analysis, the rectangular DRA is a geometry that can be easily analyzed. A single, probe-fed rectangular DRA placed on an in nite ground plane and radiating in free space, as shown in Fig. 3(a), is considered rst, and is analyzed by commercial Method of Moments (MoM) software WIPL-D

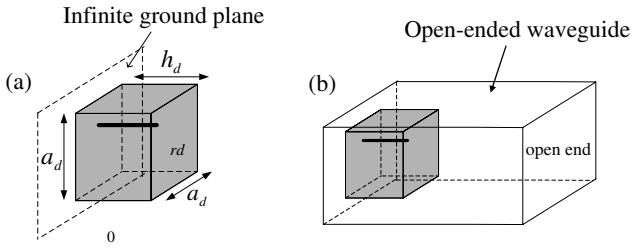


Fig. 3. (a) Geometry of in nite conductor-backed, probe-fed DRA; (b) Geometry of probe-fed DRA inside semi-in nite waveguide.

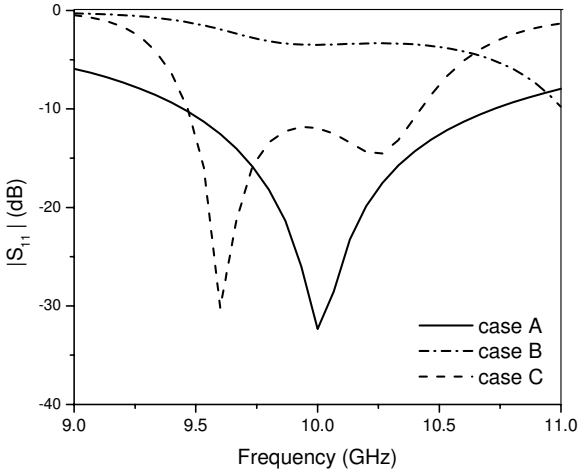


Fig. 4. Re ection coef cient for different con gurations of the DRA. Case A: DRA of Fig. 3(a); Case B: DRA with parameters of Fig. 3(a) placed in waveguide as in Fig. 3(b); Case C: DRA in waveguide with $h_d = 9.5$ mm and $\delta_d = 1.5$ mm as in Fig. 3(b).

[22]. The initial dimensions of the DRA structure $a_d = 5.0$ mm, $h_d = 12.0$ mm, $\varepsilon_{rd} = 12.0$ are chosen so that the resonant frequency of the $TE_{11\delta}$ mode is centered around 10 GHz [29]. The probe length $l_d$ is 4 mm, the probe axis is offset by $\delta_d = 1.0$ mm from the waveguide centerline in the vertical direction, and the probe radius $r_w$ is 0.3 mm. Then, the probe-fed DRA with dimensions from case A (Fig. 3(a)) was placed into an open-ended standard X-band waveguide with cross-sectional dimensions $a = 22.86$ mm and $b = 10.16$ mm (case B with geometry shown in Fig. 3(b)).

Figs. 4 shows dispersion behavior of the re ection coef - cient for the geometries shown in Figs. 3(a) and 3(b) (cases A and B in Fig. 4). Due to placement of the DRA inside of the rectangular waveguide, the resonant frequency of the DRA in case B is shifted to a frequency higher than 11 GHz, which is out of frequency band of interest. Subsequently, the height of the DRA and the probe position were tuned to $h_d = 9.5$ mm and $\delta_d = 1.5$ mm, respectively, and results are presented as case C. Considerable changes of the resonant frequency and bandwidth are observed in Fig. 4. These dimensions serve as starting values for a numerical study that follows.

An analysis of the waveguide-based coaxial probe-fed DRA (Fig. 1) with the parameters from case C is performed by the full-wave FDTD method described in Section II. For the rectangular coax of radius 1.2 mm and lled with the dielectric

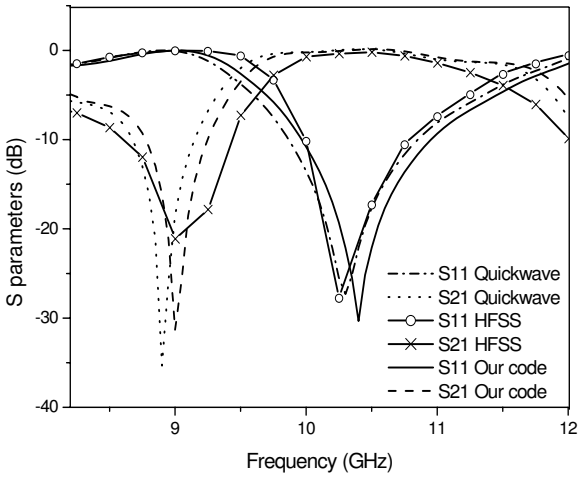


Fig. 5. S-parameters for the waveguide-based probe-fed DRA ($a_d = 5.0$mm, $h_d = 9.5$mm, $\delta_d = 1.5$mm, $l_d = 4.0$mm).

of permittivity $\varepsilon_r = 2.56$, the characteristic impedance $Z_0$ is $51.98\ \Omega$, and only the TEM mode is supported as the cutoff frequency of the $TE_{11}$ coaxial line mode is approximately 26 GHz [30]. The probe length $l_d$ is 4 mm and the probe position is offset by $\delta_d = 1.5$ mm from the waveguide centerline in the vertical direction. Fig. 5 shows the dispersion behavior of the S-parameters. The bandwidth for this case, based on -10 dB level, is 10% (compared to the 3% bandwidth of a microstrip patch antenna used in a similar con guration [31]). The results in Fig. 5 are veri ed with commercial FDTD software QuickWave3D [20] and HFSS [21] and exhibit very good agreement. Once our FDTD code is veri ed, we depend on it in the following analysis.

The effect on port matching and bandwidth of different parameters of the DRA are then investigated. For the structure operating in the X-band, it is found that position and length of the probe both have a signi cant effect on the matching as well as the overall frequency response. Figs. 6(a) and 6(b) show the return loss and insertion loss of the structure with different values of $l_d$. It is found that a short probe couples weakly to the DRA. As the probe length increases, the coupling is increased and a shift to lower resonant frequency is observed. When the probe lengths equal 3.5 mm and 4.0 mm, wide bandwidth and less re ections are achieved, respectively. As the probe is increased to 4.5 mm and beyond, the coupling to the DRA starts decreasing.

The effect of the probe position $\delta_d$ with respect to the waveguide centerline is illustrated in Figs. 7(a) and 7(b), which show the return loss and insertion loss of the structure for different values of $\delta_d$ with $l_d = 4.0$ mm. It is found that the maximum -10 dB bandwidth occurs when $\delta_d$ reaches 2.0 mm and also good insersion loss is achieved. It is clear that both the probe length and position can be used to tune and control the response for both port matching as well as wide bandwidth.

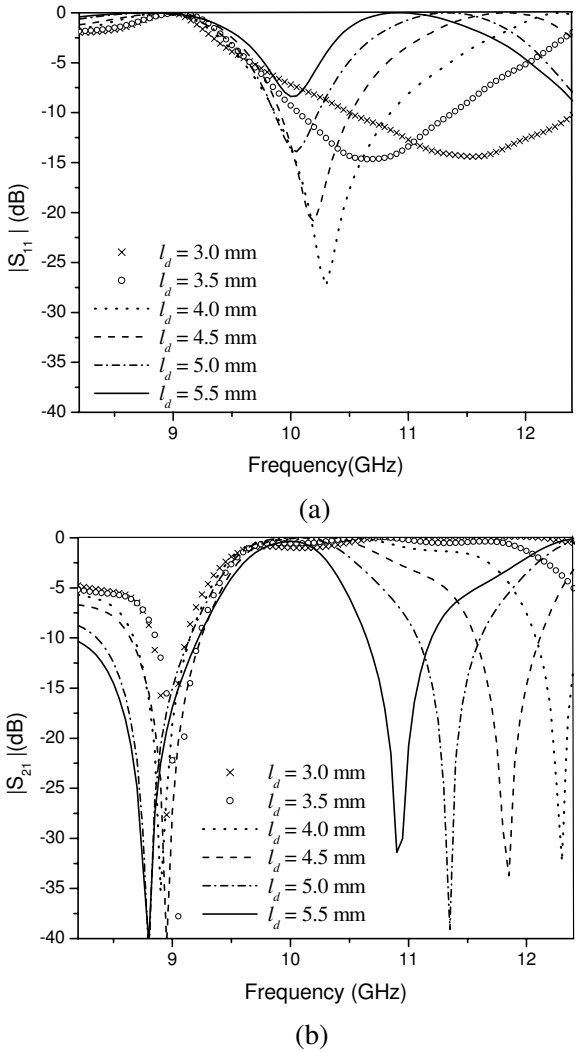


Fig. 6. Effect of varying the probe length $l_d$ in the DRA on (a) return loss and (b) insertion loss, ($a_d = 5.0$mm, $h_d = 9.5$mm, $\delta_d = 1.5$mm).

## IV. Single DRA element in dielectric loaded rectangular waveguide

The ultimate goal of this work is to design an ef cient spatial power combining system which needs to achieve a uniform power division among the antenna elements in the DRA array by using hard walls. For one element design, hard electromagnetic walls in the hollow rectangular waveguide can be created by loading its narrow walls with dielectric material. By appropriately choosing the dielectric thickness for a given dielectric material, a uniform eld distribution can be achieved over the cross-section of the waveguide. In a standard X-band waveguide, the PEC boundary de nes the $TE_{10}$ mode of propagation. The dielectric material loading along the sidewalls in the rectangular waveguide changes the boundary condition so that the $LSE_{10}$ mode will propagate. The $LSE_{10}$ mode provides a uniform eld distribution in the inner waveguide region (in between dielectric slabs) when the dielectric thickness $d$ is calculated according to the following

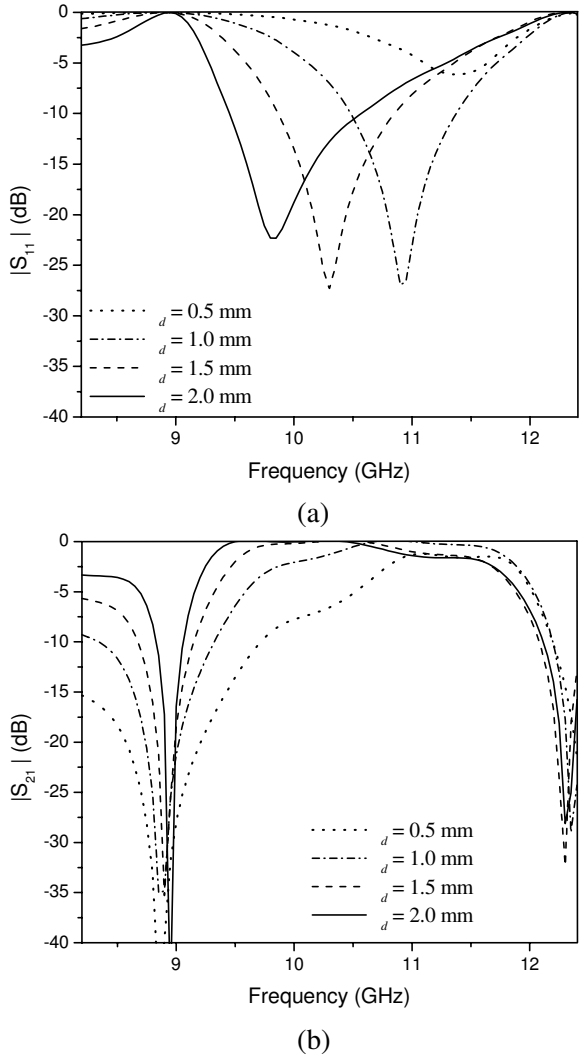


Fig. 7. Effect of varying the probe position $\delta_d$ with respect to the DRA centerline on (a) return loss and (b) insertion loss, ($a_d = 5.0$mm, $h_d = 9.5$mm, $l_d = 4.0$mm).

formula [32]:

$$d = \frac{\lambda}{4\sqrt{\varepsilon_r - 1}} \tag{10}$$

where $\lambda$ is the wavelength in free space and $\varepsilon_r$ is the relative permittivity of the dielectric material. Hence, at the center frequency of operation, the thickness of the dielectric wall is approximately $\lambda_d/4$, where $\lambda_d$ is the wavelength in the dielectric. In Fig. 8, the electric eld amplitudes for the $\mathrm{LSE}_{10}$ mode of the dielectric loaded waveguide and the $\mathrm{TE}_{10}$ mode of the hollow waveguide are plotted along the $x$-axis at 10 GHz. Both of these amplitudes are normalized to unity power.

Since the eld distribution for the $\mathrm{TE}_{10}$ mode of operation in a standard X-band rectangular waveguide is sinusoidal in the waveguide cross-section as shown in Fig. 8, the electric eld in the middle of the waveguide is stronger than that offset from the centerline. Consequently, the coaxial probe-fed DRA couples more energy when it is placed in the middle

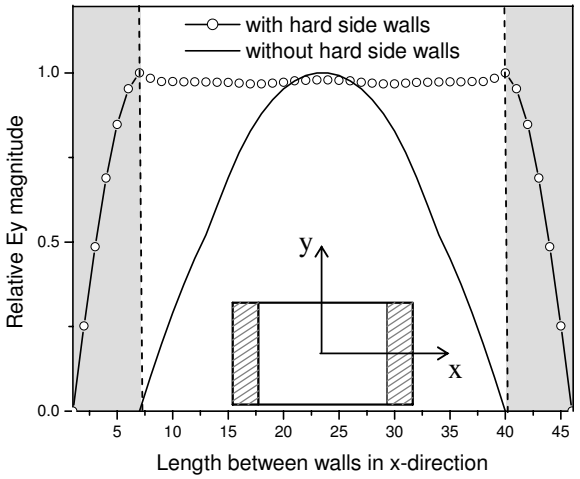


Fig. 8. The electric eld magnitude of the $\mathrm{TE}_{10}$ mode in a hollow rectangular waveguide and the $\mathrm{LSE}_{10}$ mode in rectangular waveguide with hard walls at 10 GHz.

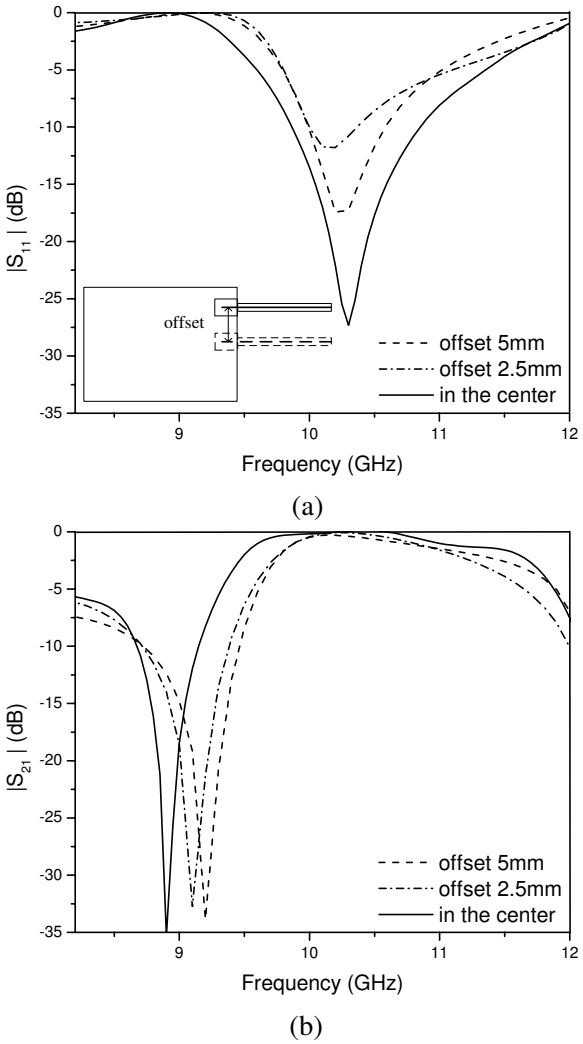


Fig. 9. (a) return loss and (b) insertion loss of the DRA element offset from the centerline of the waveguide, ($a_d = 5.0$mm, $h_d = 9.5$mm, $\delta_d = 1.5$mm, $l_d = 4.0$mm).

of the waveguide. As seen in Figs. 9(a) and 9(b), the scattering parameters are obtained for the cases when the DRA is placed in three different positions: in the first case the DRA is in the middle of waveguide, the second and the third cases are for the DRA placed 2.5 mm and 5 mm offset from the waveguide centerline in the horizontal direction, respectively. Figs. 10(a) and 10(b) show the field distributions (at 10 GHz and $\lambda/2$ away from the surface of the DRA) for the coaxial probe-fed DRA in the center of the waveguide and 5 mm offset from the centerline, respectively. In Fig. 10(b), 8 dB power difference between the middle and 5 mm offset can be observed from the magnitude of the field. These results verify that the element closest to the side wall of the waveguide will couple less power from the source than the one in the middle.

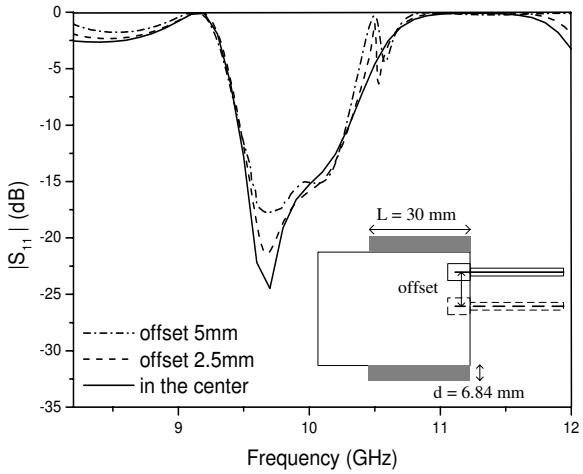


Fig. 10. (a) return loss and (b) insertion loss of the DRA element offset from the centerline of the waveguide loaded with hard walls, ($a_d = 5.0$mm, $h_d = 7.5$mm, $\delta_d = 2.0$mm, $l_d = 3.5$mm).

As seen in the inset in Fig. 11(a), a coaxial probe-fed DRA is placed in the rectangular waveguide with dielectric hard walls. The approximate depth of the hard wall, $d = 6.48$ mm, is calculated by Eq. (10) and the length of the hard wall $L$ equals to 30 mm. The choice of dielectric material affects the bandwidth of the uniform field. It has been found that dielectrics with permittivities from 1.2 to 2.2 can be used to achieve a good uniform field distribution across the waveguide aperture [32] and, therefore, $\varepsilon_r = 2.2$ is used in our analysis. The coaxial probe-fed DRA element is placed in three different positions: in the middle of waveguide, and 2.5 mm and 5 mm offset from the waveguide centerline. Figs. 10(a) and 10(b) demonstrate that the resonance frequency and scattering parameters of these three cases do not change significantly as compared to the cases of DRA in the waveguide without hard walls (Figs. 9(a) and 9(b)). The field distributions (at 10 GHz and $\lambda/2$ away from the surface of the DRA) for the coaxial probe-fed DRA in the center of the waveguide loaded with hard walls and 5 mm offset from the centerline are shown in Figs. 12(a) and 12(b). One can see (Fig. 12(b)) that 3 dB power difference between the middle and 5 mm offset is achieved, so the DRA element couples approximately the same energy around the center frequency for these three different positions, which verifies that the uniform field distribution is achieved across the waveguide aperture as shown in Fig. 8.

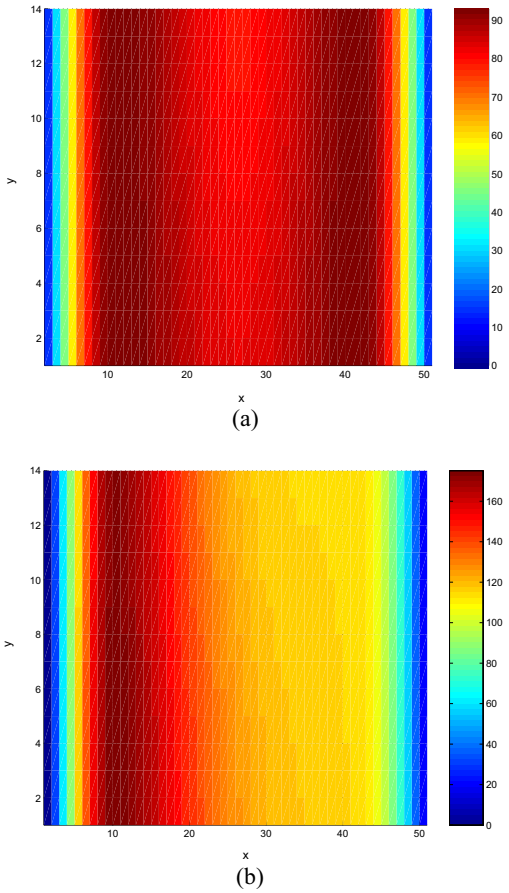


Fig. 11. Field distribution of the DRA element; (a) in the center of the harded waveguide and (b) offset 5 mm from the centerline of the waveguide loaded with hard walls, ($a_d = 5.0$mm, $h_d = 9.5$mm, $\delta_d = 2.0$mm, $l_d = 3.5$mm).

## V. Conclusion

A coaxial probe-fed DRA in a rectangular waveguide excited by the dominant mode was analyzed by using a custom FDTD technique. This analysis provides the necessary information for the optimization of design parameters, such as DRA dimensions and the position and length of the feeding probe. Consequently, 10% bandwidth was achieved over the frequency band of interest. A waveguide loaded with hard walls was studied to obtain a uniform eld distribution at the waveguide aperture. It is shown that the DRA element couples approximately the same energy around the center frequency when it is placed in the middle of the waveguide and offset from the centerline. This study is a useful step in the extension to the case of the DRA array for increasing the output power and the power combining ef cienc y of waveguide-based spatial power combiner.

## Acknowledgment

This work was partially supported by the National Science Foundation under Grant No. ECS-0220218 and NASA EPSCoR Cooperative Agreement No. NCC5-574.

## References

[1] S. A. Long, M. W. McAllister, and L. C. Shen, "The resonant cylindrical dielectric cavity antenna," *IEEE Trans. Antennas Propagat.*, vol. AP-31, pp. 406-412, May 1983.

[2] M. S. Al Salameh and Y. M. M. Antar, "Coplanar-waveguide-fed slot-coupled rectangular dielectric resonator antenna," *IEEE Trans. Antennas Propagat.*, vol. 50, no. 10, pp. 1415-1419, Oct. 2002.

[3] G. P. Junker, A. A. Kishk, and A. W. Glisson, "Input impedance of dielectric resonator antennas excited by a coaxial probe," *IEEE Trans. Antennas Propagat.*, vol. 42, pp. 960-966, July 1994.

[4] G. P. Junker, A. A. Kishk, and A. W. Glisson, "Input impedance of aperture coupled dielectric resonator antennas," *IEEE Trans. Antennas Propagat.*, vol. 44, pp. 600-607, May 1996.

[5] O. Sager and F. Tisi, "On eigenmodes and forced resonance modes of dielectric sphere," *Proc. IEEE*, vol. 56, pp. 1593-1594, Sept. 1968.

[6] M. W. McAllister, S. A. Long, and G. L. Conway, "Rectangular dielectric resonator antenna," *Electron. Lett.*, vol. 19, pp. 219-220, Mar. 1983.

[7] M. W. McAllister and S. A. Long, "Resonant hemispherical dielectric antenna," *Electron. Lett.*, vol. 20, pp. 657-659, Aug. 1984.

[8] A. A. Kishk, H. A. Auda, and B. Ahn, "Radiation characteristics of cylindrical dielectric resonator antenna with new applications," *IEEE Trans. Antennas Propagat. Soc. Newsletter*, vol. 31, pp. 7-16, Feb. 1989.

[9] A. A. Kishk, B. Ahn, and D. Kajfez, "Broadband stacked dielectric resonator antennas," *Electron. Lett.*, vol. 25, pp. 1232-1233, Aug. 1989.

[10] A. A. Kishk, M. R. Zunoubi, and D. Kajfez, "A numerical study of a dielectric disk antenna above grounded dielectric substrate," *IEEE Trans. Antennas Propagat.*, vol. 41, pp. 813-821, June 1993.

[11] A. A. Kishk, Y. Yin, and A. W. Glisson, "Conical dielectric resonator antennas for wideband applications," *IEEE Trans. Antennas Propagat.*, vol. 50, pp. 469-474, Apr. 2002.

[12] A. A. Kishk, "Wideband dielectric resonator antenna in a truncated tetrahedron form excited by a coaxial probe," *IEEE Trans. Antennas Propagat.*, vol. 51, pp. 2913-2917, Oct. 2003.

[13] A. B. Yakovlev, S. Ortiz, M. Ozkar, A. Mortazawi, and M. B. Steer, "A waveguide-based aperture-coupled patch ampli er array – full-wave system analysis and experimental validation," *IEEE Trans. Microwave. Theory Tech.*, vol. 48, no. 12, pp. 2692-2699, Dec. 2000.

[14] S. Ortiz, J. Hubert, L. Mirth, E. Schlecht, and A. Mortazawi, "A high-power Ka-band quasioptical ampli er array," *IEEE Trans. Microwave. Theory Tech.*, vol. 50, no. 2, pp. 487-494, Feb. 2002.

[15] M. Ozkar and A. Mortazawi, "Electromagnetic modeling and optimization of spatial power combiners/dividers with hard horns," *IEEE Trans. Antennas Propagat.*, vol. 53, pp. 144-150, Jan. 2005.

[16] M. A. Ali, S. C. Ortiz, T. Ivanov, and A. Mortazawi, "Analysis and measurement of hard-horn feeds for the excitation of quasioptical ampli ers, " *IEEE Trans. Microwave Theory Tech.*, vol. 47, pp. 479-487, Apr. 1999.

[17] M. N. M. Kehn and P. S. Kildal, "Miniaturized rectangular hard waveguides for use in multifrequency phased arrays," *IEEE Trans. Antennas Propagat.*, vol. 53, no. 1, pp. 100-109, Jan. 2005.

[18] K. S. Yee, "Numerical solution of initial boundary value problems involving Maxwell's equations in isotropic media," *IEEE Trans. Antennas Propagat.*, vol. 14, pp. 302-307, 1966.

[19] A. Ta o ve and S. C. Hagness, , *Computational Electrodynamics: The Finite-Difference Time-Domain Method, 3rd edition*, Norwood, MA: Artech House, 2005.

[20] QuickWave3D: *A General Purpose Electromagnetic Simulator Based on Conformal Finite-Difference Time-Domain Method*, v. 2.2, QWED Sp. Zo.o, Dec. 1998.

[21] HFSS: *High Frequency Structure Simulator Based on the Finite Element Method*, v. 9.2.1, Ansoft corporation, 2004.

[22] B. M. Kolundzija, J. S. Ognjanovic, and T. K. Sarkar, *WIPL-D: Electromagnetic Modeling of Composite Metallic and Dielectric Structures, Software and User's Manual*. Reading, MA: Artech House, 2000.

[23] J. P. Berenger, "A perfectly matched layer for the absorption of electromagnetic waves," *J. Comp. Phys.*, vol. 114, pp. 185-200, 1994.

[24] C. E. Reuter, R. M. Joseph, E. T. Thiele, D. S. Katz, and A. Ta o ve, "Ultrawideband absorbing boundary condition for termination of waveguiding structures in FDTD simulations," *IEEE Microwave Guided Wave Lett.*, vol. 4, pp. 344-346, Oct. 1994.

[25] J. Fang and D. Xeu, "Numerical errors in the computation of impedances by FDTD method and ways to eliminate them," *IEEE Microwave Guided Wave Lett.*, vol. 5, pp. 6-8, Jan. 1995.

[26] R. E. Collin, *Field Theory of Guided Waves*, 2nd ed. New York: McGraw-Hill, IEEE Press, 1991.

[27] C. Wu, K. -L. Wu, Z. Bi, and J. Litva, "Modeling of coaxial-fed microstrip patch antenna by nite difference time domain method," *IEEE Eletrocnics Lett.*, vol. 27, pp. 1691-1692, Sept. 1991.

[28] K. R. Umashankar, A. Ta o ve, and B. Beker, "Calculation and experimental validation of induced currents on coupled wires in an arbitrary shaped cavity," *IEEE Trans. Antennas Propagat.*, vol. 35, pp. 1248-1257, Nov. 1987.

[29] K. M. Luk and K. W. Leung, *Dielectric Resonator Antennas*, Hertfordshire, England: Research Studies Press Ltd., 2002.

[30] D. M. Pozar, *Microwave Engineering*, 2nd ed, NY: Wiley, 1998.

[31] M. Ozkar, *Electromagnetic Modeling for the Optimized Design of Spatial Power Ampli er s with Hard Horn Feeds*, Ph.D. Dissertation, North Carolina State University, 2001.

[32] G. N. Tsandoulas and W. D. Fitzgerald, "Aperture ef cienc y enhancement in dielectrically loaded horns," *IEEE Trans. Antennas Propagat.*, vol. 20, pp. 69-74, 1972.

**Yizhe Zhang** received the B.Sc and M.Sc degrees in electrical engineering from Southeast University, China, in 2000 and 2003, respectively. She is currently working toward the Ph.D. degree in electrical engineering at the University of Mississippi, University.

From 2000 to 2003, she was a Research Assistant in the Department of Electrical Engineering, Southeast University. Her research interests include dielectric resonator antennas, microstrip antennas, numerical methods in electromagnetics, and modeling of high-frequency ampli er arrays for spatial power combining.

**Ahmed A. Kishk** is a Professor of Electrical Engineering, University of Mississippi (since 1995). He was an Associate Editor of Antennas & Propagation Magazine from 1990 to 1993. He is now an Editor of Antennas & Propagation Magazine. He was a Co-editor of the special issue on Advances in the Application of the Method of Moments to Electromagnetic Scattering Problems in the ACES Journal. He was also an editor of the ACES Journal during 1997. He was an Editor-in-Chief of the ACES Journal from 1998 to 2001. He was the chair of Physics and Engineering division of the Mississippi Academy of Science (2001-2002). He was a guest Editor of the special issue on arti cial magnetic conductors, soft/hard surfaces, and other complex surfaces, on the IEEE Transactions on Antennas and Propagation, January 2005.

His research interest includes the areas of design of millimeter frequency antennas, feeds for parabolic re ectors, dielectric resonator antennas, microstrip antennas, soft and hard surfaces, phased array antennas, and computer aided design for antennas. He has published over 150 refereed Journal articles and book chapters. He is a coauthor of the Microwave Horns and Feeds book (London, UK, IEE, 1994; New York: IEEE, 1994) and a coauthor of chapter 2 on Handbook of Microstrip Antennas (Peter Peregrinus Limited, United Kingdom, Ed. J. R. James and P. S. Hall, Ch. 2, 1989). Dr. Kishk received the 1995 outstanding paper award for a paper published in the Applied Computational Electromagnetic Society Journal. He received the 1997 Outstanding Engineering Educator Award from Memphis section of the IEEE. He received the Outstanding Engineering Faculty Member of the 1998. He received the Award of Distinguished Technical Communication for the entry of IEEE Antennas and Propagation Magazine, 2001. He received the 2001 Faculty research award for outstanding performance in research. He received the 2005 School of Engineering Senior Faculty Research Award. He received the 2005 Faculty research award for outstanding performance in research. He also received The Valued Contribution Award for outstanding Invited Presentation, "EM Modeling of Surfaces with STOP or GO Characteristics - Arti cial Magnetic Conductors and Soft and Hard Surfaces" from the Applied Computational Electromagnetic Society. He received the Microwave Theory and Techniques Society Microwave Prize 2004. Dr. Kishk is a Fellow member of IEEE since 1998 (Antennas and Propagation Society and Microwave Theory and Techniques), a member of Sigma Xi society, a member of the U.S. National Committee of International Union of Radio Science (URSI) Commission B, a member of the Applied Computational Electromagnetics Society, a member of the Electromagnetic Academy, and a member of Phi Kappa Phi Society.

**Alexander B. Yakovlev** was born in the Ukraine in 1964. He received the Ph.D. degree in Radiophysics from the Institute of Radiophysics and Electronics, National Academy of Sciences, Ukraine, in 1992, and the Ph.D. degree in Electrical Engineering from the University of Wisconsin at Milwaukee, in 1997.

From 1992 to 1994, he was an Assistant Professor with the Department of Radiophysics at Dniepropetrovsk State University, Ukraine. From 1994 to 1997, while working toward his doctorate degree, he was employed as a Research and Teaching Assistant in the Department of Electrical Engineering and Computer Science at the University of Wisconsin in Milwaukee. From 1997 to 1998, he was an R&D Engineer in Ansoft Corporation/Compact Software Division, Paterson, NJ, and in Ansoft Corporation, Pittsburgh, PA. From 1998 to 2000, he was a Postdoctoral Research Associate with the Electrical and Computer Engineering Department at North Carolina State University, Raleigh, NC. In summer of 2000, he joined the Department of Electrical Engineering at the University of Mississippi as an Assistant Professor, and was promoted to the rank of Associate Professor in 2004.

His research interests include mathematical methods in applied electromagnetics, analysis of arti cial magnetic conductor surfaces and guided-wave structures, modeling of high-frequency interconnection structures and ampli er arrays for spatial and quasi-optical power combining, microstrip and waveguide discontinuities, integrated-circuit elements and devices, theory of leaky waves, transient elds in layered media, catastrophe and bifurcation theories.

Dr. Yakovlev received the Young Scientist Award at the 1992 URSI International Symposium on Electromagnetic Theory, Sydney, Australia, and the Young Scientist Award at the 1996 International Symposium on Antennas and Propagation, Chiba, Japan. In 2003, he received a Junior Faculty Research Award in the School of Engineering at The University of Mississippi. Dr. Yakovlev is an Associate Editor-in-Chief of the ACES Journal and in September 2005 he became an Associate Editor of the IEEE Transactions on Microwave Theory and Techniques. He is a Senior Member of the IEEE (Microwave Theory and Techniques Society and Antennas and Propagation Society) and Member of URSI Commission B. He is coauthor of the book Operator Theory for Electromagnetics: An Introduction, Springer, New York, NY, 2001.

**Allen W. Glisson** received the B.S., M.S., and Ph.D. degrees in electrical engineering from the University of Mississippi, in 1973, 1975, and 1978, respectively. In 1978, he joined the faculty of the University of Mississippi, where he is currently a Professor and Chair of the Department of Electrical Engineering. He was selected as the Outstanding Engineering Faculty Member in 1986, 1996, and 2004. He received a Ralph R. Teetor Educational Award in 1989 and in 2002 he received the Faculty Service Award in the School of Engineering. His current research interests include the development and application of numerical techniques for treating electromagnetic radiation and scattering problems, and modeling of dielectric resonators and dielectric resonator antennas.

Dr. Glisson is a Fellow of the IEEE, a member of Commission B of the International Union of Radio Science, and a member of the Applied Computational Electromagnetics Society. He has received a best paper award from the SUMMA Foundation, twice received a citation for excellence in refereeing from the American Geophysical Union, and he was a recipient of the 2004 Microwave Prize awarded by the Microwave Theory and Techniques Society. Since 1984, he has served as the Associate Editor for Book Reviews and Abstracts for the IEEE Antennas and Propagation Society Magazine. He has served on the Board of Directors of the Applied Computational Electromagnetics Society, is currently Treasurer of ACES, and is a member of the AP-S IEEE Press Liaison Committee. He has previously served as a member of the IEEE Antennas and Propagation Society Administrative Committee, as the secretary of Commission B of the U.S. National Committee of URSI, as an Associate Editor for Radio Science, as Co-Editor-in-Chief of the Applied Computational Electromagnetics Society Journal, and as the Editor-in-Chief of the IEEE Transactions on Antennas and Propagation.

# Introducing a Sub-cell Tensor Technique into a (2, 4) FDTD Method

R.S. Schechter, S.T. Chun, M.S. Kluskens, M. Kragalott, and D. A. Zolnick

Authors are in Code 5310 of the Radar Division of the Naval Research Laboratory, Washington DC 20375
richard.schechter@nrl.navy.mil

**Abstract**: A sub-cell tensor based technique for modeling dielectric interfaces is introduced into a (2,4) FDTD method. For each cell containing an interface, a tensor based method that enforces continuity conditions is used to determine the fields on both sides the sloped interface. These fields are then volumetrically averaged. The approach is used to calculate a corrected field value at each grid point of the large fourth-order stencil. The combined algorithm is computationally homogeneous, unlike most previous algorithms of this type, and thus lends itself to parallel processing. Additionally, the method may be used with other higher-order stencils. The accuracy is tested using the exact Mie series solution for scattering from a dielectric sphere. It is shown that using the (2,4) tensor method results in ~50-70% less error than the (2,4) standard Yee method in the vicinity of a dielectric sphere.

**Introduction:** The finite-difference time domain (FDTD) method is one of the most widely employed methods in computational electromagnetics. As it has been pointed out in many articles, the method has problems when there are curved boundaries, which are represented by staircases on a Cartesian grid. If continuity conditions are not properly maintained across these curved interfaces, inaccuracies in the field components can occur. Nadobny et. al. [1] developed a 3D tensor method for the treatment of dielectric interfaces to enforce continuity of the appropriate field components. Their paper was a major extension of the work of Lee and Myung [2] and demonstrated much improved accuracy for the standard (2,2) algorithm.

In this paper we adapt the tensor method for use with fourth-order methods. Fourth and other higher order methods permit modeling on coarser grids. This is important because fourth-order methods, although very accurate in homogeneous regions, generally present accuracy problems at material boundaries. One remedy for this problem is to employ a hybrid formulation of (2,4) FDTD and sub-grid (2,2) FDTD methods [3], where (2,4) stands for second-order accurate in time and fourth-order accurate in space. In [3] a coarse (2,4) grid is used in the homogeneous regions and a finer (2,2) sub-grid near conducting walls and other structures. Another method [4] uses a large (2,4) region and a buffer layer of (2,2) cells between the (2,4) region and the interfaces.

In [5] an efficient higher-order alternating-direction implicit (ADI) finite-difference time-domain method for unconditionally stable analysis of curvilinear electromagnetic compatibility (EMC) problems is presented. The method is practically dispersionless and offers improved accuracy for curved boundaries. Another paper [6] also discusses the reduction of numerical dispersion of the finite-difference time-domain method based on a (2,4) computational stencil. Rather than implementing the conventional approach, based on Taylor analysis for the determination of the finite-difference operators, two alternative procedures that result in numerical schemes with diverse wide-band behavior are proposed. The method is shown to outperform the standard (2,4) method.

The method proposed here uses the same (2,4) algorithm and grid spacing for the homogenous regions and across boundaries as opposed to mixing different accuracy (second and fourth-order) algorithms. This is important for parallel processing, i.e. using the Message Passing Interface (MPI), where having a homogeneous algorithm is a great advantage so that each processor executes the same instructions. It also is an advantage computationally if a fourth-order accurate method can be used to model an electrically large structure on a smaller coarser grid, without any special sub-gridding. We gauge the relative accuracy of the standard Yee fourth-order and combined sub-cell tensor fourth-order methods by comparing computed results with the exact Mie series solution for plane waves scattering from a dielectric sphere.

**Sub-cell Tensor Method:** The differential form of Maxwell's equations is given by:

$$\nabla \times \mathbf{E} = -\mu \frac{\partial \mathbf{H}}{\partial t} \ , \tag{1}$$

$$\nabla \times \mathbf{H} = \frac{\partial \mathbf{D}}{\partial t} + \mathbf{J} \ , \tag{2}$$

where

$$\mathbf{D} = \varepsilon \mathbf{E} \ . \tag{3}$$

In the homogeneous cells, where there are no interfaces, Eq. (3) can be used to obtain **E**. However, in those cells with interfaces, boundary conditions must be explicitly satisfied.

At a dielectric interface these continuity conditions must be maintained at the interface between media 1 and 2:

$$(\varepsilon_1 \mathbf{E}_1 - \varepsilon_2 \mathbf{E}_2) \cdot \mathbf{n} = 0 \, , \tag{4}$$

(Continuity of the normal components of **D**),

$$(\mathbf{E}_1 - \mathbf{E}_2) \times \mathbf{n} = 0 \, , \tag{5}$$

(Continuity of the tangential components of **E**),

where $\mathbf{n}$ is the unit normal vector to the interface.

Eqs. (4) and (5) can be solved for $\mathbf{E}_2$ in terms of $\mathbf{E}_1$:

$$\mathbf{E}_2 = \widetilde{A} \mathbf{E}_1 \tag{6}$$

where the elements of the transformation matrix $\widetilde{A}$ are:

$$a_{11} = n_x^2 \left( \frac{\varepsilon_1}{\varepsilon_2} \right) + n_y^2 + n_z^2 \, ,$$

$$a_{12} = n_x n_y \left( \frac{\varepsilon_1}{\varepsilon_2} - 1 \right) ,$$

$$a_{13} = n_x n_z \left( \frac{\varepsilon_1}{\varepsilon_2} - 1 \right) ,$$

$$a_{21} = a_{12} \, ,$$

$$a_{22} = n_x^2 + n_y^2 \left( \frac{\varepsilon_1}{\varepsilon_2} \right) + n_z^2 \, ,$$

$$a_{23} = n_y n_z \left( \frac{\varepsilon_1}{\varepsilon_2} - 1 \right) ,$$

$$a_{31} = a_{13} \, ,$$

$$a_{32} = a_{23} \, ,$$

$$a_{33} = n_x^2 + n_y^2 + n_z^2 \left( \frac{\varepsilon_1}{\varepsilon_2} \right) \, .$$

For Yee cell faces cut by an interface the electric fluxes through the faces are broken into two parts:

$$\begin{aligned} \iint D_x dS &= \varepsilon_1 E_x^1 S_x^1 + \varepsilon_2 E_x^2 S_x^2 \, , \\ \iint D_y dS &= \varepsilon_1 E_y^1 S_y^1 + \varepsilon_2 E_y^2 S_y^2 \, , \\ \iint D_z dS &= \varepsilon_1 E_z^1 S_z^1 + \varepsilon_2 E_z^2 S_z^2 \, , \end{aligned} \tag{7}$$

where the S's are areas and the superscripts stand for side 1 or 2. This is illustrated in Fig. 1.

Combining Eqs. (6) with (7), the following tensor relationship is obtained between the average electric flux density and electric field in medium 1,

$$\overline{\mathbf{D}} = \widetilde{\boldsymbol{\varepsilon}} \cdot \mathbf{E}_1 \tag{8}$$

where $\widetilde{\boldsymbol{\varepsilon}}$ is a 3 by 3 permittivity tensor with components:

$$\varepsilon_{11} = \varepsilon_1 \left( \frac{S_x^1}{S} \right) + \varepsilon_2 \left( \frac{S_x^2}{S} \right) a_{11} \, ,$$

$$\varepsilon_{12} = \varepsilon_2 \left( \frac{S_x^2}{S} \right) a_{12} \, ,$$

$$\varepsilon_{13} = \varepsilon_2 \left( \frac{S_x^2}{S} \right) a_{13} \, ,$$

$$\varepsilon_{21} = \varepsilon_2 \left( \frac{S_y^2}{S} \right) a_{21} \, ,$$

$$\varepsilon_{22} = \varepsilon_1 \left( \frac{S_y^1}{S} \right) + \varepsilon_2 \left( \frac{S_y^2}{S} \right) a_{22} \, ,$$

$$\varepsilon_{23} = \varepsilon_2 \left( \frac{S_y^2}{S} \right) a_{23} \, ,$$

$$\varepsilon_{31} = \varepsilon_2 \left( \frac{S_z^2}{S} \right) a_{31} \, ,$$

$$\varepsilon_{32} = \varepsilon_2 \left( \frac{S_z^2}{S} \right) a_{32} \, ,$$

$$\varepsilon_{33} = \varepsilon_1 \left( \frac{S_z^1}{S} \right) + \varepsilon_2 \left( \frac{S_z^2}{S} \right) a_{33} \, ,$$

and where $S = S^1 + S^2$ .

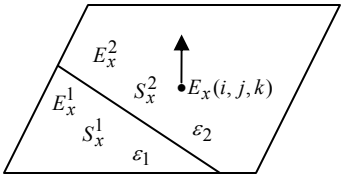


Fig. 1. Center slice (face) of Yee cell centered around $E_x(i,j,k)$. There are two flux areas separated by the dielectric interface.

At each point in the stencil for updating the H field components the volume average of the E fields is used. The fourth-order update equation for $H_z$ obtained by discretizing Eq. 1 is:

$$H_z^{n+1/2}(i,j,k) = H_z^{n-1/2}(i,j,k) + \frac{r}{24}\times$$
$$[(-\overline{E}_x^n(i,j+2,k) + 27\overline{E}_x^n(i,j+1,k)$$
$$-27\overline{E}_x^n(i,j,k) + \overline{E}_x^n(i,j-1,k)) - \quad (9)$$
$$(-\overline{E}_y^n(i+2,j,k) + 27\overline{E}_y^n(i+1,j,k)$$
$$-27\overline{E}_y^n(i,j,k) + \overline{E}_y^n(i-1,j,k))]$$

where $r = \dfrac{\Delta t}{\Delta x \mu_0}$ and for example,

$$\overline{E}_x = \frac{(V_1 E_x^1 + V_2 E_x^2)}{V}, \quad V = V_1 + V_2, \quad (10)$$

where $V_1$ and $V_2$ are the volumes on sides one and two of the interface. It should be noted that Eq. (9) is identical in form to the standard (2,4) update equation, the only difference being that each term is replaced by the volume averaged field. There are analogous update equations for $H_x$ and $H_y$.

Standard fourth-order update equations for $D_x, D_y$ and $D_z$ may be obtained by discretizing Eq. 2. For example:

$$\overline{D}_y^{n+1}(i,j,k) = \overline{D}_y^n(i,j,k) + \frac{s}{24}\times$$
$$[(-H_x^{n+1/2}(i,j,k+1) + 27H_x^{n+1/2}(i,j,k)$$
$$-27H_x^{n+1/2}(i,j,k-1) + H_x^{n+1/2}(i,j,k-2)) - \quad (11)$$
$$(-H_z^{n+1/2}(i+1,j,k) + 27H_z^{n+1/2}(i+1,j,k)$$
$$-27H_z^{n+1/2}(i-1,j,k) + H_z^{n+1/2}(i-2,j,k))]$$

where $s = \dfrac{\Delta t}{\Delta x \varepsilon_0}$.

The term $\overline{E}_x(i,j,k)$ in Eq. (9) represents the volume averaged field in the Yee cell centered on $E_x(i,j,k)$. For any point in the stencil with an interface in that cell, Eq. (10) is used to correct for the interface. This concept is illustrated in Fig. 2. If there is no interface, then

$$\overline{E}_x = \frac{\overline{D}_x}{\varepsilon}. \quad (12)$$

This algorithm amounts to using a corrected field value at each point in the stencil to account for any interfaces cutting through the stencil volume in an arbitrary way. If the stencil volume has no interfaces the algorithm reduces to the standard (2,4). The entire algorithm may be briefly summarized as follows for one update:

[1] Perform standard (2,4) update of $\overline{\mathbf{D}}$ using $H_x$, $H_y$ and $H_z$.

[2] Test all 8 $E$ cells for interfaces within the fourth-order stencil for updating $H$.
If $E$ cell has an interface then use the sub-cell tensor method:

(a) Compute electric field from average electric flux density, $\mathbf{E}_1 = \tilde{\boldsymbol{\varepsilon}}^{-1} \cdot \overline{\mathbf{D}}$.

(b) Obtain electric field on other side of interface, $\mathbf{E}_2 = \tilde{A}\mathbf{E}_1$.

(c) Volume average electric field, $\overline{E}_x = \dfrac{\left(V_1 E_x^1 + V_2 E_x^2\right)}{V}$

else if the $E$ cell has no interface then,

(a) Compute electric field from $\overline{E}_x = \dfrac{\overline{D}_x}{\varepsilon}$

[3] Perform standard (2,4) update for $\mathbf{H}$ using $\overline{E}_x$, $\overline{E}_y$ and $\overline{E}_z$.

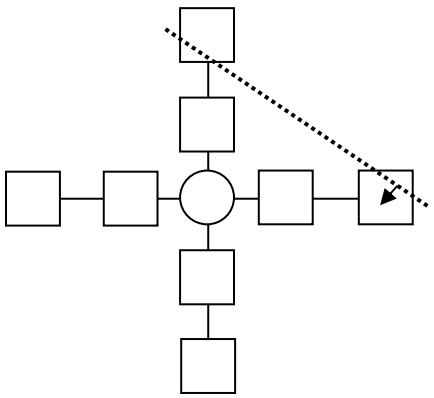

Fig. 2. The stencil for the (2,4) FDTD method showing the 8 E field cells (squares) and H field cell (circle). Two of the E field cells are cut by an interface (dotted line) at an angle and require the sub-cell corrections.

**Computational Cases**: Six computational cases are performed to test the accuracy of the standard (2,4) and tensor (2,4) algorithms. Scattering problems are done with a plane wave scattering from a dielectric sphere with a large dielectric change to emphasize errors near the interface. The incident plane wave is polarized in the z direction and travels in the +y direction, as illustrated in Fig. 3. The total-field/scattered-field (TF/SF) formulation is used to introduce a plane wave into the volume. Uniaxial perfectly matched layers (UPML), 10 cells wide, are used for the absorbing boundaries. Case I uses a sphere with a relative dielectric constant of 4 and a uniform grid spacing of 10 points per wavelength (ppw) in the sphere. The parameters for various cases are summarized in Table I.

**Table I. Parameters for Cases.**

| | Freq. (GHz) | Dielectric Constant | ppw | Sphere Radius |
|---|---|---|---|---|
| **Case I** | 5.0 | 4 | 10 | 7.5 |
| **Case II** | 5.0 | 4 | 20 | 15.0 |
| **Case III** | 5.0 | 8 | 10 | 7.5 |
| **Case IV** | 5.0 | 8 | 20 | 15.0 |
| **Case V** | 5.0 | 12 | 10 | 7.5 |
| **Case VI** | 5.0 | 12 | 20 | 15.0 |

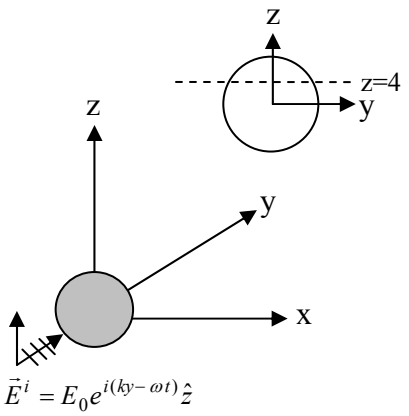


Fig. 3. Diagram of incident wave, dielectric sphere, coordinate system and y-cut at z value.

Fig. 4 shows a typical computed cut for Case III, parallel to the y-axis and through grid point (x=0,z=1), near the sphere center. Shown is $E_y(0,y,1)$ computed using the (2,4) tensor method and the (2,4) standard Yee method against the exact Mie series solution. Fig. 4 shows that the (2,4) tensor method agrees much better with the exact solution than the (2,4) standard method, along the entire cut.

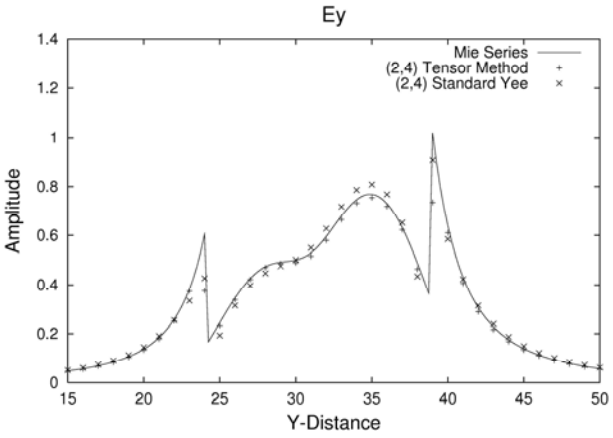


Fig. 4. Case III. Comparison of (2,4) tensor and (2,4) standard methods with exact Mie series. The sphere lies between grid points 24 and 40.

Fig. 5 shows a comparable cut for $E_y(0,y,5)$ for Case V. The (2,4) tensor method is closer to the exact solution inside the sphere, at the sphere boundaries, and outside the sphere. The standard Yee method also exhibits pronounced overshoots at the interfaces.

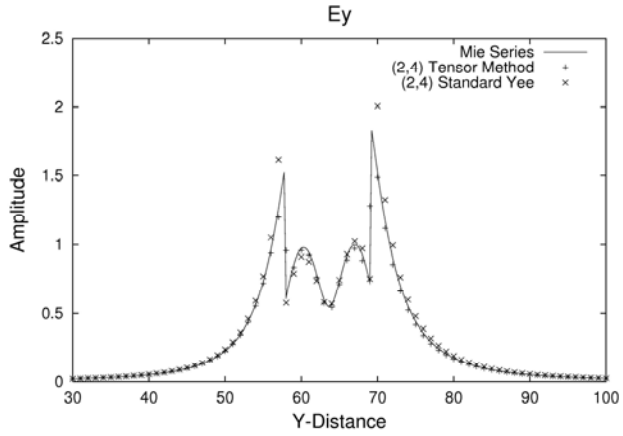


Fig. 5. Case V. Comparison of (2,4) tensor and (2,4) standard methods with exact Mie series. The sphere lies between grid points 56 and 72.

**Error Evaluation:** In order to assess the relative errors of the tensor and standard methods a numerical comparison is made between the computed values and the exact Mie series solution. The solution is computed in spherical coordinates and transformed into Cartesian coordinates along cuts through the sphere (shown in Fig. 3), to correspond in space to the FDTD spatial cuts.

The following error measure function is used:

$$error = \frac{\sum \left| E_{exact} - E_{computed} \right|}{\sum \left| E_{exact} \right|} \quad . \tag{13}$$

This error function is computed along a cut through the sphere and extending 1 radius beyond the sphere boundary on both sides so that the cuts are 4 radii in length. The exact value is taken to be the average of the analytical value at center of the Yee cell, obtained from the Mie series solution. Using the spatial average of the exact solution is necessary near the jump discontinuities to properly compare to the computed values which are really the average values at the center of the Yee cells. Table II shows the errors computed for the six cases along y-cuts at 4 different z values for increasing dielectric constants. The ratio r shown is the tensor average error divided by the standard average. Table II shows that r is about 0.3 at 20 ppw and .6 at 10 ppw for the six cases. Cases II and IV both show a decrease of about 50% in the average error by going from 10 ppw to 20 ppw for the tensor method. The standard method shows worse convergence. Case VI shows only about a 20% decrease in the average error by going to 20 ppw.

**Table II. Errors for Cases I – VI.**

| **Case I** | **ez(1)** | **ez(4.5)** | **ey(1)** | **ey(4)** | **av.** |
|---|---|---|---|---|---|
| **ten(2,4)** | 1.79 | 2.30 | 2.31 | 2.11 | 2.13 |
| **sta(2,4)** | 1.94 | 3.53 | 4.85 | 4.06 | 3.60 |
| | | | | | r=.59 |
| **Case II** | **ez(1)** | **ez(8.5)** | **ey(1)** | **ey(8)** | **av.** |
| **ten(2,4)** | 0.61 | 0.88 | 1.46 | 0.98 | 0.98 |
| **sta(2,4)** | 1.80 | 1.78 | 4.83 | 4.41 | 3.21 |
| | | | | | r=.31 |
| **Case III** | **ez(1)** | **ez(4.5)** | **ey(1)** | **ey(4)** | **av.** |
| **ten(2,4)** | 3.98 | 5.62 | 2.54 | 3.13 | 3.82 |
| **sta(2,4)** | 6.67 | 11.30 | 6.99 | 5.68 | 7.66 |
| | | | | | r=.50 |
| **Case IV** | **ez(1)** | **ez(8.5)** | **ey(1)** | **ey(8)** | **av.** |
| **ten(2,4)** | 2.15 | 2.16 | 1.94 | 1.48 | 1.93 |
| **sta(2,4)** | 4.64 | 4.95 | 6.26 | 7.00 | 5.71 |
| | | | | | r=.34 |
| **Case V** | **ez(1)** | **ez(4.5)** | **ey(1)** | **ey(4)** | **av.** |
| **ten(2,4)** | 3.45 | 3.25 | 2.77 | 3.26 | 3.18 |
| **sta(2,4)** | 3.86 | 5.33 | 8.31 | 5.32 | 5.71 |
| | | | | | r=.56 |
| **Case VI** | **ez(1)** | **ez(8.5)** | **ey(1)** | **ey(8)** | **av.** |
| **ten(2,4)** | 2.66 | 2.90 | 2.67 | 1.67 | 2.48 |
| **sta(2,4)** | 5.87 | 3.55 | 8.48 | 8.88 | 6.70 |
| | | | | | r=.37 |

**Efficiency:** The (2,4) tensor is compared with the (2,4) standard Yee for total CPU time and additional memory requirements. The computations were all performed on an IBM p690 parallel computer using 16 processors. This case uses a grid size of 168×168×168 and 2000 time steps. The (2,4) tensor method uses 373 s of CPU time compared to 251s for the (2,4) standard Yee, or a ratio of 1.49. The tensor method also requires some additional memory primarily to store the 9 $\widetilde{\boldsymbol{\varepsilon}}^{-1}$ tensor components and the 9 transformation matrix components of the $\widetilde{A}$ matrix for each interface cell. For this case there are 786 interface cells for each of the staggered field positions $E_x$, $E_y$ and $E_z$. Also the volume fractions must be stored for each interface cell. The total additional memory overhead compared with the standard (2,4) method amounts to only about 0.2 Mbytes for this case.

**Conclusions:** A tensor method to handle dielectric interfaces has been combined in a straightforward way with a standard (2,4) FDTD algorithm and results in a computationally homogeneous algorithm suitable for parallel computing. The numerical cases, using scattering from a dielectric sphere, demonstrate that the combined (2,4) tensor method significantly improves the accuracy of the (2,4) standard Yee method near interfaces. The tensor method may be combined with any higher-order FDTD algorithm, involving a large stencil.

**References**

[1] J. Nadobny, D. Sullivan, W. Wlodarczyk, P. Deuflhard, and P. Wust, "A 3-D Tensor FDTD-Formulation for Treatment of Sloped Interfaces in Electrically Inhomogeneous Media," *IEEE Trans. Antenn. Prop.* , Vol 51, No.8, pp. 1760-1770, Aug. 2003.

[2] J. Lee and N. Myung, "Locally Tensor Conformal FDTD Method for Modeling Arbitrary Dielectric Surfaces," *Microwave and Optical Technology Letters*, Vol. 23, No. 4, pp. 245-249, Nov. 1999.

[3] S. V. Georgakopoulos, C. R. Birtcher, C. A. Balanis, and R. A. Renaut, " Higher-Order Finite-Difference Schemes for Electromagnetic Radiation, Scattering, and Penetration, Part 2: Applications," *IEEE Antenna's and Propagation Magazine*, Vol. 44, No. 2. pp. 92-101, April 2002.

[4] M. F. Hadi and M. Piket-May, "A Modified FDTD (2,4) Scheme for Modeling Electrically Large Structure with High-Phase Accuracy," *IEEE Trans. Antenna. Prop.*, Vol. 45, No. 2, pp. 254-264, Feb. 1997.

[5] N. V. Kantartzis, T.T, Zygiridis, T. D. Tsiboukis, "An Unconditionally Stable Higher Order ADI-FDTD Technique for the Dispersionless Analysis of Generalized 3-D EMC Structures," *IEEE Trans. Magn.,* Vol. 40, No. 2, pp. 1436-1439, March 2004.

[6] T. T. Zygiridis and T.D. Tsiboukis, "Low-Dispersion Algorithms Based on the Higher Order (2,4) FDTD Method," *IEEE Trans. MTT*, Vol. 52, No. 4, pp. 1321-1327, April 2004.

Richard Schechter is a physicist in the Radar Division at Naval Research Laboratory in Washington DC. His current interests are the finite-difference time domain method, parallel computing, and modeling electromagnetic bandgap structures and left-handed materials. He also has conducted research and published articles on simulating ultrasonic wave propagation on parallel computers. He obtained his B.S. in Physics from the University of Maryland in 1974 and took further graduate studies in physics and applied mathematics 1974-1980 at American University and Catholic University, both in Washington DC.

Michael S. Kluskens received B.S. and M.S. degrees in electrical engineering from Michigan Technological University, Houghton, MI, in 1984 and 1985, respectively, and the Ph.D degree from The Ohio State University, Columbus, OH, in 1991. From 1986 to 1991, he was a Graduate Research Associate at the Electroscience Laboratory, Department of Electrical Engineering, the Ohio State University, where he conducted research on the method of moments and chiral media. He has been with the Radar Division of the Naval Research Laboratory, Washington D.C. since 1991 and is currently with the Electromagnetics Section of the Analysis Branch of the Radar Division. His primary research is in computational electromagnetics with emphasis on the method of moments, finite-difference time domain, and scattering from large complex structures.

Mark Kragalott received the B.A. degree in physics and economics at Kenyon College in 1983, and M.S. and Ph.D. degrees in electrical engineering from The Ohio State University, in 1988 and 1993, respectively. As a Graduate Research Associate at the ElectroScience Laboratory at The Ohio State University, he conducted research on method of moments and extremely low frequency shielding. Since 1994 he has been with the Electromagnetics Section in the Analysis Branch of the Radar Division at the Naval Research Laboratory, Washington, D.C, where he has conducted research in topics ranging from computational electromagnetics to ultrawideband radiation and scattering.

Sung-Taek Chun received the B.A.N.E degree from Han-Yang University, Seoul, Korea, in 1980, and studied theoretical plasma physics at the Seoul National University in 1981. He received the M.S and Ph.D. degrees in Nuclear Engineering and Engineering Physics from University of Wisconsin-Madison in 1984 and 1986, respectively. From 1987 to 1989, he was a Research Associate in the Courant Institute of Mathematical Sciences, New York University, N.Y. During 1997 and 1999, he was an Associate Professor in Physics in Taejon, Korea, and since 2001, he has been a Research Physicist at the Naval Research Laboratory, Washington, DC. His research interests include theoretical and computational electromagnetics and plasma physics, photonic bandgap materials, RF and pulse discharge plasma, and electromagnetic wave interaction with charged particles and complex media.

# MIXED ELEMENT FORMULATION FOR THE FINITE ELEMENT-BOUNDARY INTEGRAL METHOD

J. Meese[1], L.C. Kempel[2], and S.W. Schneider[3]
[1]General Dynamics Advanced Information Systems, Ypsilanti, MI 48197
[2]Michigan State University, East Lansing, MI 48824-1226
[3]Air Force Research Laboratory, Sensors Directorate, Wright-Patterson AFB, OH 45433

**Abstract – A mixed element approach using right hexahedral elements and right prism elements for the finite element-boundary integral method is presented and discussed for the study of planar cavity-backed antennas. The mixed element method is shown to decrease the required computation time for geometrically constrained geometries by reducing the unknown count on the open aperture on the cavity. By reducing the unknown count on the surface, the memory and computational cost associated with the boundary integral portion of the solution is decreased versus solutions using only prism elements. The accuracy of the mixed element approach is shown to be comparable with that of a single element approach, especially for far field parameters such as radiation pattern and radar cross section.**

## I. INTRODUCTION

Efficient numerical modeling of antennas is an integral part of the antenna design process. Numerical modeling can aid in the rapid design of an antenna prior to prototype fabrication, therefore drastically reducing the design time and reducing cost. One of the challenges inherent in the numerical modeling of antennas is how to model the antenna in the most accurate, yet efficient manner.

Various numerical techniques have been used to model antennas with size on the order of a few wavelengths. One of the most popular of these techniques is formulated using an integral equation (IE) and implemented using the Method of Moments (MoM) or one of its variants. One particularly relevant example, a spiral antenna, is given in [0]. While this method is highly accurate and well studied, it suffers from the fact that it produces fully dense matrices leading to memory demands of $O(N^2)$ and computational complexity of $O(N^3)$ where $N$ is the order of system. In addition, the most efficient MoM formulations are based on surface equivalence and hence are restricted to piecewise homogeneous materials.

Recently, techniques have been developed to reduce the computational complexity of integral equation formulations to $O(N \log_2 N)$ by exploiting the fact that many of the unknowns are physically distant from other unknowns [0]. A different approach, the Finite Element (FE) method [0-0], is based on a partial differential equation (PDE) approach and therefore leads to very sparse system matrices that can be stored and solved in a very efficient manner. In addition, since it is a PDE-based approach, the FE method readily permits analysis of inhomogeneous materials in an antenna design. However, the FE method does not enforce the Sommerfeld radiation condition for electromagnetic waves as part of its formulation and hence is susceptible to spurious reflections from the mesh truncation surface. To solve this problem, often local conditions, such as an absorbing boundary condition (ABC) or

Perfectly Matched Layers (PML) are used. These methods are particularly useful for scattering calculations since the Radar Cross Section (RCS) is a far-zone quantity and hence the effect of local errors on the solution tends to be diminished via integration. Solution accuracy is a particular concern for antenna modeling using such an approximate condition since important antenna parameters (e.g. input impedance, mutual impedance, etc.) depend on accurate local field solutions. A technique combining the FE method and an integral equation, termed the Finite Element-Boundary Integral (FE-BI) method, is an attractive alternative since it implements an exact relationship between tangential electric and magnetic fields on the mesh boundary as well as the Sommerfeld radiation condition [0-0] via a properly constructed Green's function. A third approach uses a harmonic expansion of the exterior field as a mesh closure condition [0]. An excellent summary of these various conditions is given in [0].

However, the FE-BI method suffers from a well-known drawback: The boundary integral portion of the system takes up the majority of memory and time for solution. In two dimensional cases, the use of triangular elements on the surface of the geometry to achieve the greatest modeling flexibility can lead to electrical oversampling which causes larger than needed memory demand and computational time. Quadrilateral elements, while not as flexible in modeling, can be used to reduce the unknown count for some cases [0], e.g. narrow slots. The mixture of triangular and quadrilateral elements can therefore allow a flexible modeling solution while reducing the effects of oversampling. For the case of three-dimensional cavity-backed antennas, quadrilateral elements can be extruded into right hexahedral elements while triangular elements can be extruded into right prism elements. Hence, the volumetric efficiency of quadrilateral elements can be combined with the flexibility of prisms to reduce overall complexity of a solution.

This paper presents the mixed element formulation as applied to three-dimensional cavity-backed antennas. Section II of the paper develops the theory for the mixed element formulation. Section III shows some numerical results comparing the mixed element formulation with the single element formulation. Section IV compares the computational time required for the two methods. Section V presents some conclusions and future directions for this work.

## II. FORMULATION

Figure 1 illustrates a cavity-backed aperture lying in an infinite, metallic groundplane. The computational, and antenna, volume is denoted by V while the aperture is denoted by S. The portion of the groundplane, including any metal in the aperture, is indicated by $S_{pec}$. The fields within the computational volume are denoted by $(\mathbf{E}^{int}, \mathbf{H}^{int})$ while the external fields are indicated by $(\mathbf{E}^{ext}, \mathbf{H}^{ext})$. The material within the cavity may in general be inhomogeneous and anisotropic; however, for this work a simplified formulation assuming isotropic materials is presented. Expressions for anisotropic cases can be found for prisms in [0] while expressions for hexahedral elements may be similarly developed.

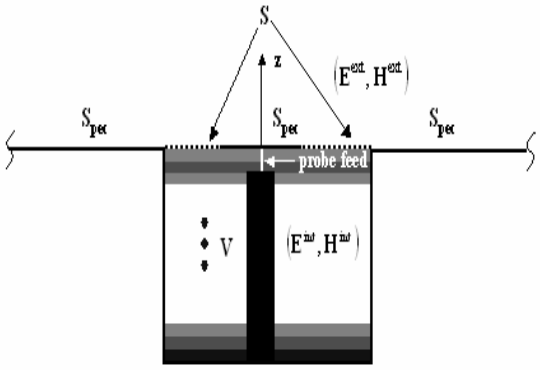


**Figure 1: Cavity backed aperture recessed in an infinite ground plane with multiple loading layers.**

This type of geometry represents flush-mounted cavity-backed antennas where the local surface in the vicinity of the antenna is planar. Antennas found in this type of configuration include both narrow bandwidth apertures (e.g. microstrip and slot antennas) as well as wide bandwidth apertures (e.g. packed elements such as I-dipoles as well as spiral and log-periodic antennas). A systematic modeling of these antennas through the use of highly efficient computational algorithms is important to determine the optimal configuration of these systems.

The problem domain is separated into two distinct regions, the region composed of the interior volume of the geometry, and the region composed of the surrounding free space area above the ground plane. The interior, FE, region is then coupled to the exterior, BI, region by enforcing tangential magnetic field continuity, $\hat{\mathrm{n}} \times \mathbf{H}^{\mathrm{ext}} = \hat{\mathrm{n}} \times \mathbf{H}^{\mathrm{int}}$, on the aperture surface $(S)$ while tangential electric field continuity, $\hat{\mathrm{n}} \times \mathbf{E}^{\mathrm{ext}} = \hat{\mathrm{n}} \times \mathbf{E}^{\mathrm{int}}$, on that same surface is assured via the use of similar basis function for the interior and exterior representations. The final hybrid expression, usually known as the finite element-boundary integral equation, is given by

$$\frac{1}{\mu_r}\int_{V_i}\left(\nabla\times\mathbf{L}_i\right)\cdot\left(\nabla\times\mathbf{E}^{\mathrm{int}}\right)\,dV-k_0^2\varepsilon_r\int_{V_i}\mathbf{L}_i\cdot\mathbf{E}^{\mathrm{int}}\,dV-$$
$$k_0^2\int_{S_i}\int_{S_j}\mathbf{L}_i\cdot\left(\hat{z}\times\overline{\overline{G}}_{e2}\left(x,y|x',y'\right)\times\hat{z}\right)\cdot\mathbf{E}^{\mathrm{int}}\,dS'\,dS=$$
$$-jk_0Z_0\int_{V_i}\mathbf{L}_i\cdot\mathbf{J}^{imp}\,dV \qquad (1)$$

where $\mathbf{L}_{\mathrm{i}}$ is the vector testing function associated with the $\mathrm{i}^{\mathrm{th}}$ row while $\mathbf{J}^{\mathrm{imp}}$ represents an impressed current source as the antenna feed. The relative material parameters, $\varepsilon_{\mathrm{r}}$ and $\mu_{\mathrm{r}}$, are associated with each element and may vary on an element-by-element basis while $\mathrm{k}_0$ and $Z_0$ are the free-space wavenumber and wave impedance, respectively. The electric dyadic Green's function of the second kind, $\overline{\overline{\mathrm{G}}}_{\mathrm{e2}}$, is taken to be the half-space Green's function [0].

The unknown electric field is expanded using the same functions as used for testing (e.g. Galerkin's method) is

$$\mathbf{E}^{\mathrm{int}} = \sum_{\mathrm{j}=1}^{\mathrm{N}} \mathrm{E}_{\mathrm{j}}\mathbf{L}_{\mathrm{j}} \qquad (2)$$

where $\mathrm{E}_{\mathrm{j}}$ indicates complex-valued unknown expansion coefficients. Inserting (2) into (1), the final expression is given as

$$\sum_{j=1}^{N}E_j\left\{\begin{array}{l}\frac{1}{\mu_r}\int_{V_i}\left(\nabla\times\mathbf{L}_i\right)\cdot\left(\nabla\times\mathbf{L}_j\right)\,dV-k_0^2\varepsilon_r\int_{V_i}\mathbf{L}_i\cdot\mathbf{L}_j\,dV\\ -k_0^2\int_{S_i}\int_{S_j}\mathbf{L}_i\cdot\left(\hat{z}\times\overline{\overline{G}}_{e2}\left(x,y|x',y'\right)\times\hat{z}\right)\cdot\mathbf{L}_j\,dS'dS\end{array}\right\}=$$
$$-jk_0Z_0\int_{V_i}\mathbf{L}_i\cdot\mathbf{J}^{imp}dV. \qquad (3)$$

This matrix equation is separated into two parts, one representing the finite element portion, written as $\mathrm{I}_{\mathrm{ij}}^{\mathrm{FE}}$, and the other representing the boundary integral portion, written as $\mathrm{I}_{\mathrm{ij}}^{\mathrm{BI}}$ as

$$I_{ij}^{FE} = \frac{1}{\mu_r}\int_{V_i}\left(\nabla\times\mathbf{L}_i\right)\cdot\left(\nabla\times\mathbf{L}_j\right)\,dV$$
$$-k_0^2\varepsilon_r\int_{V_i}\mathbf{L}_i\cdot\mathbf{L}_j\,dV\ , \qquad (4)$$

$$\mathrm{I}_{\mathrm{ij}}^{\mathrm{BI}} =$$
$$-\mathrm{k}_0^2\int_{\mathrm{S_i}}\int_{\mathrm{S_j}}\mathbf{L}_{\mathrm{i}}\cdot\left(\hat{\mathrm{z}}\times\overline{\overline{\mathrm{G}}}_{\mathrm{e2}}\left(\mathrm{x},\mathrm{y}|\mathrm{x}',\mathrm{y}'\right)\times\hat{\mathrm{z}}\right)\cdot\mathbf{L}_{\mathrm{j}}\,\mathrm{dS'dS} \qquad (5)$$

where the latter has support only when both test and source edges lie in the aperture. These integrals represent the matrix entries in the following linear system

$$\begin{bmatrix}\mathrm{I}_{\mathrm{ij}}^{\mathrm{FE}}+\mathrm{I}_{\mathrm{ij}}^{\mathrm{BI}} & \mathrm{I}_{\mathrm{ij}}^{\mathrm{FE}}\\ \mathrm{I}_{\mathrm{ij}}^{\mathrm{FE}} & \mathrm{I}_{\mathrm{ij}}^{\mathrm{FE}}\end{bmatrix}\begin{Bmatrix}\mathrm{E}_{\mathrm{j}}^{\mathrm{S}}\\ \mathrm{E}_{\mathrm{j}}^{\mathrm{int}}\end{Bmatrix}=\begin{Bmatrix}0\\ \mathrm{f}_{\mathrm{i}}^{\mathrm{int}}\end{Bmatrix} \qquad (6)$$

where $\mathrm{E}_{\mathrm{j}}^{\mathrm{S}}$ indicates unknown field expansion coefficients associates with the aperture surface, $\mathrm{E}_{\mathrm{j}}^{\mathrm{int}}$ are the expansion coefficients for the interior basis vectors and $\mathrm{f}_{\mathrm{i}}^{\mathrm{int}}$ is the excitation term associated with an interior

current source. Evaluation of (4) and (5) require specification of the basis functions, $\mathbf{L}_j$. These will be different for the different types of elements used in the mesh; hence their will be two different specifications of $I_{ij}^{FE}$, one for prisms and one for hexahedra, and four different specifications of $I_{ij}^{BI}$ to represent all possible combinations of surface element coupling. The functions for a right prism are presented first followed by those for a right hexahedral.

Right Prisms

Right prism elements have been used successfully in the FE-BI method in the past [0]. These basis functions posses the required properties to be used in the FE-BI method. They enforce tangential field continuity across element faces and are curl conforming. The elements used in this work are also divergence-free and CT/LN elements [0].

Prisms have the advantage of providing great flexibility in modeling geometries that are irregular in two dimensions but regular in the third dimension, such as cavities recessed in ground planes, the case presented here. Prisms also have the advantage of making it quite simple to extrude a three-dimensional mesh from a two-dimensional mesh composed of triangles. In addition, the prism basis functions are derived from the two dimensional basis functions for triangles so they reduce to the two-dimensional triangular basis functions used in the boundary integral; hence, prisms are similar to triangle elements and therefore automatically enforce the essential boundary condition in the aperture. However, for some geometries such as narrow slot spiral antennas, prism elements have the disadvantage of oversampling the aperture and therefore inefficiently using resources. Figure 2 illustrates one possible realization of a right prism element where the local node numbering scheme is shown along with the encircled local edge numbering scheme.

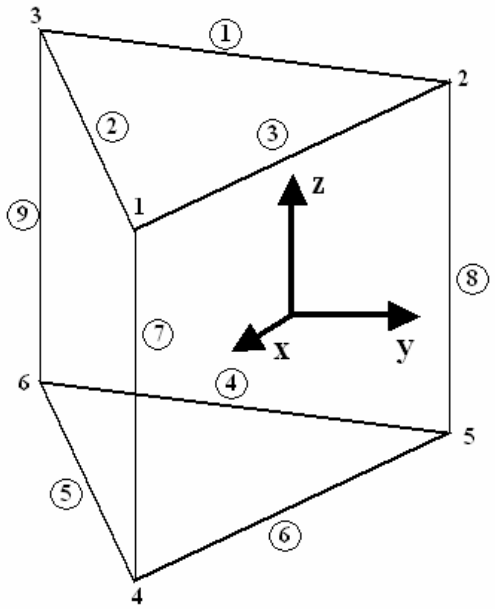


**Figure 2: Right prism element shown with its defined local nodes and local edges (encircled numbers).**

The nodes are ordered in a counter-clockwise direction in order to ensure that the normal vector of the element points towards the top of the element and therefore points out of the computational volume in the aperture of a cavity-backed antenna. The edge-based expansion functions for the prism element are derived from the Rao-Wilton-Glisson (RWG) basis functions for triangles [0] with a linear depth variation to allow for three-dimensional support. Assigning prism vector expansion functions as $\mathbf{L}_i = \mathbf{W}_i$, the nine vector functions associated with the prism are given by

$$\begin{aligned}
\mathbf{W}_{\chi i} = \mathbf{V}_i &= \frac{(z-z_i)}{c}\frac{l_i s_i}{2S^e}\left[(x-x_i)\hat{\mathbf{y}} - (y-y_i)\hat{\mathbf{x}}\right], && \chi = 1,2,3,\\
\mathbf{W}_{\chi i} = \mathbf{M}_i &= \frac{(z_i-z)}{c}\frac{l_i s_i}{2S^e}\left[(x-x_i)\hat{\mathbf{y}} - (y-y_i)\hat{\mathbf{x}}\right], && \chi = 4,5,6,\\
\mathbf{W}_{\chi i} = \mathbf{K}_i &= \frac{\hat{\mathbf{z}}}{2S^e}\left[(x_{k1}y_{k2} - x_{k2}y_{k1}) + (y_{k1}-y_{k2})x + (x_{k2}-x_{k1})y\right], && \chi = 7,8,9,
\end{aligned} \tag{7}$$

where $l_i$ is the length of the $i^{th}$ edge, $s_i$ is the sign of the $i^{th}$ edge to ensure field continuity between elements , $(x_i, y_i)$ are the global coordinates the local nodes, $(z_l, z_u)$ are the global coordinates of the upper and lower faces of the prism, $c = z_u - z_l$ is the height of the prism, and $S^e$ is the area of the triangle that forms the top (or bottom) of the prism. For the vertical edges, $k_1$ and $k_2$ are defined in Table 1

**Table 1. Definition of the indices used to construct the vertical prism expansion functions.**

| $\chi$ | $k_1$ | $k_2$ |
|---|---|---|
| 7 | 2 | 3 |
| 8 | 3 | 1 |
| 9 | 1 | 2 |

where $\chi$ is the local edge number and $(k_1, k_2)$ indicate local nodes. The curls of these basis functions are defined as

$$\begin{aligned}
\nabla\times\mathbf{V}_i &= -\frac{l_i s_i}{2cS^e}[(x-x_i)\hat{\mathbf{x}} + (y-y_i)\hat{\mathbf{y}} - 2(z-z_l)\hat{\mathbf{z}}],\\
\nabla\times\mathbf{M}_i &= \frac{l_i s_i}{2cS^e}[(x-x_i)\hat{\mathbf{x}} + (y-y_i)\hat{\mathbf{y}} + 2(z_u-z)\hat{\mathbf{z}}],\\
\nabla\times\mathbf{K}_i &= \frac{[(x_{k2}-x_{k1})\hat{\mathbf{x}} + (y_{k1}-y_{k2})\hat{\mathbf{y}}]}{2S^e}.
\end{aligned} \tag{8}$$

Note that these expansion functions are functionally identical to [0]; however, since they are expressed in global rather than local coordinates, it is relatively easy to use these functions in conjunction with anisotropic materials specified in terms of global properties.

Right Distorted Hexahedrals

A common example of a regular hexahedra element is the brick element where all the edges are either parallel or orthogonal to any other edge in the element [0]. Distorted hexahedral elements have edges that are not necessarily parallel or orthogonal to the other edges. Distorted hexahedral have been used by [0] and discussed in [0]; however, not in conjunction with other elements. The edges in the extrusion direction are orthogonal to the quadrilateral element used to form the hexahedron. Distorted hexahedral elements are important because they have the ability to model irregular surface geometries with potentially fewer edges than prisms (e.g. narrow slots). This leads to less computational and memory demand for the same geometry modeled with hexahedral elements as opposed to prism elements. Distorted hexahedral elements, however, have the disadvantage of not having closed-form matrix entry formulae and hence require more computational effort as compared to prisms with similar field representation capability.

The basis functions used for hexahedral elements are the so-called rooftop functions. Rooftop basis functions are most often used in brick elements [0-0]. Brick elements are very easy to use but suffer from the fact that they can only model Cartesian-type geometries effectively. In order to model more irregular geometries distorted hexahedral elements can be used. Due to their distortion however the integrals in (5) can be very difficult to compute numerically. Numerical integration over brick shaped volumes is readily

implemented and for this reason it is advantageous if a hexahedral element is mapped into a brick before integration.

Figure 3 shows the transformation of a distorted hexahedral element in the $(x, y, z)$ coordinate system to a unit cube in the $(\xi, \eta, \varsigma)$ coordinate system.

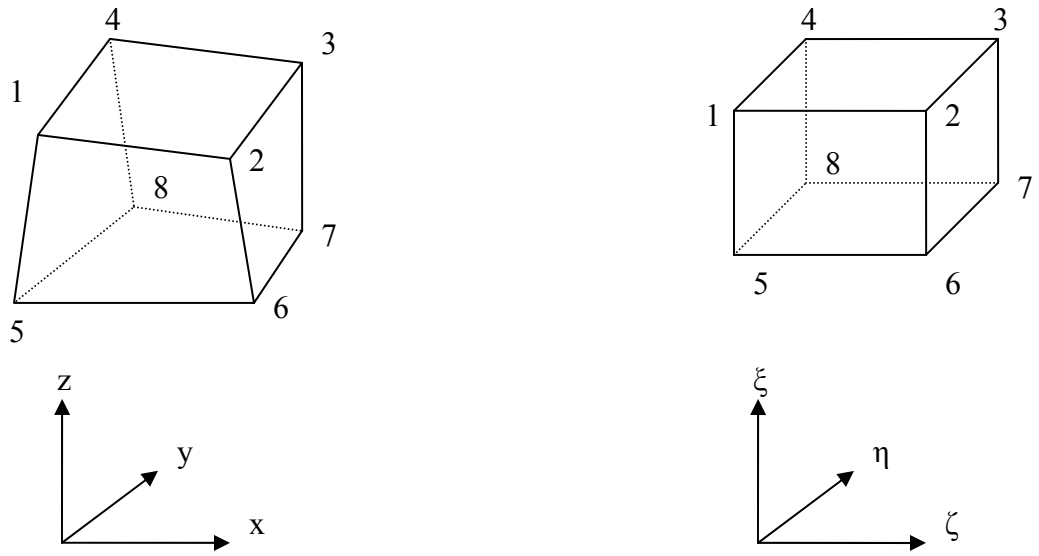


**Figure 3: Hexahedral in (x, y, z) coordinates mapped into a cube in (ξ, η, ζ) coordinates.**

where the edges of the hexahedral and the brick are defined in Table 2.

**Table 2 : Local edge numbering for a distorted hexahedral element.**

| Edge | Node 1 | Node2 |
|---|---|---|
| 1 | 1 | 2 |
| 2 | 3 | 4 |
| 3 | 1 | 4 |
| 4 | 2 | 3 |
| 5 | 5 | 6 |
| 6 | 7 | 8 |
| 7 | 5 | 8 |
| 8 | 6 | 7 |
| 9 | 1 | 5 |
| 10 | 2 | 6 |
| 11 | 3 | 7 |
| 12 | 2 | 6 |

From [0] the vector edge-based basis functions can be written as

$$\mathbf{N}_i = \frac{l_i s_i}{8}(1 + \eta_i \eta)(1 + \zeta_i \zeta)\nabla \xi \tag{9}$$

for the edges parallel to the ξ direction

$$\mathbf{N}_i = \frac{l_i s_i}{8}(1 + \xi_i \xi)(1 + \zeta_i \zeta)\nabla \eta \tag{10}$$

for the edges parallel to the η direction, and finally

$$\mathbf{N}_i = \frac{l_i s_i}{8}(1 + \xi_i \xi)(1 + \eta_i \eta)\nabla \zeta \tag{11}$$

for the edges parallel to the ζ direction, where $l_i$ denotes the length of the $i^{th}$ edge. Based on the definition of the gradient, these equations can be equivalently written as

$$\begin{aligned}
\mathbf{N}_i &= \frac{l_i s_i}{8}(1+\eta_i\eta)(1+\zeta_i\zeta)\hat{\xi}, \\
\mathbf{N}_i &= \frac{l_i s_i}{8}(1+\xi_i\xi)(1+\zeta_i\zeta)\hat{\eta}, \\
\mathbf{N}_i &= \frac{l_i s_i}{8}(1+\eta_i\eta)(1+\xi_i\xi)\hat{\zeta}.
\end{aligned} \tag{12}$$

Therefore, the basis functions for hexahedral elements are now defined in the mapped coordinate system where numerical integration can be performed over a cube rather than a hexahedral volume.

The integrands in (5) are still represented in terms of global Cartesian coordinates. Defining the Jacobian matrix as

$$\mathbf{J} = \begin{bmatrix} \frac{\partial x}{\partial \xi} & \frac{\partial y}{\partial \xi} & \frac{\partial z}{\partial \xi} \\ \frac{\partial x}{\partial \eta} & \frac{\partial y}{\partial \eta} & \frac{\partial z}{\partial \eta} \\ \frac{\partial x}{\partial \zeta} & \frac{\partial y}{\partial \zeta} & \frac{\partial z}{\partial \zeta} \end{bmatrix} \tag{13}$$

the elemental volume of the integral can be written as [0]

$$dV = dxdydz = \det[\mathbf{J}]d\xi d\eta d\zeta \ . \tag{14}$$

From [0] the following vector operations can be defined

$$\hat{\mathbf{z}} \cdot (\nabla \times \mathbf{N}) = \frac{1}{\det[\mathbf{J}]}\left[\frac{\partial N^{\eta}}{\partial \xi} - \frac{\partial N^{\xi}}{\partial \eta}\right], \tag{15}$$

$$(\nabla \times \mathbf{N}) = \frac{1}{\det[\mathbf{J}]} \times \left[\hat{\boldsymbol{\xi}}\left(\frac{\partial N^{\zeta}}{\partial \eta} - \frac{\partial N^{\eta}}{\partial \zeta}\right) + \hat{\boldsymbol{\eta}}\left(\frac{\partial N^{\xi}}{\partial \zeta} - \frac{\partial N^{\zeta}}{\partial \xi}\right) + \hat{\boldsymbol{\zeta}}\left(\frac{\partial N^{\eta}}{\partial \xi} - \frac{\partial N^{\xi}}{\partial \eta}\right)\right].$$

The above equations can be used to derive the equations needed to implement the FE-BI method using hexahedral elements.

Mixed Element Formulation

Traditional formulations of the FE-BI method use one of the previous two elements described as the sole type of element used to model the geometry. This works well in practice and many implementations of this type have been successful. Each method has its advantages and disadvantages as described previously. To gain benefits not obtainable using one element or the other, the two types of elements can be combined. This allows the use of prism elements where their flexibility is needed, such as at sharp contours and areas of rapid varying fields, while still allowing the use of hexahedral elements where fewer unknowns are needed, such as areas of slowly varying fields or for narrow slots. Only a few additional equations need to be introduced in order to make this mixed element formulation possible. To be more specific, only the boundary integral terms where a prism edge is interacting with a hexahedral edge need to be derived.

The equations for mixed element interactions via the boundary integral can be derived by using the basis functions for the triangular and quadrilateral elements in (5). For the case when triangles are used as test elements and quadrilaterals are used as source elements, the following equations are used

$$I_{ij}^{BI(1)} = -\frac{k_0^2}{2\pi}\int_S \int_{-1}^{1}\int_{-1}^{1} [\mathbf{W}_i \cdot (\hat{\mathbf{x}}\hat{\mathbf{x}} + \hat{\mathbf{y}}\hat{\mathbf{y}}) \cdot \mathbf{N}_j] \frac{e^{-jk_0 R}}{R} \det[\mathbf{J}_j] d\xi' d\eta' dS, \tag{17}$$

$$I_{ij}^{BI(2)} = \frac{1}{2\pi}\int_S \int_{-1}^{1}\int_{-1}^{1} \nabla \cdot (\hat{\mathbf{z}} \times \mathbf{W}_i) \nabla' \cdot (\hat{\mathbf{z}} \times \mathbf{N}_j) \frac{e^{-jk_0 R}}{R} \det[\mathbf{J}_j] d\xi' d\eta' dS, \tag{18}$$

where $R = \sqrt{(x - x')^2 + (y - y')^2}$ (16)

Conversely when quadrilaterals are used as test elements and triangles are used as source elements, the following equations are derived.

$$I_{ij}^{BI(1)} = -\frac{k_0^2}{2\pi}\int_{-1}^{1}\int_{-1}^{1}\int_{S'} [\mathbf{N}_i \cdot (\hat{\mathbf{x}}\hat{\mathbf{x}} + \hat{\mathbf{y}}\hat{\mathbf{y}}) \cdot \mathbf{W}_j] \frac{e^{-jk_0 R}}{R} \det[\mathbf{J}_i] dS' d\xi d\eta, \tag{19}$$

$$I_{ij}^{BI(2)} = \frac{1}{2\pi}\int_{-1}^{1}\int_{-1}^{1}\int_{S'} \nabla \cdot (\hat{\mathbf{z}} \times \mathbf{N}_i) \nabla' \cdot (\hat{\mathbf{z}} \times \mathbf{W}_j) \frac{e^{-jk_0 R}}{R} \det[\mathbf{J}_i] dS' d\xi d\eta. \tag{20}$$

Using the following relations

$$\nabla \cdot (\hat{\mathbf{z}} \times \mathbf{N}_i) = \frac{l_i s_i}{\det[\mathbf{J}_i]}\left(\frac{\partial N_i^{\xi}}{\partial \eta} - \frac{\partial N_i^{\eta}}{\partial \xi}\right), \tag{21}$$

$$\nabla \cdot (\hat{\mathbf{z}} \times \mathbf{W}_i) = -\frac{l_i s_i}{S_i^e}, \tag{22}$$

the equations needed to implement the mixed element formulation are written

$$\begin{aligned}
{}^{\xi p}I_{ij}^{BI(1)} &= -\frac{k_0^2 l_i l_j s_i s_j}{16\pi S_j^e}\int_{-1}^{1}\int_{-1}^{1}\int_{S'}(1+\eta_i\eta)\left[(x'-x_j)\frac{\partial\xi}{\partial y}-(y'-y_j)\frac{\partial\xi}{\partial x}\right]\frac{e^{-jk_0R}}{R}\det[\mathbf{J}_i]dS'd\xi d\eta,\\
{}^{\eta p}I_{ij}^{BI(1)} &= -\frac{k_0^2 l_i l_j s_i s_j}{16\pi S_j^e}\int_{-1}^{1}\int_{-1}^{1}\int_{S'}(1+\xi_i\xi)\left[(x'-x_j)\frac{\partial\eta}{\partial y}-(y'-y_j)\frac{\partial\eta}{\partial x}\right]\frac{e^{-jk_0R}}{R}\det[\mathbf{J}_i]dS'd\xi d\eta,\\
{}^{p\xi}I_{ij}^{BI(1)} &= -\frac{k_0^2 l_i l_j s_i s_j}{16\pi S_i^e}\int_{S}\int_{-1}^{1}\int_{-1}^{1}(1+\eta_j\eta)\left[(x-x_i)\frac{\partial\xi'}{\partial y}-(y-y)\frac{\partial\xi'}{\partial x}\right]\frac{e^{-jk_0R}}{R}\det[\mathbf{J}_j]dSd\xi' d\eta',\\
{}^{p\eta}I_{ij}^{BI(1)} &= -\frac{k_0^2 l_i l_j s_i s_j}{16\pi S_i^e}\int_{S}\int_{-1}^{1}\int_{-1}^{1}(1+\xi_j\xi)\left[(x-x_i)\frac{\partial\eta'}{\partial y}-(y-y)\frac{\partial\eta'}{\partial x}\right]\frac{e^{-jk_0R}}{R}\det[\mathbf{J}_j]dSd\xi' d\eta',
\end{aligned} \tag{23}$$

and

$$\begin{aligned}
{}^{\xi p}I_{ij}^{BI(2)} &= -\frac{l_i l_j s_i s_j \eta_i}{8\pi S_j^e}\int_{-1}^{1}\int_{-1}^{1}\int_{S}\frac{e^{-jk_0R}}{R}dS'd\xi d\eta,\\
{}^{\eta p}I_{ij}^{BI(2)} &= \frac{l_i l_j s_i s_j \xi_i}{8\pi S_j^e}\int_{-1}^{1}\int_{-1}^{1}\int_{S}\frac{e^{-jk_0R}}{R}dS'd\xi d\eta,\\
{}^{p\xi}I_{ij}^{BI(2)} &= -\frac{l_i l_j s_i s_j \eta_j}{8\pi S_i^e}\int_{S}\int_{-1}^{1}\int_{-1}^{1}\frac{e^{-jk_0R}}{R}dSd\xi' d\eta',\\
{}^{p\eta}I_{ij}^{BI(2)} &= \frac{l_i l_j s_i s_j \xi_j}{8\pi S_i^e}\int_{S}\int_{-1}^{1}\int_{-1}^{1}\frac{e^{-jk_0R}}{R}dSd\xi' d\eta',
\end{aligned} \tag{24}$$

where p denotes the fact the either the test or source edge are associated with a prism element.

## III. Numerical Results

To validate this mixed element formulation, two simple test cases were constructed. The first was a 3cm x 2cm slot antenna cut into a 6cm x 5cm x 2cm cavity. The cavity was filled with a dielectric material with a dielectric constant of $\varepsilon_r = 2.17$. The geometry was modeled once with only prism elements and a second time with a mixture of prism elements and hexahedral elements. The RCS of this antenna is shown in Figures 4 and 5.

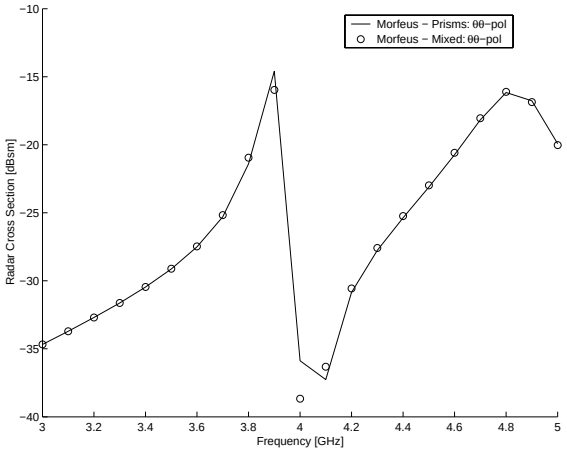


**Figure 4: Radar Cross Section of a 6cm x 5cm x 2cm cavity with a 3cm x 2cm slot aperture, θθ-pol.**

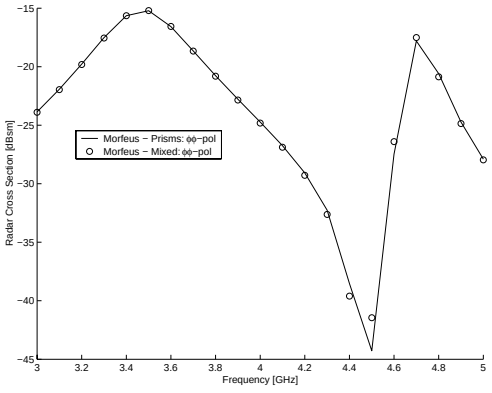


**Figure 5: Radar Cross Section of a 6cm x 5cm x 2cm cavity with a 3cm x 2cm slot aperture, φφ-pol.**

The results above show that the mixed element formulation is nearly identical to the single element formulation when modeling the radar cross-section of the slot antenna.

The second test case consisted of a 3cm x 2cm patch antenna residing in a 6cm x 4cm x 0.0762cm cavity filled with a dielectric material with $\varepsilon_r = 3.2$. The patch antenna was excited by a probe feed located at x = 3cm, y = 2.1cm. As with the slot antenna this antenna was modeled once with only prisms and again with a mixture of prism elements and hexahedral elements. Figure 6 shows the radiation pattern of the patch antenna at 5.4 GHz and Figure 7 shows the input resistance of the probe feed from 5-6 GHz.

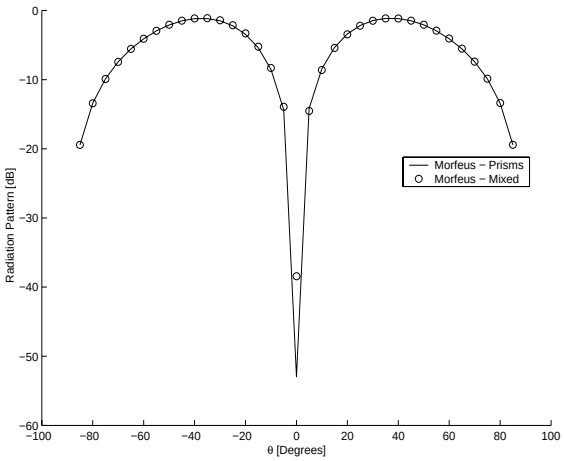


**Figure 6: Normalized radiation pattern for a 3cm x 2cm patch antenna in 6cm x 4cm x 0.0762cm cavity.**

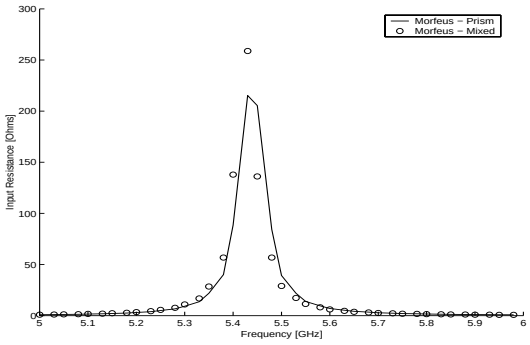


**Figure 7: Input resistance of a 3cm x 2cm patch antenna in 6cm x 4cm x 0.0762cm cavity.**

The above results show that the mixed element formulation again matches the prism-only formulation results very closely. Different mesh densities around the feed point for the two different methods cause the discrepancy in the value of the input resistance at the resonant point of the patch antenna. Due to the extreme local nature of input impedance small changes in electric field values caused by slightly different sampling rates at the feed point can lead to moderately different results for the value of the input impedance. Also, probe feeds such as the one used in the above example can be extremely sensitive to small changes in the field, which makes them somewhat unreliable for accurate simulations of input impedance value. The most important result in the above example is that the structure has a resonant point at the same frequency using both the prism element formulation and the mixed element formulation.

## IV. Solution Efficiency Comparison

To compare and contrast the computational demand required to model geometries with only prism elements as opposed to a mixture of prism and hexahedral elements a few, more complex, cases were considered. These cases were chosen since they represent a class of problems where the triangles used with prisms to represent the aperture, “oversample” the aperture from an electromagnetic viewpoint. This is best understood by considering a narrow slot antenna. Since the electric fields in the slot have only a component perpendicular to the slot sides, quadrilateral elements very efficiently model this slot. In contrast, using an identical sampling density, triangle elements would require one additional degree-of-freedom (e.g. edge) per equivalent quadrilateral element.

The first of these cases included a four-arm spiral antenna with one, two, and three turns. The second was an I-dipole array consisting of one, four, nine, and sixteen dipoles. The time required computing a single radiation pattern

cut, with an INTEL XEON 550 MHz processor running the Linux operating system, was recorded for each of the aforementioned geometries. Figure 8 shows examples of the different geometries used for the results along with the meshing used. Table 3 describes the different mesh parameters for the example geometries. A single pattern cut was computed in the X-Z plane at a frequency of 12 GHz for the spiral antenna and 4GHz for the I-dipole array. Figure 9 illustrates the time required to compute a radiation pattern cut for the four-arm spiral antenna versus the number of turns in the spiral. Figure 10 illustrates the time required to compute a single radiation pattern cut for the I-dipole array versus the number of dipoles in the array.

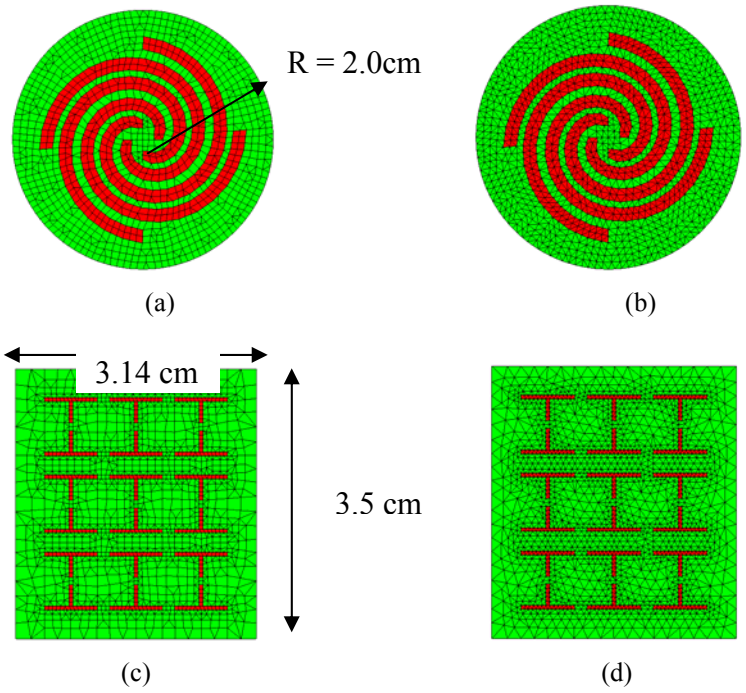


**Figure 8: A four-arm, one-turn spiral and a 3x3 I-Dipole array (a) spiral with mixed elements, (b) spiral with prism elements, (c) I-Dipole array with mixed elements, (d) I-Dipole with prism elements.**

**Table 3: Mesh comparison for a four-arm, one-turn spiral antenna and a 3x3 I-Dipole array.**

| | Spiral Mixed | Spiral Prism | I-Dipole Mixed | I-Dipole Prism |
|---|---|---|---|---|
| Surface Elements | 1313 | 2338 | 2280 | 3600 |
| Surface Edges | 2544 | 3569 | 3980 | 5437 |
| Surface Unknowns | **1296** | **1941** | **2880** | **4013** |
| Total Elements | 14443 | 25718 | 15960 | 25200 |
| Total Edges | 44080 | 56380 | 43747 | 56362 |
| Total Unknowns | **37684** | **48579** | **37705** | **48539** |

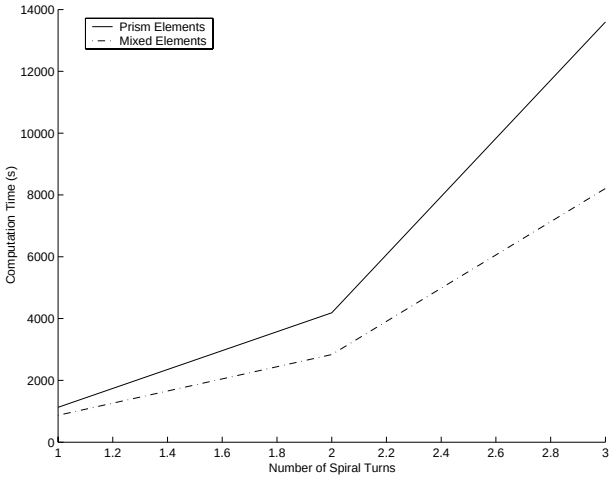


**Figure 9: Required computation time for a single radiation pattern cut for a four arm spiral antenna.**

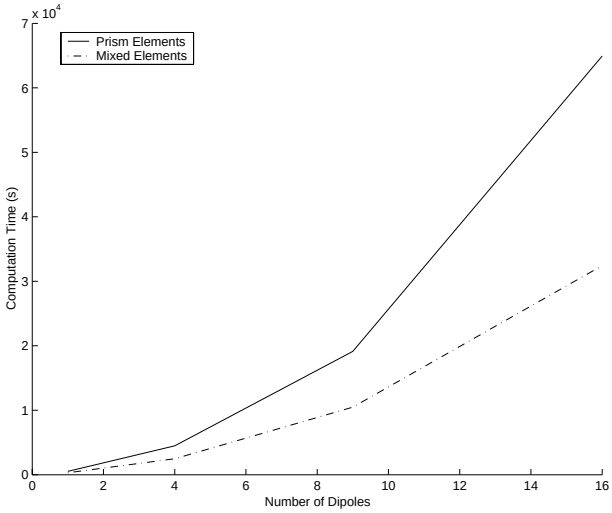


**Figure 10: Required computation time for a single radiation pattern cut for an I-dipole array antenna.**

As can be seen from the above results the mixed element formulation scales much better for geometrically constrained problems, such as spiral antennas and I-dipole arrays, as compared to the prism-only formulation.

## V. Conclusions

A mixed element formulation was developed to model three-dimensional planar cavity-backed aperture antennas. This formulation was shown to be equivalent to a formulation using only prism elements but was more efficient in terms of memory and computational demand. The main memory and computational savings were due to the fact that the mixed element formulation produced fewer surface unknowns, for a comparable electromagnetic representation, than the prism element formulation for the same geometry.

Slight discrepancies between the mixed element and prism element formulations were seen in the modeling of impedance for complex geometries. Dissimilar mesh densities surrounding the feed points causing different input powers to be produced at the feeds caused these discrepancies. These discrepancies were not seen in radar cross-section simulations as RCS measurements do not include a feed model.

## REFERENCES

[1] H. Nakano, K. Hirose, I. Ohshima, and J. Yamauchi, "An integral equation and its application to spiral antennas on semi-infinite dielectric materials," *IEEE Transactions on Antennas and Propagation*, 47, p. 267-274, Feb. 1998.

[2] W.C. Chew, J.M. Jin, E. Michielssen, and J.M. Song, Fast and Efficient Algorithms in Computational Electromagnetics, Artech House, 2001.

[3] J.L. Volakis, A. Chatterjee, L.C. Kempel. Finite Element Method for Electromagnetics. IEEE Press, New York, 1998.

[4] J.M. Jin. The Finite Element Method in Electromagnetics. John Wiley and Sons Inc, 1993.

[5] J. Gong, J.L. Volakis, A. Woo, and H.T. Wang, "A hybrid finite element-boundary integral method for the analysis of cavity-backed antennas of arbitrary shape," *IEEE Transactions on Antennas and Propagation*, 42, p. 1233-1242, Sept. 1994.

[6] L.C. Kempel and J.L. Volakis, "Scattering by cavity-backed antennas on a circular cylinder," *IEEE Trans.*

*Antennas Propagation*., 42, pp. 1268-1279, Sept. 1994.

[7] L.C. Kempel, J.L. Volakis, and R.J. Sliva, "Radiation by cavity-backed antennas on circular cylinder," *IEE Proc.-Microw. Antennas Propag*., 142, pp. 233-239, June 1995.

[8] X-Q Sheng, J-M Jin, J. Song, C-C Lu, and W.C. Chew, "On the formulation of hybrid finite-element and boundary-integral methods for 3-D scattering," *IEEE Transactions on Antennas and Propagation*, 46, p. 303-311, March. 1998.

[9] C.A. Macon, L.C. Kempel, and S.W. Schneider, "Radiation and Scattering by Complex Conformal Antennas on a Circular Cylinder," *Adv. Comp. Math*., 16, pp. 191-209, 2002.

[10] F. Bilotti, A. Toscano, and L. Vegni, "FEM-BEM formulation for the analysis of cavity-backed patch antennas on chiral substrates," *IEEE Transactions on Antennas and Propagations*, 51, pp. 1829-1836, August 2003.

[11] C-W Wu, L.C. Kempel, and E.J. Rothwell, "Hybrid Finite Element-Boundary Integral Method for Cavities Recessed in an Elliptic Cylinder," *IEEE Transactions on Antennas and Propagations*, 51, pp. 306-311, Feb. 2003.

[12] C.A. Macon, L.C. Kempel, S.W. Schneider, and K.D. Trott, "Modeling Conformal Antennas on Metallic Prolate Spheroid Surfaces Using a Hybrid Finite Element Method," *IEEE Transactions on Antennas and Propagations*, 52, pp. 750-758, March 2004.

[13] K.K. Mei, "Unimoment method of solving antenna and scattering problems," *IEEE Transactions on Antennas and Propagations*, 22, p. 760-766, Nov. 1974.

[14] J. Liu and J.M. Jin, "A novel hybridization of higher order finite element and boundary integral methods for electromagnetic scattering and radiation problems, *IEEE Transactions on Antennas and Propagations*, 49, p. 1794-1806, Dec. 2001.

[15] G.E. Antilla, Radiation and Scattering from Complex Three-Dimensional Geometries using a Curvilinear Hybrid Finite Element-Integral Equation Approach, Ph.D. Dissertation, University of California at Los Angeles, 1993.

[16] L.C. Kempel, "Implementation of Various Hybrid Finite Element-Boundary Integral Methods: Bricks, Prisms, and Tets," 1999 ACES Meeting, Monterey, CA, pp. 242-249, 1999.

[17] C-T Tai, Dyadic Green Functions in Electromagnetic Theory, 2nd ed., Piscataway, NJ: IEEE Press, 1994.

[18] A.F. Peterson, S.L. Ray, R.Mittra. Computational Methods for Electromagnetics. IEEE Press, New York, 1998.

[19] S.M. Rao, D.R. Wilton, A.W. Glisson. "Electromagnetic Scattering by Surfaces of Arbitrary Shape", *IEEE Transactions on Antennas and Propagations*, 30, pp. 409-418, May 1982.

[20] T. Ozdemir and J.L. Volakis, "Triangular prisms for edge-based vector finite element analysis of conformal antennas *IEEE Transactions on Antennas and Propagations*, 45, p. 788-797, May 1997.

# Investigation of an Explicit, Residual-Based, a Posteriori Error Indicator for the Adaptive Finite Element Analysis of Waveguide Structures

Matthys M. Botha and David B. Davidson

*Department of Electrical and Electronic Engineering, University of Stellenbosch, Private Bag X1, Matieland 7602, Stellenbosch, South Africa*

***Abstract*— The performance of an explicit, residual-based, a posteriori error indicator for directing a single level $p$-refinement of the finite element method, electromagnetic analysis of multi-port waveguide structures is evaluated experimentally by considering three different structures. The error indicator consists of a linear combination of element volume and element face residuals. It is found that the indicator is generally very effective in identifying elements that need to be refined. It is also found that the relative weighting of the volume and face residual contributions to the error indicator plays an important role in its performance.**

## I. Introduction

The Finite Element Method (FEM) can be used very effectively in the analysis of waveguide structures. References [1], [2], [3], [4] represent some examples of the driven problem and [5], [6] represent some examples of the eigenvalue problem. There are fundamental differences between the driven- and eigenvalue problems. The eigenvalue problem is typically a 2D analysis of the waveguide transverse plane with the purpose of finding the modal field distributions and cutoff frequencies, whereas the driven problem can be in 2D (see [4]), but is generally constructed in 3D (see [1], [2], [3]). The driven problem needs to include the waveguide port(s) within the variational formulation as an inhomogeneous, Dirichlet boundary condition (the voltage-current approach, see [4]) or as a special type of Neumann boundary condition (the incident-reflected approach, see [1], [2], [3]).

In this paper we will use curl-conforming, vector elements to analyze 3D, multi-port, inhomogeneously filled, waveguide structures at specific frequencies (a driven problem), using Neumann boundary conditions to model the ports. These elements posses fundamental advantages over scalar elements, as discussed in numerous publications [6], [7], [8], [9]. The waveguide port variational boundary value problem and the resulting FEM is discussed in Section II.

The main contribution of this paper is the experimental performance evaluation of an explicit, residual-based, a posteriori error indicator when used to direct a single level $p$-refinement. Error indicators are commonly used for refining finite element discretizations in an iterative manner.

The error indicator is presented in Section III and is a proper bound on an approximate energy norm. It can be derived from the waveguide port variational boundary value problem, as shown in [10], [11]. It is explicit in nature and based on volume and trace residuals. The indicator is of the same general form as a residual-based indicator presented in [12, eq.(3.18)] for the general, scalar, elliptic boundary value problem case, bounding the proper energy norm. There are clearly some important differences between our indicator and the one in [12], but these will not be discussed further. Other examples of indicators, similar to the one used here, can be found in the literature. Reference [6, Appendix G] presents an explicit, residual-based indicator tailored to the vector wave equation, but it does not incorporate the waveguide port formulation that we employ and only deals with 2D problems. Reference [13] presents an explicit, residual-based estimator for 3D, electrostatic problems. Explicit, residual-based indicators that bound the $L^2$ norm of the error as opposed to the (approximate) energy norm, can also be derived — see [12], [14] for the scalar elliptic case and [15] for the Maxwell system case where an open boundary, hybrid FEM is considered, employing spherical harmonics, similar in some respect to the unimoment method [16].

Ideally, one would like to investigate the performance of an error indicator experimentally by considering problems with analytical solutions. Unfortunately, very few such problems are available for the type of multi-port waveguide structures that are considered here. Therefore, we resorted to considering the errors with respect to higher order solutions as a measure of the true performance. This still is of great practical value, since the maximum available order solution represents the closest possible approximation of the true solution for a given discretization, in any case. We restrict ourselves to two elements of different order that are widely used: the Constant Tangential/Linear Normal (CT/LN) and Linear Tangential/Quadratic Normal (LT/QN) elements [9]. Section IV describes the investigative procedure followed. In Sections V, VI and VII, investigative results of three different waveguide port structures are presented and discussed.

We end by drawing some overall conclusions in light of all the available results.

In this paper, the subscript $w$ will indicate entities associated with the feeding waveguides and/or their corresponding port apertures.

1054-4887 ' 2006 ACES

## II. THE WAVEGUIDE, FINITE ELEMENT FORMULATION

The electric field, vector wave equation, boundary value problem on the volume $\Omega$, is as follows [1]:

$$\begin{cases} \nabla \times \dfrac{1}{\mu_r} \nabla \times \mathbf{E} - k_0^2 \epsilon_r \mathbf{E} = -jk_0 Z_0 \mathbf{J} & \text{on } \Omega, \\ \hat{n} \times \mathbf{E} = 0 & \text{on } \Gamma_D, \\ \hat{n} \times \nabla \times \mathbf{E} = \mathbf{N} & \text{on } \Gamma_N, \end{cases} \tag{1}$$

where $\Gamma_D$ represents the homogeneous, Dirichlet boundary and $\Gamma_N$ represents the inhomogeneous, Neumann boundary. $\mathbf{J}$ represents an impressed current distribution and $\mathbf{N}$ represents a general Neumann boundary condition.

The electric field, vector wave equation, boundary value problem can be expressed as a variational boundary value problem [11], yielding

$$\begin{cases} \displaystyle\int_\Omega \left\{ \frac{1}{\mu_r} \nabla \times \mathbf{E} \cdot \nabla \times \mathbf{W} - k_0^2 \epsilon_r \mathbf{E} \cdot \mathbf{W} \right\} dV \\ \displaystyle = -\int_{\Gamma_N} \frac{1}{\mu_r} \mathbf{N} \cdot \mathbf{W} \, dS - jk_0 Z_0 \int_\Omega \mathbf{J} \cdot \mathbf{W} \, dV \\ \forall \ \mathbf{W} \in W; \quad \mathbf{E} \in W \end{cases} \tag{2}$$

with

$$W = \{ \mathbf{a} \in H(\text{curl}, \Omega) \mid \hat{n} \times \mathbf{a} = 0 \text{ on } \Gamma_D \}. \tag{3}$$

Dominant, $TE_{10}$ mode modeling of a waveguide port is included in the variational boundary value problem via a Neumann boundary condition at the port aperture $S_w$, as described in [1]. The resulting variational boundary value problem is as follows:

$$\begin{cases} \displaystyle\int_\Omega \left\{ \frac{1}{\mu_r} \nabla \times \mathbf{E} \cdot \nabla \times \mathbf{W} - k_0^2 \epsilon_r \mathbf{E} \cdot \mathbf{W} \right\} dV \\ \quad \displaystyle + \frac{jk_w}{\mu_{rw}} \int_{S_w} (\hat{n} \times \mathbf{E}) \cdot (\hat{n} \times \mathbf{W}) \, dS \\ \displaystyle = \frac{2jk_w}{\mu_{rw}} \int_{S_w} (\hat{n} \times \mathbf{E}_w^{\text{inc}}) \cdot (\hat{n} \times \mathbf{W}) \, dS \\ \forall \ \mathbf{W} \in W; \quad \mathbf{E} \in W. \end{cases} \tag{4}$$

Note that the impressed, electric current source term was dropped in equation (4), since no such sources will be present in the waveguide problems considered here.

$\mathbf{E}_w^{\text{inc}}$ and $k_w$ represent the incident, $TE_{10}$ wave at the port and the feeding waveguide, $TE_{10}$ mode propagation constant, respectively. They are defined in terms of the local port coordinate system shown in Figure 1, as follows [17]:

$$\mathbf{E}_w^{\text{inc}} = E_w^{\text{inc}} \sin\left(\frac{\pi x}{a}\right) \hat{y}. \tag{5}$$

$$k_w = \sqrt{k_0^2 - \left(\frac{\pi}{a}\right)^2}. \tag{6}$$

A finite element discretization is employed in order to solve equation (4) in an approximate manner. The electric field is represented as

$$\mathbf{E}_h = \sum_{i=1}^{N_F} E_i \mathbf{N}_i, \tag{7}$$

with the $E_i$ representing the unknown degrees of freedom and the $\mathbf{N}_i$ representing the basis functions. By choosing the testing functions equal to the basis functions, equation (4) leads to a symmetric matrix equation $[A]\{E\} = \{b\}$ in terms of the degrees of freedom.

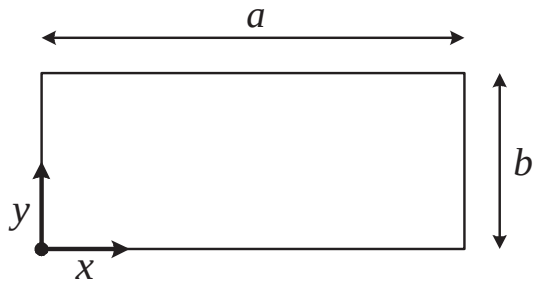


Fig. 1. Waveguide aperture. Definitions of the local coordinate system and dimensions.

Curl-conforming, hierarchal, vector basis functions of mixed order are used [9]. Since the elements are of mixed order, they model the unknown field and its curl to the same polynomial degree, with the least possible degrees of freedom [18]. Note that both of these quantities play roles of equal importance in equation (4). Normal field continuity is not enforced by curl-conforming elements; the associated benefits are outlined in [7]. The elements are hierarchal, which means that elements of different polynomial order can easily be used within the same mesh.

In the rest of this paper, the hierarchal property of the elements is of great importance, since CT/LN ($\text{H}_0(\text{curl})$) and LT/QN ($\text{H}_1(\text{curl})$) elements are used together. The definitions of the basis functions used, can be found in [19].

## III. THE WAVEGUIDE, EXPLICIT, RESIDUAL-BASED, ERROR INDICATOR

Define the error field as

$$\mathbf{e}_h = \mathbf{E} - \mathbf{E}_h. \tag{8}$$

Define $K$ as a single, elemental volume of the mesh and define $f$ as a single, facial area of the mesh, with $N_K$ as the number of elements in the mesh and $N_f$ as the number of faces in the mesh. Further define

$$h_{K(i)} = \text{diam}(K_i), \tag{9}$$

$$h_{f(m)} = \begin{cases} \max\left\{\text{diam}(K^{(1)}), \text{diam}(K^{(2)})\right\} & \text{internal face,} \\ \text{diam}(K^{(1)}) & \text{boundary face,} \end{cases} \tag{10}$$

where the superscripts $(1)$ and $(2)$ indicate the two elements sharing the face concerned and $\text{diam}(K)$ indicates the diameter (maximum dimension) of element $K$.

The following explicit, residual-based, error bound can be derived for the discretized, waveguide variational boundary value problem of equation (4) [10], [11]:

$$\begin{aligned} \|\mathbf{e}_h\|^2_{E^a(\Omega)} \quad \leq \quad & C_V \sum_{i=1}^{N_K} h^2_{K(i)} \|\mathbf{R}_V\|^2_{L^2(K_i)} \\ & + C_f \sum_{m=1}^{N_f} h_{f(m)} \|\mathbf{R}_f\|^2_{L^2(f_m)}, \end{aligned} \tag{11}$$

with the approximate energy norm defined as

$$\|\mathbf{a}\|_{E^a(\Omega)} \equiv \left[\sum_{i=1}^{N_K} |\mathbf{a}|^2_{(H^1(K_i))^3}\right]^{-\frac{1}{2}} \cdot \left| \int_\Omega \left\{ \frac{1}{\mu_r} \nabla \times \mathbf{a} \cdot \nabla \times \mathbf{a} - k_0^2 \epsilon_r \mathbf{a} \cdot \mathbf{a} \right\} dV + \frac{jk_w}{\mu_{rw}} \int_{S_w} (\hat{n} \times \mathbf{a}) \cdot (\hat{n} \times \mathbf{a})\, dS \right| \quad (12)$$

where $|\mathbf{a}|_{(H^1(K))^3}$ designates the Sobolev semi-norm of order 1, on elemental volume $K$ [20]. The volume and face residuals in equation (11) are defined as

$$\mathbf{R}_V = -\nabla \times \frac{1}{\mu_r} \nabla \times \mathbf{E}_h + k_0^2 \epsilon_r \mathbf{E}_h \quad \text{in } K_i;\ i = 1, ..., N_K. \quad (13)$$

$$\mathbf{R}_f = \begin{cases} \hat{n}^{(12)} \times \left[ \frac{1}{\mu_r^{(1)}} \nabla \times \mathbf{E}_h^{(1)} - \frac{1}{\mu_r^{(2)}} \nabla \times \mathbf{E}_h^{(2)} \right] \\ \qquad \text{on } f_m \setminus S_w;\ m = 1, ..., N_f \\ \frac{1}{\mu_r} \hat{n} \times \nabla \times \mathbf{E}_h - \frac{jk_w}{\mu_{rw}} \hat{n} \times \left[ \hat{n} \times \left( 2\mathbf{E}_w^{\text{inc}} - \mathbf{E}_h \right) \right] \\ \qquad \text{on } f_m \cap S_w;\ m = 1, ..., N_f. \end{cases} \quad (14)$$

It is clear that $\|\mathbf{e}_h\|_{E^a(\Omega)}$ is not a proper norm of the error field, because it does not conform to the well known specifications of a proper norm [21], since $\|\mathbf{e}_h\|_{E^a(\Omega)} = 0 \not\Rightarrow \mathbf{e}_h = 0$. However, $\mathbf{e}_h = 0 \Rightarrow \|\mathbf{e}_h\|_{E^a(\Omega)} = 0$ and one can further observe that the residuals (and therefore the RHS of equation (11)) will go to zero when $\mathbf{E}_h$ satisfies the vector wave equation and the Maxwell continuity conditions [17]. Therefore: the RHS of equation (11) can reliably indicate the presence of an error, but not the absence thereof. This is not ideal, but it will be shown to be quite useful.

Equation (11) can be rewritten in terms of elemental contributions to the bound on $\|\mathbf{e}_h\|^2_{E^a(\Omega)}$. It is assumed that the facial contributions are shared equally between elements. The boundary face contributions are also scaled by $1/2$ even though they are not shared, since they represent the same Maxwell continuity condition as the internal face residuals and should therefore be treated in the same way. Equation (11) becomes a summation of elemental error indicators:

$$\|\mathbf{e}_h\|^2_{E^a(\Omega)} \leq \sum_{i=1}^{N_K} \left( C_V h^2_{K(i)} \|\mathbf{R}_V\|^2_{L^2(K_i)} + \frac{1}{2} C_f \sum_{f_m \subset \partial K_i} h_{f(m)} \|\mathbf{R}_f\|^2_{L^2(f_m)} \right). \quad (15)$$

The unknown constants $C_V$ and $C_f$ in equation (15) can be replaced with two new constants, $C$ and $\alpha$, resulting in

$$\|\mathbf{e}_h\|^2_{E^a(\Omega)} \leq C \sum_{i=1}^{N_K} \left( \alpha h^2_{K(i)} \|\mathbf{R}_V\|^2_{L^2(K_i)} + \frac{1}{2}(1-\alpha) \sum_{f_m \subset \partial K_i} h_{f(m)} \|\mathbf{R}_f\|^2_{L^2(f_m)} \right), \quad (16)$$

with

$$0 \leq \alpha \leq 1. \quad (17)$$

The value $\alpha$ clearly represents the relative contributions of the volume- and facial residuals to the elemental indicators. The effect of this parameter on the indicator performance will be studied in the subsequent sections.

## IV. Investigative procedure

This section describes a procedure for evaluating the effect of the parameter $\alpha$ on the performance of the error indicator of equation (16), for a specific problem and at a specific frequency.

After an all-CT/LN solution, the following elemental error indicator is calculated for every element $K_i$, $i = 1, .., N_K$, with fixed $\alpha$:

$$\alpha h^2_{K(i)} \|\mathbf{R}_V\|^2_{L^2(K_i)} + \frac{1}{2}(1-\alpha) \sum_{f_m \subset \partial K_i} h_{f(m)} \|\mathbf{R}_f\|^2_{L^2(f_m)}. \quad (18)$$

The problem is then re-solved, but with a percentage of elements with the highest error indicator values upgraded to LT/QN elements. Since the quality of the upgraded solution must lie between that of an all-CT/LN- and an all-LT/QN solution, the relative solution quality error $\epsilon_Q$, measured in terms of the reflection coefficient $S_{11}$, is defined as follows:

$$\epsilon_Q = \left| \frac{S_{11} - S_{11}^{\text{LT/QN}}}{S_{11}^{\text{LT/QN}}} \right|. \quad (19)$$

The value $\epsilon_Q$ is called relative, since it is a measure of the solution quality error $\left| S_{11} - S_{11}^{\text{LT/QN}} \right|$, *relative* to the magnitude of the highest order solution, $\left| S_{11}^{\text{LT/QN}} \right|$.

Various $\epsilon_Q$ values are obtained for the current value of $\alpha$, by changing the percentage of elements that are upgraded to LT/QN. In all graphs to be presented, the following set of percentages were used: $0.0\%$, $2.5\%$, $5.0\%$, $7.5\%$, $10.0\%$, $12.5\%$ and $100.0\%$. This defines a curve of $\epsilon_Q$ as a function of the number of degrees of freedom. A set of such curves is generated at a given frequency point by considering a range of $\alpha$ values and will henceforth be referred to as a *performance graph*. On every performance graph a curve denoted "Random" is included for reference purposes. These curves were generated by upgrading randomly selected elements. Considering a specific problem, a distinct performance graph can be generated by the above described procedure, at any frequency.

As an example, consider Figure 4, the performance graph of a waveguide through problem at $f = 8.5$ GHz, to be discussed in Section V. The first cluster of data points, around 1500 degrees of freedom, represents an upgrade of $2.5\%$ of the elements. Following clusters represent the other upgrade percentages used. These clusters can be quite spread out, since the upgrading of two neighbouring elements results in fewer additional degrees of freedom than the upgrading of two free-standing elements (upgrading an element necessitates the partial upgrading of its neighbours in order to maintain tangential field continuity). At a specific upgrade percentage,

the number of degrees of freedom depends on the element selection scheme and will thus vary with $\alpha$. The number of degrees of freedom (rather than the upgrade percentage) was chosen as the $x$-axis variable of the performance graphs, since it is a good indicator of relative computational effort.

Various performance graphs of various problems will be considered in order to ascertain whether a pattern is present.

## V. Results: performance graphs of a waveguide through problem

This section considers a waveguide through problem. The geometry of the problem is a straight, empty length of standard X-band waveguide. Figure 2 shows the finite element mesh. Figure 3 compares the reflection coefficient values obtained with all-CT/LN- and all-LT/QN elements, with the analytical solution, showing that the LT/QN result is indeed an improvement upon the CT/LN result.

Performance graphs for this structure were calculated at $f = 8.5$ GHz, $f = 9.5$ GHz, and $f = 10.5$ GHz. In this case the solution quality error was not divided by $\left|S_{11}^{\text{LT/QN}}\right|$, because the true reflection coefficient is zero. Figures 4, 5 and 6 show the performance graphs.

There seems to be no consistent tendency in the performance graphs. The error indicator performance is generally poor. We propose the following reason for this behaviour:

The actual field possesses no variation in amplitude along the guide length, only a sinusoidal variation in phase. In the transverse plane there is only a sinusoidal, amplitude variation in the local (see Figure 1) $x$-direction. Since the actual field variations are clearly very slow and uniform throughout the whole structure, the actual error distribution is relatively flat, compared to the other problems considered in this paper. Thus, one actually needs to upgrade the mesh uniformly, rather than selectively, for optimal error reduction.

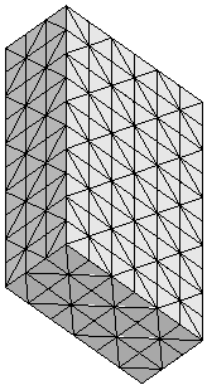

Fig. 2. Finite element mesh of the waveguide through problem. 1194 elements, average edge length is 4.5 mm. The ports are transverse to the longest dimension of the structure. The transverse waveguide geometry is as shown in Figure 1, with $a = 22.86$ mm and $b = 10.16$ mm.

## VI. Results: performance graphs of a waveguide iris problem

This section considers a waveguide iris problem. The geometry of the problem is a straight, empty length of X-band waveguide, except for an infinitely thin PEC iris located at its center. Figure 7 shows the iris geometry. Figure 8 shows the finite element mesh. Figure 9 compares the reflection coefficient values obtained with all-CT/LN- and all-LT/QN elements, with an approximate, analytical result by Marcuvitz [22], showing that the LT/QN result is indeed an improvement upon the CT/LN result. Marcuvitz's results are lumped-element circuit models; in [3] the procedure required to obtain $s$-parameters from these was outlined.

Performance graphs for this structure were calculated at $f = 8.5$ GHz, $f = 9.5$ GHz and $f = 10.5$ GHz. Figures 10, 11 and 12 show the performance graphs.

Observe the following tendency in the performance graphs: when considering only a small increase in the number of degrees of freedom ($\leq 2.5\%$ upgraded elements), a dominant surface contribution leads to superior results ($\alpha < 0.5$), but if one intends to upgrade $\geq 5\%$ of the elements, a value of

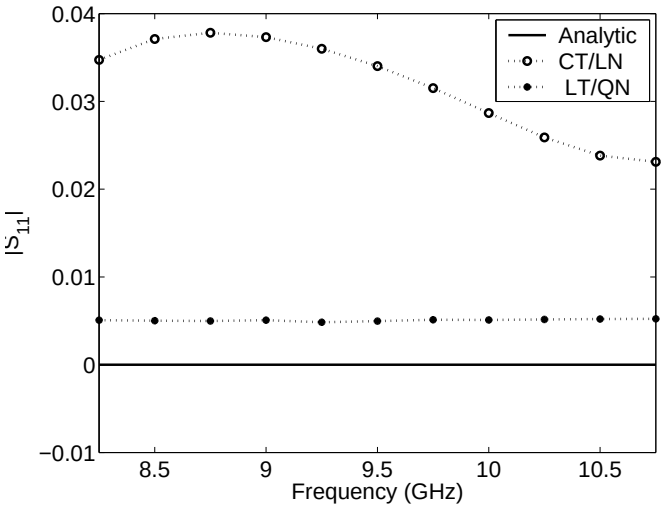


Fig. 3. $S_{11}$ vs. frequency of the waveguide through problem.

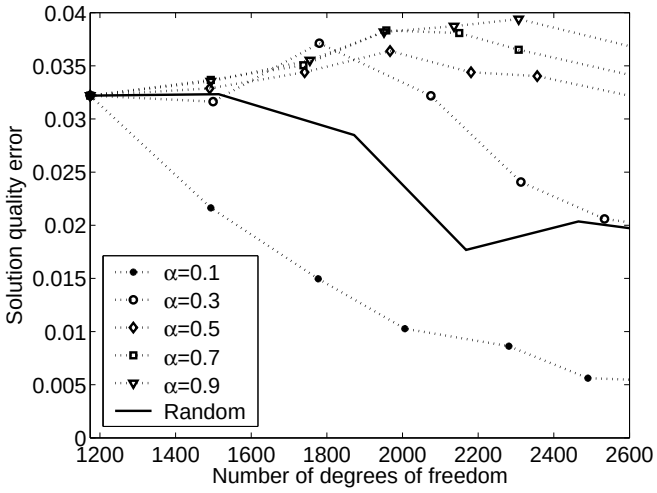


Fig. 4. Solution quality error vs. number of degrees of freedom for the waveguide through problem at $f = 8.5$ GHz. The all LT/QN number of degrees of freedom, at which the solution quality error is zero for all $\alpha$, is 6836.

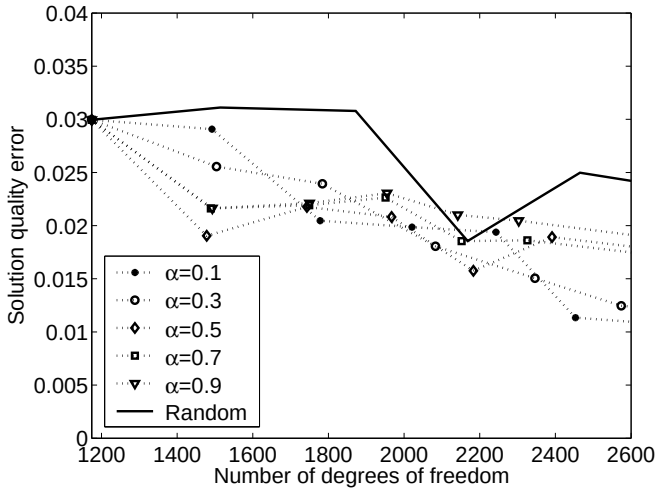


Fig. 5. Solution quality error vs. number of degrees of freedom for the waveguide through problem at $f = 9.5$ GHz. The all LT/QN number of degrees of freedom, at which the solution quality error is zero for all $\alpha$, is 6836.

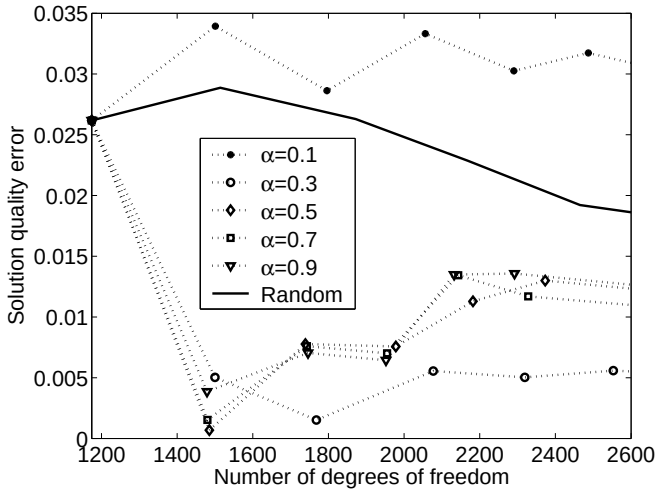


Fig. 6. Solution quality error vs. number of degrees of freedom for the waveguide through problem at $f = 10.5$ GHz. The all LT/QN number of degrees of freedom, at which the solution quality error is zero for all $\alpha$, is 6836.

$\alpha \geq 0.5$ seems to be required.

A possible explanation for this tendency, which is also confirmed by inspection of the geometric distribution of the volume and face residual values, is as follows:

When a small enough number of elements are to be upgraded, exclusive use of the face residuals leads to the best results, because they are most effective in identifying the elements along the iris edge, where one would expect the greatest error in the approximate field representation to occur. It is well known that the electric field strength at such a reentrant corner is singular and changes direction extremely fast in its vicinity [7]. The elements are of finite size and the polynomial orders of the basis functions are also finite, thus large inter-element discontinuities will be present as a matter of course. Away from the singularity, the variation in the true field is less intense and the volume residuals overshadow the face residuals in importance.

Figures 13 and 14 show the $2.5\%$ elements with the largest error indicator values at $f = 9.5$ GHz, as identified by the $\alpha = 0.1$ and $\alpha = 0.9$ indicators respectively. Comparison of these two figures clearly shows the initial, superior capability of the $\alpha = 0.1$ indicator in identifying the elements along the iris edge in the middle of the waveguide.

From the performance graphs it can be seen via inspection that $\alpha = 0.5$ leads to the best all-round results for the waveguide iris problem. The value $\alpha = 0.5$ causes the relative solution quality error to decrease at a near optimal initial gradient in two out of three cases and leads to optimal relative solution quality error values at the highest upgrade percentage ($12.5\%$) in all three cases.

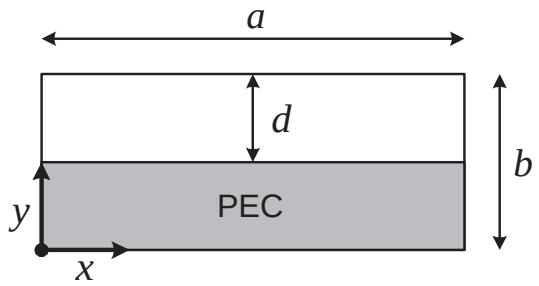


Fig. 7. Waveguide iris geometry. $a = 22.86$ mm, $b = 10.16$ mm and $d = 5.08$ mm.

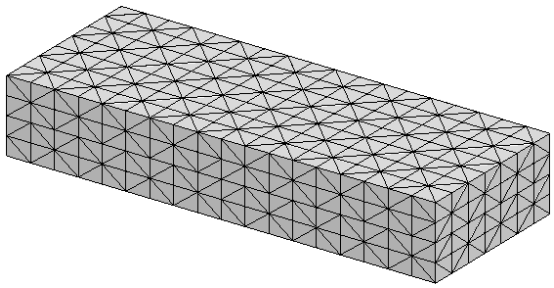

Fig. 8. Finite element mesh of the iris problem. 1889 elements, average edge length is 4.3 mm.

## VII. Results: Performance Graphs of a Waveguide Bend Problem

This section considers a waveguide bend problem. The problem geometry is an E-plane, $90°$, standard X-band, waveguide bend. Figure 15 shows the finite element mesh. Figure 16 compares the reflection coefficient values obtained with all-CT/LN- and all-LT/QN elements, with an approximate, analytical result by Marcuvitz [22], showing that the LT/QN result is indeed an improvement upon the CT/LN result. Again, [3] discusses the relevant manipulations of Marcuvitz's lumped-element model.

Performance graphs for this structure were calculated at $f = 8.5$ GHz, $f = 9.5$ GHz and $f = 10.5$ GHz. Figures 17, 18 and 19 show the performance graphs.

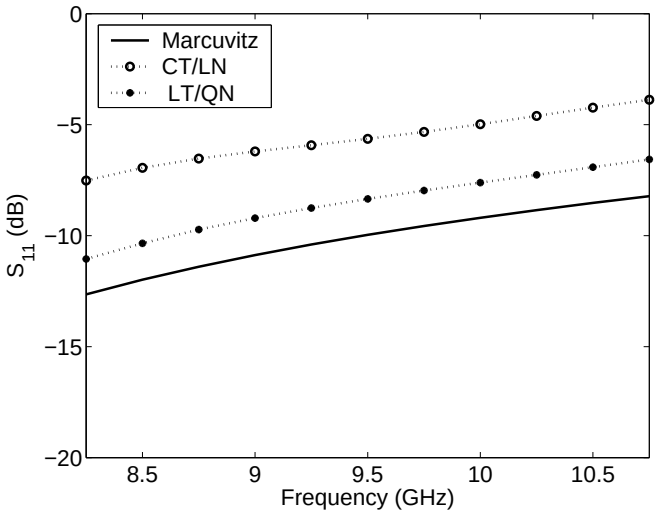


Fig. 9. $S_{11}$ vs. frequency of the waveguide iris problem.

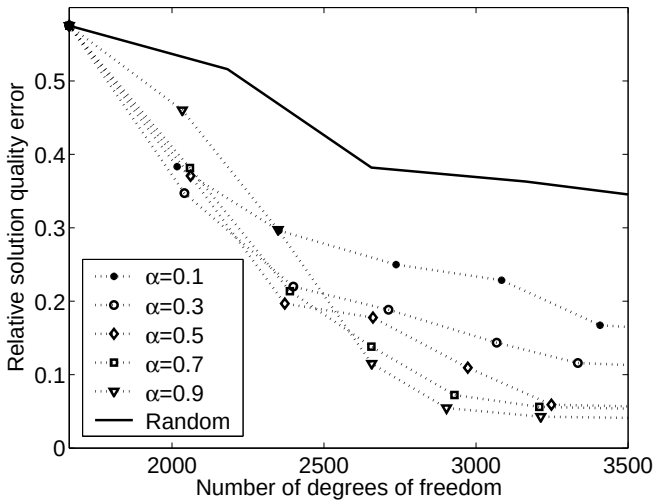


Fig. 10. Relative solution quality error vs. number of degrees of freedom for the waveguide iris problem at $f = 8.5$ GHz. The all LT/QN number of degrees of freedom, at which $\epsilon_Q = 0$ for all $\alpha$, is 10144.

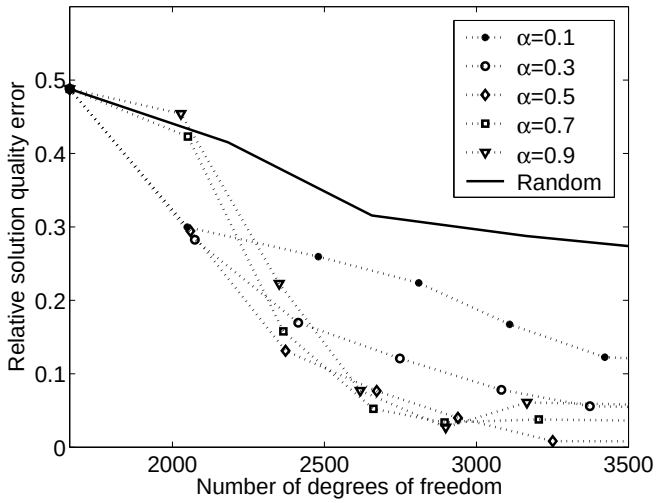


Fig. 11. Relative solution quality error vs. number of degrees of freedom for the waveguide iris problem at $f = 9.5$ GHz. The all LT/QN number of degrees of freedom, at which $\epsilon_Q = 0$ for all $\alpha$, is 10144.

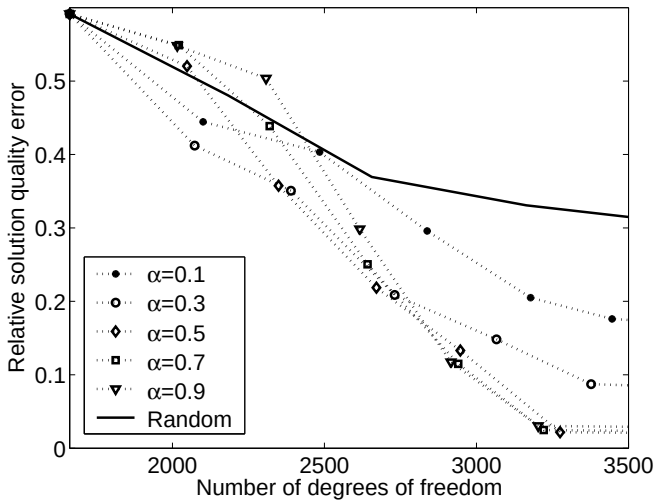


Fig. 12. Relative solution quality error vs. number of degrees of freedom for the waveguide iris problem at $f = 10.5$ GHz. The all LT/QN number of degrees of freedom, at which $\epsilon_Q = 0$ for all $\alpha$, is 10144.

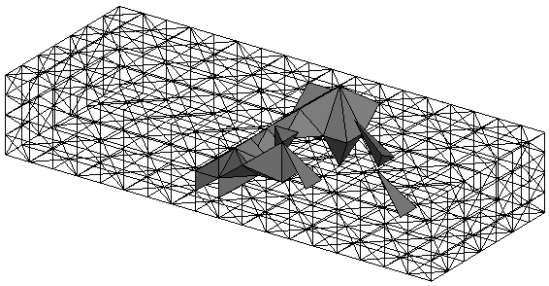

Fig. 13. The $2.5\%$ elements with the largest error indicator values for the waveguide iris problem at $f = 9.5$ GHz, $\alpha = 0.1$.

Observe the following tendency in the performance graphs: throughout the range of degrees of freedom (upgrade percentages) considered, the $\alpha \geq 0.5$ indicators resulted in superior, near-identical performances in every graph.

The observed tendency is close to that of the waveguide iris problem in Section VI, except that at small upgrade percentages ($\leq 5\%$), the $\alpha \geq 0.5$ indicators remain superior to the $\alpha < 0.5$ indicators.

In the light of this similarity, we propose that the reason for the behaviour exhibited by the waveguide bend performance graphs are the same as that proposed for the waveguide iris problem's performance graphs. The difference in behaviour in the case of small upgrade percentages can be accounted for by noting that the field singularity at the re-entrant corner of the waveguide bend is of a lower order than that of the iris problem ($r^{-\frac{1}{3}}$ vs. $r^{-\frac{1}{2}}$, where $r$ is a radial coordinate perpendicular to the re-entrant corner — see [23, p.178] for details). This means that the upgrade percentage below which the exclusive use of face residuals leads to superior results, is smaller than in the waveguide iris case. In fact, this percentage

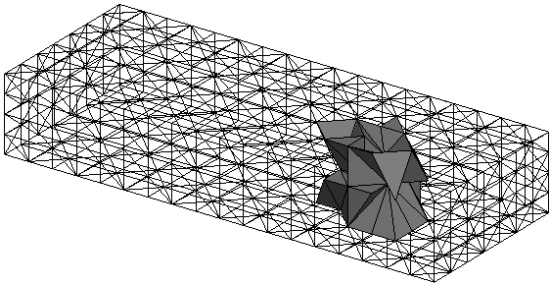

Fig. 14. The $2.5\%$ elements with the largest error indicator values for the waveguide iris problem at $f = 9.5$ GHz, $\alpha = 0.9$.

is below $2.5\%$ and thus, it is not shown in Figures 17, 18 and 19.

Figure 20 shows the $2.5\%$ elements with the highest error indicator values in the case of $\alpha = 0.5$ and $f = 9.5$ GHz. Note how the re-entrant corner of the bend is covered, as one would expect (as motivated in Section VI for the iris edge).

As noted before within this section, $\alpha \geq 0.5$ leads to the best results for the waveguide bend problem.

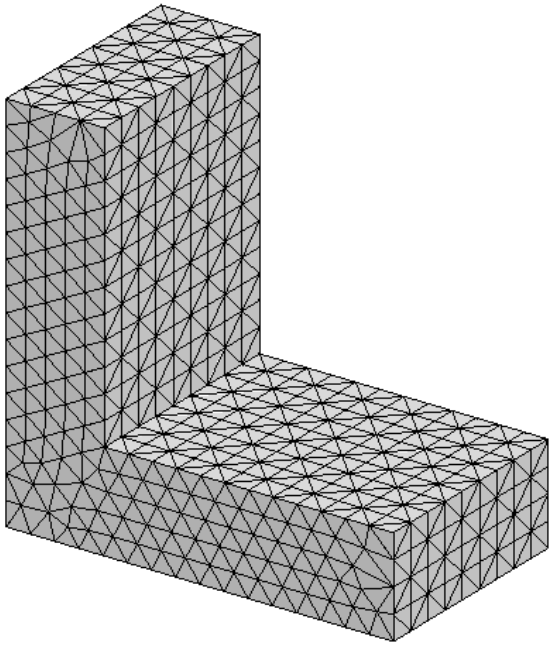

Fig. 15. Finite element mesh of the waveguide bend problem. 3331 elements, average edge length is 3.5 mm. The port geometries are as shown in Figure 1, with $a = 22.86$ mm and $b = 10.16$ mm.

## VIII. Conclusion

In this experimental investigation of an explicit, residual-based, a posteriori error indicator (presented in Section III) for driving a single level $p$-refinement of a related waveguide FEM formulation (presented in Section II), it seemed that the error indicator's performance is far superior to a benchmark, random selection, element upgrade scheme. The only poor results were encountered when considering the uniform, through problem, but as it is proposed in Section V, the through problem

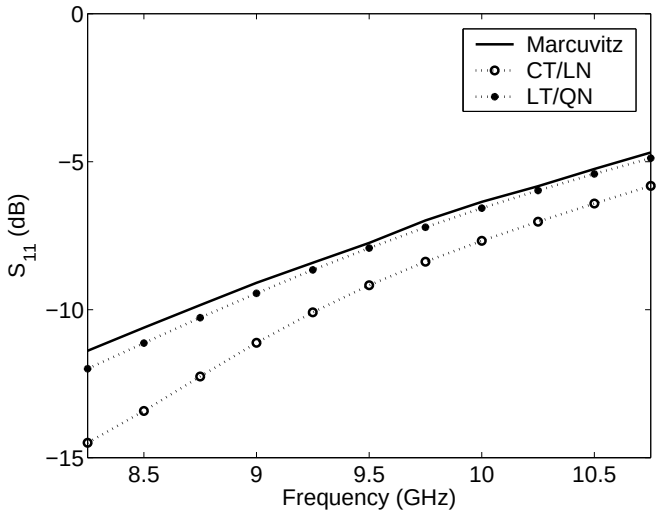


Fig. 16. $S_{11}$ vs. frequency of the waveguide bend problem.

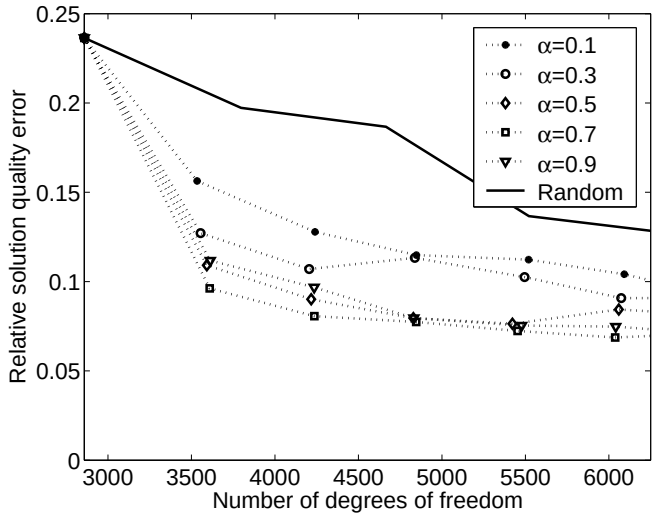


Fig. 17. Relative solution quality error vs. number of degrees of freedom for the waveguide bend problem at $f = 8.5$ GHz. The all LT/QN number of degrees of freedom, at which $\epsilon_Q = 0$ for all $\alpha$, is 17628.

represents a special case that should be considered separately when evaluating the error indicator's general behaviour.

Though it was seen in Section VI that the face residuals may prove more important than the volume residuals in some regions and vice a versa, it is important to keep in mind that both residuals together are needed to form an upper bound on the approximate energy norm of the error field (see equation (11)), therefore they should both be present within a general indicator. This brings us to the choice of the parameter $\alpha$ in equation (18). Although it was found that the use of the indicator nearly always results in element selections that are superior to the random scheme, no matter the value of $\alpha$, it does seem from the available results, that $\alpha \approx 0.5$ gives the most consistent results, but only marginally.

It was seen that the indicator considered here can be very effective; however, a couple of limitations should be kept in

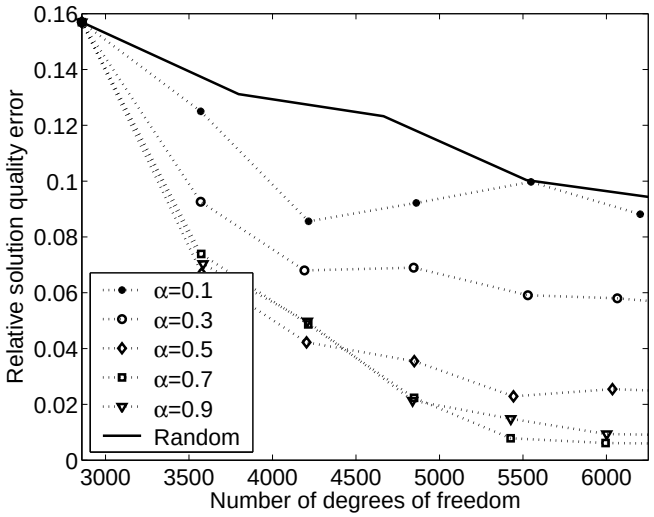


Fig. 18. Relative solution quality error vs. number of degrees of freedom for the waveguide bend problem at $f = 9.5$ GHz. The all LT/QN number of degrees of freedom, at which $\epsilon_Q = 0$ for all $\alpha$, is 17628.

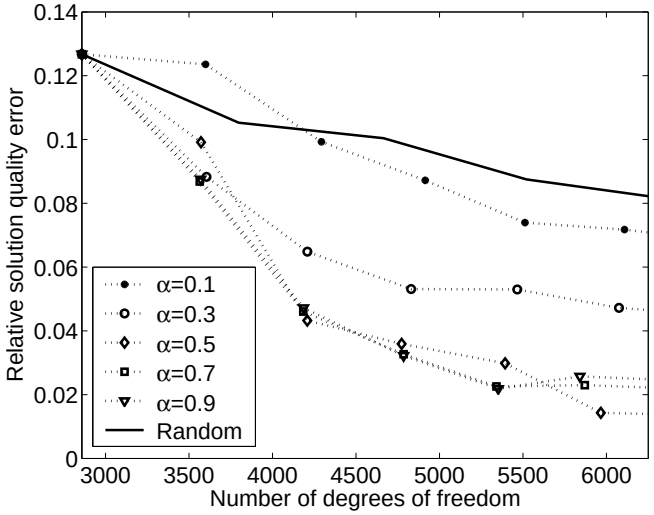


Fig. 19. Relative solution quality error vs. number of degrees of freedom for the waveguide bend problem at $f = 10.5$ GHz. The all LT/QN number of degrees of freedom, at which $\epsilon_Q = 0$ for all $\alpha$, is 17628.

mind. Firstly, the error indicator only indicates relative error and not absolute error, which is a consequence of the unknown constants present within equation (11). This implies that it cannot be used as a termination condition of an iterative analysis procedure that guarantees a specified solution error bound. Secondly, the error indicator does not bound a proper norm of the true error and is therefore not guaranteed to perform consistently. Both of these limitations, which are inherently part of the indicator considered here, may possibly be overcome, to varying degrees, by considering other types of error indicators, error estimators and/or measures of the error.

Although not the topic of this present work, which has considered only the usual mixed-order elements, subsequent work has shown that for specific problems, full-order elements may be desirable. The waveguide iris problem is a good example of such a structure. An extended discussion and results may be found in [24], and an adaptive scheme targeted specifically at such problems has been presented in [25]. A general adaptive scheme within which the error indicator discussed here could be employed, is presented in [26].

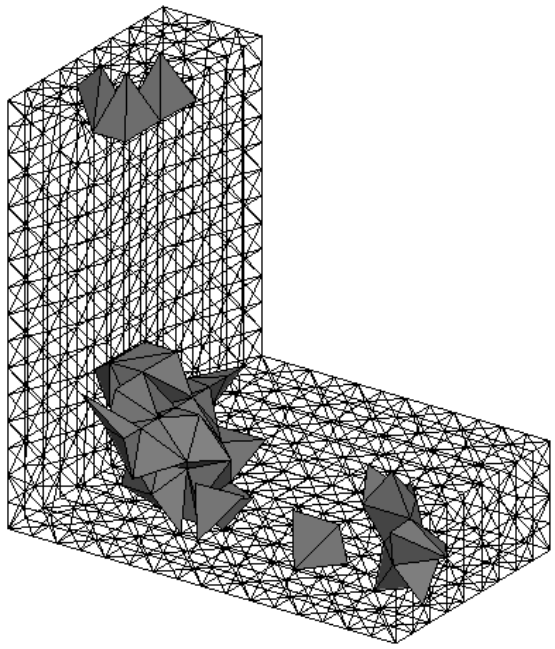

Fig. 20. The $2.5\%$ elements with the largest error indicator values for the waveguide bend problem at $f = 9.5$ GHz, $\alpha = 0.5$.

## REFERENCES

[1] J.-M. Jin, *The Finite Element Method in Electromagnetics*, 2nd ed. New York: John Wiley and Sons, 2002.

[2] C. J. Reddy, M. D. Deshpande, C. R. Cockrell, and F. B. Beck, "Analysis of three-dimensional-cavity-backed aperture antennas using a combined finite element method/method of moments/geometrical theory of diffraction technique," NASA, Langley Research Center, Tech. Rep. 3548, November 1995.

[3] D. B. Davidson, "Higher-order (LT/QN) vector finite elements for waveguide analysis," *Applied Computational Electromagnetics Society Journal*, vol. 17, no. 1, pp. 1–10, March 2002, special Issue on Approaches to Better Accuracy/Resolution in Computational Electromagnetics.

[4] J. P. Webb, "Finite element methods for junctions of microwave and optical waveguides," *IEEE Trans. Magn.*, vol. 26, no. 5, pp. 1754–1758, September 1990.

[5] J.-F. Lee, D.-K. Sun, and Z. J. Cendes, "Full-wave analysis of dielectric waveguides using tangential vector finite elements," *IEEE Trans. Microwave Theory Tech.*, vol. 39, no. 8, pp. 1262–1271, August 1991.

[6] M. Salazar-Palma, T. K. Sarkar, L.-E. García-Castillo, T. Roy, and A. Djordjević, *Iterative and Self-Adaptive Finite-Elements in Electromagnetic Modeling*. Boston: Artech House, 1998.

[7] J. P. Webb, "Edge elements and what they can do for you," *IEEE Trans. Magn.*, vol. 29, no. 2, pp. 1460–1465, March 1993.

[8] G. Mur, "Edge elements, their advantages and their disadvantages," *IEEE Trans. Magn.*, vol. 30, no. 5, pp. 3552–3557, March 1994.

[9] A. F. Peterson and D. R. Wilton, "Curl-conforming mixed-order edge elements for discretizing the 2D and 3D vector Helmholtz equation," in *Finite Element Software for Microwave Engineering*, T. Itoh, G. Pelosi, and P. P. Silvester, Eds. New York: John Wiley and Sons, 1996, pp. 101–125.

[10] M. M. Botha and D. B. Davidson, "An explicit a posteriori error indicator for electromagnetic, finite element-boundary integral analysis," *IEEE Trans. Antennas Propagat.*, vol. 53, no. 11, pp. 3717–3725, November 2005.

[11] M. M. Botha, "Efficient finite element electromagnetic analysis of antennas and microwave devices: the FE-BI-FMM formulation and a posteriori error estimation for $p$ adaptive analysis," Ph.D. dissertation, University of Stellenbosch, Stellenbosch, South Africa, December 2002.
[12] M. Ainsworth and J. T. Oden, "A posteriori error estimation in finite element analysis," *Computer Meth. in Appl. Mech. and Eng*, vol. 142, pp. 1–88, 1997.
[13] S. Polstyanko and J.-F. Lee, "Adaptive finite element electrostatic solver," *IEEE Trans. Magn.*, vol. 37, no. 5, pp. 3120–3124, September 2001.
[14] J. R. Stewart and T. J. R. Hughes, "A tutorial in elementary finite element error analysis: A systematic presentation of a priori and a posteriori error estimates," *Computer Meth. in Appl. Mech. and Eng*, vol. 158, pp. 1–22, 1998.
[15] P. Monk, "A posteriori error indicators for Maxwell's equations," *Jnl of Comp. and Appl. Math.*, vol. 100, pp. 173–190, 1998.
[16] K. K. Mei, "Unimoment Method for Electromagnetic Wave Scattering," *Journal of Electromagnetic Waves and Applications*, vol. 1, no. 3, pp. 201–222, 1987.
[17] S. Ramo, J. R. Whinnery, and T. van Duzer, *Fields and Waves in Communication Electronics*, 3rd ed. John Wiley and Sons, 1994.
[18] J. C. Nédélec, "Mixed finite elements in $\Re^3$," *Numerische Mathematik*, vol. 35, pp. 315–341, 1980.
[19] J. S. Savage, "Comparing high order vector basis functions," in *Proceedings of the 14th Annual Review of Progress in Applied Computational Electromagnetics*, March 1998, pp. 742–749, monterey, CA.
[20] P. G. Ciarlet, *The finite element method for elliptic problems*, ser. Studies in mathematics and its applications 4. Amsterdam: North-Holland, 1978.
[21] E. Kreyszig, *Introductory Functional Analysis with Applications*. New York: John Wiley and Sons, 1978.
[22] N. Marcuvitz, *Waveguide Handbook*. Peter Peregrinus, on behalf of IEE, 1986, originally published 1951.
[23] H. A. Haus and J. R. Melcher, *Electromagnetic Fields and Energy*. Englewood Cliffs, New Jersey: Prentice-Hall, 1989.
[24] D. B. Davidson, "An evaluation of mixed-order versus full-order vector finite elements," *IEEE Trans. Antennas Propagat.*, vol. 51, no. 9, pp. 2430–2441, Sept. 2003.
[25] M. M. Botha and D. B. Davidson, "A quasi-static condition for enhancing $p$-adaptive, mixed-order element, FE analysis," *Electromagnetics*, vol. 24, no. 1–2, pp. 13–24, January–March 2004.
[26] M. M. Botha and J.-M. Jin, "Adaptive finite element-boundary integral analysis for electromagnetic fields in 3-D," *IEEE Trans. Antennas Propagat.*, vol. 53, no. 5, pp. 1710–1720, May 2005.

**Matthys M. Botha** Matthys M. Botha was born in Stellenbosch, South Africa, 1976. He received the B.Eng. degree (cum laude) in 1998, in electrical and electronic engineering, and the Ph.D. degree in 2002; both from the University of Stellenbosch, Stellenbosch, South Africa. In January 2003, he joined the Center for Computational Electromagnetics, University of Illinois at Urbana-Champaign as a post-doctoral research associate, until September 2004, when he took up his present position as post-doctoral research fellow at the University of Stellenbosch. His primary research interest is in computational electromagnetics, with current focus on finite element and boundary element methods. He is a member of the IEEE.

**David B. Davidson** David Bruce Davidson was born in London, U.K., 1961. He received the B.Eng, B.Eng (Hons), and M.Eng degrees (all cum laude) from the University of Pretoria, South Africa, in 1982, 1983 and 1986 respectively, and the Ph.D. degree from the University of Stellenbosch, South Africa, in 1991.

Following national service (1984-5) in the then South African Defence Force, he was with the Council for Scientific and Industrial Research, Pretoria, South Africa, prior to joining the University of Stellenbosch in 1988. He is presently a Professor there. He was a Visiting Scholar at the University of Arizona in 1993, a Visiting Fellow at Trinity College, Cambridge University, England in 1997, and a Guest Professor at the IRCTR, Delft University of Technology, the Netherlands, in 2003.

He main research interest is computational electromagnetics (CEM), and he has published extensively on this topic. He is presently joint editor of the "EM Programmer's Notebook" column of the IEEE Antennas and Propagation Magazine. His first book, "Computational Electromagnetics for RF and Microwave Engineering", has been published by Cambridge University Press in 2005.

He is a member of the IEEE, ACES and SAIEE and is past chairman of the IEEE AP/MTT Chapter of South Africa. He is a recipient of the (South African) FRD (now NRF) President's Award.

# Multiscale Analysis of Panel Gaps in a Large Parabolic Reflector

Nader Farahat* and Raj Mittra**
*Polytechnic University of Puerto Rico
P.O. box 192017 San Juan, PR 00919
**The Pennsylvania State University, 319 EE East
University Park, PA, 16802, USA

**Abstract**

The effect of the gaps between the panels of a reflector, used as a radio-telescope, is analyzed in this paper via the multiscale and array factor approach. Initially, the simulation is carried out by numerical integration as well as the Finite Difference Time Domain (FDTD) Method for a reflector with a moderately large diameter, and the results are then scaled for the actual size, which is thousands of wavelengths in diameter in the frequency range of interest. The array factor concept is employed to demonstrate the fact that the grating lobe cannot arise for the typical gap size of the reflector.

**Multiscale approach**

We investigate a large reflector antenna, which is a 120 ft (36.57 m) diameter radio-telescope, originally designed for operation up to 10 GHz, but now being considered for application at higher frequencies. However, in higher frequencies the quasi-periodic structure of the gaps in the reflector might cause grating lobes in the far-field pattern. The gaps consist of the hollow rings and strips dividing the panels similar to the Fig. 1. The width of the gaps is one wavelength (in the frequency of interest) whereas the length of the panels is in order of 1000 wavelengths. The diameter of the main parabolic reflector is on the order of 10,000 wavelengths, which makes it impractical for the direct numerical simulation. Therefore we use a multiscale approach to study the grating lobes.

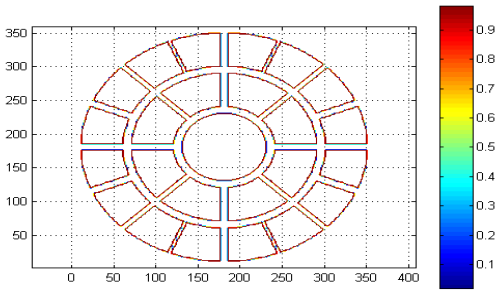


Fig.1. Illustration of circular reflector (diameter 34 lambda); panels (5 lambda) and gap width 1 lambda; x and y axes show the cell numbers.

To estimate the level of the grating lobes, first we compute the far-field pattern due to the circular aperture of 34 wavelength diameter with the gaps of one wavelength (where the surface current is set to zero in the shadow of the gaps in the aperture) between the 5-wavelength long panels shown in Fig. 1. In this approach (shadowing) the assumption is that the current is uniformly distributed on the panels. The H- and E-plane far-filed patterns of the circular aperture (solid panel) vs. slotted (with panels) are shown in Figs. 2 and 3, respectively. It is seen that the first grating lobe arises around 10 degrees.

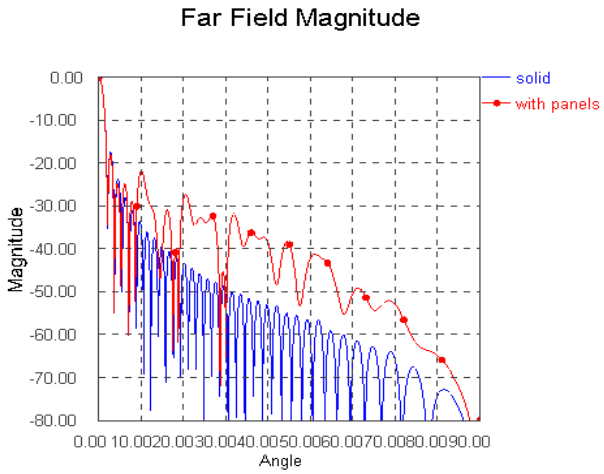


Fig.2. H-plane far-field pattern of circular aperture with and without panels with diameter of 34 lambda (shadowing approach).

In the next step to validate the shadowing approach we compute the scattered far-field of the same size flat circular reflector with and without the gaps, illuminated by a normally incident plane wave using the Finite Difference Time Domain (FDTD) Method [1]. The scattered-field formulation of the FDTD Method is used to simulate the flat reflector [2]. The normally incident wave is analytically introduced everywhere in the computational domain particularly on the surface of the perfect electric conductor of the reflector. Next the scattered field is computed throughout the domain by setting the tangential components of scattered electric fields to

negative of those of incident field on the surface of the reflector. Upon the completion of the simulation the equivalent surface currents at the frequency of interest on the Huygens box surrounding the reflector, which was stored throughout the simulation is used to compute the scattered far-field pattern via the near-to-far-field transformation.

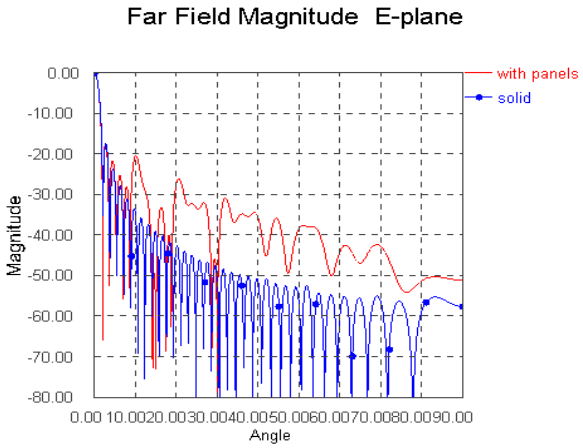


Fig.3. E-plane far-field pattern of circular aperture with and without panels with diameter of 34 lambda (shadowing approach).

The comparison of the patterns for the solid panels in both H- and E-planes using the two methods, presented in Figs. 4 and 5, respectively, shows that the difference is limited to the far-end lobes. This is due to the fact that in the shadowing approach the edge diffraction is ignored. The same comparison is shown in Figs. 6 and 7 for the slotted case using these two methods. Once again, the difference is limited to the far-end lobes. One can conclude that the diffraction effect due to the gaps is insignificant and that the shadowing approach predicts the level of the grating lobes adequately.

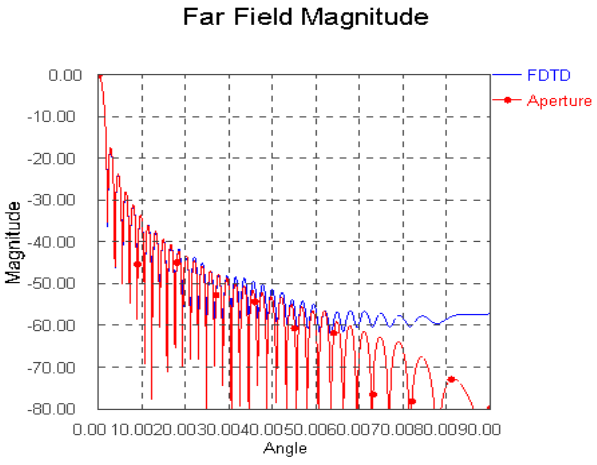


Fig.4. H-plane far-field pattern of solid circular disc with diameter of 34 lambda.

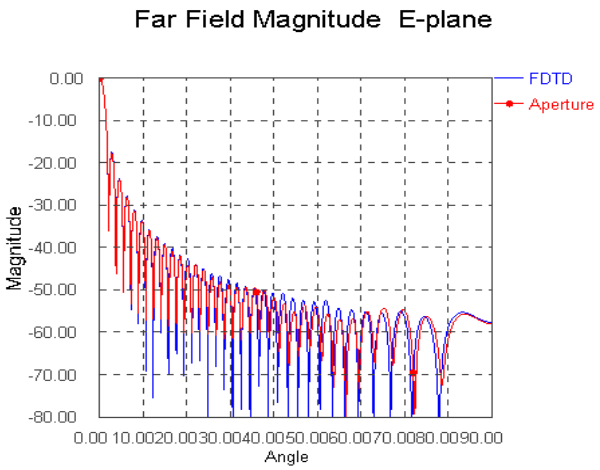


Fig.5. E-plane far-field pattern of solid circular disc with diameter of 34 lambda.

Based on the above simulation we can predict the pattern of the slotted reflector simply by arraying the panels with uniform current distributions. The grating lobes level and the locations depend on the length of each element and the inter-element separation. Consequently, we use the array factor concept to predict the performance of the slotted reflector. For simplicity we consider only the linear array of panels.

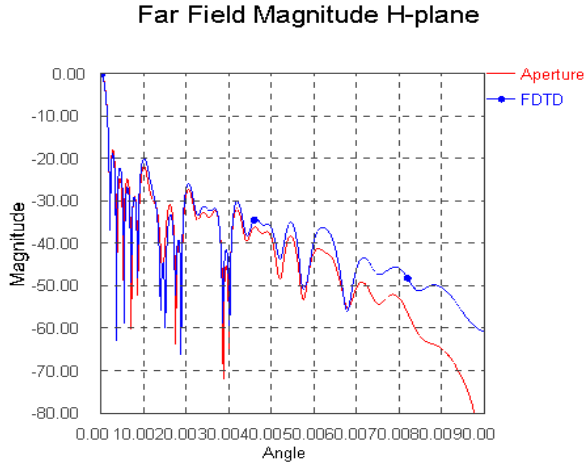


Fig.6. H-plane far-field pattern of circular reflector with diameter of 34 lambda with panels.

In the linear array of panels the grating lobe levels and locations depend on a, the length of each element and d, the inter-element separation, as shown in Fig. 8. At first we assume a linear array of 5 panels with a = 5λ, and d = 6λ (therefore the gap between the panels is g = λ). The pattern of the single element,

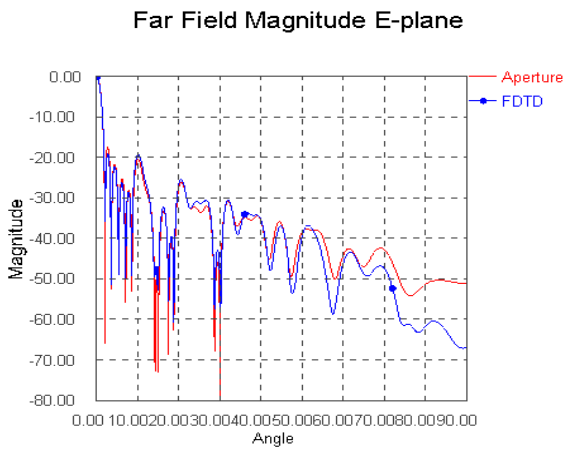


Fig.7. E-plane far-field pattern of circular reflector with diameter of 34 lambda with panels.

On the other hand, the array factor expression is given by [3] $AF = \dfrac{\sin(kNd\sin\theta/2)}{\sin(kd\sin\theta/2)}$, which has the first peak when $kd\sin\theta/2 = \pi$ hence $\theta_p = \sin^{-1}(1/d_\lambda) = \sin^{-1}(1/(a_\lambda + g_\lambda))$, where $a_\lambda$ and $g_\lambda$ are the electrical dimensions of the panel and gap respectively.

By comparing the expressions for the $\theta_p$ and $\theta_n$, one can see that as long as the gap size is small compared to the length of the panel, the difference between these angles is insignificant. This is shown in Fig.10 for the array of 11 panels, with a length of 1170λ and a gap of λ. The difference between the two patterns is seen to be insignificant, for the reason given above.

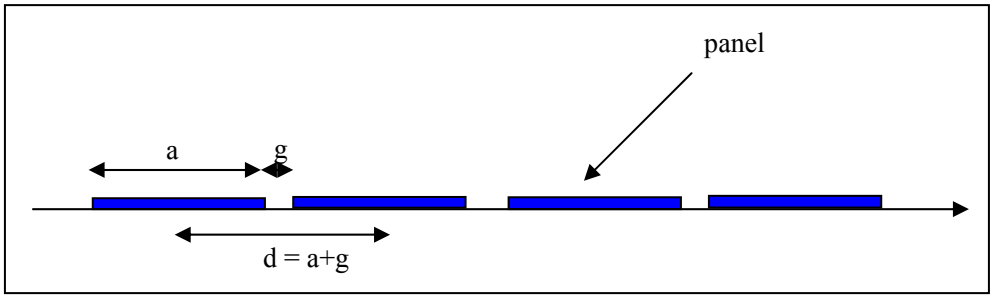


Fig.8. Illustration of linear array of N panels with length a and spacing d.

array factor, and pattern multiplication is shown in Fig. 9. The pattern multiplication is also compared by the pattern of the solid panels (a = 6λ, d = 6λ, and g = 0). The first grating lobe again shows up around 10 degrees (first peak angle $\theta_p$) where the array factor has the grating lobe. However, it can be shown as the inter-element spacing is decreased (in other words when the gap becomes small compared to the panel size) the null of the single element pattern (first null angle $\theta_n$) moves closer to the grating lobe of the array factor, and this, in turn, reduces the difference between the patterns of the solid and slotted panels.

The individual panel far-field pattern has the Sinc function form $E = \dfrac{\sin(ka\sin\theta/2)}{ka\sin\theta/2}$ and the first null occurs when the argument of the Sinc function is equal to π and, therefore, where $a_\lambda$ is the electrical length of the panel.

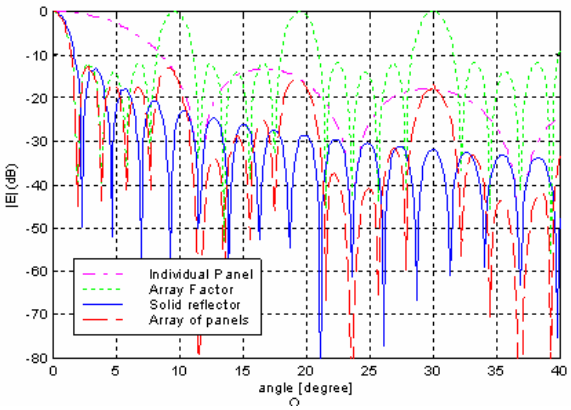


Fig.9. Far-field pattern of linear array of 5 panels (a = 5λ, d = 6λ, and g = λ).

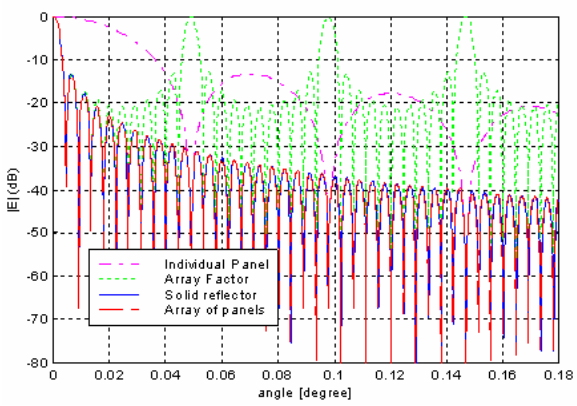


Fig.10. Far-field pattern of linear array of 11 panels (a = 1170λ, and g = λ).

**References:**

[1] K. S. Yee, "Numerical solution of initial boundary value problems involving Maxwell's equations in isotropic media," IEEE Trans. Antennas and Propagat., vol. AP-14, pp. 302-307, May 1966.

[2] A. Taflove and S. C. Hagness, Computational Electromangeics: The Finite-Difference Time-Domain Method, 2nd ed. Boston, MA: Artech, pp. 224-227, 2000.

[3] "Antenna Theory, Analysis and Design", C. A. Balanis, Second Edition, John Wiley & Sons, Inc. pp. 582–583, 1982.

**Nader Farahat** is Associate Professor in the Electrical Engineering Department of Polytechnic University of Puerto Rico. He is also adjunct research associate at Pennsylvania State University.

**Raj Mittra** is Professor in the Electrical Engineering Department of the Pennsylvania State University and the Director of the Electromagnetic Communication Laboratory. He is also the President of RM Associates, which is a consulting organization that provides services to industrial and governmental organizations, both in the U. S. and abroad.

# Equalization of Numerically Calculated Element Patterns for Root-Based Direction Finding Algorithms

**Hossam A. Abdallah, Wasyl Wasylkiwskyj, Ivica Kopriva**
Department of Electrical and Computer Engineering,
The George Washington University
Washington DC 20052, USA

***Abstract:*** Root-based direction finding algorithms (DF) have several advantages over search-based DF algorithms. A key advantage is the fact that they do not require the array steering vector; this is because these algorithms presume equalized element radiation patterns. In this paper, the WIPL-D code is used in designing an array of rectangular probe-fed patch antennas with equalized radiation patterns for measuring the range and bearing of RF emitters in the PCS band (1900-1920 MHz). Direction of arrival (DoA) estimation results based on simulations and measured data are presented and used as a measure of element patterns deviation from equality.

## 1. INTRODUCTION

Direction finding (DF) algorithms for DoA estimation is a topic that has been studied thoroughly in the past few decades mainly by researchers in the signal processing and antenna theory communities. From signal processing point of view the focus has been on maximizing the number of DoAs that can be accurately estimated and at the same time reducing the computational cost involved in this work. Several algorithms exist and can be used to estimate the DoA of incident signal on an antenna structure [1]-[3]. DF algorithms are classified as either search-based or root-based. We refer to the former class as S-DF algorithms and to the later class as R-DF algorithms. R-DF algorithms have several advantages over S-DF algorithms. In addition to their less computation cost, where DoAs are calculated by finding the roots of a polynomial of certain order rather than going through intensive search in the whole angular domain, a key advantage of using R-DF algorithms is the fact that they do not require the array steering vector. This is because these algorithms presume equalized element patterns and their accuracy depends on how much the element patterns deviate from equality.

This paper investigates the design and performance analysis of antenna structures with equalized element patterns for R-DF algorithms. Adding a number of passive elements around the center active elements and terminating them using a suitable set of loads minimize the deviation of the element patterns of the center elements from equality [4]. Return loss and element patterns of two antenna structures comprised of a number of rectangular probe-fed patch antennas are calculated using the WIPL-D code [5]. The first structure consists of four elements and no passive elements. In the second structure three passive elements are added on both sides of the four active elements and were terminated in 50 Ω. DoA estimation results using the two antenna structures are compared with DoA estimated using measured data. The DoA accuracy is used as a measure of how much element patterns deviate from equality. The paper is organized into four sections. Following this introductory section, in section two return loss and element patterns calculated using WIPL-D are presented for the two antenna structures mentioned before. DoA estimation results using either WIPL calculated patterns or measured data are compared and presented in section three. Finally conclusions are provided in section four.

## 2. EQUALIZATION OF ELEMENT PATTERNS

As shown in figure (1), equalization of element patterns is done through adding a number of passive elements around the middle active elements. The top structure in figure (1) is for an array of 4-element of patch antennas with no passive elements. In the bottom structure 3 passive elements on each side of the active elements were used, respectively. We refer to the top and bottom structures as Array1 and Array2, respectively. Figure (2) (top) shows top and bottom view of a 4-element array of patch antennas modeled in WIPL. The dimensions of the patch, ground plane and coax were identical to those given in [6]. The inter-element spacing for Array1 and Array2 was kept fixed and equal to $\lambda/2$. The bottom and top views of the 10-element array of patches (Array2) are shown in figure (2) (bottom). The whole structure is modeled in the same way as with Array1 except that passive elements were terminated in 50 Ω.

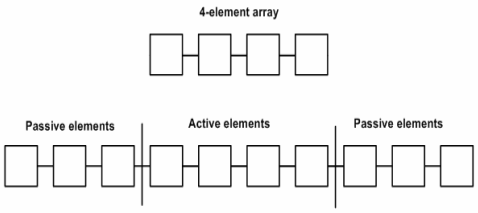


**Fig. 1.** 4-element array, top, and 10-element array with 3 passive elements on each side, bottom.

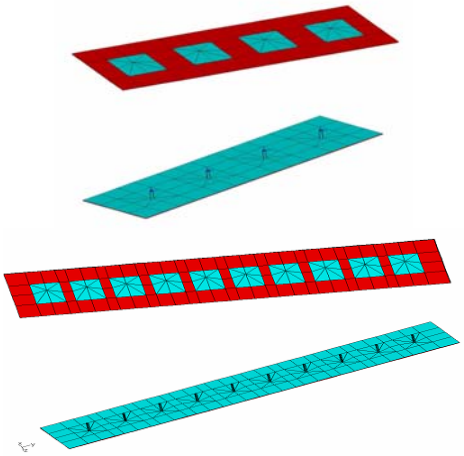

**Fig. 2.** A 4-element (top) and 10-element (bottom) array of patch antennas modeled in WIPL.

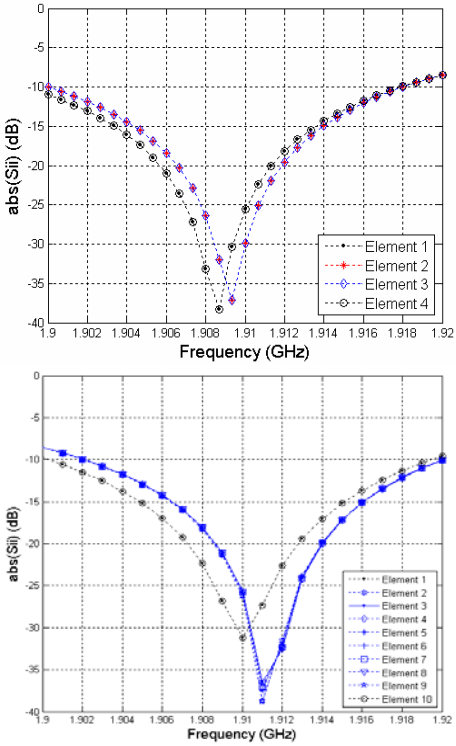


**Fig. 3.** Return loss of Array1 (top), Array2 (bottom).

The return loss in the (1.9-1.92) GHz frequency band of Array1 and Array2 calculated using the WIPL-D code and are shown in figure (3). For both arrays it is observed that the resonant frequency of each of the middle elements is tuned and shifted by 1MHz compared to the outer elements.

Element patterns of Array1 calculated at 1.91 GHz are presented in figure (4), for fixed φ and fixed θ, respectively. Results for Array2 are presented in figure (5). It is clear from the figures that the element patterns of the four elements significantly deviate from equality.

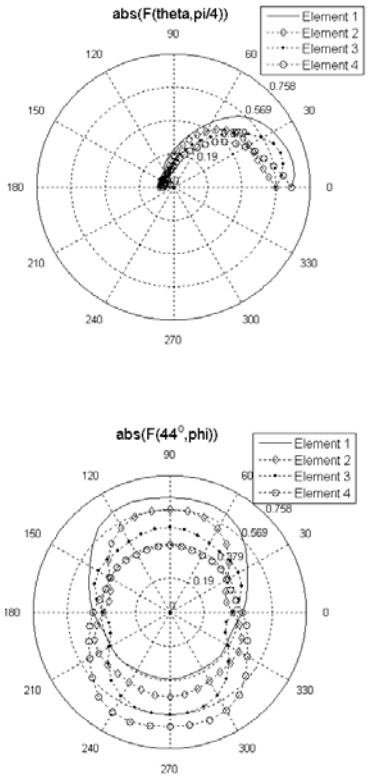


**Fig. 4.** Element patterns of array Array1 at φ=π/4 (top) and at θ=44° (bottom).

The accuracy of DoA estimation using the element patterns of Array1 and Array are presented in the following section and are compared to DoA results based on measured data with Array2.

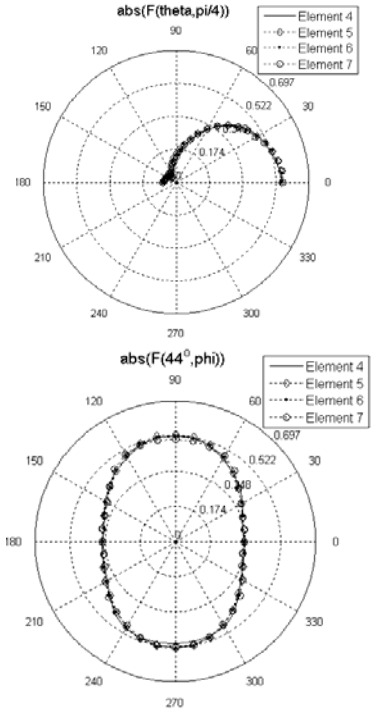


**Fig. 5.** Element patterns of the active 4 elements of Array2 at φ=π/4 and at θ=44° (bottom).

## 3. NARROWBAND ROOT-BASED DIRECTION FINDING ALGORITHMS

In this section accuracy of DoA estimation using the modified root-Pisarenko (MRP) [7] is analyzed. The analysis will be done for Array1 and Array2 and are compared to measured data collected from an antenna system consisting of Array2.

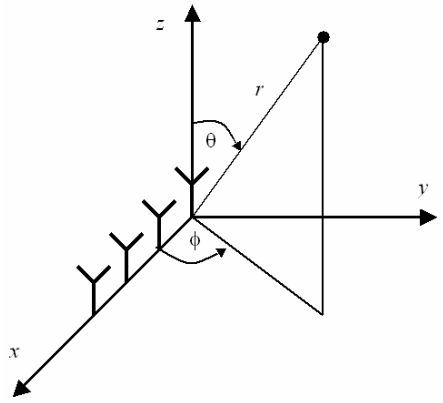


**Fig. 6**. Geometry of the antenna array.

Referring to figure (6), the narrowband signal model is assumed and is described with

$$\mathbf{z}(t) = \mathbf{A}\mathbf{s}(t) + \mathbf{v}(t) \qquad (1)$$

where **z**(t) is the output of the I-Q channels, **A** is the steering vector, **s** is the unknown source signal and **v** is vector of additive Gaussian noise. The number of antenna elements is N and the number of sources is L. Elements of the steering matrix are

$$A_{nm} = -\frac{i\lambda}{\sqrt{\zeta_0}} \hat{f}_n\left(\Omega_m\right) e^{i\mathbf{k}_m \cdot \mathbf{D}_n} \quad . \qquad (2)$$

In equation (2) $\hat{f}_n$ is n-th element pattern in the terminated array environment including mutual coupling effects. For uniformly spaced linear arrays along the x-axis, the steering vector is

$$\mathbf{a}\left(\theta,\varphi\right) \equiv -\frac{i\lambda}{\sqrt{\zeta_0}} \begin{bmatrix} \hat{f}_1(\theta,\varphi)\, \hat{f}_2(\theta,\varphi) e^{ikd\xi} ..... \\ \hat{f}_N(\theta,\varphi) e^{ik(N-1)d\xi} \end{bmatrix}^T \qquad (3)$$

where $\xi = \sin\theta\cos\varphi$ and d is the inter-element spacing. When element patterns are equalized the steering vector in equation (3) reduces to

$$\mathbf{a}\left(\theta,\varphi\right) \equiv -\frac{i\lambda}{\sqrt{\zeta_0}} \hat{f}\left(\theta,\varphi\right) \times \left[1\, e^{ikd\xi} \ldots e^{ik(N-1)d\xi}\right]^T . \qquad (4)$$

Table 1 summarizes results of DoA estimation using MRP algorithm and Uniform Linear Array (ULA) consisted of 4 active and 6 passive rectangular probe-fed patch antennas. The true position measured by transit is $19.18^0$. In DoA estimation from measured data one ULA with 6 passive and 4 active elements was used. The array was a part of the RF emitter range estimation system comprised of two antenna arrays. In DoA estimation from simulated data Array1 and Array2 configuration were used with element radiation patterns calculated numerically using the WIPL-D code [5]. ULA configuration with passive elements exhibited better DoA accuracy in both cases with measured and with simulated data.

**Table 1.** DoA estimated from simulations and measured data using Array1 and Array2.

| | |
|---|---|
| Estimated from measured data using Array2 | 19.86° |
| Estimated from simulation using Array2 | 20.25° |
| Estimated from simulation using Array1 | 21.61° |

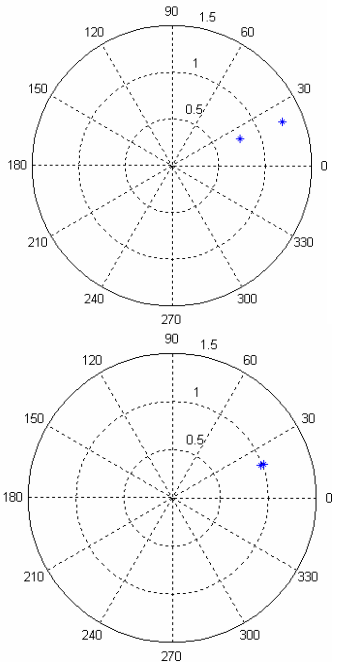


**Fig. 7.** DoA estimation roots using Array1 (top) and Array2 (bottom).

## 4. CONCLUDING REMARKS

An array of rectangular probe-fed patch antennas with equal radiation patterns for root-based direction finding algorithms was modeled using the WIPL-D code. Adding three passive elements on both sides of four active elements and terminating them in 50Ω sufficiently equalize patterns of the active elements. DoA estimation results using this array with equalized patterns shows the accuracy improvement when compared to array without passive elements. Finally, the DoA estimation results obtained from simulated data agree with DoA estimation results obtained from measured data.

## REFERENCES

[1] R.O. Schmidt, "A signal subspace approach to multiple emitter location and spectral estimation," Ph.D. Dissertation, Stanford University, 1981.

[2] V.F. Pisarenko, "The retrieval of harmonics from a covariance function," Gephys J. Royal Astron. Vol. 33, pp. 347-366, 1973.

[3] R.O. Roy, "SPRIT-Estimation of signal parameters via rotational invariance techniques," Ph.D. Dissertation, Stanford University, 1987.

[4] S. Lundgren, "A study of mutual coupling effects on direction finding performance of ESPRIT with a linear microstrip patch array using the method of moments," IEEE AP-S Symposium, pp. 1372-1375, July 1996.

[5] B. Kolundzija, J. S. Ognjanovic, and T. K. Sakar, WIPL-D: Electromagnetic Modeling of Composite Metallic and Dielectric Structures - Software and User's Manual, Artech House Inc., 2000.

[6] H. A. Abdallah, W. Wasylkiwskyj, K. Parikh, and A. Zaghloul, "Comparison of return loss calculations with measurements of narrow-band microstrip patch antennas," *ACES Journal*, vol. 19, no. 3, pp. 184-187, 2004.

[7] W. Wasylkiwskyj, I.Kopriva, M. Doroslovacki, and A. Zaghloul, "Performance evaluation of root based direction finding algorithms using hardware emulation of the antenna array," *submitted to Radio Science*.

**Hossam A. Abdallah** was born in Alexandria, Egypt, in 1973. He received his PhD in Electrical Engineering in May 2005 from the Department of Electrical and Computer Engineering, The George Washington University, Washington DC. His dissertation work and research activities are computational electromagnetics and array signal processing. Mr Abdallah received his Bachelor of Science degree in computer science in 1995 from Alexandria University, Alexandria, Egypt. In 2001 he received his MSc degree in Engineering Mathematics from Twente University, Enschede, The Netherlands. Mr. Abdallah is currently working as resolution enhancement techniques design engineer at Intel.

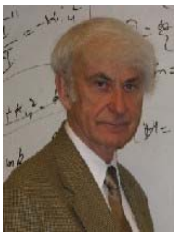

**Wasyl Wasylkiwskyj** (F'97) received his BEE degree from the City University of New York in 1957 and the MS and Ph.D. degrees in electrical engineering from the Polytechnic University in 1965 and 1968, respectively. His past research and industrial experience covers a broad spectrum of electromagnetics, including microwave components and techniques, phased array antennas, propagation and scattering, radar cross-section modeling as well as modeling of geophysical and oceanographic electromagnetic phenomena. In addition, he has extensive experience in ocean and structural acoustics with applications to active SONAR. Since 1985 Dr. Wasylkiwskyj has held the position of Professor of Engineering and Applied Science at the George Washington University, Washington, DC. His current research activities are primarily in numerical electromagnetics and array antennas for direction –of- arrival estimation.

**Ivica Kopriva** (M ’96, SM ‘04) received the B.S. degree in electrical engineering from Military Technical Faculty, Zagreb, Croatia in 1987, and M.S. and Ph.D. degrees in electrical engineering from the Faculty of Electrical Engineering and Computing, Zagreb, Croatia in 1990 and 1998, respectively. Currently, he is senior research scientist at the George Washington University, Department of Electrical and Computer Engineering. His current research activities are related to higher order statistics based array signal processing with the application on the direction finding problems and to independent component analysis and blind signal separation with application to unsupervised classification of medical and remotely sensed images.

# A STOCHASTIC ALGORITHM FOR THE EXTRACTION OF PARTIAL INDUCTANCES IN IC INTERCONNECT STRUCTURES

K. Chatterjee
Department of Electrical and Computer Engineering
The Cooper Union for the Advancement of Science and Art
New York, NY 10003-7120
Laboratory for Electromagnetic and Electronic Systems
Massachusetts Institute of Technology
Cambridge, MA 02139
Phone: (212) 353-4333
Fax: (212) 353-4341
Email: chatte@cooper.edu, kausik@mit.edu

## ABSTRACT

With recent increases in operating frequencies, the modeling and extraction of on-chip inductance is becoming an increasingly significant consideration. The inductance models include the "loop inductance" models and the "partial inductance" models. In this paper, we develop a stochastic solution methodology for the extraction of partial inductances in IC interconnect structures. An important advantage of this approach is that it requires no discretization meshing of either the volume or the surface of the problem domain. As a result, it has very low memory requirements compared to the more conventional deterministic techniques. Another advantage of this approach is that it is inherently parallelizable and a linear increase in speed is expected with the increase in the number of processors. Excellent agreement has been obtained with analytical benchmark solutions.

**Keywords:** IC Interconnect modeling, Partial Inductance, Stochastic algorithm, Monte Carlo.

## INTRODUCTION

As a consequence of scaling in sizes, the interconnect model used in the chip industry has undergone several changes. Presently, low resistance nets are described by purely capacitive models, while high resistance nets are described by relatively more accurate RC models. However, with operating frequencies reaching the multi-GHz range, the role of on-chip inductance is becoming increasingly important, as the inductive impedance is directly proportional to the frequency of operation. The inclusion of inductance in the interconnect model is particularly necessary in clock distribution networks, signal and power lines, which have wide wires and hence low resistance. The detrimental effects of inductive impedance on system performance include increase in signal delay times and signal overshoot which can cause breakdown of the gate-oxide layer. The introduction of low resistance copper interconnects has further increased the significance of inductance in IC design and accurate modeling and extraction of inductance is necessary.

The principal complexity in the extraction of inductance is that one needs to have the knowledge of currents in advance. However, the current distribution in today's complicated interconnect structures depends on the device and interconnect resistances, inductances and capacitances. Therefore, the modeling of the current distribution is a difficult proposition. The conventional approaches to inductance extraction involve loop inductance models [1], which make various simplifying assumptions in determining the current distribution. In these loop inductance models, typically the capacitive effects are omitted during resistance and inductance extraction. A RLC model is then constructed by adding lumped or distributed interconnect capacitance to the extracted resistance and inductance.

A radically different approach [2] to the modeling of inductance has been suggested in literature, which precludes the need to determine the current distribution in advance. This approach is based on the Partial Element Equivalent Circuit (PEEC) [3] method. In this approach, the interconnect lines are divided into wire segments and self and mutual inductances are extracted for these "partial elements". These extracted inductances are then glued together

with various resistances and capacitances to form an effective RLC circuit model. It has been demonstrated [2] that this PEEC-based approach is more accurate than the loop inductance models in that the latter overestimates the signal delay time and the undershoot. The primary reason behind this lies in the fact the PEEC-based models take into account the mutual inductances between the different "partial elements" of a particular loop, while the loop inductance models take into account only the mutual inductance between different loops. The subject of this paper is a stochastic extraction of the self and mutual inductance of these partial elements.

IC interconnect structures are rectilinear in nature. At low frequencies, when the wire segments are parallel to each other, exact analytical expressions [4] exist for the self and mutual inductances of the wire segments, assuming uniform current distribution across the wire cross sections. However, there is absence of such expressions for arbitrary wire-geometry, and even in the case of parallel rectangular wire segments, these analytical expressions for mutual inductance are numerically unstable for wire segments separated by a large distance.

In this work, we develop a novel stochastic algorithm [5] for the extraction of the self and mutual partial inductances. This algorithm is characterized by the absence of discretization meshing of either the volume or the surface of the problem domain. Hence, for today's complicated interconnect structures, the memory requirements are expected to be significantly less than discretization based algorithms. Another advantage of this proposed stochastic algorithm is that it should be completely parallelizable and the speed of computation is expected to increase linearly with the increase in the number of processors. The fundamentals of the algorithm were briefly presented in Ref. [6], along with its applications to frequency-independent inductance extraction. In this work, we present the details of the algorithm, along with its applications to both frequency-independent and frequency-dependent problems.

## INTEGRAL FORMULATION FOR INDUCTANCE

The most general formulation [7] for self and mutual inductance in conductor systems follows from a definition of inductance based on magnetic energy. The magnetic energy stored in a two-conductor system, where the two conductors are designated as *i* and *j* is given as

$$W = \frac{1}{2} L_i I_i^2 + \frac{1}{2} L_j I_j^2 + M_{ij} I_i I_j . \qquad (1)$$

Above, $W$ represents the magnetic energy stored in the two-conductor system; $L_i$ and $L_j$ represent the self-inductances of the *i*-th and the *j*-th conductor; $I_i$ and $I_j$ represent the respective currents, while $M_{ij}$ represents the mutual inductance between the conductors. The total magnetic energy can also be written in an integral formulation involving the current densities in the two conductors and equating that to the expression for current density in equation (1), the following expressions for self and mutual inductances are obtained [7]:

$$\begin{aligned} L_i &= \frac{\mu_o}{4\pi I_i^2} \int_{v_i} d^3 x_i \int_{v_i} d^3 x_i' \frac{\mathbf{J}(\mathbf{x_i}) \cdot \mathbf{J}(\mathbf{x_i'})}{\left| \mathbf{x_i} - \mathbf{x_i'} \right|}, \\ M_{ij} &= \frac{\mu_o}{4\pi I_i I_j} \int_{v_i} d^3 x_i \int_{v_j} d^3 x_j \frac{\mathbf{J}(\mathbf{x_i}) \cdot \mathbf{J}(\mathbf{x_j})}{\left| \mathbf{x_i} - \mathbf{x_j} \right|}. \end{aligned} \qquad (2)$$

Above, the self inductance is formulated as a six-dimensional integral over the position coordinates of the *i*-th conductor, while the mutual inductance is formulated as a six-dimensional integral over the position coordinates over the *i*-th and the *j*-th conductor; **x,** $v$, **J** with an appropriate suffix represent the position coordinate, volume and current density; $d^3 x$ with an appropriate suffix represents an infinitesimally small volume element and $\mu_0$ is the magnetic permeability of free space.

The current density **J**, is given as a solution of Maxwell-Helmholtz equation [8] and in the frequency-domain is written as

$$\nabla^2 \mathbf{J} - \gamma^2 \mathbf{J} = \mathbf{0}, \qquad (3)$$

where, $\gamma$ is the propagation constant of the medium given by $\gamma^2 = -\mu\varepsilon\omega^2 + i\mu\sigma\omega$; $\mu, \varepsilon, \sigma$ and $\omega$ are the permeability, permittivity, conductivity and frequency respectively. The current density, $\mathbf{J}(\mathbf{r})$ at a given point **r**, subject to appropriate Dirichlet boundary conditions, can be written as a surface integral over the surface of the problem domain [9]:

$$\mathbf{J}(\mathbf{r}) = \oint \mathbf{J}(\mathbf{r}')\left[\nabla_{\mathbf{r}'} G(\mathbf{r},\mathbf{r}')\cdot\hat{\mathbf{n}}\right] ds'. \qquad (4)$$

Above, $G(\mathbf{r},\mathbf{r}')$ represents the volumetric Green's function to equation (3), and is a solution to equation [9]

$$\nabla^2 G(\mathbf{r},\mathbf{r}') - \gamma^2 G(\mathbf{r},\mathbf{r}') = \delta(\mathbf{r}-\mathbf{r}'). \qquad (5)$$

Above $\delta(\mathbf{r}-\mathbf{r}')$ is a dirac-delta function centered at $\mathbf{r}'$ and homogeneous Dirichlet boundary conditions are imposed in calculating the volumetric Green's function. The integral formulation given in (4) can be substituted in equation (2) for the calculation of self and mutual inductances. As a result, the task of inductance extraction involves evaluating a multi-dimensional integral, which in this work has been done stochastically. At low frequencies, the current densities in equation (2) can be assumed to be constant. Hence the stochastic evaluation of self and mutual inductances is in effect a Monte Carlo integration [10] of the integrals given in equation (2) over the position coordinates of the respective conductors. We will now describe briefly the fundamentals of the Monte Carlo integration technique used in this work, known as the Sample Mean Monte Carlo [10].

Let us consider a function $f(x)$ defined over the interval $a \le x \le b$. Our desire is to estimate the integral

$$\mathbf{I} = \int_a^b dx f(x). \qquad (6)$$

In the event, the integral is improper, absolute convergence [11] is assumed. We select an arbitrary probability density function $p(x)$. A random variable $\xi$ is defined corresponding to a probability density function $p(x)$. We now introduce another random variable $\kappa$ defined as

$$\kappa = \frac{f(\xi)}{p(\xi)}. \qquad (7)$$

Then, the expectation value of the random variable $\kappa$, written as $M(\kappa)$, is an estimate of the integral $\mathbf{I}$, which can be rewritten as

$$\mathbf{I} = M(\kappa) = \int_a^b dx \left[\frac{f(x)}{p(x)}\right] p(x). \qquad (8)$$

The integral can be evaluated by sampling the quantity $f(x)/p(x)$ within box brackets according to the probability density function $p(x)$ with the help of a random-number generator [12] and averaging over a statistically large number of such samples. It can be noted that the Monte Carlo integration technique is ideally adapted to the estimation of multi-dimensional integrals such as the ones in equation (2), as only the integrand needs to be sampled irrespective of the dimensionality of the integral. Also, the integration technique is inherently parallelizable, as the stochastically independent samples can be sampled in different processors with very little inter-processor communication.

For the extraction of frequency-dependent inductance, an expression for the volumetric Green's function to the Helmholtz equation in (3) needs to be obtained in heterogeneous problem domains. However, there is an absence of an analytical expression for the volumetric Green's function in materials of arbitrary heterogeneity. Keeping that in mind, we have developed an approximate expression for the solution of equation (5) based on iterative perturbation theory. The details of this work have been published [13, 14] and we will discuss it briefly within the context of two-dimensional problems.

The Green's function $G(\mathbf{r},\mathbf{r}')$ is estimated over a circular problem domain and is assumed to be zero on the boundary of the circular domain, as the frequency-dependent problem studied in this work is a Dirichlet problem.

Let us define the zeroth-order approximation $G^{(0)}$ for $G$, subject to Dirichlet boundary conditions. Therefore,

$$\nabla^2 G^{(0)} = \delta(\mathbf{r}-\mathbf{r_o}). \qquad (9)$$

Above, $\mathbf{r}(\rho, \theta)$ is the point where the zeroth-order approximation is calculated given a delta function centered at $\mathbf{r_o}(\rho_o, \theta_o)$. Using (5) for iteration, we can then generate a first-order approximation $G^{(1)}$ in terms of $G^{(0)}$:

$$\nabla^2 G^{(1)} = \delta(\mathbf{r}-\mathbf{r_o}) + \gamma^2 G^{(0)}. \qquad (10)$$

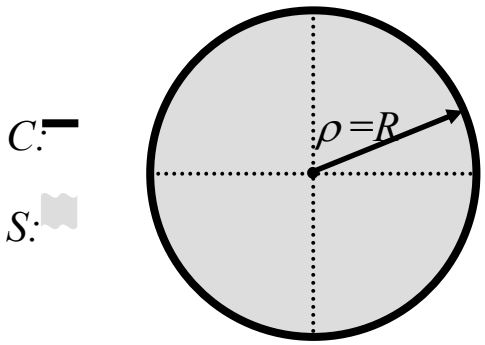


Figure 1. A circle of arbitrary radius $R$ over which the Green's function given by the solution of equation (5) is estimated.

The solution to Poisson equation (9) is well known; it has the form, in polar coordinates [9]

$$G^{(0)} = \frac{1}{4\pi}\ln\left[R^2\,\frac{A}{B}\right],$$
$$A = \rho^2 + \rho_o^2 - 2\rho\rho_o\cos(\theta-\theta_o), \quad (11)$$
$$B = \rho^2\rho_o^2 + R^4 - 2\rho\rho_o R^2\cos(\theta-\theta_o).$$

Now, we are in a position to evaluate $G^{(1)}$ from equation (10). Using the expression for $G^{(0)}$ from equation (11) and with the right hand side of equation (10) as the Poisson source term, we find an expression for the first-order approximation to the solution of equation (5) given by

$$G^{(1)}(\mathbf{r}\,|\,\mathbf{r_o}) = \iint_S d^2 r_S G^{(0)}(\mathbf{r}\,|\,\mathbf{r}_S)$$
$$\left[\delta(\mathbf{r}_S-\mathbf{r_o}) + \gamma^2(\mathbf{r}_S)G^{(0)}(\mathbf{r}_S\,|\,\mathbf{r_o})\right] \quad (12)$$
$$= G^{(0)}(\mathbf{r}\,|\,\mathbf{r_o}) +$$
$$\iint_S d^2 r_S\,\gamma^2(\mathbf{r}_S)\,G^{(0)}(\mathbf{r}\,|\,\mathbf{r}_S)G^{(0)}(\mathbf{r}_S\,|\,\mathbf{r_o}).$$

Note that $G^{(1)}$ given by equation (12), is an approximate expression for $G$ as given by the solution of equation (5). The integration variable in equation (12) represents an infinitesimal area element on the circular-domain surface $S$ in Fig. 1. It can be noted that homogeneous Dirichlet conditions are satisfied by the approximate Green's function expression in Eq. (12).

We next use this approximate Green's function $G^{(1)}$ to develop a general solution to equation (3) within our circular domain in Fig. 1. In our problem, the two-dimensional problem domain is in $x$-$y$ plane, and a time-harmonic current at a given frequency is impressed in the $z$-direction. Based on [9] and equations (4) and (12), the current density at the center of the circular domain is given by a line integral about the domain circumference $C$ as

$$J_z(\text{center}) \approx \int_0^{2\pi} d\theta\, J_z(R,\theta)$$
$$\left[\frac{1}{2\pi} + \frac{1}{4\pi^2}\sum_q W_q(\theta)\right], \quad (13)$$

where

$$W_q(\theta) = \gamma_q^2\int_0^R d\eta\int_{(q-1)\pi/2}^{q\pi/2} d\xi\,\frac{C}{D},$$
$$C = \eta\ln(\eta/R)(R^2-\eta^2), \quad (14)$$
$$D = R^2+\eta^2-2R\eta\cos(\theta-\xi).$$

For simplicity, above, we take $\gamma^2$ to be piecewise constant with respective values $\gamma_q$ in $\theta$-quadrants $q$ = 1, 2, 3, and 4. The quantities within square brackets in equation (13) are 2D versions, respectively, of surface and volume Green's functions encountered in 3D problem domains. The function $W_q$ represents perturbative corrections arising from the $\gamma^2\mathbf{J}$ term in the original Maxwell-Helmholtz equation (3). In equations (13) and (14), $\eta$ and $\xi$ are variables of integration. $\eta$ takes values between 0 and $R$, while $\theta$ assumes values between $(q-1)\pi/2$ to $q\pi/2$ for a particular quadrant. Equations (13) and (14) constitute the starting point for defining a random-walk [13, 14] algorithm for solving (3) in 2D domains with arbitrary piecewise-constant spatial variation in $\gamma$, subject to arbitrary Dirichlet boundary conditions.

The total current, $I_z$, through the cross section can be calculated by integrating the current density given in equation (3) over the problem domain ($ds$ being an infinitesimal area unit) and can be written as

$$I_z = \iint_S ds\,J_z. \quad (15)$$

The integral expression for the current density from equation (13) is substituted in equation (15)

to obtain a multi-dimensional integral expression for total current through the conductor surface.

The internal impedance per unit length is defined as [8]

$$Z_i = \frac{E_z(dc\ value)}{I_z}. \tag{16}$$

At this point, the crucial thing to note is that for estimating frequency-dependent impedance, we need not estimate electric field or current density at any point within the problem domain. The problem of impedance extraction is reduced to estimating the overall multi-dimensional integral expression for current obtained from (15) using the floating random-walk method [13, 14] and then using (16) to evaluate the internal impedance per unit length. We will now discuss the details of the floating random-walk method.

The floating random-walk algorithm is a Monte Carlo evaluation of an infinite series of multi-dimensional integrals. In our chosen benchmark problem, a time-harmonic current density in the *z*-direction at a single frequency is impressed on a circular conductor in the *x*-*y* plane. Our goal is to calculate the current through the conductor as given by equation (15). The starting point of a random-walk is based on a pre-determined probability distribution.

The random-walks propagate as "hops" of different sizes from circle centers to circumferences, consistent with a statistical interpretation [13, 14] of equation (15). Maximally sized circles, subject to limitations imposed by iterative perturbation theory, are used with hop-location probability rules again consistent with equation (15).

We define, with each hop, a numerical weight factor derived from equation (15) in conjunction with equations (12), (13) and (14). The product of these weight factors over a walk, multiplied by the solution at the problem boundary—where the walk must terminate—gives a statistical estimate for $I_z$. We can thus obtain an accurate statistical estimate for $I_z$ by averaging over a statistically large number of random-walks. Mathematically, we can write such an estimate as

$$I_z \approx \frac{1}{N}\sum_{n=1}^{N} I_z^{(n)}, \tag{17}$$

where $N$ is the number of walks and $I^{(n)}$ is the contribution from the $n$th-walk. The error in the result has two components:

1) A deterministic error arising from the truncation of the iterative perturbation based Green's function in equation (12) and can be controlled by controlling the radius of the hop.

2) A statistical 1-σ error, $\sigma$, given by [15]

$$\sigma = \frac{\sigma_E}{\sqrt{N}}, \tag{18}$$

where $\sigma_E$ is the standard deviation of the estimates from different random-walks and $N$ is the number of random-walks. As a result, the statistical error can be controlled by controlling the number of random-walks.

It can be seen that computational resources need not be wasted in evaluating the currents or fields at any point in the problem domain. Instead one just needs to evaluate the multi-dimensional integrals given by equation (15). It can again be noted that similar to the situation of the frequency-independent problem, the approach is completely parallelizable, as the integrand can be sampled in different processors at the same time. We now give the details of the benchmark problems that have been handled in this work.

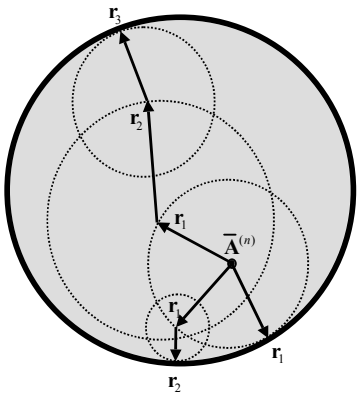


Figure 2. A schematic diagram of a circular cross section is shown. One-, two-, and three- hop random-walks are represented.

## RESULTS

*Frequency-independent benchmark problems:* The algorithm has been benchmarked against several mutual inductance extraction problems in one, two and three dimensions. The numerical

results have been matched with analytical solutions given in Ref. [4] and excellent agreement has been obtained. The results are given in Table 1 and the benchmark problem geometries are presented in Figures (3) to (7). In these benchmark problems, A = B = C = D = R = T = 5 μm and Q = S = U = V = 1 μm. For each of these problems, we have taken 5000 sample points and the error from the analytical solution has been restricted to a fraction of one percent in each case. The computational time for each one of these benchmark problems has been seen to be a fraction of a second in MATLAB 6.1 on a 1.8 GHz Intel Pentium IV personal computer. The exact and statistical errors are computed and they are seen to be in close agreement.

Table 1. Analytical and numerical results for the benchmark problems. Columns: A = Benchmark problems, B = Analytical results (pH), C = Numerical results (pH), D = Exact errors normalized to the analytical results, E = Statistical errors normalized to the analytical results.

| A | B | C | D | E |
|---|---|---|---|---|
| 1. | 0.35844 | 0.35859 | 0.0004 | 0.0005 |
| 2. | 0.28797 | 0.28830 | 0.0011 | 0.0010 |
| 3. | 0.28698 | 0.28630 | 0.0023 | 0.0025 |
| 4. | 0.21326 | 0.21323 | 0.0001 | 0.0002 |
| 5. | 0.28800 | 0.28878 | 0.0027 | 0.0024 |

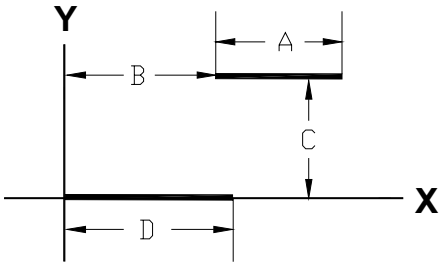


Figure 3. Two parallel filaments of negligible width and thickness. The current is in the *x*-direction.

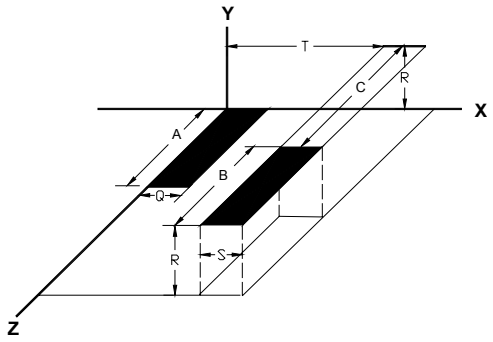


Figure 4. Two parallel tapes of negligible thickness. The current is in the *z*-direction.

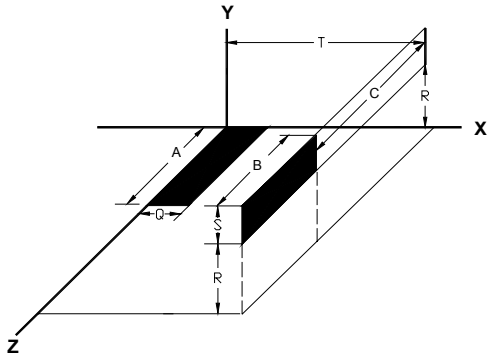


Figure 5. Two tapes of negligible thickness, whose axis are parallel and widths are perpendicular. The current is in the *z*-direction.

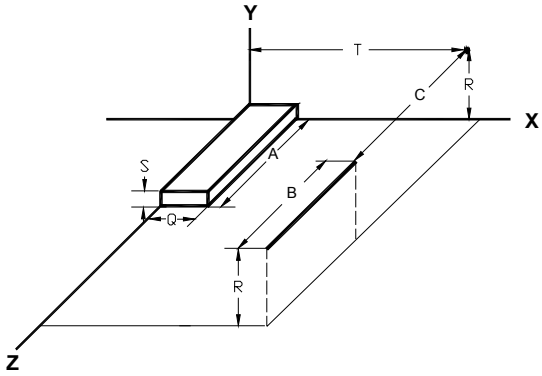


Figure 6. A thin filament of negligible width and thickness is placed parallel to a rectangular bar. The current is in the *z*-direction.

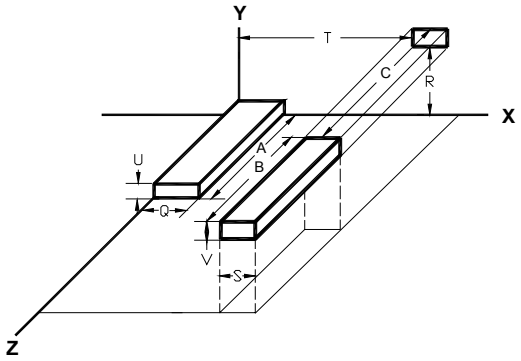


Figure 7. Two rectangular bars placed parallel to each other. The current is in the *z*-direction.

*Frequency-dependent benchmark problem:* For the frequency-dependent problem, a *z*-directed time-harmonic and spatially invariant current is impressed on a single circular conductor. The frequency-dependent impedance contains a resistive term and an inductive term. Table (2) shows the results for the frequency-dependent self impedance of a cross section of radius 1.0 $\mu$m at frequencies ranging from 1 GHz to 25 GHz. The resistivity for conducting material is given by $\rho = 1.8\,\mu\Omega - \mathrm{cm}$ and the magnetic permeability is assumed to be that of free space. For extracting impedance, a total of only 1000 random-walks were performed at each frequency. It can be seen from Table (2), that the error in the estimate of frequency-dependent resistance and inductive impedance is around 1 percent and the absolute error is comparable to the statistical error. The resistance and inductive impedances are plotted as a function of frequency in figures (8) and (9) respectively. As in the case of the frequency-independent problem, numerical computations have been performed in MatLab 6.1 on a 1.8 GHz Intel Pentium IV personal computer, and the computation time at 25 GHz frequency is of the order of a few seconds.

Table 2. Numerical results for the frequency-dependent self-impedance of a conducting circular cross section. Columns: A = Frequency (GHz), B = Skin depth as a fraction of radius, C = Analytical result (ohm/meter), D = Random-walk result (ohm/meter), E = Exact error (ohm/meter), F = Statistical error (ohm/meter).

| A | B | C | D | E | F |
|---|---|---|---|---|---|
| 1 | 2.14 | 5735+ 314i | 5738+ 312i | 3-2i | 1+1i |
| 5 | 0.96 | 5870+ 1552i | 5917+ 1534i | 47-18i | 40+1 5i |
| 10 | 0.68 | 6262+ 2997i | 6315+ 2962i | 53-35i | 55+3 0i |
| 15 | 0.55 | 6827+ 4268i | 6888+ 4225i | 61-43i | 59+4 1i |
| 20 | 0.48 | 7482+ 5347i | 7549+ 5297i | 67-50i | 70+4 5i |
| 25 | 0.43 | 8159+ 6252i | 8234+ 6193i | 75-59i | 72+5 1i |

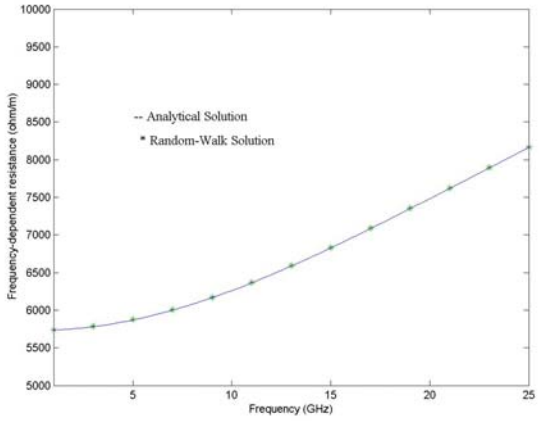


Figure 8. Frequency-dependent resistance per unit length for a conductor of 1 μm radius with a resistivity of $1.8\,\mu\Omega - \mathrm{cm}$ and magnetic permeability of free space.

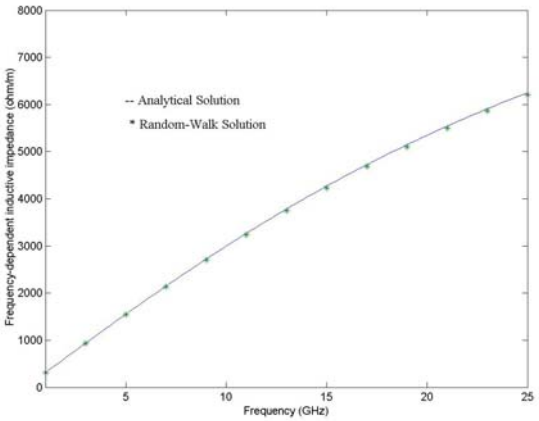


Figure 9. Frequency-dependent inductive impedance per unit length for a conductor of 1 μm radius with a resistivity of $1.8\mu\Omega-\text{cm}$ and magnetic permeability of free space.

## CONCLUSION & FUTURE WORK

Summarizing, a stochastic algorithm for the extraction of partial inductances in IC interconnect structures has been developed. The algorithm has been validated with the help of frequency-independent and frequency-dependent benchmarks. The extension of this algorithm to more complicated frequency-dependent benchmark problems will form the basis of future work. Stochastic solution of the PEEC-based RLC circuit matrix will also be emphasized. It is believed that with additional development, this algorithm can be developed into an IC CAD tool for inductance extraction.

## REFERENCES

[1] B. Krauter and S. Mehrotra, "Layout based frequency depended inductance and resistance extraction for on-chip interconnect timing analysis," *Proceedings Design Automation Conference*, pp. 303-308, June, 1998.

[2] K. Gala, D. Blauuw, V. Zolotov, P. Vaidya and A. Joshi, "Inductance model and analysis methodology for high-speed on-chip interconnect", *IEEE Transactions on Very Large-Scale Integration Systems*, Vol. 10, No. 6, pp. 730-745, December 2002.

[3] A. E. Ruehli, "Inductance calculations in a complex integrated circuit environment," *IBM Journal of Research and Development*, pp. 470-481, September 1972.

[4] C. Hoer and C. Love, "Exact inductance equations for rectangular conductors with applications to more complicated geometries," *Journal of Research of the National Bureau of Standards*, Vol. 69C, No. 2, pp. 127-137, April, 1965.

[5] See, for example, K. K. Sabelfeld, *Monte Carlo Methods in Boundary Value Problems*, Springer Verlag, 1991.

[6] K. Chatterjee, P. Matos and B. Hawkins, "A novel stochastic algorithm for the extraction of frequency-independent partial inductances in digital IC interconnect structures and a frequency-dependent generalization," 20th Annual Review of the Applied Computational Electromagnetics Society, Syracuse, NY, April 19-23, 2004.

[7] J. D. Jackson, *Classical Electrodynamics*, Third Edition, pp. 215-216, John Wiley & Sons, New York, NY, 1999.

[8] S. Ramo, J. R. Whinnery and T. van Duzer, *Fields and Waves in Communication Electronics*, Third Edition, pp. 180-181, John Wiley & Sons, New York, NY, 1993.

[9] R. Haberman, *Elementary Applied Partial Differential Equations*, Third Edition, pp. 411-413, Prentice Hall, Upper Saddle River, NJ, 1998.

[10] Ilya M. Sobol, *A Primer for the Monte Carlo Method*, CRC Press, Boca Raton, 1994.

[11] R. Courant and F. John, *Introduction to Calculus and Analysis, Volume 1*, Springer, 1999.

[12] J. Banks and J. Carson, *Discrete Event System Simulation*, Prentice Hall, pp. 257-288, 1984.

[13] K. Chatterjee, *Development of a Floating Random-Walk Algorithm for Solving Maxwell's Equations in Complex IC-Interconnect Structures*, Rensselaer Polytechnic Institute, May 2002, UMI Dissertation Services, 300 North Zeeb Road, P.O. Box 1346, Ann Arbor, Michigan 48106-1346, USA, UMI Number: 3045374, Web Address: www.il.proquest.com.

[14] K. Chatterjee, R.B. Iverson and Y.L. Le Coz, "Development of a Random-Walk Algorithm for IC-Interconnect Analysis: 2D TE Benchmarks, Materially Heterogeneous Domains," VLSI Multilevel Interconnection Conference, Santa Clara, CA, pp. 374-379, June 2000.

[15] J. M. Hammersley, D. C. Handscomb, Monte Carlo Methods, John Wiley & Sons, New York, NY, 1964, pp. 50-54.

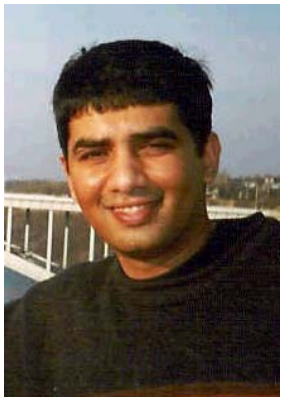

**Kausik Chatterjee** was born in India in 1969. In 1992, he received a Bachelor of Engineering degree in Electrical Engineering from Jadavpur University, Calcutta, India. Subsequently, in 1995, he received a Master of Technology degree in Nuclear Engineering from Indian Institute of Technology, Kanpur, India, and in 2002, he received his Ph.D degree in Electrical Engineering from Rensselaer Polytechnic Institute, Troy, New York. In 2002, he joined the faculty at California State University, Fresno as an Assistant Professor of Electrical and Computer Engineering, a position he held till 2005. He had been a visiting scientist at MIT Laboratory for Electromagnetic and Electronic Systems (2004-2005), a National Research Council Faculty Associate at Air Force Research Laboratory, Wright-Patterson Air Force Base (2004) and NASA, Langley Research Center (2005) and a Junior Engineer at Durgapur Steel Plant, India (1992-1993). He is currently an Assistant Professor in the Department of Electrical and Computer Engineering at Cooper Union and an Adjunct Scientist at the MIT Laboratory for Electromagnetic and Electronic Systems. His research interests include the development of stochastic algorithms for important deterministic equations in nature and a theory for high temperature superconductors.

# An Extrapolation Method Based on Current for Rapid Frequency and Angle Sweeps in Far-Field Calculation in an Integral Equation Algorithm[+]

C. C. Lu

Department of Electrical Engineering
University of Kentucky
Lexington, KY 40506
cclu@engr.uky.edu

***Abstract:*** An extrapolation method based on the solution of induce current is introduced to rapidly perform angle and frequency sweep in the far-field calculation using the sparsely sampled solutions. This method is based on the observation of the characteristics of the current distribution as a function of incident angles and frequency. It is easy to be implemented for in core processing, and needs a small extra memory. In addition, the extrapolation applies to both angle and frequency sweeps. Numerical examples for conducting and material scatterers show that the far-field scattering results generated by the extrapolation method agree to that provided by the direct solution, but the extrapolation method uses about the same amount of memory, and much less CPU time than that of the brute-force approach.

## I. Introduction

The algorithms based on the iterative solution of the integral equations and accelerated by fast solvers provide efficient and accurate ways to calculate the scattering by large and complex objects. The application of the fast solvers such as the multilevel fast multipole algorithm [1] has greatly reduced the computational complexity of a matrix vector multiplication for the iteration process. To further increase the efficiency in producing multi-angle and multi-frequency scattering data, attentions are focused on (a) developing precondition techniques to reduce the number of iterations for a converged solution, (b) developing advanced post processing methods which use the information of the existing solution to predict as much scattering data as possible. Several algorithms have been studied such as the frequency interpolation on current or scattered field, and the bi-static to mono-static approximation [2, 3, 5-10].

For frequency loop acceleration, a straight forward method is to perform interpolation using the scattered field samples that are obtained directly via a numerical solver. This method is simple in implementation, but it applies to densely sampled scattered field only, and has poor prediction accuracy if applied to frequencies outside the frequency samples. A more sophisticated algorithm exploits the characteristics of scattered field vs the frequency. Basically, it assumes that scattered field at a given frequency can be written as a series of exponentials. This method tries to estimate the expansion coefficients using a set of scattering field samples. Since only the field samples are used, it can be implemented out of core (i.e., it can be performed when all the field samples are available). This method can also be applied to the induced current. In this case, the induced current at target mesh samples must be saved for every frequency samples, leading to increased memory requirement and processing CPU time for in-core processing.

For angle loop acceleration, there are also similar methods as above. One of the popular and effective methods is the approximation of mono-static RCS using bi-static results. This method was originally applied to process the measurement RCS data where the exact mono-static configuration is difficult to realize.

In this paper, an approximate extrapolation method is introduced to rapidly fill the angular and frequency far-field points using the solutions at sparsely sampled points. This method is based on the characteristics of the induced current on the target surface. It assumes that the leading term of

[+] This work was supported in part by the Office of Naval Research under Award No. N00014-00-1-0605, and in part by National Science Foundation under award No. ECS-0093692.

the induced current at every surface depends on the frequency and incident angles via a complex exponential function. With this assumption, the solution at a fixed angle can be processed by replacing the angle dependency factor with a similar factor for the new incident angles. This process is called "normalization". One advantage of this method is that the normalization can be performed for angle variables as well as frequency. In the following, the exponential dependency is first verified from the point of view of the method of moment solution. Then numerical verification and application examples are provided. The time factor used in this paper is $\exp(-i\omega t)$ and is suppressed from the equations.

## II. Formulation

The following derivation is for a three-dimensional perfectly conducting scatterer. The procedure can also be applied to scatterers of dielectric material and material coating on conducting object. In fact, in Sec. 3, there is an example that shows the application of extrapolation to material coated object. Consider the discretization of the surface integral equation for a scattering problem by the method of moments. For simplicity, it is assumed that the target surface is divided into a set of patches, each of which has dimension of one tenth of a wavelength. The induced current on the target surface is represented by a set of $N$ basis functions. Each basis function $\vec{f}_n(\vec{r})$ is defined for an interior edge, which is shared by two patches. Following the standard MoM procedure with Galerkin testing scheme, a set of linear algebra equations is obtained as

$$\sum_n Z_{mn} a_n = V_m \tag{1}$$

where, $Z_{mn}$ is an impedance matrix element, $a_n$ is an expansion coefficient for basis function $\vec{f}_n(\vec{r})$, and $V_m$ is an element of excitation vector that is related to the excitation field $\vec{E}^{inc}$ (also called incident field) as

$$V_m = -\int_{S_m} \vec{f}_m(\vec{r}) \cdot \vec{E}^{inc}(\vec{r}) dS \,. \tag{2}$$

For a plane wave incidence at direction $\hat{k}^i$, $\vec{E}^{inc} = \vec{E}_0 \exp(i\vec{k}^i \cdot \vec{r})$, where $\vec{k}^i = k_0 \hat{k}^i$, and $k_0$ is the free-space wave number. Using a numerical quadrature rule to approximately evaluate (2) gives rise to

$$\begin{aligned} V_m &= \sum_q w_q \left[ -\vec{f}_m(\vec{r}_q) \right] \cdot \vec{E}_0 e^{i\vec{k}^i \cdot \vec{r}_q} \\ &= e^{i\vec{k}^i \cdot \vec{r}_m} \sum_q w_q \left[ -\vec{f}_m(\vec{r}_q) \right] \cdot \vec{E}_0 e^{i\vec{k}^i \cdot (\vec{r}_q - \vec{r}_m)} . \end{aligned}$$

In the above equation, $\vec{r}_m$ is the center position of basis-$m$, $w_q$ is the weighting coefficient, $\vec{r}_q$ is the quadrature point that lies inside the domain $s_m$ of basis-$m$. Since $|\vec{r}_q - \vec{r}_m|$ is at most of the size of the domain which is about two tenth of the wavelength, the factor $\exp(i\vec{k}^i \cdot (\vec{r}_q - \vec{r}_m))$ is a slow varying function of frequency and angle. Also, $\vec{E}_0$, $w_q$, and the test function $\vec{f}_m$ are not functions of angle and frequency. As a result, the excitation element $V_m$ can be written as

$$V_m = \tilde{V}_m e^{i\vec{k}^i \cdot \vec{r}_m} \tag{3}$$

where $\tilde{V}_m$ is a slow varying function of frequency and incident angle. If the system of equations in (1) is inverted symbolically and the right hand side in (3) is used to replace $V_m$ in (1), then the solution for the unknown expansion coefficient $a_n$ will be given by

$$\begin{aligned} a_n &= \sum_m [Z^{-1}]_{nm} \tilde{V}_m e^{i\vec{k}^i \cdot \vec{r}_m} \\ &= e^{i\vec{k}^i \cdot \vec{r}_n} \sum_m [Z^{-1}]_{nm} \tilde{V}_m e^{i\vec{k}^i \cdot (\vec{r}_m - \vec{r}_n)} \end{aligned} \tag{4}$$

where $[Z^{-1}]_{nm}$ is an element of the inverse impedance matrix. It is known that the impedance matrix elements are related to the 3D Green's function, hence it contains the factor of $\exp(ik_0|\vec{r}_m - \vec{r}_n|)$. As a result, if $\vec{r}_n$ is close to $\vec{r}_m$, it is a slow varying function of frequency (it is not a function of incident angles) compared to the factor of $\exp(i\hat{k}^i \cdot \vec{r}_n)$. For the exponential factor $\exp(i\vec{k}^i \cdot (\vec{r}_m - \vec{r}_n))$ in (4), it is also a slow varying function of frequency and angle if $\vec{r}_n$ is close to $\vec{r}_m$. If the two positions are far away, this factor becomes a rapidly varying function of frequency and angles. However, for most of the elements, the interaction becomes weaker when they are far from each other (there are exceptions that will be stated later in the numerical result sections). As a

result, it is concluded that

$$a_n = \tilde{a}_n e^{i\hat{k}^i \cdot \vec{r}_n}, \quad (5)$$

where $\tilde{a}_n$ is a slow varying function of frequency and angles for most of the elements. In the following, $\tilde{a}_n$ is called the normalized coefficient, and $a_n$ is the un-normalized coefficient. Based on this observation, the solution of the current coefficient for the same basis function for any near-by incident plane wave $\vec{k}_2^i$ can be approximated by $\tilde{a}_n \exp\{i(\vec{k}^i + \vec{\Delta}^i) \cdot \vec{r}_n\}$. In this expression, $\vec{\Delta}^i = \vec{k}_2^i - \vec{k}^i$ is small in magnitude, and it represents the small shift in frequency and angles from the previous plane wave with $\vec{k}^i$. Since the induced current at a point in a patch is a superposition of the basis functions that are associated with that patch, the current solution has the same expression as (4), i.e., $J(r) = \tilde{J}(\vec{r}) \exp(i\hat{k}^i \cdot \vec{r})$, where $\tilde{J}(\vec{r})$, a component of surface induced current, is a slow varying function of frequency and angle, but it is a function of position.

To demonstrate the above observations, consider a target that is made by five spheres that are uniformly placed on x-axis, each of which has radius of 0.3 m, as shown in Figure 1. The center distance between two neighbor spheres is 0.45 m. The spheres are discretized into 3,000 quadrilateral patches. The frequency of the incident plane wave is 1 GHz and is vertically polarized. Figure 2 shows the solution for basis number 1345 which is centered at (0,0.18,0). It can be seen that the normalized coefficient (dash lines) is indeed varying slowly with incident angle $\phi^i$ compared to the un-normalized version of the same coefficient (the solid lines). Because of this property of the normalized coefficient, it can be accurately represented by a linear interpolation for a large angular range.

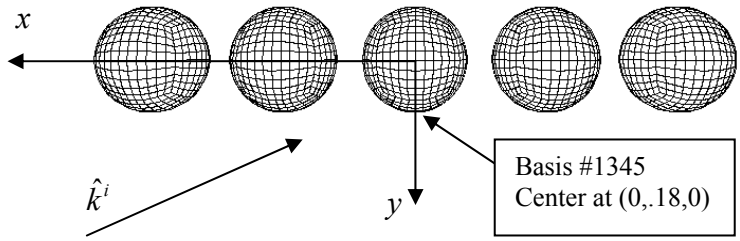


**Figure 1**. *Five conducting spheres on x-axis. Each sphere has radius 0.3m, and the center distance of two neighbor spheres is 0.45 m.*

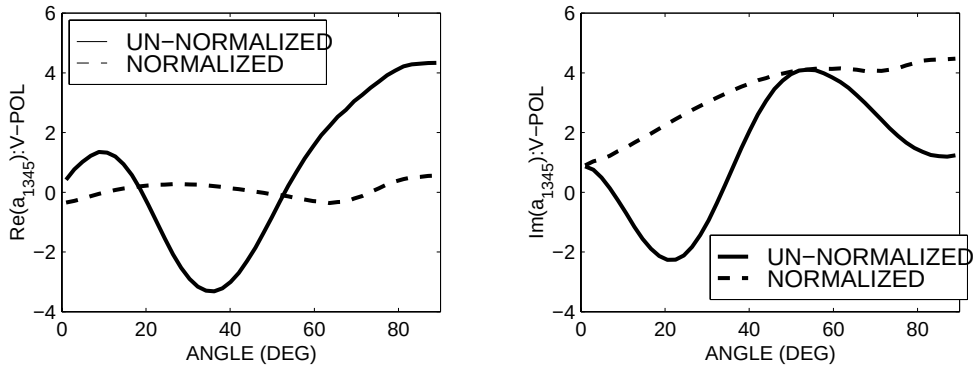


**Figure 2.** *The real part (left) and imaginary part (right) of the solution for basis number 1345. The incident angle* $\theta^i = 90^o$*, and the horizontal variable* $\phi^i$ *varies from* $0^o$ *to* $90^o$.

The implementation of the current extrapolation is straighforward. It only involves two steps. First the system of equations (1) is solved to obtain the coefficient for one angle/frequency sample. From this solution, the normalized coefficient is extracted using equation (4). Then, in the second step, the normalized coefficient is multiplied by a correction factor of $\exp(i(\vec{k}^i+\vec{\Delta})\cdot\vec{r}_n)$ to obtain the basis function coefficient for any near-by frequency and angle samples.

## III. Numerical Results

In this section, examples will be shown to demonstrate the application of the current extrapolation method. The results are generated using a multilevel fast multipole algorithm [11] that is implemented for the solution of hybrid surface-volume integral equations [1]. The first example shows the comparison of the RCS for the five-sphere target given in Figure 1. The results are plotted in Figure 3 for the V-V and H-H polarized incident cases. It can be seen that the extrapolated results using five samples are very close to that obtained by brute-force method (in which, the solution to the system equation is obtained for every incident angles). In the plot of Figure 3, the horizontal axis AZ is defined as $-\phi^i$.

The second example consists of a simple airplane model that is made by two conducting plates (as wings) attached to a cone-cylinder-hemisphere structure. The mesh description is shown in Figure 4 and the radar cross sections as function of frequency, calculated using the brute-force approach (solution for every point of RCS output) and the extrapolation method, are shown in Figure 5. The mono-static angles for this result are $\theta^i = 30^o$, $\phi^i = 30^o$.

The third example considers scattering of a model airplane VFY218 [1] at 300 MHz. Figure 6 shows the comparison of the 361 RCS points (0.5 degrees step size) on the horizontal plane ($0^o$–$180^o$ range) using (1) the brute-force approach which calculates the solution for every output point (the solid dots), (2) the current extrapolation method of this paper (the solid line) using the solutions at the sampling points (the circles), and (3) the bi-static to mono-static approximation method provided in [3] (the dash line). In both of the two approximations ((2) and (3)), the number of sampling angles is 31. This sampling rate is determined by the approximate formula that the angle increments between two neighbor samples is $25\sqrt{\lambda/D}$, with $D$ being the target's physical dimension. It can be seen that the agreements of the approximate methods with the direct solution are reasonably well.

It should be pointed out that the overall saving of the CPU time is slightly smaller that the ratio of the numbers of the dense sample (brute-force solution) and the sparse sample (for extrapolation). For example, in the VFY218 example introduced above, the CPU time for the direct solution of all output points is 12.03 hours on a HP Supercomputer, and the CPU times for both of the two approximate methods are 142 minutes, and 138 minutes, respectively (a theoretically expected values for the approximate method would be 120 minutes which is 6 times less than that of the brute-force approach). The reason behind the phenomena is the increased iteration number for the same convergence criterion in the brute-force solution and the extrapolation. The algorithm used in generating the data of the above examples employed an implementation for the iteration, in which the solution from the previous incidence is applied to approximate the initial guess of the next incident point. It is known that the denser the solution samples, the closer the two solutions of the adjacent sampling points.

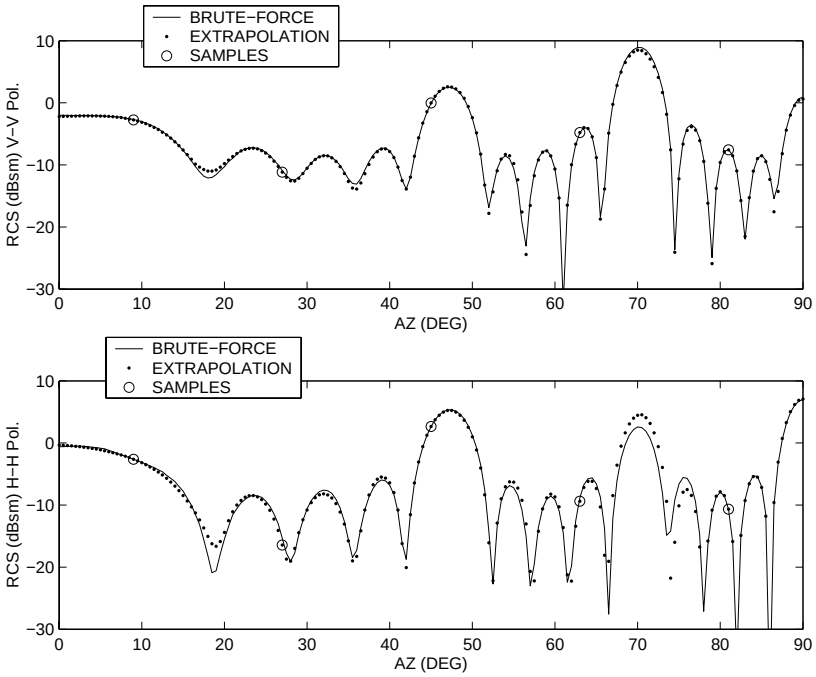


**Figure 3**. *The comparison between brute-force solution and extrapolation for the RCS of the five conducting spheres shown in Figure 1.*

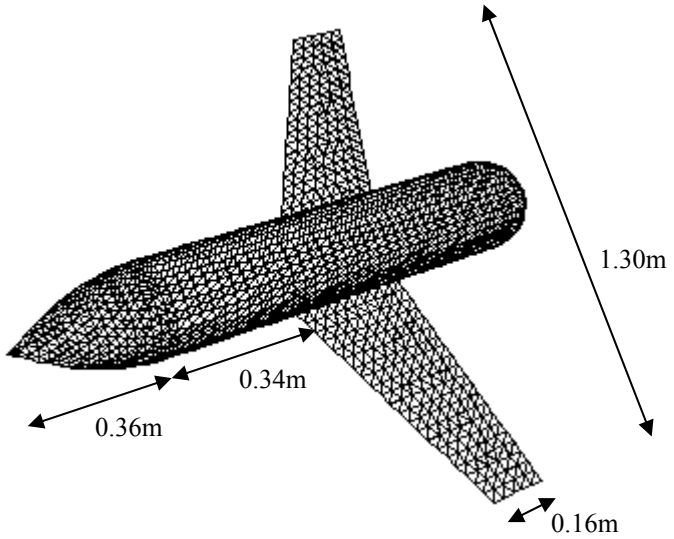


**Figure 4.** *An airplane-like model made of 5 pieces: two trapezoidal plates (as wings), a cone, a circular cylinder, and a hemisphere. The cone's profile is parabolic with height 0.36 m, the radius of the circular cylinder and the hemisphere tail is 0.12 m, the length of the cylindrical part is 1.0 m, the two plates are identical in shape and size, the two parallel sides are 0.32 m and 0.16 m, respectively. The other parameters are shown in the sketch.*

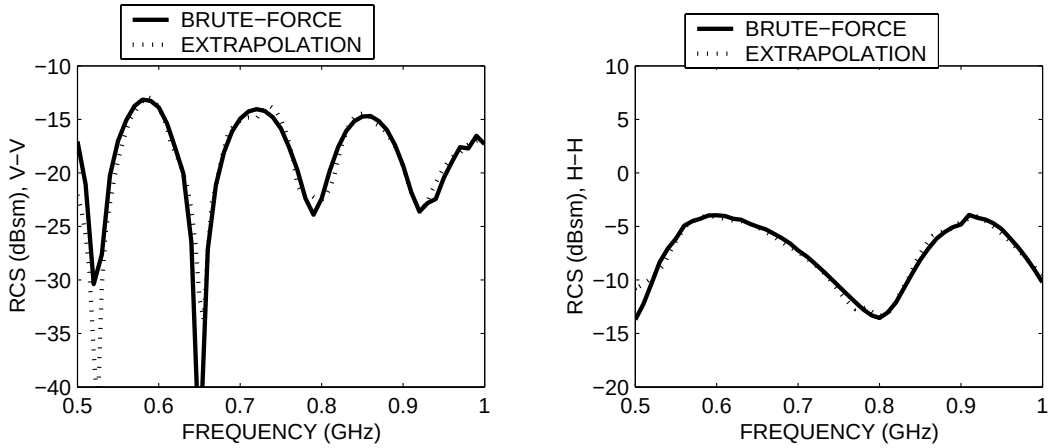


**Figure 5**. *The comparisons of RCS that is directly calculated and extrapolated for the simple airplane model in Figure 4. The number of frequency samples used to generate the extrapolated result is 10.*

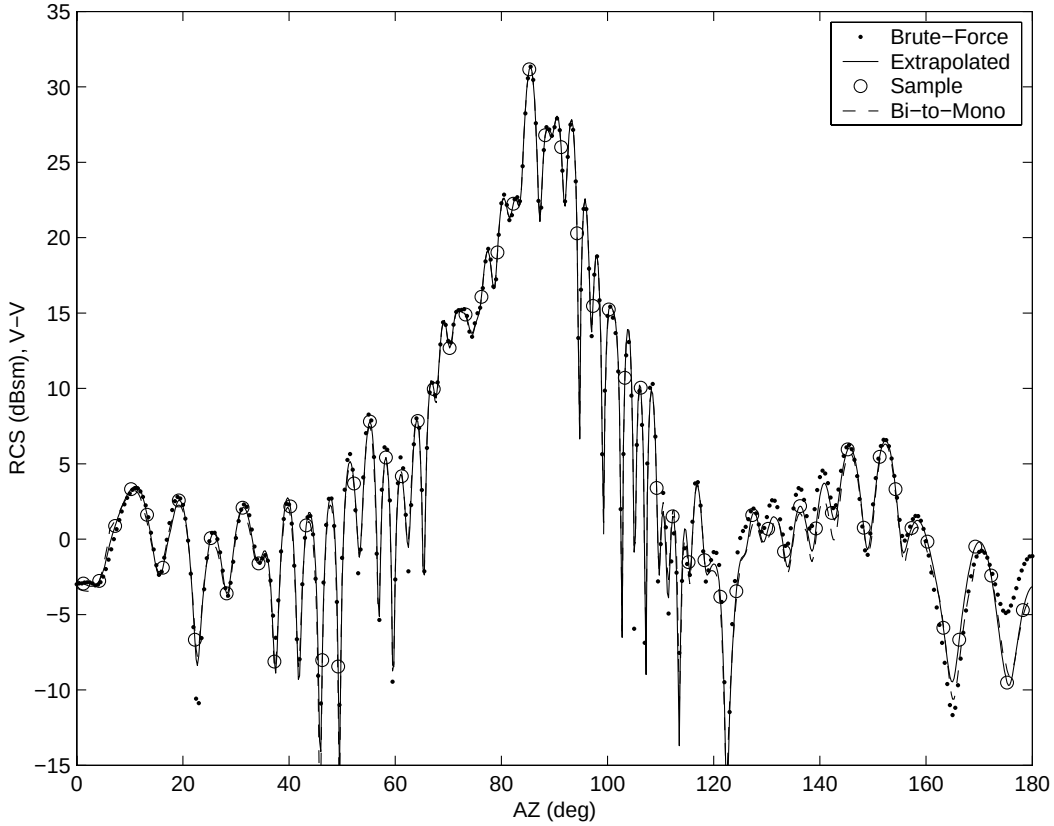


**Figure 6.** *The directly calculated (brute-force) and the extrapolated RCS results of VFY 218 at 300 MHz in the horizontal plane ($\theta^i = 90^o$). The circles indicate the sampling points from which the RCS of the dense output points (the solid line) are generated. The dot-dash line is the result using the bi-static to mono-static approximation method.*

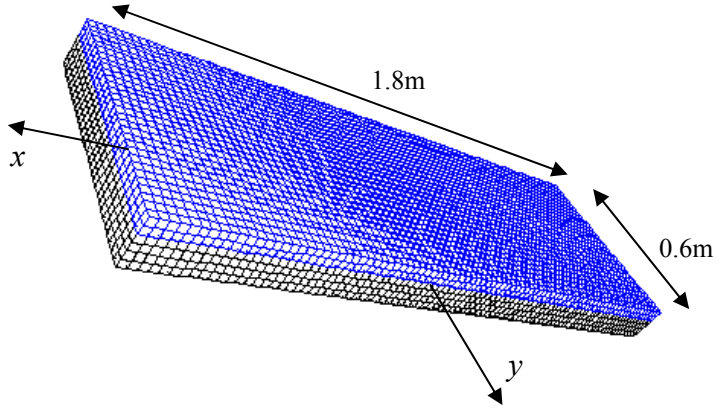


**Figure 7.** *A conducting box with dielectric coating. The thickness of the box (bottom part) is 0.08 m, and the coating slab thickness is 0.04 m. The number unknowns for the conducting part is 12720, and the number of unknowns for the material part is 19140.*

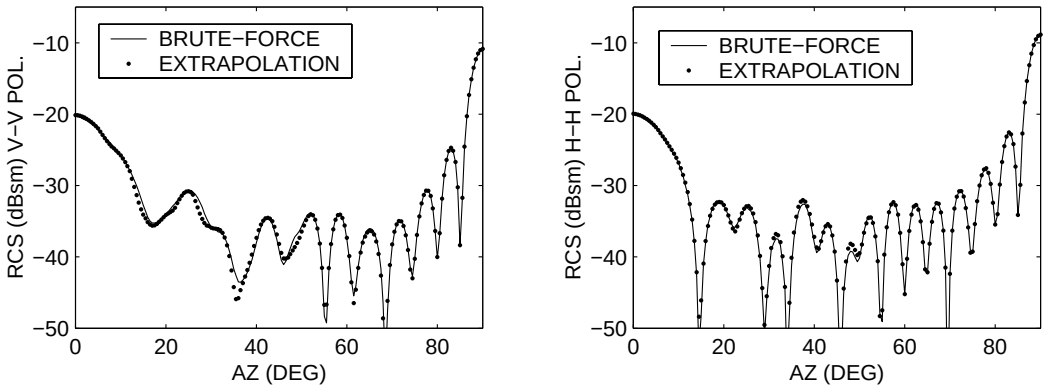


**Figure 8.** *The mono-static RCS of dielectric slab calculated by brute-force, and by extrapolation. The number of RCS points is 181, and the number of samples is 13 for the extrapolation.*

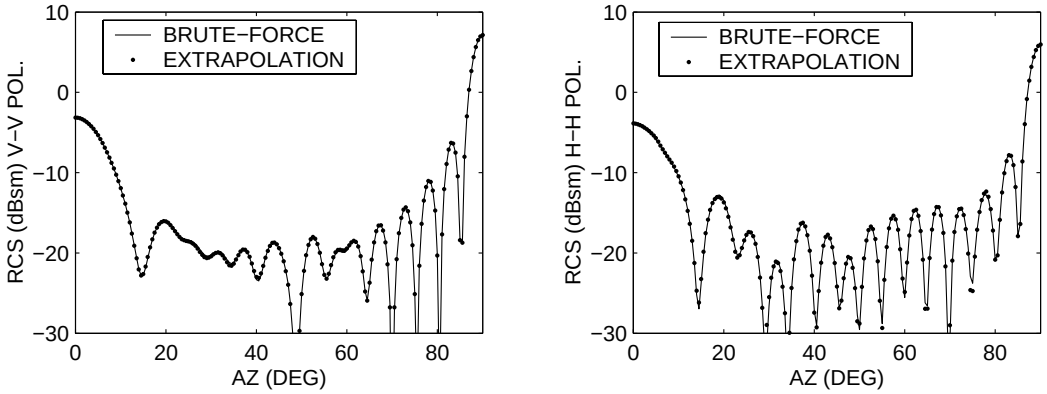


**Figure 9.** *The mono-static RCS of a conducting box coated by a layer of dielectric slab calculated by brute-force, and by extrapolation. The number of RCS points is 181, and the number of samples is 13 for the extrapolation.*

## IV. Discussions and Summary

There are some remarks that must be pointed out for this method. First, in section 2 above, it has been assumed that the interactions among the basis functions are typically strong when they are close, and are weak when they are far away from each other. This assumption is not valid if there are strong multi-bounce contributions to the far-field. An example is a single 90 degree corner reflector (or aligned array of such reflectors). It has strong two bounce interactions that contribute directly to the backscattered field. Another example is a deep cavity which has multiple wave bounces inside the interior walls. As a result, the simple current extrapolation method introduced above does not apply to these two types of targets. Secondly, as is seen in the numerical example, the CPU time saving does not necessarily proportional to the ratio between the numbers of actual output points and the samples. This is due to the use of the current solution as initial guess to predict the next near-by solutions. In an iterative solver, the number of iterations is normally small if a better initial guess is built. When the output points (angle and frequency) are close, then the solutions are expected to be close as well. As a result, the solution at one point can be used as the initial guess for the next (near-by) point. For the brute-force approach, solution is made for each output point. Hence, the "distance" between two neighbor points is much smaller than that of the samples in the extrapolation method, leading to a smaller number of iterations per solution in the brute-force approach. Finally, it is also noted that for the angular loop, the extrapolation method has about the same level of accuracy as the bi-static to mono-static approximation approach.

To summarize, a current extrapolation method is introduced to rapidly perform angle and frequency sweep in the far-field calculation using the sparsely sampled solutions. Numerical examples show that the results agree reasonably well to that provided by the direct solution, but the extrapolation method uses about the same amount of memory, and much less CPU time than that of the brute-force approach. There are two advantageous for this method. First, it is easy to implement (no out-of-core processing is needed), and it has small extra memory (in fact, the extra memory required is equal to $N$ complex numbers, where $N$ is the number of basis functions used in the solution). Secondly, the extrapolation applies to both angle and frequency sweeps.

## V. References


[1] J. M. Song, C. C. Lu, and W.C. Chew, "MLFMA for electromagnetic scattering by large complex objects," *IEEE Trans. Antennas Propagat*., vol. 45, no. 10, pp. 1488-1493, Oct. 1997.

[2] Y. Wang and H. Ling, "RCS interpolation in frequency and angle using adaptive feature extraction," *1999 IEEE Int. Antennas Propagat. Symp. Dig.* vol. 37, pp. 450 - 453, June 1999.

[3] Y. Wang, H. Ling, J. Song, and W. C. Chew, "A frequency extrapolation algorithm for FISC," *IEEE Trans. Antennas Propagat.,* vol. 45, pp. 1891 - 1893, Dec. 1997.

[4] M. J. Schuh and A. C. Woo, "The monostatic/Bistatic Approximation", *IEEE Antennas and Propagation Magazine*, vol. 36, No. 4, pp. 76-78, Aug. 1994.

[5] G. J. Burke, E. K. Miller, S. Chakrabarti, K. Demarest, "Using model-based parameter estimation to increase the efficiency of computing electromagnetic transfer functions," *IEEE Trans. Magn*., vol. 25, pp. 2807 - 2809, July 1989.

[6] Yuanxun Wang, Hao Ling; "Radar signature prediction using moment method codes via a frequency extrapolation technique," *IEEE Trans. Antennas Propagat*., vol. 47, pp. 1008 - 1015, June 1999.

[7] K. Kottapalli, T. K. Sarkar, Y. Hua, E. K. Miller, G. L. Burke, "Accurate computation of wide-band response of electromagnetic systems utilizing narrow-band information," *IEEE Trans. Microwave Theory Tech.,* vol. 39, pp. 682 - 687, Apr. 1991.

[8] Edward H. Newman, "Generation of wide-band data from the method of moments by interpolating the impedance matrix," *IEEE Trans. Antennas Propagat.,* vol. 36, pp. 1820 - 1824, December 1988.

[9] Z. Altman and R. Mittra, "A technique for extrapolating numerically rigorous solutions of electromagnetic scattering problems to higher frequencies and their scaling properties," *IEEE Trans. Antennas Propagat.,* vol. 47, pp. 744 - 751, April 1999.

[10] Y. E. Erdemli, J. Gong, C. J. Reddy, J. L. Volakis, "Fast RCS pattern fill using AWE technique," *IEEE Trans. Antennas Propagat.*, vol. 46, pp. 1752 - 1753, Nov.r 1998.

[11] C. C. Lu and W. C. Chew, "A coupled integral equation technique for the calculation of electromagnetic scattering from composite metallic and dielectric targets," *IEEE Trans. Antenna Propagat.*, vol. 48, no. 12, pp. 1866-1868, Dec. 2000

Dr. Cai-Cheng Lu got his Ph.D. degree from University of Illinois at Urbana-Champaign in 1995, and now he is an associate professor in the Department of Electrical and Computer Engineering at the University of Kentucky. Prior to join University of Kentucky, he was with Demaco, Inc. (now SAIC). His research interests are in wave scattering, microwave circuit simulation, and antenna analysis, and is one of the authors for a CEM code FISC. He is a recipient of the 2000 Young Investigator Award from the Office of Naval Research, and a CAREER Award from the National Science Foundation. Dr. Lu is a senior member of IEEE.

# Asymptotic Waveform Evaluation Technique Based on Fast Lifting Wavelet Transform

Chen Ming-Sheng Wu Xian-liang Sha Wei
Key Lab of Intelligent Computing & Signal Processing,
Anhui University, Ministry of Education
Hefei 230039, China

**Abstract:** The asymptotic waveform evaluation (AWE) technique based on fast lifting wavelet transform (LWT) is applied to the method of moments to solve the combined-field integral equation (CFIE). The wide-band radar cross section of an arbitrarily shaped two-dimensional perfectly electric conduct object is calculated. The employment of CFIE eliminates the interior resonance problems. Numerical results presented in this paper are compared with the results obtained by the method of moments. It is shown that the computational efficiency is improved greatly.

## I. INTRODUCTION

The solution of the combined-field integral equation (CFIE) via the method of moments (MOM) has been a very useful method for accurately predicting the radar cross section (RCS) at a certain frequency [1], but many electro-magnetic applications require the computation of frequency responses over a broad band rather than at one or a few isolated frequencies. To obtain the RCS over a wide band using MOM, a set of algebraic equations must be solved repeatedly, which will greatly increase the central processing unit time and the storage required. Therefore, there is a need to find approximate solution techniques that can efficiently simulate a frequency response over a broad band.

Over past few years, a similar technique called asymptotic waveform evaluation (AWE) has been proposed for the timing analysis of very large scale integration (VLSI) circuits [2], [3]. Recently, a detailed description of AWE applied to frequency-domain electromagnetic analysis was presented in [4], [5]. The traditional AWE presents great superiority when the electrical size of the problem is small enough. But the interior resonance problems take place frequently as the target size increasing, and the dimension of the dense impedance matrix also increased. Based on these facts, the traditional AWE almost can hardly deal with electrically large targets. Therefore, a new method called asymptotic waveform evaluation technique based on fast lifting wavelet transform (LWT-AWE) is presented here [6], in which the combined-field integral equation (CFIE) is reduced to a matrix equation, and the LWT is applied to the equation to get a new sparse matrix equation. Then the AWE technique is applied to the new equation, and finally, the inverse LWT is employed to obtain the electric current distribution quickly at any frequency point within the given frequency band. Numerical results are compared with the results obtained by the method of moments; CPU time and storage required are decreased drastically.

## II. FORMULATION

For a perfectly conducting object, the CFIE can be shown to be

$$-\hat{\mathbf{n}}\times\mathbf{H}^{S}(\mathbf{J})-\frac{\alpha}{\eta}\mathbf{E}^{S}_{\tan}(\mathbf{J}) = \hat{\mathbf{n}}\times\mathbf{H}^{i}+\frac{\alpha}{\eta}\mathbf{E}^{i}_{\tan} \quad (1)$$

where $\hat{\mathbf{n}}$ is the surface normal, $\mathbf{E}^{i}$ and $\mathbf{H}^{i}$, denote the incident electric and magnetic fields respectively, and $\eta$ is the wave impedance. The weighting parameter $\alpha$ can be viewed as an arbitrary real constant range between 0 and 1 [7].

### *AWE implementation*

By MOM method, Eq.1 can result in a matrix equation in the following form:

$$\mathbf{Z}(k)\mathbf{I}(k)=\mathbf{V}(k). \quad (2)$$

Now let us consider a wavelet matrix transform; Eq.2 is transformed to

$$\tilde{\mathbf{Z}}(k)\tilde{\mathbf{I}}(k)=\tilde{\mathbf{V}}(k) \quad (3)$$

where $\tilde{\mathbf{Z}}(k)=\mathbf{W}\,\mathbf{Z}(k)\,\mathbf{W}^{H}$, $\tilde{\mathbf{I}}(k)=\mathbf{W}\,\mathbf{I}(k)$, and $\tilde{\mathbf{V}}(k)=\mathbf{W}\mathbf{V}(k)$; $\mathbf{W}$ is assumed to be a $N\times N$ orthogonal wavelet matrix.

The *i*th derivative of $\tilde{\mathbf{Z}}$ and the *n*th derivative of $\tilde{\mathbf{V}}$ can be computed by

$$\tilde{\mathbf{Z}}^{(i)}(k)=\mathbf{W}\,\mathbf{Z}^{(i)}(k)\,\mathbf{W}^{H}, \quad (4)$$

$$\tilde{\mathbf{V}}^{(n)}(k)=\mathbf{W}\,\mathbf{V}^{(n)}(k). \quad (5)$$

To obtain the solution of (3) over a wide frequency band, we expand $\mathbf{I}(k)$ into a Taylor series

$$\tilde{\mathbf{I}}(k)=\sum_{n=0}^{N}\mathbf{m}_n(k-k_0)^n \tag{6}$$

where $k_0$ is the expansion point, $\mathbf{m}_n$ denotes the unknown coefficients, and $N$ denotes the total number of such coefficients. Substituting this into (3), one can obtain

$$\tilde{\mathbf{Z}}(k_0)\mathbf{m}_0=\tilde{\mathbf{V}}(k_0) \tag{7}$$

$$\tilde{\mathbf{Z}}(k_0)\mathbf{m}_n=[\frac{\tilde{\mathbf{V}}^{(n)}(k_0)}{n!}-\sum_{i=1}^{n}\frac{\tilde{\mathbf{Z}}^{(i)}(k_0)\mathbf{m}_{n-i}}{i!}]. \tag{8}$$

To improve the computational efficiency, substitute (4) and (5) into (8) and carry out the associative law, one can obtain

$$\tilde{\mathbf{Z}}(k_0)\mathbf{m}_n=\mathbf{W}[\frac{\mathbf{V}^{(n)}(k_0)}{n!}-\sum_{i=1}^{n}\frac{\mathbf{Z}^{(i)}(k_0)(\mathbf{W}^H\mathbf{m}_{n-i})}{i!}] . \tag{9}$$

Then the multiplications between matrices in Eq.4 degenerated to be multiplications between matrixes and vectors. Computing the coefficients $\mathbf{m}_n$ $(n=0,1,2,\cdots N)$ by iterative solvers, one can easily obtain $\tilde{\mathbf{I}}(k)$ in the given frequency band from Eq.6. Then the wavelet inverse transform is applied to $\tilde{\mathbf{I}}(k)$ ( $\mathbf{I}(k)=\mathbf{W}^H\mathbf{I}(k)$ ); the electric current distribution $\mathbf{I}(k)$ and the radar cross section over a wide band will be obtained.

For a given threshold value, $\tilde{\mathbf{Z}}(k_0)$ will become a sparse matrix, namely, Eq.7 and Eq.9 become sparse matrix equations, which can be efficiently solved by a sparse solver.

Since the Taylor expansion has a limited bandwidth, $\tilde{\mathbf{I}}(k)$ can be represented with a better-behaved rational Padé function [2],

$$\tilde{\mathbf{I}}(k)=\frac{\sum_{i=0}^{L}\mathbf{a}_i(k-k_0)^i}{\sum_{j=0}^{M}\mathbf{b}_j(k-k_0)^j} \tag{10}$$

where $L+M=N$ , $L=M$ or $M+1$ , and $b_0=1$. The unknown coefficients can be calculated by substituting (6) into (10). Multiplying (10) by the denominator of the Padé expansion and matching the coefficients of the equal powers of $k-k_0$, leads to the matrix equation

$$\begin{bmatrix}\mathbf{m}_L & \mathbf{m}_{L-1} & \mathbf{m}_{L-2} & \cdots & \mathbf{m}_{L-M+1}\\ \mathbf{m}_{L+1} & \mathbf{m}_L & \mathbf{m}_{L-1} & \cdots & \mathbf{m}_{L-M+2}\\ \mathbf{m}_{L+2} & \mathbf{m}_{L+1} & \mathbf{m}_L & \cdots & \mathbf{m}_{L-M+3}\\ \vdots & \vdots & \vdots & \ddots & \vdots\\ \mathbf{m}_{L+M-1} & \mathbf{m}_{L+M-2} & \mathbf{m}_{L+M-3} & \cdots & \mathbf{m}_L\end{bmatrix}\begin{bmatrix}\mathbf{b}_1\\ \mathbf{b}_2\\ \mathbf{b}_3\\ \vdots\\ \mathbf{b}_M\end{bmatrix}=-\begin{bmatrix}\mathbf{m}_{L+1}\\ \mathbf{m}_{L+2}\\ \mathbf{m}_{L+3}\\ \vdots\\ \mathbf{m}_{L+M}\end{bmatrix}, \tag{11}$$

$$\begin{bmatrix}\mathbf{a}_0\\ \mathbf{a}_1\\ \mathbf{a}_2\\ \vdots\\ \mathbf{a}_L\end{bmatrix}=\begin{bmatrix}\mathbf{m}_0 & 0 & 0 & \cdots & 0\\ \mathbf{m}_1 & \mathbf{m}_0 & 0 & \cdots & 0\\ \mathbf{m}_2 & \mathbf{m}_1 & \mathbf{m}_0 & \cdots & 0\\ \vdots & \vdots & \vdots & \ddots & \vdots\\ \mathbf{m}_L & \mathbf{m}_{L-1} & \mathbf{m}_{L-2} & \cdots & \mathbf{m}_{L-M}\end{bmatrix}\begin{bmatrix}1\\ \mathbf{b}_1\\ \mathbf{b}_2\\ \vdots\\ \mathbf{b}_M\end{bmatrix}. \tag{12}$$

## *Fast lifting wavelet transform scheme*

In discrete wavelet transform (DWT), the wavelet matrix $\mathbf{W}$ can be constructed by wavelet filter coefficients [8].

However, traditional implementation method caused auxiliary memories consumed by wavelet matrices, while operating wavelet using lifting scheme can avoid this limitation.

In the lifting scheme, we don't need to construct a wavelet matrix $\mathbf{W}$, but to operate the impedance matrix itself directly.

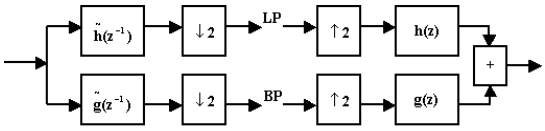


Fig. 1. Filter bank for wavelet transform.

The finite filter wavelet transform can be viewed as subband transform using finite impulse response (FIR) filters illustrated in Fig. 1. Forward transform uses two analysis filters $\tilde{h}$ (low pass) and $\tilde{g}$ (high pass), followed by subsampling, while inverse transform first upsamples and then uses two synthesis filters $h$ (low pass) and $g$

(high pass). The perfect reconstruction (PR) property is defined by Eq. (13) [6],

$$\begin{aligned}\tilde{h}(z^{-1})h(z)+\tilde{g}(z^{-1})g(z)&=2\\ \tilde{h}(-z^{-1})h(z)+\tilde{g}(-z^{-1})g(z)&=0\end{aligned} \tag{13}$$

where $z^{-1}$ in analysis filters is time reversion that compensates the delays in filters.

The polyphase representation of filter $h$, is given by

$$h(z)=h_e(z^2)+z^{-1}h_o(z^2) \tag{14}$$

where $h_e(z)=\sum_k h_{2k}z^{-k}$ contains the even coefficients, $h_o(z)=\sum_k h_{2k+1}z^{-k}$.

Define the new polyphase matrices

$$P(z)=\begin{bmatrix}h_e(z) & g_e(z)\\ h_o(z) & g_o(z)\end{bmatrix}, \tag{15a}$$

$$\tilde{P}(z)=\begin{bmatrix}\tilde{h}_e(z) & \tilde{g}_e(z)\\ \tilde{h}_o(z) & \tilde{g}_o(z)\end{bmatrix}. \tag{15b}$$

Then the PR condition can be rewritten as

$$P(z)\tilde{P}(z^{-1})^H=u \tag{16}$$

where $u$ is an identity matrix.

The problem of finding an FIR wavelet transform thus amounts to finding a matrix $P(z)$. Once we have such a matrix, $\tilde{P}(z)$ and other filters for the wavelet transforms follow immediately. From (16) it follows that

$$\tilde{h}_e(z)=g_o(z^{-1}),\quad \tilde{h}_o(z)=-g_e(z^{-1}), \tag{17a}$$

$$\tilde{g}_e(z)=-h_o(z^{-1}),\ \tilde{g}_o(z)=h_e(z^{-1}). \tag{17b}$$

For the transforms with Daubechies wavelets, $h_i$ and $g_i$ are the coefficients involved in the two-scale relations of the Daubechies wavelets:

$$\phi(x)=\sqrt{2}\sum_{n=0}^{2N_m-1}h_n\phi(2x-n), \tag{18a}$$

$$\psi(x)=\sqrt{2}\sum_{n=0}^{2N_m-1}g_n\phi(2x-n) \tag{18b}$$

where $\phi$ and $\psi$ are the scaling and wavelet functions, respectively. $N_m$ is the number of vanishing moments.

Daubechies has proved that given a complementary filter pair $\{h,g\}$ or $\{\tilde{h},\tilde{g}\}$, then there always exist Laurent polynomials $s_i(z)$ and $t_i(z)$ for $1\le i\le m$ and a nonzero constant $K$ so that

$$P(z)=\prod_{i=1}^{m}\begin{bmatrix}1 & s_i(z)\\ 0 & 1\end{bmatrix}\begin{bmatrix}1 & 0\\ t_i(z) & 1\end{bmatrix}\begin{bmatrix}K & 0\\ 0 & 1/K\end{bmatrix}, \tag{19a}$$

$$\tilde{P}(z)=\prod_{i=1}^{m}\begin{bmatrix}1 & 0\\ -s_i(z^{-1}) & 1\end{bmatrix}\begin{bmatrix}1 & -t_i(z^{-1})\\ 0 & 1\end{bmatrix}\begin{bmatrix}1/K & 0\\ 0 & K\end{bmatrix}. \tag{19b}$$

We can get inverse wavelet transform factoring formulation by simply inverse the forward formulation, switch additions and subtractions, and switch multiplications and divisions,

$$P^{-1}(z)=\prod_{i=m}^{1}\begin{bmatrix}1/K & 0\\ 0 & K\end{bmatrix}\begin{bmatrix}1 & 0\\ -t_i(z) & 1\end{bmatrix}\begin{bmatrix}1 & -s_i(z)\\ 0 & 1\end{bmatrix}, \tag{20a}$$

$$\tilde{P}^{-1}(z)=\prod_{i=m}^{1}\begin{bmatrix}K & 0\\ 0 & 1/K\end{bmatrix}\begin{bmatrix}1 & t_i(z^{-1})\\ 0 & 1\end{bmatrix}\begin{bmatrix}1 & 0\\ s_i(z^{-1}) & 1\end{bmatrix}. \tag{20b}$$

We also describe lifting step by predict step and update step, which can be outlined in the following three basic operations.

Split: Divide the original data ($\mathbf{x}[n]$) into odd subsets ($\mathbf{x}_o[n]$) and even subsets ($\mathbf{x}_e[n]$),

$$\mathbf{x}_o[n]=\mathbf{x}[2n-1],\ \mathbf{x}_e[n]=\mathbf{x}[2n]. \tag{21a}$$

Predict: Generate high frequency component $\mathbf{d}(n)$ as the error in predicting odd subsets from even subsets using prediction operator $Q$,

$$d[n]=x_o[n]-Q(x_e[n]). \tag{21b}$$

Update: Generate low frequency component $\mathbf{c}[n]$ as a coarse similarity to original signal by applying an update operator $U$ to the wavelet coefficients and adding to even subsets,

$$\mathbf{c}[n] = \mathbf{x}_e[n] + U(\mathbf{d}[n]). \qquad (21c)$$

The operators $Q$ and $U$ are decided by the polyphase matrixes.

To illuminate the steps for the fast lifting wavelet transform scheme, a D4 wavelet example is presented here.

The $h$ and $g$ filters are given by:

$$h(z) = h_0 + h_1 z^{-1} + h_2 z^{-2} + h_3 z^{-3}, \qquad (22a)$$

$$g(z) = -h_3 z^{2} + h_2 z^{1} - h_1 + h_0 z^{-1} \qquad (22b)$$

with $h_0 = \frac{1+\sqrt{3}}{4\sqrt{2}}$, $h_1 = \frac{3+\sqrt{3}}{4\sqrt{2}}$, $h_2 = \frac{3-\sqrt{3}}{4\sqrt{2}}$, and $h_3 = \frac{1-\sqrt{3}}{4\sqrt{2}}$.

The polyphase matrix is

$$P(z) = \begin{bmatrix} h_0 + h_2 z^{-1} & -h_3 z^{1} - h_1 \\ h_1 + h_3 z^{-1} & h_2 z^{1} + h_0 \end{bmatrix} \qquad (23)$$

and the factorization is given by

$$P(z) = \begin{bmatrix} 1 & -\sqrt{3} \\ 0 & 1 \end{bmatrix} \begin{bmatrix} 1 & 0 \\ \frac{\sqrt{3}}{4} + \frac{\sqrt{3}-2}{4} z^{-1} & 1 \end{bmatrix} \times \begin{bmatrix} 1 & z \\ 0 & 1 \end{bmatrix} \begin{bmatrix} \frac{\sqrt{3}+1}{\sqrt{2}} & 0 \\ 0 & \frac{\sqrt{3}-1}{\sqrt{2}} \end{bmatrix}.$$

Forward row transforms ( $\mathbf{Z}(k)\mathbf{W}^H$ ) for impedance matrix $\mathbf{Z}(k)$ will be given by $P(z)$ :

Set $\mathbf{x}$ to be one row of impedance matrix $\mathbf{Z}(k)$, $\tilde{\mathbf{x}}$ to be one row of impedance matrix $\tilde{\mathbf{Z}}(k)$ correspondingly.

Step1 (Split):

$$\mathbf{d}^{(0)}[n] = \mathbf{x}[2n-1], \mathbf{c}^{(0)}[n] = \mathbf{x}[2n].$$

Step2 (Predict):

$$\mathbf{d}^{(1)}[n] = \mathbf{d}^{(0)}[n] - \sqrt{3}\mathbf{c}^{(0)}[n].$$

Step3 (Update):

$$\mathbf{c}^{(1)}[n] = \mathbf{c}^{(0)}[n] + \frac{\sqrt{3}}{4}\mathbf{d}^{(1)}[n] + \frac{\sqrt{3}-2}{4}\mathbf{d}^{(1)}[n-1].$$

Then repeat step2 and step3:

$$\mathbf{d}^{(2)}[n] = \mathbf{d}^{(1)}[n] + \mathbf{c}^{(1)}[n+1] \ ,$$

$$\tilde{\mathbf{x}}[2n] = \frac{\sqrt{3}+1}{2}\mathbf{c}^{(1)}[n] \ ,$$

$$\tilde{\mathbf{x}}[2n-1] = \frac{\sqrt{3}-1}{2}\mathbf{d}^{(2)}[n] \ .$$

Similarly, the forward column transforms ( $\mathbf{WZ}(k)$ or $\mathbf{WV}(k)$ ) for impedance matrix $\mathbf{Z}(k)$ will give by $\tilde{P}(z)$ which can be computed by Eq.17 and Eq.15b; the inverse current vector transform $\mathbf{W}^H\tilde{\mathbf{I}}(k)$ will be operated by $\tilde{P}^{-1}(z)$. The transform $\mathbf{Z}(k)\mathbf{W}$ is not needed in this paper, and it can be operated by $P^{-1}(z)$.

## III. NUMERICAL RESULTS

To validate the analysis presented in the previous sections, a few numerical examples are considered. For perfectly conducting infinite objects excited by a TM plane wave at an angle of incident $\theta_i$, RCS calculations over a frequency band are done for a cylinder with perimeter $C = 0.36$ m ( $\theta_i = 0$ ), a square cylinder with length $a = 0.1$ m ( $\theta_i = 0$ ), and a strip with length $w$ =0.25m and width $d = 0.001$m ( $\theta_i = \pi/4$ ). In the numerical examples presented below, the expansion frequency is chosen to be the center frequency of the band of interest. Fig.2 shows the nonzero components distribution of the impedance matrix after transforms. The results over a given

frequency band are calculated by the LWT-AWE method with Padé approximation ( $L = 4$ , $M = 3$ ).

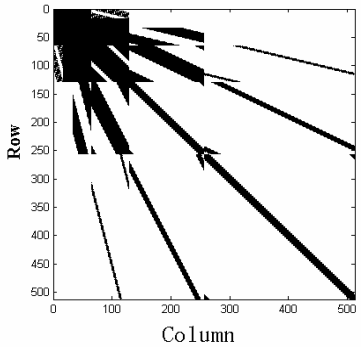


Fig. 2. Impedance matrix of cylinder after transforms.

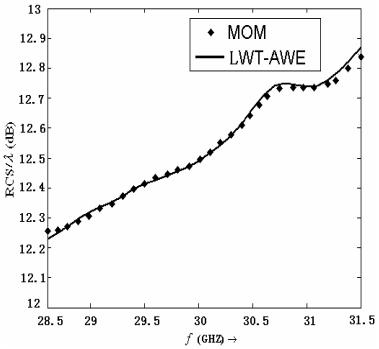


Fig. 3. RCS frequency response of the cylinder.

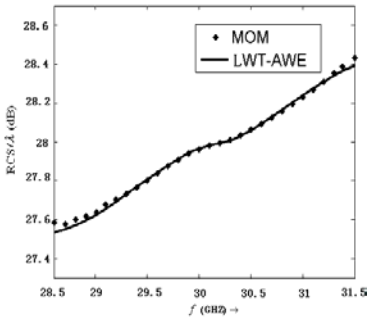


Fig. 4. RCS frequency response of the square cylinder.

The CPU time consumed by LWT-AWE and the moment methods are given in Table I. All the computations reported are done on a PIV 2.66G/256MB computer.

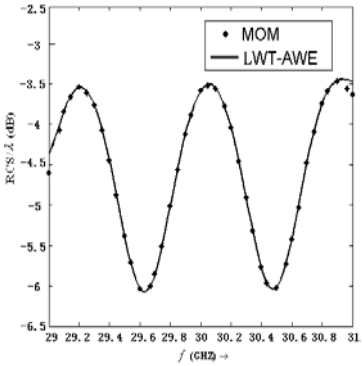


Fig. 5. RCS frequency response of the strip.

Table I. CPU time required comparison.

| Examples | Figure 3 | | Figure 5 | |
|---|---|---|---|---|
| | time(s) | frequencies | time(s) | frequencies |
| MOM | 763.7 | 31 | 947.4 | 41 |
| LWT-AWE | 194.2 | 301 | 279.1 | 401 |

## IV. CONCLUSIONS

An implementation of AWE combined with LWT for frequency-domain MOM is presented. The RCS for different PEC objects are computed. From the numerical examples presented, LWT-AWE method is found to be superior in terms of the CPU time to obtain a frequency response: CFIE eliminates interior resonance problem, and the employment of LWT produces a sparse system of linear equations that are treated effectively by a sparse linear system solver.

## References

[1] R. F. Harrington. *Field computation by moment methods.* New York: Macmillan, 1968.

[2] L. T. Pillage and R. A. Rohrer, "Asymptotic waveform evaluation for timing analysis," *IEEE Trans. Comput.-Aided Design,* pp. 352-366, Apr.1990.

[3] T. K. Tang, M. S. Nakhla, and R. Griffith, "Analysis of lossy multiconductor transmission lines using the asymptotic waveform evaluation technique," *IEEE Trans.*

*Microwave Theory and Techniques,* vol. 39, pp. 2107-2116, Dec. 1991.

[4] C. R. Cockcell and F. B. Beck, "Asymptotic wave form evaluation (AWE) technique for frequency domain electromagnetic analysis," *NASA Tech*. Memo 110292, Nov.1996.

[5] C. J. Reddy and M. D. Deshpande, "Application of AWE for RCS frequency response calculations using method of moments," *NASA Contractor* Rep.4758, Oct. 1996.

[6] I. Daubechies, and W. Sweldens, "Factoring wavelet transforms into lifting steps," *J. Fourier Anal.* Appl., vol. 4, No. 3, Preprint, 1998.

[7] J. R. Mautz and R. F. Harringtong, "H-Field, E-Field, and Combined-Field Solutions for Conducting Bodies of Revolution," *AEÜ,* 32, pp.157-164, Apr. 1978.

[8] Wojciech L.Golik, "Sparsity and Conditioning of Impedance Matrixes Obtained with Semi-Orthogonal and Bi- Orthogonal Wavelet Bases," *IEEE Trans. Antennas Propagat.,* vol. 48, pp. 473-481, Apr. 2000.


**Chen Ming-sheng** was born in Anhui, China, in1981. He is currently pursuing a Ph.D. degree in Anhui University. His research interests include wavelet transform, method of moment and parabolic equation methods for electromagnetics.

**Wu Xian-liang** was born in 1955. He is currently a professor of Anhui University, doctor supervisor. His research interests include signal processing, target tracking and numerical method for electromagnetics.

# 2006 INSTITUTIONAL MEMBERS

AUSTRALIAN DEFENCE LIBRARY
Northcott Drive
Campbell, A.C.T. 2600 AUSTRALIA

BEIJING BOOK COMPANY, INC
701 E Lindon Ave.
Linden, NJ 07036-2495

BRITISH LIBRARY
Boston SPA, Wetherby
West Yorkshire, UK LS23 7BQ

DARMSTADT U. OF TECHNOLOGY
Schlossgartenstrasse 8
Darmstadt, Hessen
GERMANY D-64289

DARTMOUTH COLL-FELDBERG LIB
6193 Murdough Center
Hanover, NH 03755-3560

DEFENCE RESEARCH ESTAB. LIB.
3701 Carling Avenue
Ottowa, ON, K1A 0Z4 CANADA

DLR-STANDORTBIBLIOTEK
Muenchnerstrasse 20
Wessling, Germany 82234

DPS/LIBRARY (EABV)
Alion Science & Technology
185 Admiral Cochrane Drive
Annapolis, MD 214017307

DSTO-DSTORL EDINBURGH
Jets AU/33851-99, PO Box 562
Milsons Point, NSW
AUSTRALIA 1565

DTIC-OCP/LIBRARY
8725 John J. Kingman Rd. Ste 0944
Ft. Belvoir, VA 22060-6218

ELLEDIEMME SRL
Via Baccina 30
Roma, Italy 00184

ELSEVIER
Bibliographic Databases
PO Box 2227
Amsterdam, Netherlands 1000 CE

ENGINEERING INFORMATION, INC
PO Box 543
Amsterdam, Netherlands 1000 Am

ETSE TELECOMUNICACION
Biblioteca, Campus Lagoas
Vigo, 36200 SPAIN

FGAN-FHR
Neuenahrerstrasse 20
Wachtberg, Germany 53343

FLORIDA INTERNATIONAL UNIV.
ECE Dept./EAS-3983
10555 W. Flagler St
Miami, FL 33174

GEORGIA TECH LIBRARY
225 North Avenue, NW
Atlanta, GA 30332-0001

HRL LABS, RESEARCH LIBRARY
3011 Malibu Canyon
Malibu, CA 90265

IEE INSPEC/Acquisitions Section
Michael Faraday House
6 Hills Way
Stevenage, Herts UK SG1 2AY

IND CANTABRIA
PO Box 830470
Birmingham, AL 35283

INSTITUTE FOR SCIENTIFIC INFO.
Publication Processing Dept.
3501 Market St.
Philadelphia, PA 19104-3302

LIBRARY of CONGRESS
Reg. Of Copyrights
Attn: 40T Deposits
Washington DC, 20559

LINDA HALL LIBRARY
5109 Cherry Street
Kansas City, MO 64110-2498

MISSISSIPPI STATE UNIV LIBRARY
PO Box 9570
Mississippi State, MS 39762

MIT LINCOLN LABORATORY
Periodicals Library
244 Wood Street
Lexington, MA 02420

NA KANSAI KINOKUNNA CO.
Attn: M. MIYOSHI
PO Box 36 (NDLA KANSAI)
Hongo, Tokyo, JAPAN 113-8688

NATL. CTR. FOR HIGH-PERFORMANCE COMPUTING LIB.
PO Box 117-00930
Taipei City, Taiwan (ROC) 10699

NATL. GROUND INTELL. CENTER
2055 Boulders Road
Charlottesville, VA 22911-8318

NAVAL POSTGRADUATE SCHOOL
Attn:J. Rozdal/411 Dyer Rd./ Rm 111
Monterey, CA 93943-5101

NAVAL RESEARCH LABORATORY
C. Office, 4555 Overlook Avenue, SW
Washington, DC 20375

OHIO STATE UNIVERSITY
1320 Kinnear Road
Columbus, OH 43212

OVIEDO LIBRARY
PO BOX 830679
Birmingham, AL 35283

PAIKNAM ACAD. INFO CTR LIB.
Hanyang U/17 Haengdang-Dong
Seongdong-ki, Seoul, S Korea 133-791

PENN STATE UNIVERSITY
126 Paterno Library
University Park, PA 16802-1808

PHILIPS RESEARCH LAB
Cross Oak Lane, Stella Cox, Salfords
Red Hill, UK RH1 5HA

RENTON TECH LIBRARY/BOEING
PO BOX 3707
SEATTLE, WA 98124-2207

SOUTHWEST RESEARCH INST.
6220 Culebra Road
San Antonio, TX 78238

SWEDISH DEFENCE RES. AGENCY (FOI)
PO Box 1165
Linkoping, Sweden S-58111

SWETS INFORMATION SERVICES
160 Ninth Avenue, Suite A
Runnemede, NJ 08078

SYRACUSE UNIVERSITY
EECS, 121 Link Hall
Syracuse, NY 13244

TECHNISCHE UNIV. DELFT
Mekelweg 4, Delft, Holland, 2628 CD
NETHERLANDS

TIB & UNIV. BIB. HANNOVER
DE/5100/G1/0001
Welfengarten 1B
Hannover, GERMANY 30167

TOKYO KOKA UNIVERSITY
1404-1 Katakura-Cho
Hachioji, Tokyo, JAPAN 192-0914

UNIV OF CENTRAL FLORIDA LIB.
4000 Central Florida Boulevard
Orlando, FL 32816-8005

UNIV OF COLORADO LIBRARY
Campus Box 184
Boulder, CO 80309-0184

UNIVERSITY OF MISSISSIPPI
John Davis Williams Library
PO Box 1848
University, MS 38677-1848

UNIV OF MISSOURI-ROLLA LIB.
1870 Miner Circle
Rolla, MO 65409-0001

USAE ENG. RES. & DEV. CENTER
Attn: Library/Journals
72 Lyme Road
Hanover, NH 03755-1290

USP POLI
Av: Elmira Martins Moreira, 455
Jacarei, Sao Paulo, Brazil 12306-730

# ACES COPYRIGHT FORM

This form is intended for original, previously unpublished manuscripts submitted to ACES periodicals and conference publications. The signed form, appropriately completed, MUST ACCOMPANY any paper in order to be published by ACES. PLEASE READ REVERSE SIDE OF THIS FORM FOR FURTHER DETAILS.

TITLE OF PAPER:

AUTHORS(S)

PUBLICATION TITLE/DATE:

RETURN FORM TO:

Dr. Atef Z. Elsherbeni
University of Mississippi
Dept. of Electrical Engineering
Anderson Hall Box 13
University, MS 38677 USA

## PART A - COPYRIGHT TRANSFER FORM

(NOTE: Company or other forms may not be substituted for this form. U.S. Government employees whose work is not subject to copyright may so certify by signing Part B below. Authors whose work is subject to Crown Copyright may sign Part C overleaf).

The undersigned, desiring to publish the above paper in a publication of ACES, hereby transfer their copyrights in the above paper to The Applied Computational Electromagnetics Society (ACES). The undersigned hereby represents and warrants that the paper is original and that he/she is the author of the paper or otherwise has the power and authority to make and execute this assignment.

**Returned Rights**: In return for these rights, ACES hereby grants to the above authors, and the employers for whom the work was performed, royalty-free permission to:

1. Retain all proprietary rights other than copyright, such as patent rights.
2. Reuse all or portions of the above paper in other works.
3. Reproduce, or have reproduced, the above paper for the author's personal use or for internal company use provided that (a) the source and ACES copyright are indicated, (b) the copies are not used in a way that implies ACES endorsement of a product or service of an employer, and (c) the copies per se are not offered for sale.
4. Make limited distribution of all or portions of the above paper prior to publication.
5. In the case of work performed under U.S. Government contract, ACES grants the U.S. Government royalty-free permission to reproduce all or portions of the above paper, and to authorize others to do so, for U.S. Government purposes only.

**ACES Obligations**: In exercising its rights under copyright, ACES will make all reasonable efforts to act in the interests of the authors and employers as well as in its own interest. In particular, ACES REQUIRES that:

1. The consent of the first-named author be sought as a condition in granting re-publication permission to others.
2. The consent of the undersigned employer be obtained as a condition in granting permission to others to reuse all or portions of the paper for promotion or marketing purposes.

In the event the above paper is not accepted and published by ACES or is withdrawn by the author(s) before acceptance by ACES, this agreement becomes null and void.

AUTHORIZED SIGNATURE — TITLE (IF NOT AUTHOR)

EMPLOYER FOR WHOM WORK WAS PERFORMED — DATE FORM SIGNED

## Part B - U.S. GOVERNMENT EMPLOYEE CERTIFICATION

(NOTE: if your work was performed under Government contract but you are not a Government employee, sign transfer form above and see item 5 under Returned Rights).

This certifies that all authors of the above paper are employees of the U.S. Government and performed this work as part of their employment and that the paper is therefor not subject to U.S. copyright protection.

AUTHORIZED SIGNATURE — TITLE (IF NOT AUTHOR)

NAME OF GOVERNMENT ORGANIZATION — DATE FORM SIGNED

## PART C - CROWN COPYRIGHT

(NOTE: ACES recognizes and will honor Crown Copyright as it does U.S. Copyright. It is understood that, in asserting Crown Copyright, ACES in no way diminishes its rights as publisher. Sign only if *ALL* authors are subject to Crown Copyright).

This certifies that all authors of the above Paper are subject to Crown Copyright. (Appropriate documentation and instructions regarding form of Crown Copyright notice may be attached).

AUTHORIZED SIGNATURE TITLE OF SIGNEE

NAME OF GOVERNMENT BRANCH DATE FORM SIGNED

**Information to Authors**

**ACES POLICY**

ACES distributes its technical publications throughout the world, and it may be necessary to translate and abstract its publications, and articles contained therein, for inclusion in various compendiums and similar publications, etc. When an article is submitted for publication by ACES, acceptance of the article implies that ACES has the rights to do all of the things it normally does with such an article.

In connection with its publishing activities, it is the policy of ACES to own the copyrights in its technical publications, and to the contributions contained therein, in order to protect the interests of ACES, its authors and their employers, and at the same time to facilitate the appropriate re-use of this material by others.

The new United States copyright law requires that the transfer of copyrights in each contribution from the author to ACES be confirmed in writing. It is therefore necessary that you execute either Part A-Copyright Transfer Form or Part B-U.S. Government Employee Certification or Part C-Crown Copyright on this sheet and return it to the Managing Editor (or person who supplied this sheet) as promptly as possible.

**CLEARANCE OF PAPERS**

ACES must of necessity assume that materials presented at its meetings or submitted to its publications is properly available for general dissemination to the audiences these activities are organized to serve. It is the responsibility of the authors, not ACES, to determine whether disclosure of their material requires the prior consent of other parties and if so, to obtain it. Furthermore, ACES must assume that, if an author uses within his/her article previously published and/or copyrighted material that permission has been obtained for such use and that any required credit lines, copyright notices, etc. are duly noted.

**AUTHOR/COMPANY RIGHTS**

If you are employed and you prepared your paper as a part of your job, the rights to your paper initially rest with your employer. In that case, when you sign the copyright form, we assume you are authorized to do so by your employer and that your employer has consented to all of the terms and conditions of this form. If not, it should be signed by someone so authorized.

**NOTE RE RETURNED RIGHTS**: Just as ACES now requires a signed copyright transfer form in order to do "business as usual", it is the intent of this form to return rights to the author and employer so that they too may do "business as usual". If further clarification is required, please contact: The Managing Editor, R. W. Adler, Naval Postgraduate School, Code EC/AB, Monterey, CA, 93943, USA (831)656-2352.

Please note that, although authors are permitted to re-use all or portions of their ACES copyrighted material in other works, this does not include granting third party requests for reprinting, republishing, or other types of re-use.

**JOINT AUTHORSHIP**

For jointly authored papers, only one signature is required, but we assume all authors have been advised and have consented to the terms of this form.

**U.S. GOVERNMENT EMPLOYEES**

Authors who are U.S. Government employees are not required to sign the Copyright Transfer Form (Part A), but any co-authors outside the Government are.

Part B of the form is to be used instead of Part A only if all authors are U.S. Government employees and prepared the paper as part of their job.

**NOTE RE GOVERNMENT CONTRACT WORK**: Authors whose work was performed under a U.S. Government contract but who are not Government employees are required so sign Part A-Copyright Transfer Form. However, item 5 of the form returns reproduction rights to the U. S. Government when required, even though ACES copyright policy is in effect with respect to the reuse of material by the general public.

**APPLIED COMPUTATIONAL ELECTROMAGNETICS SOCIETY JOURNAL**
**http://aces.ee.olemiss.edu**

# INFORMATION FOR AUTHORS

## PUBLICATION CRITERIA

Each paper is required to manifest some relation to applied computational electromagnetics. **Papers may address general issues in applied computational electromagnetics, or they may focus on specific applications, techniques, codes, or computational issues.** While the following list is not exhaustive, each paper will generally relate to at least one of these areas:

1. **Code validation.** This is done using internal checks or experimental, analytical or other computational data. Measured data of potential utility to code validation efforts will also be considered for publication.

2. **Code performance analysis.** This usually involves identification of numerical accuracy or other limitations, solution convergence, numerical and physical modeling error, and parameter tradeoffs. However, it is also permissible to address issues such as ease-of-use, set-up time, run time, special outputs, or other special features.

3. **Computational studies of basic physics.** This involves using a code, algorithm, or computational technique to simulate reality in such a way that better, or new physical insight or understanding, is achieved.

4. **New computational techniques**, or new applications for existing computational techniques or codes.

5. **"Tricks of the trade"** in selecting and applying codes and techniques.

6. **New codes, algorithms, code enhancement, and code fixes.** This category is self-explanatory, but includes significant changes to existing codes, such as applicability extensions, algorithm optimization, problem correction, limitation removal, or other performance improvement. **Note: Code (or algorithm) capability descriptions are not acceptable, unless they contain sufficient technical material to justify consideration.**

7. **Code input/output issues.** This normally involves innovations in input (such as input geometry standardization, automatic mesh generation, or computer-aided design) or in output (whether it be tabular, graphical, statistical, Fourier-transformed, or otherwise signal-processed). Material dealing with input/output database management, output interpretation, or other input/output issues will also be considered for publication.

8. **Computer hardware issues.** This is the category for analysis of hardware capabilities and limitations of various types of electromagnetics computational requirements. Vector and parallel computational techniques and implementation are of particular interest.

Applications of interest include, but are not limited to, antennas (and their electromagnetic environments), networks, static fields, radar cross section, shielding, radiation hazards, biological effects, electromagnetic pulse (EMP), electromagnetic interference (EMI), electromagnetic compatibility (EMC), power transmission, charge transport, dielectric, magnetic and nonlinear materials, microwave components, MEMS technology, MMIC technology, remote sensing and geometrical and physical optics, radar and communications systems, fiber optics, plasmas, particle accelerators, generators and motors, electromagnetic wave propagation, non-destructive evaluation, eddy currents, and inverse scattering.

Techniques of interest include frequency-domain and time-domain techniques, integral equation and differential equation techniques, diffraction theories, physical optics, moment methods, finite differences and finite element techniques, modal expansions, perturbation methods, and hybrid methods. This list is not exhaustive.

A unique feature of the Journal is the publication of unsuccessful efforts in applied computational electromagnetics. Publication of such material provides a means to discuss problem areas in electromagnetic modeling. Material representing an unsuccessful application or negative results in computational electromgnetics will be considered for publication only if a reasonable expectation of success (and a reasonable effort) are reflected. Moreover, such material must represent a problem area of potential interest to the ACES membership.

Where possible and appropriate, authors are required to provide statements of quantitative accuracy for measured and/or computed data. This issue is discussed in "Accuracy & Publication: Requiring, quantitative accuracy statements to accompany data," by E. K. Miller, *ACES Newsletter*, Vol. 9, No. 3, pp. 23-29, 1994, ISBN 1056-9170.

## EDITORIAL REVIEW

**In order to ensure an appropriate level of quality control**, papers are peer reviewed. They are reviewed both for technical correctness and for adherence to the listed guidelines regarding information content.

## JOURNAL CAMERA-READY SUBMISSION DATES

| | |
|---|---|
| March issue | deadline 8 January |
| July issue | deadline 20 May |
| November issue | deadline 20 September |

Uploading an acceptable camera-ready article after the deadlines will result in a delay in publishing this article.

## STYLE FOR CAMERA-READY COPY

The ACES Journal is flexible, within reason, in regard to style. However, certain requirements are in effect:

1. The paper title should NOT be placed on a separate page. The title, author(s), abstract, and (space permitting) beginning of the paper itself should all be on the first page. The title, author(s), and author affiliations should be centered (center-justified) on the first page.

2. An abstract is REQUIRED. The abstract should be a brief summary of the work described in the paper. It should state the computer codes, computational techniques, and applications discussed in the paper (as applicable) and should otherwise be usable by technical abstracting and indexing services.

3. Either British English or American English spellings may be used, provided that each word is spelled consistently throughout the paper.

4. Any commonly-accepted format for referencing is permitted, provided that internal consistency of format is maintained. As a guideline for authors who have no other preference, we recommend that references be given by author(s) name and year in the body of the paper (with alphabetical listing of all references at the end of the paper). Titles of Journals, monographs, and similar publications should be in italic font or should be underlined. Titles of papers or articles should be in quotation marks.

5. Internal consistency shall also be maintained for other elements of style, such as equation numbering. As a guideline for authors who have no other preference, we suggest that equation numbers be placed in parentheses at the right column margin.

6. The intent and meaning of all text must be clear. For authors who are NOT masters of the English language, the ACES Editorial Staff will provide assistance with grammar (subject to clarity of intent and meaning).

7. Unused space should be minimized. Sections and subsections should not normally begin on a new page.

## PAPER FORMAT

The preferred format for initial submission and camera-ready manuscripts is 12 point Times Roman font, single line spacing and double column format, similar to that used here, with top, bottom, left, and right 1 inch margins. Manuscripts should be prepared on standard 8.5x11 inch paper.

Only camera-ready electronic files are accepted for publication. The term **"camera-ready" means that the material is neat, legible, and reproducible.** Full details can be found on ACES site, Journal section.

ACES reserves the right to edit any uploaded material, however, this is not generally done. It is the author(s) responsibility to provide acceptable camera-ready pdf files. Incompatible or incomplete pdf files will not be processed, and authors will be requested to re-upload a revised acceptable version.

## SUBMITTAL PROCEDURE

All submissions should be uploaded to ACES server through ACES web site (http://aces.ee.olemiss.edu) by using the upload button, journal section. Only pdf files are accepted for submission. The file size should not be larger than 5MB, otherwise permission from the Editor-in-Chief should be obtained first. The Editor-in-Chief will acknowledge the electronic submission after the upload process is successfully completed.

## COPYRIGHTS AND RELEASES

Each primary author must sign a copyright form and obtain a release from his/her organization vesting the copyright with ACES. Copyright forms are available at ACES, web site (http://aces.ee.olemiss.edu). To shorten the review process time, the executed copyright form should be forwarded to the Editor-in-Chief immediately after the completion of the upload (electronic submission) process. Both the author and his/her organization are allowed to use the copyrighted material freely for their own private purposes.

Permission is granted to quote short passages and reproduce figures and tables from and ACES Journal issue provided the source is cited. Copies of ACES Journal articles may be made in accordance with usage permitted by Sections 107 or 108 of the U.S. Copyright Law. This consent does not extend to other kinds of copying, such as for general distribution, for advertising or promotional purposes, for creating new collective works, or for resale. The reproduction of multiple copies and the use of articles or extracts for commercial purposes require the consent of the author and specific permission from ACES. Institutional members are allowed to copy any ACES Journal issue for their internal distribution only.

## PUBLICATION CHARGES

ACES members are allowed 12 printed pages per paper without charge; non-members are allowed 8 printed pages per paper without charge. Mandatory page charges of $75 a page apply to all pages in excess of 12 for members or 8 for non-members. Voluntary page charges are requested for the free (12 or 8) pages, but are NOT mandatory or required for publication. A priority courtesy guideline, which favors members, applies to paper backlogs. Authors are entitled to 15 free reprints of their articles and must request these from the Managing Editor. Additional reprints are available to authors, and reprints available to non-authors, for a nominal fee.

**ACES Journal is abstracted in INSPEC, in Engineering Index, and in DTIC.**